Faculty of Engineering, Computer and Mathematical Sciences
SCHOOL OF MECHANICAL ENGINEERING

Modelling and design of magnetic levitation systems for vibration isolation

William Samuel Parker Robertson

A thesis submitted in fulfilment of the requirements for the degree of Doctor of Philosophy

November 2013

Supervisors: Assoc. Prof. Ben Cazzolato
Assoc. Prof. Anthony Zander

Submission date: August 9, 2013
Amendment date: November 26, 2013

School of Mechanical Engineering
The University of Adelaide, 5005
SA, Australia

Declaration

I certify that this work contains no material which has been accepted for the award of any other degree or diploma in any university or other tertiary institution and, to the best of my knowledge and belief, contains no material previously published or written by another person, except where due reference has been made in the text. In addition, I certify that no part of this work will, in the future, be used in a submission for any other degree or diploma in any university or other tertiary institution without the prior approval of the University of Adelaide and where applicable, any partner institution responsible for the joint-award of this degree. ¶ I give consent to this copy of my thesis, when deposited in the University Library, being made available for loan and photocopying, subject to the provisions of the Copyright Act 1968. ¶ I also give permission for the digital version of my thesis to be made available on the web, via the University's digital research repository, the Library catalogue and also through web search engines, unless permission has been granted by the University to restrict access for a period of time.

SIGNED DATED

Acknowledgements & Dedication

Thanks to my supervisors Ben and Anthony, who gave me the freedom to be myself and who inspired me beyond my work. My appreciation couldn't be greater for the long leash they allowed me. With stricter guidance I may have finished sooner, but I believe neither I nor this thesis would have been the better for it.

This thesis is dedicated to those many with whom I've shared this happy life, especially to those in this time who have come into this strange world and to those who have departed from it.

Abstract

Vibration disturbance has a consistent negative impact on equipment and processes. The central theme of this thesis is the investigation of using permanent magnets in the design of a system for vibration isolation.

The thesis begins with a comprehensive literature review on the subjects of passive and active vibration isolation, permanent magnetic systems, and the common area between these on nonlinear vibration systems using magnetic forces. The use of cylindrical and cuboid magnets is the primary focus of this work for which analytical solutions are known for calculating forces and torques. Subsequently, the state of the art in analytical modelling of permanent magnet systems is covered, including a contribution in this area for calculating the forces between cylindrical magnets.

A range of load bearing designs using simple permanent magnet arrangements are examined, with multiple designs suitable for a variety of objectives. A particular emphasis is placed on a system using inclined magnets, which can exhibit a load-independent resonance frequency. Load bearing using multipole magnet arrays is also discussed, in which a large number of magnets are used to generate more complex magnetic fields. A variety of multipole arrays are compared against each other, including linear and planar magnetisation patterns, and an optimisation is performed on a linear array with some resulting guidelines for designing such systems for load bearing.

Permanent magnet levitation requires either passive or active stabilisation; therefore, the design of electromagnetic actuators for active control is covered with a new efficient method for calculating the forces between a cylindrical magnet and a solenoid. The optimisation of a solenoid actuator is performed and geometric parameters are found which are near-optimal for a range of operating conditions.

Two quasi–zero stiffness systems are introduced and analysed next. These systems are designed with a nonlinearity such that low stiffnesses are achieved while bearing large loads. The first system analysed is a purely mechanical device using linear springs; unlike most analyses of this design, the horizontal forces are also considered and it is shown that quasi–zero stiffness is capable in all translational directions simultaneously. However, a notable disadvantage of such spring systems is their difficulty in online tuning to adapt to changing operating conditions. A magnetic quasi–zero stiffness system is then analysed in detail and design criteria are introduced, providing a design framework for such systems and showing how the complex interaction of variables affects the resulting dynamic behaviour. Although the system is nonlinear, the effects of the nonlinearities on the vibration response are shown to be generally negligible.

The thesis concludes with some experimental results of the same quasi–zero stiffness system, constructed as a single degree of freedom prototype. The quasi-static and dynamic behaviour of the system matches the theory well, and active vibration control is performed to improve the vibration isolation characteristics of the device.

Table of Contents

List of Tables

List of Figures

Most mathematical symbols used in this document are listed herein with page number cross-referencing. Page numbers listed will not include where these symbols are used in graphs or some figures. There are some cases where the same symbol has been used for multiple purposes; these should be unambiguous based on the context of the work.

In mathematical contexts, care has been take to be consistent in the use of parentheses for function arguments (such as $f(x) = x^2$) and square brackets for both grouping ($A \times \left[B \times C\right]$) and vector/matrix notation ($\mathbf{F} = \left[F_x, F_y, F_z\right]^\mathsf{T}$).

Symbol	Description	Page
$\mathbf{A}$	Vector area (direction normal to plane)	48, 52
A	Area	58, 59
A_e	Amplitude of sinusoidal base excitation	40, 208–211
a	Half-length of cuboid magnet, $\hat{x}$ direction	60, 62, 65, 67, 68
a	Cuboid magnet depth	80, 84, 109, 110
a	Cube magnet side length	xii, xiii, 64, 65, 192–194, 196–209
a_w	Cross-sectional area of the wire in the coil	166
$\mathbf{B}$	Magnetic flux density vector	28, 33, 48–52, 57, 59, 158
B_r	Remanence magnetisation	50–52, 55, 58, 61–68, 73, 75, 76, 120, 144, 146, 155, 157–159, 161, 164, 167, 195–197, 215
b	Cuboid magnet face side length	80, 84, 108–110, 133–136, 138, 139, 141
b	Half-length of cuboid magnet, $\hat{y}$ direction	60, 62, 65, 67–69
$\left[BH\right]_{\max}$	Maximum energy product	51, 55
C_i	Compression of the inclined springs at quasi–zero stiffness	189
C_v	Compression of the vertical spring at quasi–zero stiffness	189
c	Relative velocity damping coefficient	xxiii, 5, 7, 8, 16, 119, 120
c	Damping coefficient	5, 7–10, 18, 41, 43, 85, 206, 208, 226, 231–233
c	Half-length of cuboid magnet, $\hat{z}$ direction	60, 62, 65, 67, 68
c	Cube magnet side length	91, 103, 106

Symbol	Description	Page
c_a	Damping coefficient of the vibration neutraliser	16, 18
$\mathbf{d}$	Distance vector between the centres of two magnets, $\mathbf{d} = \left[d_x, d_y, d_z\right]^\mathsf{T}$	xv, 60, 62, 63, 65–67, 73
$\mathbf{d}_1$	Position vector for differential magnet volume in cylindrical coordinates $\mathbf{d}_1 = \left[r_1, \phi_1, z_1\right]^\mathsf{T}$	xv, 158
$\mathbf{d}_2$	Position vector for differential coil volume in cylindrical coordinates, $\mathbf{d}_2 = \left[r_2, \phi_2, z_2\right]^\mathsf{T}$	xv, 158
d	Inclined magnets horizontal offset at the nominal position	108–112, 114, 117–120
d	Normalised magnet gap	xii, xiii, xix, 192–195, 197–211
d	Magnetic spring depth	103, 105, 106, 133
d_w	Diameter of wire	166–171, 173
e_r	Radial distance between two cylindrical objects	164, 165
$\mathbf{F}$	Force vector	57, 58, 68, 99, 109, 110, 116, 118, 119, 158
$\mathbf{F}_{z,x}$	Force between two cuboid magnets; the first magnetised in the $\hat{z}$ direction, the second in $\hat{x}$	66
$\mathbf{F}_{z,y}$	Force between two cuboid magnets; the first magnetised in the $\hat{z}$ direction, the second in $\hat{y}$	xxiii, 63, 66, 78
$\mathbf{F}_{z,z}$	Force between two cuboid magnets both magnetised in the $\hat{z}$ direction	xxiv, 61, 65, 66, 78, 80, 81, 109, 118
$\mathbf{F}_{\text{eddy}}$	Eddy current force vector	33
F	Magnitude of force	41, 68, 78, 80, 81, 85, 93, 102, 107, 110–113, 119, 120, 169–171, 173, 224
$F(s)$	Force input response, Laplace domain	231, 232
F_c	Axial force between a thick coil and a magnet	156–159, 164, 167–169, 175, 176
F_f	Axial force between two circular current loops	156, 164
F_g	Gravity force	102
F_r	Radial force between two cylindrical thin coils/magnets	78
F_T	Quasi–zero stiffness vertical magnet force function	194, 206
F_z	Axial force between two cylindrical thin coils/magnets	76, 78, 157
F_{attr}	Magnet force (attraction magnet)	194
F_{repl}	Magnet force (repulsion magnet)	194

Symbol	Description	Page
F_i	Force characteristic of the inclined spring, with vertical component F_{i_v} and horizontal component F_{i_h}	xvi, 182, 186
F_v	Force characteristic of the vertical spring, with vertical component F_{v_v} and horizontal component F_{v_h}	xvi, 182, 186
F_t	Force characteristic of the overall inclined spring quasi–zero stiffness mechanism, with vertical component F_{t_v} and horizontal component F_{t_h}	xvi, 182–186
F_s	Magnet force for coaxial cube magnets	64, 81, 193, 194, 196, 197
f	Force input	5–7, 231, 233
f_a	Active force input for an inertial mass or vibration neutraliser	viii, 16, 17
f_d	Force disturbance	5
f_q	Normalised force at equilibrium	198, 199
f_T	Normalised Quasi–zero stiffness vertical magnet force	194, 197–200, 206
f_s	Normalised magnet force for coaxial cube magnets	64, 193–195
$\mathbf{G}$	Force vector between inclined magnets in the local coordinate systems of the fixed magnet	109
G	Axial gap between the dual coils	175, 176, 219
G	Gap between magnets in various magnetic spring designs	91, 99, 100, 103, 133, 141, 142
$G(s)$	Transfer function	231–233
g	Acceleration due to gravity	85, 107, 111, 119, 120, 179, 198, 200, 206, 224
g	Normalised magnet gap	222, 226
g_a	Feedback gain on relative acceleration	7–9, 11
g_c	Feedback gain on relative velocity	7, 8, 10, 11
g_d	Feedback gain on absolute acceleration	7–9, 11
g_k	Feedback gain on relative displacement	7–9, 11, 85
g_m	Feedback gain on absolute displacement	7–9, 11
g_v	Feedback gain on absolute velocity	7, 8, 10, 11, 232, 233
$\mathbf{H}$	Magnetic field strength vector	48–51
H	Height of the apparatus	214, 215, 222–224
H	Length of vertical spring under load	181, 183, 186, 189
H_0	Undeflected vertical spring length	180, 181, 183, 189
H_c	Coercivity	51, 52
h	Inclined spring vertical dimension	180–183, 186

Symbol	Description	Page
h	Multipole array height	133, 136–138, 140, 141
h	Normalised nominal magnet displacement	192, 194, 195, 197–199, 201, 206, 210
h_b	Beam height	215, 223
h_c	Height of the coil	219
h_m	Height of the magnets support	214, 215, 222–224
h_q	Normalised displacement at equilibrium	198–201, 205, 206, 208
h_s	Height of the laser sensor	214, 215, 223
h_ϵ	Height 'buffer' to account for additional thicknesses	222, 224
I	Current	48, 75, 155–159, 161, 164, 167, 170, 171, 175
I_m	Inclined magnet system moment of inertia	119, 120
i	The imaginary number $\sqrt{-1}$	7, 8, 10, 226
i	Magnet index in the $\hat{x}$ direction.	144–147
$\mathbf{J}$	Current density vector	48, 158
$\mathbf{J}_m$	Equivalent 'surface current' vector due to magnetisation	48
$\mathbf{J}_{\text{eddy}}$	Eddy current density vector	33
j	Magnet index in the $\hat{y}$ direction.	144–147
$\mathbf{K}_{z,y}$	Stiffness between two cuboid magnets; the first magnetised in the $\hat{z}$ direction, the second in $\hat{x}$	63
$\mathbf{K}_{z,z}$	Stiffness between two cuboid magnets magnetised in the $\hat{z}$ direction	xxiii, 62
K	Magnitude of stiffness characteristic (derivative of force with respect to displacement)	87–90, 92
$K_c(s)$	Controller transfer function	232, 233
K_h	Stiffness characteristic in the horizontal direction	186, 187
K_q	Stiffness at equilibrium	200, 205, 208, 210
K_T	Quasi–zero stiffness vertical magnet stiffness function	194, 200, 206, 208, 210
K_v	Stiffness characteristic in the vertical direction	184
K_{attr}	Magnet stiffness (attraction magnet)	205
K_{repl}	Magnet stiffness (repulsion magnet)	205
K_s	Magnet stiffness characteristic for coaxial cube magnets	64, 193

Symbol	Description	Page
k	Stiffness coefficient	xxiii, xxiv, 5, 7–10, 16, 18, 39, 41, 43, 107, 110, 111, 113, 120, 179, 224, 226, 231–233
k_i	Inclined spring stiffness	180–184, 187
k_v	Vertical spring stiffness	180–183, 186
k_a	Stiffness of the vibration neutraliser	16, 18
k_T	Normalised Quasi–zero stiffness vertical magnet stiffness	194, 197, 206
k_{lin}	Linearised stiffness at a certain point	43
k_s	Normalised magnet stiffness characteristic for coaxial cube magnets	64, 65, 193, 194
L	Length of inclined spring under load	181, 182, 186, 189
L_0	Undeflected inclined spring length	180–182, 186, 189
L_b	Beam length	215
L_c	Coil length	75, 154, 155, 157–159, 161, 164, 166, 167
L_m	Magnet length	82–84, 154, 155, 157–159, 161, 164, 167, 172, 215, 219, 222–224
$\mathbf{l}$	Displacement vector between magnet centre and centre of mass (lever arm)	118
l	Lever arm	103, 105, 117–120
l	Multipole array length	133–136, 138
l	Normalised nominal magnet displacement	64, 65, 193, 195
l_m	Horizontal offset of the magnets support	214, 215, 223
l_s	Horizontal offset of the laser sensor	214, 215, 223
l_w	Length of the wire in the coil	166, 167
$\mathbf{M}$	Magnetisation vector	28, 48–50, 57, 144, 158
$\hat{\mathbf{M}}$	Unit magnetisation vector	144–147
M_{sat}	Magnetisation at saturation	50, 51
$\mathbf{m}$	Magnetic dipole	48
m	Mass	xxiii, xxiv, 5, 7–10, 16, 18, 41, 43, 85, 107, 119, 120, 179, 198–202, 204–209, 226, 231–233
m_a	Vibration neutraliser mass	16, 18

Symbol	Description	Page
m_{eq}	Equivalent mass	111, 224
N	Magnet grade, units MG Oe	55
N	Multipole array number of magnets	133–136, 144, 146
N	Number of turns in the coil	75, 155, 158, 159, 164, 175
N_m	Magnet equivalent 'turns' for filament current model	156, 157, 161
N_r	Number of turns in the radial direction	155–157, 160, 161, 166, 167, 175
N_z	Number of turns in the axial direction	155–157, 161, 166, 167
$\hat{\mathbf{n}}$	Surface normal vector	57, 158
n	Exponential for empirical magnet force equation	195–197, 200
$P_{bb}(\omega)$	Power spectrum accelerometer measurements of the base disturbance	39, 40, 228
$P_{mb}(\omega)$	Cross spectrum accelerometer measurements between the moving magnet and base disturbance	39, 40
$P_{mm}(\omega)$	Power spectrum accelerometer measurements of the moving magnet	228
$\mathbf{p}$	Displacement vector due to rotation around centre of mass	118
p	Disturbance	41, 43, 85, 86
p	Dual-multipole array horizontal offset	150, 151
p_b	Beam pin origin height	214, 215, 223
p_g	Magnet gap	222, 223
p_m	Low magnet height	214, 215, 222, 224
p_n	High magnet height	214, 215, 222–224
p_q	Quasi–zero stiffness position	222, 223
Q_0	Coefficient for empirical magnet force equation	195–197, 200
Q_1	Coefficient for empirical magnet force equation	195–197, 200
Q_2	Coefficient for empirical magnet force equation	195
Q_3	Coefficient for empirical magnet force equation	195
$q_0(d)$	Polynomial coefficient for modelling magnet force	194, 195
$q_2(d)$	Polynomial coefficient for modelling magnet force	194, 195
$q_4(d)$	Polynomial coefficient for modelling magnet force	194, 195
$\mathbf{R}_x$	Planar rotation matrix around the $\hat{x}$ axis	66, 67
$\mathbf{R}_y$	Planar rotation matrix around the $\hat{y}$ axis	66
$\mathbf{R}_z$	Planar rotation matrix around the $\hat{z}$ axis	66, 109, 118
$\mathbf{R}$	Distance vector between a magnet's centre and one of its corners/nodes (floating magnet)	62, 63, 73

Symbol	Description	Page
R	Multipole array number of magnets per wavelength	133–139
R	Coil resistance	166–171, 173, 218, 219
R_c	Thick coil outer radius	155, 157–159, 161, 164, 166, 167, 175, 219
R_m	Magnet outer radius	82–84, 154–159, 161, 164, 166, 167, 172, 215, 219
$\mathbf{r}$	Distance vector between a magnet's centre and one of its corners/nodes (fixed magnet)	62, 63
r	Euclidean distance of δ, $\sqrt{\delta_x^2 + \delta_y^2 + \delta_z^2}$	62–64
r	Radial component of distance vector in cylindrical coordinates	xv, 158, 163, 164
r	Radius	156, 164, 165
r_c	Thick coil inner radius	154, 155, 157–159, 161, 164, 166, 167, 175, 219
r_g	Clearance between magnet and inner coil radii	154, 167
$\mathbf{S}$	Vector of magnet side lengths (floating)	65–67
S	Integration surface	57, 158
S_f	Factor of safety	171, 173
S_w	White noise variance	41–43
$\mathbf{s}$	Position vector	109, 118
$\mathbf{s}$	Vector of magnet side lengths (fixed)	65–67
s	Differential region of the integration surface	57, 158
s	Laplace variable	xv–xvii, xx, xxi, 7, 8, 231–233
$\mathbf{T}_{z,y}$	Torque between two cuboid magnets; the first magnetised in the $\hat{z}$ direction, the second in $\hat{y}$	78
$\mathbf{T}_{z,z}$	Torque between two cuboid magnets magnetised in the $\hat{z}$ direction	xxiv, 73, 78
T	Period	40
$T(s), T(\omega)$	Transmissibility	xxi, 8, 10, 39, 226, 228, 230, 231
T_{RSS}	Root-sum-square of the transmissibility magnitude	10, 230, 231
T_z	Inclined magnets torque	118, 119
$\mathbf{t}$	Displacement vectors from the spring magnet centres to the centre of rotation in the coordinate system of the magnets	118

Symbol	Description	Page
t	Time	7, 40, 41, 43, 208, 231
t_b	Beam shell thickness	215, 223
U	Potential energy	28
u	Cuboid magnet unit length, cube root of volume	110–112, 114, 117, 119, 120
V	Volume	33, 48, 80, 81, 83, 110, 114, 158, 167–171, 173
$V(\omega)$	Variance gain, alternative of transmissibility T	40
$\mathbf{v}$	Velocity vector	33
v	Differential region of the integration volume	33, 158
W	Multipole array number of wavelengths	133–140
w	Inclined spring horizontal dimension	180–182, 186
w_b	Beam width	215
$X_1(s)$	Base response, Laplace domain	7, 8, 18, 231–233
$X_2(s)$	Vibration mass response, Laplace domain	7, 8, 18, 231–233
$\mathbf{x}$	Displacement vector	57–59
x	Horizontal displacement of the inclined spring	180–187, 189
$\hat{x}$	Cartesian unit vector	x, xiv, xvi–xviii, xx, xxiii, 60, 61, 66, 67, 69, 78, 88, 91, 92, 94–99, 101–103, 105, 106, 109, 118, 121, 124, 144–146, 149, 150
x	Displacement	41, 43, 80, 81, 179, 222, 223
x	Inclined magnets horizontal displacement	109, 110, 112, 118, 119, 121–123
x_1	Base displacement	viii, 5, 7, 8, 16, 40, 192, 206, 208, 220, 221, 231, 233
x_2	Displacement of the vibration mass	viii, 5, 7, 8, 16, 40, 192, 194, 206, 220, 221, 231, 233
x_a	Vibration neutraliser displacement	16
x_b	Displacement of the beam at the position of the laser sensor from 'zero'	223
x_m	Displacement of the magnets support	223, 224

Symbol	Description	Page
x_p	Projected displacement of the beam to the magnets support	223
x_s	Displacement measured by the laser sensor	214, 215, 222, 223
x_m	Magnet centre position	224
$\hat{y}$	Cartesian unit vector	x, xiv, xvi, xvii, xx, xxiii, 60, 61, 63, 66, 68, 70, 71, 86, 90, 94–98, 103–105, 107, 109, 121, 123, 124, 144–146, 149–151
y	Horizontal displacement	85, 86, 149, 150
y	Inclined magnets vertical displacement	108–111, 113, 118–123
$\hat{z}$	Cartesian unit vector	x, xiv, xvi, xviii, xx, xxiii, xxiv, 60, 61, 63, 66, 68, 70, 71, 86, 88, 91–99, 101–107, 109, 117, 118, 144–146, 149, 150
z	Axial displacement	155–159, 164, 165, 167–169, 175, 176
z	Vertical displacement	85, 86, 99, 100, 103, 136, 140, 141, 149, 150, 180–186, 189, 217
z	Axial component of distance vector in cylindrical coordinates	xv, 158, 164
z	Inclined magnets out-of-plane displacement	109, 110, 118
$z_{\min}$	Maximum deflection of the vertical spring	183
α	Ratio between the inclined and vertical spring stiffnesses	180, 181, 183, 184, 187–190
α	Cylindrical magnet aspect ratio	82–84, 154, 155, 167–170, 173
β	Coil aspect ratio	154, 155, 167–170, 173
γ	Ratio between the inclined spring width and height	xxii, 182–187, 189
γ	Ratio between magnet lengths in a quasi-Halbach array	138, 140
γ	Square-face cuboid magnet aspect ratio	80, 81, 84, 110, 120
$\boldsymbol{\delta}$	Distance vector between a pair of corners/nodes of two magnets, $\boldsymbol{\delta} = \left[\delta_x, \delta_y, \delta_z\right]^\mathsf{T}$	xx, xxii, 61–63, 73

Symbol	Description	Page
δ	Maximum displacement bound	199, 201–203, 205–207
δ	Displacement increment	110, 111, 113
ϵ	Percentage difference between γ and γ_{QZS}	185, 186
ϵ	Closest (normalised) allowable displacement from quasi–zero stiffness to avoid instability	199, 201–203, 205, 207
ζ	Damping ratio, $0.5c/\sqrt{km}$.	xxiv, 120, 208, 226, 232, 236
η	Ratio between inclined and vertical spring lengths	180, 181, 183, 184, 186–190
η_k	Nonlinearity measure	206–208, 210
θ	Magnet rotation/inclination	67–70, 72, 108–112, 114, 117–120
ϑ	Multipole array magnetisation rotation between successive magnets	133–135, 146
ϑ_0	Magnetisation direction of the first magnet in a multipole array	133, 146
ϑ_{xz}	Magnetisation direction in the $\hat{x}$–$\hat{z}$ plane of the first magnet in a multipole array	146
ϑ_{yz}	Magnetisation direction in the $\hat{y}$–$\hat{z}$ plane of the first magnet in a multipole array	146
$\boldsymbol{\kappa}_{z,y}$	'Stiffness' between two magnetic nodes for cuboid magnets magnetised in the $\hat{z}$ and $\hat{y}$ directions respectively, used to calculate $\mathbf{K}_{z,z}$	63, 64
$\boldsymbol{\kappa}_{z,z}$	'Stiffness' between two magnetic nodes for cuboid magnets magnetised in the $\hat{z}$ direction, used to calculate $\mathbf{K}_{z,z}$	62, 63
κ	Stiffness ratio	205
λ	Multipole array wavelength	133–136, 139
μ	Magnetic permeability of a material	30, 31, 49, 52
μ_0	Magnetic permeability of the vacuum	48–52, 55, 57, 58, 61–65, 68, 73, 75, 76, 156–158, 164, 274
μ_r	Relative permeability of a material	49, 50
ν	Ratio of magnet length squared to face area	84
ξ	Inclined spring normalised displacement in the load bearing direction	182–185, 187, 188, 190
ρ	Resistivity	166, 167
σ	Conductivity	33
$\boldsymbol{\Phi}$	Magnetic flux vector	52
$\boldsymbol{\phi}_{z,y}$	'Force' between two magnetic nodes for orthogonally-magnetised cuboid magnets, used to calculate $\mathbf{F}_{z,y}$	63

Symbol	Description	Page
$\boldsymbol{\phi}_{z,z}$	'Force' between two magnetic nodes for cuboid magnets magnetised in the $\hat{z}$ direction, used to calculate $\mathbf{F}_{z,z}$	61, 62, 73
ϕ	Angular component of distance vector in cylindrical coordinates	xv, 158, 163, 164
φ	Inclined magnets planar rotation	116–123
$\boldsymbol{\psi}$	'Torque' between two magnetic nodes for cuboid magnets magnetised in the $\hat{z}$ direction, used to calculate $\mathbf{T}_{z,z}$	73
ω	Frequency	xix–xxi, 7, 8, 10, 39, 40, 202, 204, 205, 226, 228, 230–232
ω_d	Resonance frequency, $\omega_n\sqrt{1-\zeta^2}$	200, 206, 207
ω_n	Natural frequency, $\sqrt{k/m}$	xxiv, 107, 111, 179, 208, 224–226

CHAPTER 1

Introduction

§1.1 The central themes of this thesis

Before launching into detail into the various topics under investigation, this section briefly touches on the issues addressed over the entire thesis: vibrations and their isolation and suppression in Section 1.1.1; permanent magnets and their role in the design of supporting structures and other devices in Section 1.1.2; and 'quasi–zero stiffness' systems, which unify in this thesis the fields of vibrations and magnets, in Section 1.1.3. The remainder of this chapter is then devoted to investigating these three broad areas in more detail in Sections 1.2 to 1.4, concluding with the structure and contributions of this thesis (§1.5).

§1.1.1 *The problem of vibrations*

The disturbing effects of vibrations are a well-known and everlasting problem. The transmission of vibrations from a source can only ever be reduced, not eliminated — that is, not without removing the source entirely from the local region affected. And in many cases there is no single source; the very ground itself may be a medium through which undesirable vibrations are transmitted. Earthquakes are an extreme example of this, but on a smaller scale there are continuous time-varying displacements of the 'fixed' ground beneath us.[1] The earth should in fact be considered as a distributed vibrating structure, of very great mass in total, that has a range of displacement profiles dependent on the local surrounding impedance conditions.

Whether the source of the disturbance is near or far, or how it propagates through the ground to arrive at the region of interest, these disturbances can cause a variety of problems on equipment that is required to, ideally, remain absolutely still. A good example is during the electro-lithography performed to construct computer processors, in which nanometre-sized disturbances can affect the overall quality and yield of the silicon wafer produced. Mitigating the effects of a disturbance through the base on which a structure is supported is known as 'vibration isolation' and is the over-arching problem in which the work of this thesis should be put in context.

1. Not to be too earth-centric, but many of the ideas here have a different relevance in off-planet circumstances.

A contrasting vibration problem occurs when some manner of machine causes its own vibration; a well-known example is a washing machine that exerts an oscillating disturbance force on itself through a mass imbalance. This type of vibration problem requires a rather different set of design solutions and often its solution acts in opposition to the vibration isolation problem discussed previously. Reducing the effects of self-induced vibration disturbance will be termed 'vibration suppression' for the purposes of this thesis and will be revisited on occasion herein.

There are a variety of 'classic' solutions for both vibration isolation and vibration suppression. A particularly simple solution for *both* problems is to mount the equipment on a many-tonne slab of concrete, steel, or granite. This is not always practical. Another common approach for vibration isolation is to support the equipment with pneumatic springs. When in operation, these springs provide a low supporting stiffness and low static deflection; they can typically be used to support hundreds of kilograms with a resonance frequency of less than five hertz. Research in these various methods is still ongoing [68, 129, 147, 305].

Other support methods besides pneumatics are able to achieve low stiffness; this is an area that will be further investigated in the literature review. But one method in particular is interesting in this context: permanent magnets can provide low stiffness support without energy expenditure or air supply. Their nonlinear forces in both attraction and repulsion allows the possibility of interesting supporting designs, and their non-contact nature allows their use in vacuum and 'clean-room' environments.

§1.1.2 *Permanent magnets used for mechanical design*

The last twenty years has seen the maturation of the rare earth permanent magnet industry. These magnets are now widely available in large sizes and strong magnetisation at relatively low prices. They are now used in a variety of mechanical designs, including bearings, couplings, and maglev trains, all of which take advantage of non-contact attractive and/or repulsive forces. Magnets can be used to make other magnets move or to keep them in place; there is little limit to the ingenuity of their application. However, due in part to this complex behaviour between them there are few design guidelines to aid their use:

> *It would be virtually impossible to find more than ten men in the United States who can properly design a permanent magnet for a wide variety of products in which the magnet is a critical operational element. [204]*

Their integrated use in force design can be discussed broadly: magnets can be used in conjunction with current-carrying coils to effect time-varying forces (as in shakers and speakers); soft iron can be used to guide the magnetic fields into desired regions or away from unwanted areas (for example, latches and motors); or magnets can be used alone for unique force–displacement characteristics or simply for applying non-contact forces (for example, rotational bearings).

These ideas in mechanics and dynamics have application back to the field of vibrations. A 'synergy' between the two fields is seen in areas such as energy harvesting from ambient vibration, the study of vibration in high-speed magnetic bearings, and one of the main themes of this thesis — nonlinear and/or non-contact forces for vibration isolation supports.

Supporting a mass with a non-contact force can also be called 'levitation', a topic that deserves its own mention. In the mid-1800s, Earnshaw [91] proved that levitation with the force of permanent magnets alone was impossible, although this did not become common knowledge[2] until much later. Exceptions to 'Earnshaw's Theorem', those being systems in which non-contact levitation is possible, include the use of diamagnetic materials and actively-controlled electromagnetics, amongst some others. It is the possibility of overcoming the instability of levitated magnets by active means that is of interest in this thesis.

§1.1.3 *Quasi–zero stiffness systems*

The transition between stable and unstable forces becomes interesting in the context of vibration isolation. Between positive and negative stiffness in a force versus displacement characteristic, there is an inflection point of zero stiffness. This point is termed a 'quasi–zero stiffness' position to emphasise that the dynamic behaviour of the system in this condition can be rather complex and usually unstable. 'True' zero stiffness would imply *no* connection between between the levitated object and the base, as if they were floating in free space — the motion of one would have no effect on the motion of the other.

As systems approach quasi–zero stiffness, their vibration isolation improves as the resonance frequency decreases. Operation at the quasi–zero stiffness position is not possible as the system is, at best, only marginally stable, and the system must be tuned (based on the applied loading) as close to the quasi–zero stiffness position as possible to achieve best results.

2. If it can even be said to be 'commonly known' today. Anecdotal evidence suggests otherwise.

Certain magnetic systems are not the only ones to exhibit quasi–zero stiffness, as will be examined in more detail in Section 1.4.3. The phenomenon was first proposed using inclined springs to achieve negative stiffness with a 'snap-through' mechanism. Magnets are more convenient in many ways than inclined or buckling springs in that the negative stiffness can be applied directly without having to exploit the byproduct of a mechanical spring or linkage arrangement, which can be more bulky.

Active control systems can be used with quasi–zero stiffness systems to improve their performance in one of three ways:

1. Standard active vibration control with velocity feedback;
2. Remove or limit the instability at the quasi–zero stiffness location with a control system;
3. Online tuning of the system for load-independent operation.

Only the first of these strategies is investigated in this thesis.

§1.1.4 *Project context*

The original seed of the idea for this project was to design and build a vibration isolation table using non-contact magnetic springs [115]. This goal can be split into two: the design of a non-contact magnetic spring (suitable for a vibration isolation table); and the design of the vibration isolation table itself.

Vibration isolation tables are generally designed to attenuate natural disturbances from the ground to the tabletop. Current commercial models use pneumatic springs to perform this task, and this project arose out of curiosity: could magnetic springs be used instead?

Using magnets for load bearing brings its own set of challenges. For completely non-contact support, active control must be used to stabilise *at least* one degree of freedom. For the design to be worth investigating, some advantage to using magnets should also be demonstrated.[3]

However, the field of active control has been well-established and the feat of building a stabilising controller for a system with relatively simple dynamics is not worthy of the research for a Ph. D. The work presented in this thesis is the multiplicity of investigations that arose around the idea of building a 'table that floats on magnets', pulling out enough interesting nuggets to prove worthy of the title of 'research'.

3. Although I took much pleasure in explaining over the years that my Ph. D. project was simply to 'build a table that floats on magnets'.

§1.2 Vibrations

The field of active vibration isolation is a broad topic to cover in review; not everything will be able to be covered here, but it is important to have an overview of what has gone before to place this work in context. The literature review that follows is strongly biased towards papers that have been recently published. Tracking their citations backwards will yield a tangled web of prior art in the field of vibration control.

§1.2.1 *Forms of vibration control*

Many descriptions are given to various systems and types of vibration control. As mentioned in the introduction to this chapter, 'vibration isolation' is the main objective of this literature review. It is instructive to illustrate some of the alternatives and define specifically the terminology used in this thesis.

The most basic vibratory or oscillating system is shown in Figure 1.1(a), in which a mass is excited by an external source and behaves with resultant dynamics determined by the linear stiffness and damping of the connection. Such a system can also be excited by internal forces such as a rotating imbalance. The ground to which it is fixed is assumed to have infinite impedance and to have zero displacement. In this system, motion of the mass can be suppressed by increasing the stiffness of the support, since as the mass becomes more greatly coupled with the ground, the input force has a diminishing influence. This behaviour is referred to as 'vibration suppression' in this thesis.

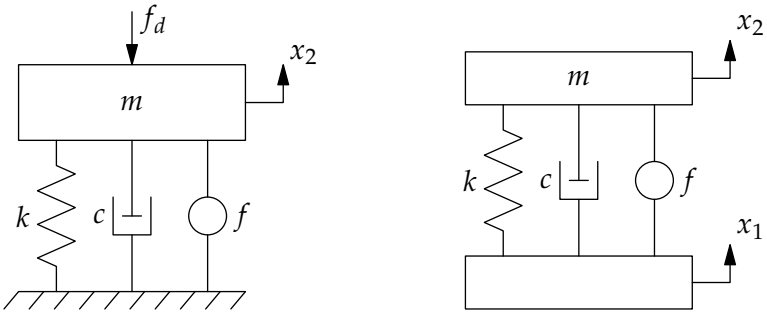

(a) Vibration suppression from disturbance force f_d.

(b) Vibration isolation from disturbance input x_1.

Figure 1.1: Two main types of vibration control problem. In both cases, mass m is being excited and has dynamics according to linear stiffness k and damping c parameters. Input control force f can be generated using feedforward or feedback control to minimise the displacement x_2 of the mass.

If the attachment of the mass in Figure 1.1(a) is assumed *not* to be infinitely massive and stiff, the problem becomes not only to suppress the motion of the mass but also to prevent force transmission from the input disturbance into the base itself. This dual problem is not so easily solved; there is a trade-off in the self-induced displacements of the machinery and the force transmitted to the ground. By lowering the stiffness of the support, the transmitted force is reduced but the self-induced displacements are increased. Due to reciprocity, decreasing the transmitted force from the mass to the ground is equivalent to decreasing any disturbances transmitted from the ground to the mass. Isolating the mass from ground vibration is known in this thesis as 'vibration isolation' and is the main vibratory problem considered herein. For the purposes of this research, there is assumed to be no self-induced vibration in the system. A schematic of this type of vibration isolation system is shown in Figure 1.1(b), for which a practical example is protecting sensitive equipment from ground-based disturbances.

The schematics illustrating vibration suppression and vibration isolation have been shown with active input forces f that can be used to tune or adjust oscillations of the systems. In these examples, it is assumed that the input forces have a negligible effect on the dynamics of the ground or base. Further complications arise when this assumption no longer holds, such as when the device is mounted on a flexible structure with mass that is not much greater than the mass being supported. For the sake of this work, this more complex case is not examined in detail.

§1.2.2 *Shock isolation*

It should be noted that vibration isolation is generally designed to prevent the transmission of broadband noise. For transient signals, a broadband vibration isolation system may not perform as well as a system designed to reject 'shock' inputs. Balandin et al. [26] review the field of optimal control as applied to shock and vibration isolation problems.[4] They differentiate shock and vibration isolation succinctly:

> *The operating quality of shock isolators is usually described in terms of certain characteristics of the transient motion of the body being isolated, whereas the quality of vibration isolators is determined by the characteristics of steady-state forced oscillations.*

4. Their comment that the 'number of papers is so great that there is little incentive to discuss them here' does not bode well for any attempts by me to even summarise their review.

That is, optimising for shock will result in minimising, say, the peak displacement of the mass, whereas optimising for vibration will result in a low natural frequency (characterised by a minimum achievable root-mean-square displacement). Since an optimal controller is based around a cost function that will be dependent both on the vibratory system itself and the mode of disturbance (transient, broadband noise, and so on), such control approaches are heavily case-specific and are best used when a plant is pre-determined and a vibration problem needs to be considered after the fact. Bolotnik et al. [45] discusses these methods in more detail; in this thesis only vibration isolation shall be discussed.

§1.2.3 *Fundamentals of active vibration isolation*

Introduced in the previous section, Figure 1.1(b) shows the simplest form of vibration isolation in which a mass m is mounted with stiffness k and damping c, and with disturbance input x_1. Passive isolation is achieved for zero input control force, $f = 0$. Feedback control allows the properties of the system to be adjusted according the desired vibration response.

The dynamic response of the isolated mass m is

$$m\ddot{x}_2(t) + c\left[\dot{x}_2(t) - \dot{x}_1(t)\right] + k\left[x_2(t) - x_1(t)\right] = f(t)\,. \tag{1.1}$$

First assume that there is no input force; taking the Laplace transform and rearranging produces the transfer function of the system in the frequency domain:

$$\frac{X_2(s)}{X_1(s)} = \frac{cs + k}{ms^2 + cs + k} = \frac{i\omega c + k}{-m\omega^2 + i\omega c + k}. \tag{1.2}$$

For ideal linear state feedback control, the input force can be represented as a linear combination of measured relative displacement $\left[x_2 - x_1\right]$, relative velocity $\left[\dot{x}_2 - \dot{x}_1\right]$, and acceleration $\ddot{x}_2$ of the mass. A force sensor can also be used for feedback purposes, but this yields results for lumped-parameter systems equivalent to acceleration feedback; for vibration isolation of flexible systems, there is evidence to suggest force feedback giving greater stability than acceleration feedback, especially for lightly damped structures [221]. Absolute velocity $\dot{x}_2$ of the mass can be estimated by integrating the acceleration or through geophone measurements of the velocity, absolute displacement x_2 can be estimated through further integration, and for completeness the relative acceleration between the mass and the base $(\ddot{x}_2 - \ddot{x}_1)$ is also considered as a possible signal for feedback control. The generalised feedback force can then be represented by

$$f = g_a\left[\ddot{x}_2 - \ddot{x}_1\right] + g_c\left[\dot{x}_2 - \dot{x}_1\right] + g_k\left[x_2 - x_1\right] + g_m\ddot{x}_2 + g_v\dot{x}_2 + g_d x_2\,, \tag{1.3}$$

where $g_{(\cdot)}$ are feedback gains chosen appropriately for a given application. The term involving g_v is sometimes known as skyhook damping, which is discussed in more detail in Section 1.2.3. Substituting the feedback force Eq. 1.3 into the system dynamics Eq. 1.1 yields

$$g_a\left[\ddot{x}_2 - \ddot{x}_1\right] + \left[c + g_c\right]\left[\dot{x}_2 - \dot{x}_1\right] + \left[k + g_k\right]\left[x_2 - x_1\right] + \left[m + g_m\right]\ddot{x}_2 + g_v\dot{x}_2 + g_d x_2 = 0\,. \quad (1.4)$$

The transfer function, or transmissibility T, between base and mass displacement for this generalised feedback case is

$$T(s) = \frac{X_2(s)}{X_1(s)} = \frac{g_a s^2 + \left[c + g_c\right] s + \left[k + g_k\right]}{\left[m + g_a + g_m\right] s^2 + \left[c + g_v + g_c\right] s + \left[k + g_k + g_d\right]}\,, \quad (1.5)$$

where $s = i\omega$ is the Laplace variable. From Eq. 1.4 it can be seen that there is an exact equivalence between the feedback gains of three of the different signals (g_k, g_c, g_a) and a corresponding physical parameter of the system (k, c, m). Relative displacement and velocity feedback correspond to a variation in the stiffness and damping, respectively, and absolute acceleration feedback to the mass.

Eq. 1.5 describes a system which is stable for characteristic solutions of the denominator (that is, the poles of the system) which have negative real components. These can be analysed easily with the quadratic equation. Note that the feedback gains for the absolute versus relative signals always appear together in the denominator of the transfer function (for example, $g_a + g_m$), and hence affect the stability of the system identically.

To illustrate the effect of various control gains, from transfer function Eq. 1.5 the transmissibility magnitude $|T(i\omega)|$ will be drawn in the following sections with parameters $m = 1\,\mathrm{kg}$, $c = 0.5\,\mathrm{kg/s}$ and $k = 10\,\mathrm{N/m}$, and each of the six control gains $g_{(\cdot)}$ varied independently.

Displacement feedback

Figure 1.2 shows the effect of varying the control gains for relative displacement and absolute displacement (g_k and g_d). In both cases, the resonance frequency is increased with increased feedback gain. This is usually detrimental to vibration isolation performance. Relative displacement feedback corresponds to an increased stiffness and a higher resonance frequency, whereas absolute displacement feedback increases the vibration isolation at low frequencies; this scheme is notable for its less than unity response even as the frequency of excitation tends to zero, while the high frequency attenuation is unaffected.

The system with displacement feedback is stable according to

$$c > \mathrm{Re}\left(\sqrt{c^2 - 4\left[g_k + g_d + k\right] m}\right), \tag{1.6}$$

which holds for all $g_k + g_d > -k$. Therefore, negative feedback gain may be used to lower the resonance frequency of the structure by decreasing the effective stiffness of the system.

This idea presupposes that the absolute displacement is a state that can be measured. Disregarding slow and inaccurate sensors that can do this directly (such as using the Global Positioning System), the absolute displacement of an object can only be estimated based on other measurements of the system. The simplest form of this is by double-integrating an accelerometer signal, such as used by Zhu et al. [311] in combination with other control techniques for vibration isolation in micro-gravity. The filters required to avoid drift of the signal in this case add low frequency poles to the system; as a result, displacement feedback in practice is highly susceptable to low frequency instabilities and cannot reliably be implemented. This topic is discussed further in Section 1.2.5.

Acceleration feedback

Figure 1.3 shows the effect of varying the control gains for relative acceleration and absolute acceleration (g_a and g_m). Absolute acceleration feedback corresponds to an increased system mass, corresponding to a decreased resonance frequency; high frequency vibration isolation is improved. Relative acceleration feedback is only included for completeness; it has the effect of reducing the resonance peak but effectively eliminating any vibration isolation characteristics at higher frequencies. Other vibration schemes for reducing a tonal or narrowband disturbance are discussed briefly in Section 1.2.6.

The system with acceleration feedback is stable according to the inequality

$$\mathrm{Re}\left(\frac{c \pm \sqrt{c^2 - 4k\left[g_a + g_m + m\right]}}{g_a + g_m + m}\right) > 0\,, \tag{1.7}$$

which is true for all $g_a + g_m > -m$. It is therefore possible, albeit generally undesirable, to increase the resonance frequency of the system with negative acceleration gain, which corresponds to an effective decrease of the mass of the system.

Velocity feedback

Acceleration and displacement feedback both primarily affect the resonance frequency of the system; velocity feedback is different. The transmissibilities due to the influence of relative velocity and absolute velocity feedback (g_c and g_v) are shown in Figure 1.4.[5] In both cases the resonance peak is lowered; the relative velocity feedback corresponds to a reduction in attenuation at higher frequencies, while for absolute velocity feedback the high frequency response is unaffected.

Velocity feedback is stable for

$$c + g_v + g_c \pm \mathrm{Re}\left(\sqrt{\left[c + g_v + g_c\right]^2 - 4km}\right) > 0\,, \tag{1.8}$$

which is true for $g_v + g_c > -c$. While increased damping is usually desired, it is possible to reduce the effective damping in the system with negative velocity feedback gain, with the effect of increasing the amplitude of the resonance peak. Such active damping reduction has been performed to aid the efficacy of 'tuned mass dampers' or vibration neutralisers [149], which are discussed briefly in Section 1.2.6.

The absolute and relative velocity feedback results may be compared by calculating the root-sum-square transmissibilities T_{RSS} over a frequency range of interest as a function of increasing feedback gain for the two cases. The root-sum-square transmissibility is calculated as

$$T_{\mathrm{RSS}} = \sqrt{\sum_{\omega=\omega_1}^{\omega_2} \left|T(i\omega)\right|^2}\,, \tag{1.9}$$

and is of interest as it gives a relative measure of the total energy attenuation through the system. The comparison of root-sum-square transmissibilities is shown in Figure 1.5, where the relative feedback case has a local minimum whereas in the absolute feedback case it continuously decreases. It is clear in the ideal case that absolute velocity feedback is the more effective at reducing the total vibration of a system. The maximum frequency in this case was chosen to be much greater than the resonance frequency; $[\omega_1, \omega_2] = [0, 1000\,\mathrm{rad/s}]$.

Absolute velocity feedback control has been widely implemented in the vibrations literature [96, 97, 153, 297, for example]. Instability can occur in cases when the applied control force affects the dynamics of the base, but this is not a problem when considering comparatively massive support structures.

5. In the literature, absolute velocity feedback is often referred to as 'skyhook damping'. This term will generally not be used in this thesis as there is potential for confusion with 'semi-active skyhook damping', a technique discussed later in this chapter which is used in rather different contexts.

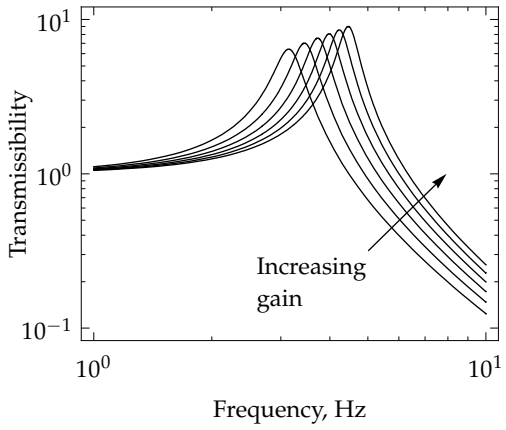

(a) Relative displacement feedback, g_k.

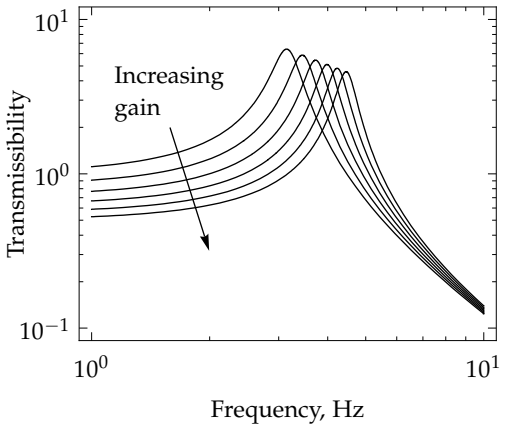

(b) Absolute displacement feedback, g_d.

FIGURE 1.2: Displacement feedback control.

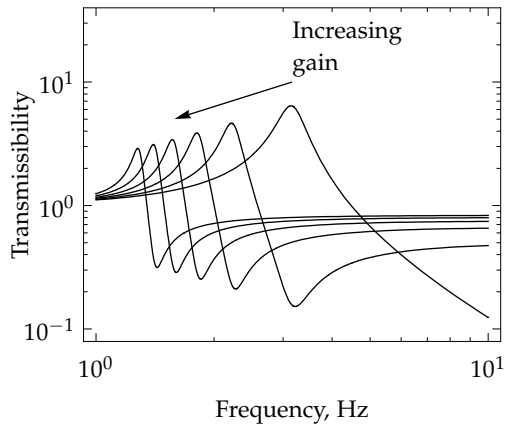

(a) Relative acceleration feedback, g_a.

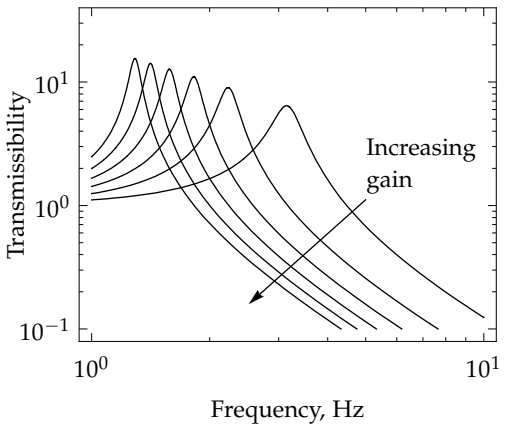

(b) Absolute acceleration feedback, g_m.

FIGURE 1.3: Acceleration feedback control.

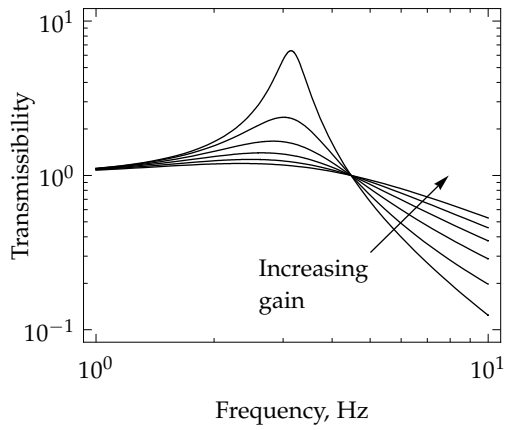

(a) Relative velocity feedback, g_c.

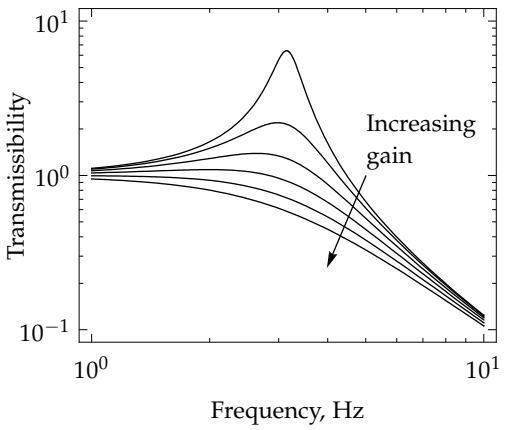

(b) Absolute velocity feedback, g_v.

FIGURE 1.4: Velocity feedback control.

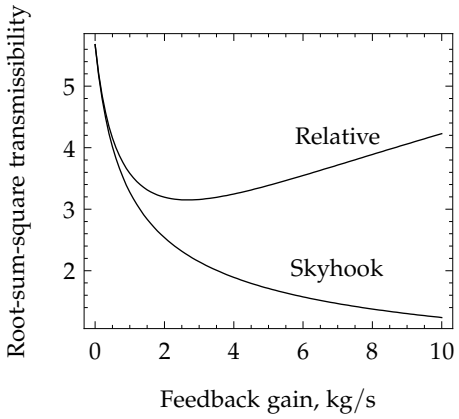

FIGURE 1.5: Root-sum-square transmissibility versus feedback gain of relative and absolute ('skyhook') velocity feedback control of a linear vibration isolation system (Fig. 1.1(b)).

The analogy with passive control

Three of the aformentioned active approaches correspond directly to variations for one of the physical parameters of the system: mass, damping, and stiffness. Active vibration control is usually only attempted when such passive control is inadequate or impractical. For example, adding mass reduces the resonance frequency, which improves vibration isolation; however, it is not always possible to do so — consider, say, weight requirements in a vehicle or airborne structure.

Adding additional damping through viscous elements, equivalent to relative velocity feedback control, will reduce the amplitude of the resonance peak, but vibration isolation at higher frequencies will be degraded. This is a common technique used for ambient energy harvesting, a recently active field of research, accomplished through electromagnetic damping through induced eddy currents in a coil experiencing relative velocity to a magnetic field [117, 273]. The technique can be considered as passive damping control with the side-effect of energy generation. The use of a nonlinear viscous damper provides transmissibility benefits that approach the performance of active absolute velocity feedback [167].

Reducing the stiffness between the mass and its supporting base has the same effect as increasing the mass: the resonance frequency is reduced and the bandwidth of vibration isolation is increased. Passive stiffness reduction can be achieved by adding a negative stiffness element in parallel with the system [170, 293]. This idea becomes a major theme of the thesis, explored later in this introduction in Section 1.4.3. Considering variable stiff-

ness elements that can act in a 'semi-active' regime, many methods exist to dynamically adjust the stiffness depending on the support being used [150, 177, 179, for example]. Semi-active stiffness modification is used more commonly in vibration neutraliser applications, described later in Section 1.2.6, since for vibration isolation applications, in general, the lower the stiffness the better; there is no need to adjust the stiffness on-line if it is already as low as possible.

§1.2.4 *Semi-active skyhook damping*

It is important to distinguish between active velocity feedback control discussed previously and semi-active skyhook damping, as both are referred to by the term 'skyhook' in the literature.

Semi-active skyhook damping control was introduced by Karnopp et al. [146], and it is often used in vehicle suspension where active systems can be impractical due to weight and power constraints (which is not always the case [119]). In this version of skyhook damping, dynamic changes in stiffness or damping are used as a feedback mechanism to approximate absolute velocity feedback control [4, 168]. This is achieved by switching on the energy dissipation element when it will resist the motion of the isolated mass and switching it off otherwise. Semi-active control has the advantages of robustness and low power requirements, especially when large forces would be required for active control. Its application is largely directed at vehicle vibration control where it is not practical to use purely active control, and thus falls outside the scope of vibration techniques of interest in this thesis; it is important to distinguish between the two different forms of 'skyhook damping', however.

In the original method of implementing skyhook control in this manner, the switching mode that is used to emulate the 'skyhook' in the controlled damping introduces higher order harmonics in the frequency response, as shown by Ahmadian et al. [3], who later proposed two 'jerk-free' skyhook algorithms to avoid this problem [4]. A number of skyhook-like semi-active damping methods, including smoothing functions to eliminate the problem of jerk, were demonstrated shortly afterwards [178]. Song et al. [271] used the nonlinearities of early semi-active skyhook control as justification for the design of an adaptive controller for vibration isolation, although they did not compare their results with recent work in the skyhook area.

§1.2.5 *Active vibration control in practice*

Velocity feedback control using integrated accelerometer measurements at the location of actuation has been used for some time as an effective vibration isolation mechanism, shown for example by Kim et al. [152]. However, the techniques discussed in Section 1.2.3 do not address the practical implications of measuring and estimating the various states (relative and absolute, displacement/velocity/acceleration feedback) for feedback in a control system. Such practical implications have a significant effect on the performance and suitability of the various control schemes. As one example, Serrand and Elliott [257] discuss absolute velocity feedback applied to a two degree of freedom structure with emphasis on the effects, for their system, due to possible base flexibility. They showed, amongst other results, that using integrated accelerometer measurements as a velocity feedback term has a low frequency phase shift due to filters in accelerometer charge amplifiers that can induce instability for sufficiently high control gains.

The general limits of control in practical applications of single degree of freedom vibration suppression systems have been studied over the last decade [12, 49]. Time delays and phase lags introduced by digital filters[6] and integrators can have quite significant effects over the ideal case of pure displacement or velocity or acceleration feedback. As stated by Williams [290]:

> *In theory integration of accelerometer signals is easily done; however, in practice, inertially referenced velocity proves to be as elusive as it is useful.*

Real integrators (as opposed to ideal integrators) and high pass filters cause instabilities at low frequencies. Acceleration feedback has a much smaller stability limit than either displacement or velocity feedback, and the effectiveness of displacement feedback is strongly reduced even with small time delays. Therefore velocity feedback control from integrated accelerometer measurements should be considered the better choice. Also, the presence of a low pass filter does not significantly affect the efficacy of velocity feedback.

A similar problem was addressed by Zhu et al. [311], who examined the use of such feedback for vibration isolation in a highly sensitive micro-gravity environment and show that accelerometer 'PD' feedback is unsuitable due to instability at high (that is, useful) control gains from quantisation and anti-aliasing side-effects. Rather, integral and double-integral feedback from

6. When absence of all vibrations are required, the side-effects of digital control (which can be as extreme as chaotic effects due to quantisation and time delays [82]) may prove deleterious for extreme applications. On the other hand, any sufficiently expensive system should be able to reduce these effects to be negligible. For the purposes of this thesis, such small effects are of no concern.

an accelerometer give better results for their system, which is consistent with later work [49].

Numerous studies have been published on similar themes, as each vibratory system analysed will have different interactions in closed loop with the filters and time delays inherent in feedback control. For example, Zhao and Xu [308] examined the vibratory behaviour of a two degree of freedom nonlinear system with time-delayed position feedback, emphasising the importance of accounting for time delays in feedback control systems.

This literature on fundamental active vibration control has been presented to suggest that absolute velocity feedback is the more robust and effective method to improve vibration isolation, with several studies successfully using it in practical systems. It is a control methodology that can be applied to multi-degree of freedom systems; for example, Engels and Elliott [98] discuss control gain selection for velocity feedback control systems for the cases of centralised and decentralised control devices. In centralised control, a global model of the system is used when allocating the feedback signals to each actuator. In decentralised control, each sensor/actuator pair operates independently at each separate mounting point. For the simple two-degree of freedom vibrating system examined by Engels and Elliott [98], centralised control performed only slightly better; in a system with more degrees of freedom, it is expected that centralised control will show greater benefit. An analogous result was shown by Hoque et al. [130] for a three-axis vibration platform supported by a so-called 'infinite stiffness' magnet/spring system (also see Section 1.4.3).

The active and semi-active feedback methods introduced thus far are orthogonal in the sense that more than one scheme may be applied in parallel. For example, acceleration feedback could be used to reduce the resonance frequency, and absolute velocity feedback used to reduce the height of the resonance peak. This approach was used by Savaresi and Spelta [253] to implement a combination absolute velocity/acceleration-feedback controller in the context of vehicle vibration control for ride smoothness. Similarly, Gavin and Zaicenco [110] discuss using negative stiffness and skyhook damping in the context of isolating machinery in a building. Once the degrees of freedom increase more complex control methodologies become necessary. Kerber et al. [148] investigated a plate-plate coupling through four contact points in a six degree of freedom system and applied active vibration isolation in the vertical direction using a range of control methods. Highlighting the relevance here, an H^∞ control method significantly outperformed the use of velocity feedback.

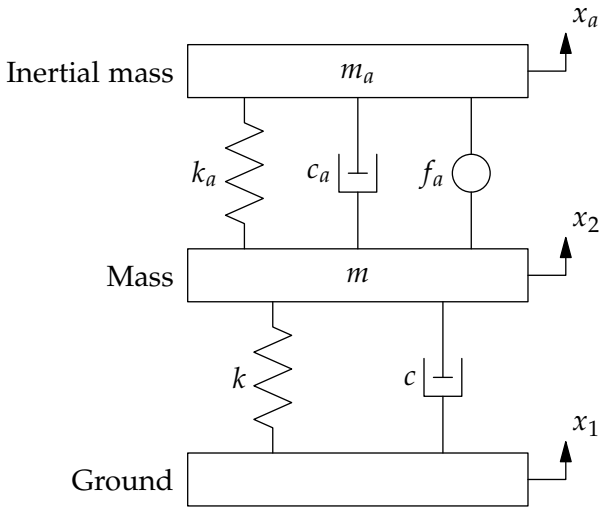

FIGURE 1.6: An inertial force f_a designed to reduce the vibration response x_2 due to disturbance x_1. The inertial actuator has dynamics of its own (m_a, k_a, c_a) that influence the overall vibration of the structure.

§1.2.6 *Vibration neutralisers and narrow-band vibration control*

Until this point in the introduction, the only focus on the vibration control literature has rested upon the area directly related to vibration isolation through modification (whether active, semi-active, or passive) of the supporting structure for the mass. The landscape for vibration control is much broader, however. Here, two minor digressions are made to place the rest of the literature in context with alternate approaches of vibration reduction, and some discussion made on why the techniques herein were deemed unsuitable for the work of this thesis.

Inertial actuators

Sometimes it is not possible to integrate the control mechanism into the support of a structure, in which case external actuators need to be added to the device to provide the control forces. These tend to be inertial electromagnetic actuators, also known as 'proof-mass' actuators, where the mass of the moving element provides an external force via coupling to the structure. This is shown schematically in Figure 1.6.

For inertial actuators, velocity feedback can have problems with stability margins at low frequencies. Benassi et al. [35] showed through experiment that stability can be improved by the addition of a phase lag controller with force feedback in conjunction with velocity feedback. The theory for such 'combined-state' feedback cases was developed at the same time [36].

A number of feedback combinations were analysed by Diaz and Gardonio [89] focussing on various forms of velocity feedback for single-, double-, and multi-degree of freedom vibration isolation systems. In the two degree of freedom system, an inertial actuator is used to provide control force; as well as additional stability constraints due to this arrangement, the resonance at low frequencies of the actuator itself compromised the control performance.

Paulitsch et al. [214] used an electromechanical actuator that serves as a self-sensing device for vibration control. The idea of self-sensing for magnetic levitation purposes (in both cases using an electromagnet) has been shown previously [41, 286]. These self-sensing devices do not perform nearly as well as when using a dedicated sensor (perhaps obviously, since the back–electromotive force is a relatively noisy signal), but the technique is particularly interesting for low-cost, low-precision devices.

The addition of inertial actuators produces additional resonances into the structure and the resonance of the actuator limits the broadband performance of the control. As such, this approach is best suited for use in *a posteriori* vibration control measures or in narrowband vibration control as discussed next in more general terms.

Narrow-band vibration control

One method of reducing vibration on a supported mass is to attach a supplementary mass that resonates in concert with the disturbance; this has the effect of adding an anti-resonance to the original system at the frequency of interest. These systems are the same schematically as shown for inertial actuators, Figure 1.6, with zero force input $f_a = 0$. They are known under various names, including 'tuned mass dampers', 'vibration neutralisers', and 'dynamic vibration absorbers'. The descriptions involving such terms as 'damper' and 'absorber' are not strictly accurate on the grounds that these devices do not primarily act as energy dissipators; rather, they direct energy into a subsystem for which continuous disturbance is not undesirable. In this thesis, the term 'vibration neutraliser' is used, following Kidner and Brennan [149], and others.

The concept of the vibration neutraliser does not lie within the focus of this research, but falls into the category of literature that is often associated with it under the umbrella of 'vibration control'. In the passive application, a vibration neutraliser is created by attaching a supplementary mass to the coupled structure for which vibration is to be removed. The stiffness of the attachment is chosen by matching the natural frequencies of the structure with that of the additional mass.

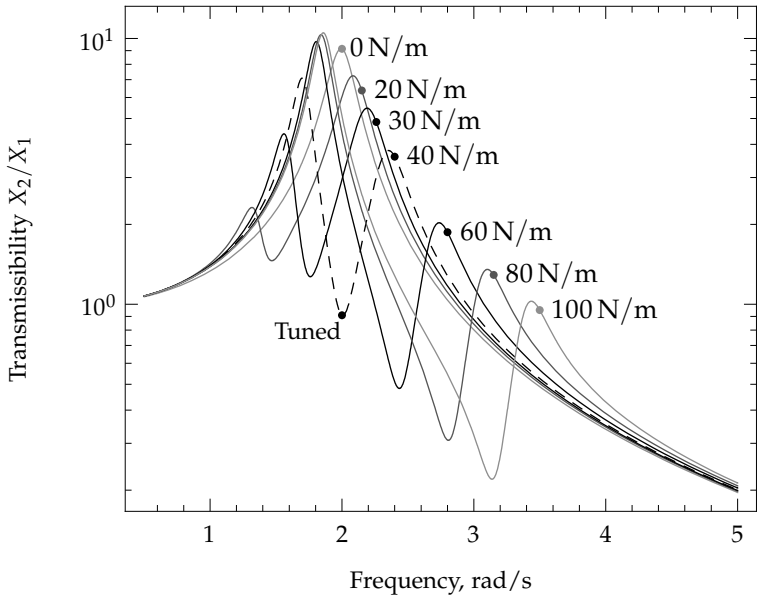

FIGURE 1.7: Transmissibility of a structure with a vibration neutraliser for a range of neutraliser stiffnesses k_a (labelled). When the neutraliser is tuned to match the natural frequency of the structure the vibration amplitude around that frequency is greatly reduced.

TABLE 1.1: Simulation parameters for the vibration neutraliser results in Figure 1.7.

m	100 kg
m_a	10 kg
c	20 kg/s
c_a	2 kg/s
k	400 N/m

To show the effect of varying the resonance frequency of the vibration neutraliser, Figure 1.7 shows the transfer function X_2/X_1 of a vibration neutraliser (as defined in Figure 1.6) with a range of neutraliser stiffnesses with other parameters as shown in Table 1.1. For each different stiffness, an 'anti-resonance' is produced in the transmissibility graph at the resonance frequency of the neutraliser. The neutraliser frequency should be chosen within the narrowband region of desired attenuation; generally, this will be at the resonance frequency of the main structure.

There is a compromise between broadband and narrowband vibration attenuation for vibration neutralisers (not unlike that between shock and vibration isolation, §1.2.2). This is illustrated by comparing the transmissi-

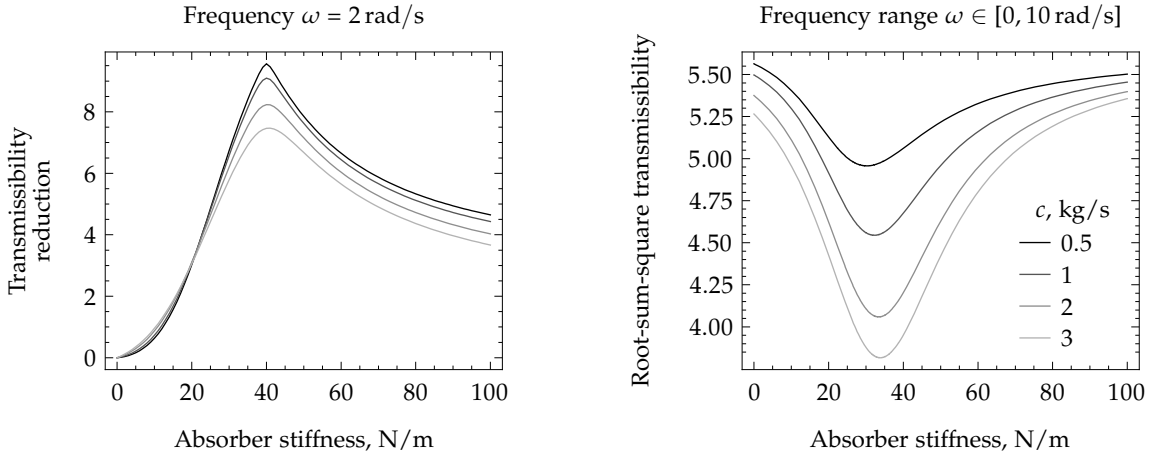

(a) Transmissibility reduction at resonance versus stiffness. Greater reductions result from *lower* damping.

(b) Root-sum-square transmissibility versus stiffness. Greater broadband reductions result from *higher* damping.

FIGURE 1.8: Single-frequency transmissibility reduction and broadband root-sum-square transmissibility versus vibration neutraliser stiffness for a range of absorber damping ratios.

bility reduction at a single target frequency versus the broadband reduction in transmissibility due to the same vibration neutraliser. Figure 1.8(a) illustrates the vibration attenuation at resonance for a system with a vibration neutraliser with various damping ratios. It can be seen that for attenuation at resonance, low absorber damping produces greater vibration attenuation. The maximum attenuation is achieved when the vibration neutraliser resonance matches the frequency of interest.

Conversely, if the root-sum-square transmissibility of an entire frequency band is calculated (Fig. 1.8(b)) it can be seen that lower absorber damping *decreases* the overall vibration reduction. It is also interesting to note that the maximum reduction in broadband transmissibility occurs when the neutraliser is tuned slightly below the resonance frequency of the support. This would be an appropriate response if the vibration neutraliser were to be used against narrowband vibration with a time-varying resonance frequency.

The efficacy of a vibration neutraliser is related to the damping between it and the structure; better results are achieved with lower damping, as shown in Figure 1.8(b). The damping of the absorber can be reduced with an active control system as shown by Kidner and Brennan [149]. This can be understood with the realisation that energy is not dissipated by the vibration 'absorber'; rather, motional energy from the vibrating structure is being *transferred* to the supplementary mass, and this process is degraded by the

presence of damping.

A vibration neutraliser is tuned for a specific resonance frequency, which means that the resonance frequency of interest must be known and largely unvarying for a passive device to achieve useful results. This is especially true for low-damping neutralisers, since their efficacy decreases rapidly as they become de-tuned (seen in Figure 1.8(a)). To avoid the problem of neutraliser de-tuning due to slow variations in the resonance frequency of the structure, semi-active methods can be used to observe or track the frequency of the disturbance and adjust the stiffness of the neutraliser appropriately in order to retain its tuning. Such neutralisers typically use a variable stiffness element, which can take many forms [128, 150, 276]. Brennan [50] discusses a wide variety of actuators that may be used to construct a vibration neutraliser:

> *There is not a single "best" way of making an* [*adaptive tuned vibration absorber*]. *It depends upon the required frequency range, the agility (speed of reaction) and cost.*

An interesting addition to this field was shown by Ivers et al. [133] with a mechanically self-tuning vibration neutraliser. While not as effective as an adaptive vibration neutraliser that uses an external power source, the ability to adapt to the excitation frequency using only the energy of the disturbance itself is commendable.

Vibration neutralisers have been used to mitigate seismic vibrations in large buildings, but their mass dependence makes their application rather tricky and often impractical. Matta and De Stefano [188] proposed a nonlinear rolling structure via which a vibration neutraliser can be mounted to good effect despite uncertain masses of either or both of the building and absorber. Their work focussed on the interesting idea of using a roof-top garden as a vibration neutraliser for a building [189].

Some researchers have analysed the use of electromagnetic actuators to provide a fully active force with which to cancel system resonances [70, 153, 291]. The advantage for such a system is the same as for semi-active controllers in general: with a suitable algorithm, changes in the plant can be taken into account in the vibration neutraliser. However, using a fully active system for this task is not very energy efficient, since all 'damping' is achieved artificially with the expenditure of actuator energy. Nonetheless, good results can be obtained via this method and the potential flexibility of the control system could be a good reason to design such a system.

Vibration neutralisers can also be used for modal systems, in which case each neutraliser is designed at the specific resonance frequency of each mode. In a recent example, Casciati and Ubertini [58] used a semi-active neutraliser

to control the vibrations of a suspended cable; some care was required for their structure as the higher frequency superharmonic behaviour posed an influence even though the targeted (low frequency) mode was damped as desired. Optimisation techniques can be used, if the mode shapes are known, to place multiple vibration neutralisers in a modal system [218].

When electrical circuits are used to absorb resonant vibrations, the energy absorbed can be redirected to produce a power output [273]. Such devices are gaining popularity for ambient vibration–powered applications such as remote sensing [15], with practical implementations beginning to appear [99]. Electromagnetic systems tend to be more suitable for larger scale energy harvesting devices, whereas piezoelectric and electrostatic devices are more suitable at the micro-vibration scale [34]. Another field of interest for regenerative damping is in vehicle suspensions, in which useable power can be extracted with the same mechanism used to provide greater ride comfort [118]. Recent work has used self-powered magnetorheological dampers as a vibration neutraliser [76].

Stephen [273] performed a thorough analysis on energy harvesting with micro-actuators. He considered a single degree of freedom mass-spring-damper coupled with a simple electrical circuit. For best performance, energy should be dissipated as much as possible by the electric components, not the mechanical damping, since in the electrical network the energy is retrievable whereas with viscous damping the energy is dissipated as heat. This idea has similarities with the concept discussed previously in this section that the effectiveness of the vibration neutraliser is reduced with the presence of increased mechanical damping.

Semi-active methods have also been explored to tune energy harvesting devices to the frequency of disturbance. Challa et al. [60] investigated a semi-active device that used variable-displacement attractive and repulsive magnets to adjust the resonance frequency of a piezoelectric cantilever. This is the same mechanism, investigated independently, that is examined in this thesis for 'quasi–zero stiffness' suspensions (see Section 1.4.3 and Section 6.3).

Finally, to relate the field of vibration neutralisers to this thesis, the work by Tentor [275] analyses in significant detail the static and dynamic nonlinear stiffness and damping terms of a magnetic system used to create a tuneable vibration neutraliser. His design is interesting with respect to this thesis in that it uses both permanent magnets for force generation and an electromagnet for active control; the dynamic response of the system can be changed by varying the current in the coil.

§1.2.7 *Summary of the vibrations literature*

The cross-section of introductory concepts and literature in this section have been chosen to illustrate the broad approaches for vibration control of simple systems. The basic vibration isolation problem was introduced and basic active control solutions presented; of the various feedback models available, absolute velocity feedback is the most effective for low-order systems as considered in this thesis, although there are implementation difficulties in estimating the absolute velocity signal, such as using integrated accelerometer measurements. Some aspects of other vibration systems were introduced, including semi-active skyhook control, inertial sensors, vibration neutralisers, and energy harvesting, to provide some context on the wider research area and the connections between the approaches taken.

§1.3 MAGNETICS

This section is a general overview of the applications of magnetic fields:

Section 1.3.1 Introduces the underlying mechanisms and shows (non-exhaustive) examples in the literature of interesting or novel uses of magnets and magnetic fields.

Section 1.3.2 Examines some more specific cases; magnetic positioners and movers are discussed (that is, using magnetic forces to cause things to move): maglev trains, single and multi degree of freedom bearings, and other uses that directly use the forces produced from magnetic fields in generally translational degrees of freedom.

Section 1.3.3 Covers magnetic levitation (that is, using forces to support objects intended to be stationary); its impossibility with permanent magnets alone, and exceptions to that restriction.

§1.3.1 *The world of magnetic applications*

Magnetic fields can be used for a vast array of scientific uses. The variety of applications for magnetic fields stems from the different ways in which they can be generated and the different ways they can interact with their environment. Magnetic fields produce forces on ferromagnetic material, as well as between paramagnetic and diamagnetic material, as well as charged particles and other magnetic field sources. Magnetic field sources can be time varying or constant, and the fields themselves within their zone of interaction can be uniform or non-uniform. Coey [77] discusses a broad range of mechanisms that can be exploited for magnetic applications, summarised

Table 1.2: Applications of permanent magnet materials, adapted from Coey [77].

Field	Magnetic effect	Examples
Uniform	Zeeman splitting	Magnetic resonance imaging
	Torque	Alignment of magnetic powder
	Hall effect	Sensors, read-heads
	Force on conductor	Dynamic Motors, actuators, loudspeakers
	Induced electromotive force	Generators, microphones
Nonuniform	Force on charged particles	Beam control, radiation sources (microwave, ultra-violet; X-ray)
	Force on magnet	Bearings, couplings, Maglev
	Force on paramagnet	Mineral separation
	Force on diamagnet	Levitation of small objects
Time varying	Varying field	Dynamic Magnetometers
	Force on iron	Dynamic Switchable clamps, holding magnets
	Eddy currents	Metal separation, brakes, dampers

in Table 1.2. The work involved in this thesis covers mainly a single line in this table: the interaction force on a permanent magnet due to a non-uniform magnetic field.

The range of application for the magnetic field mechanisms listed in Table 1.2 are too numerous to list in detail. In the case of using magnetic fields for non-contact sensing of material properties that involve variable conductivity, applications include detecting fatigue cracks, defects in printed circuit boards, and plastic landmines [205].

Magnetic resonance imaging technology is well-known for its non-invasive ability to diagnose a broad range of health issues. Other applications in the medical field include brain imaging [87, 114, 181, 255], measurements of the health of the heart [175], stimulation of the nervous system [85], and studying the effects on tumour growth and immune function [296]. An interesting biomedical application is remote localisation in six degrees of freedom within the human body [300].

Magnetic fields have been used to great effect within the robotics world, including: a haptic interface for manipulating small objects with magnetic levitation [289]; a wireless motion capture device [122]; a computer input device built with magnetic sensors placed on the wrist in order to sense single finger-tip motion from the opposite hand [121]; using a magnet attached to a cantilever excited by an external field in a water tank as an actuator to propel a robotic fish [278]; and many others.

For precise wind tunnel measurements, supporting structures can inter-

fere with the fluid flow in the working cross-section. In such cases, magnetic levitation has been used to suspend objects in a non-contact fashion [124], avoiding this problem.

In the following sections, the literature closer in scope to the research of this thesis will be discussed more detail.

§1.3.2 *Magnets assisting motion*

That magnets can apply forces to one another over a distance is quite a novel concept in a mechanical world accustomed to friction. It has been a short while, relatively speaking, that it has been possible to even produce magnets with enough coercive force to apply useful mechanical forces. Non-contact magnetics in mechanical systems is advantageous due to high precision and wear-free operation due to lack of friction. This section broadly examines some of the main applications of the field.

Maglev transportation

The largest body of research into magnetic levitation is on so-called 'maglev' transportation. Its well-known goal is to use a levitated carriage to provide extremely fast and efficient transportation.[7] This field, which is rather diverse in terms of the techniques under investigation, is finally now achieving commercial application in the real world after some thirty years of research [171]. While maglev has some concepts in common with this research (large loads, magnets), the techniques used tend to be rather distanced from those that will be applied for this project because they focus on transportation rather than *elimination* of movement.

Many approaches to the design of maglev systems have been taken, including passively stable designs [123, 206]. Earnshaw's theorem for stability (§1.3.3) is not applicable for maglev systems, at least while the vehicle is in motion, since the motion of the vehicle adds a time-varying element to the magnetic system. When at rest, maglev vehicles tend to be anchored to the tracks for stability.

Magnetic actuators

In recent years, magnetic levitation has been applied to the field of linear, planar, and multi-degree of freedom actuation systems. Such devices are generally capable of supporting small loads and applying translational forces to

7. Indeed, in my experience of explaining my thesis work to others, the first thought most people have when one mentions 'magnetic levitation' is of maglev trains.

effect displacements of up to several hundred millimetres with up to nanometre precision.[8] The initial designs allowed travel in a single direction [for example, 281] while planar actuators were shown within the decade [for example, 154, 200]. Soon after, a six degree of freedom non-contact actuator using similar principles was demonstrated [284].

Each of these devices fulfil different design requirements, and are all subject to continuing research; for example, see the recent development of:

- a single degree of freedom linear magnetic bearing [235],
- a planar actuator [155] to support 2 kg over a travel of 5 mm × 5 mm with nanometre precision,
- a five degree of freedom actuator [103] with 100 mm planar travel; and,
- a six degree of freedom actuator [136], which supports loads in the order of 10 kg with a large air gap (2 mm) and long stroke (230 mm × 230 mm).

The electromagnetic design principles of these devices are based around actuation rather than supporting a load. The methods used to design the multi-degree of freedom actuation may be applied in future research to the actuation stage of a vibration isolator, but for load bearing there are other magnetic devices to be investigated.

Magnetic bearings, couplings, and gears

The oldest dynamic mechanical application of magnetics was for rotary bearings. The classic magnetic bearing supports a shaft by applying radially centring forces on the spinning rotor. An example schematic is shown in Figure 1.9, which is axially unstable due to Earnshaw's theorem (§1.3.3). In the most simple of these bearings, this instability is constrained with a physical stop such as a thrust bearing. Control has been used for many years now to stabilise such systems (for example, early work by Shimizu and Taniguchi [259]), creating completely non-contact devices. Such devices are capable of very high speeds due to the absence of mechanical friction and avoid long-term problems associated with wear. Magnetic bearings can also be used to support axial forces with active control in the radial direction [16]; it is possible to combine radial and axial bearings to improve the passive stability characteristics of these bearings, shown by Delamare et al. [86] and analysed for non-rotational systems later in Section 3.3.9 on page 100.

8. Note that while these six degree of freedom actuators have very high static precision, they do not have the frequency response of the so-called 'nano-positioners' using piezoelectric stack actuators.

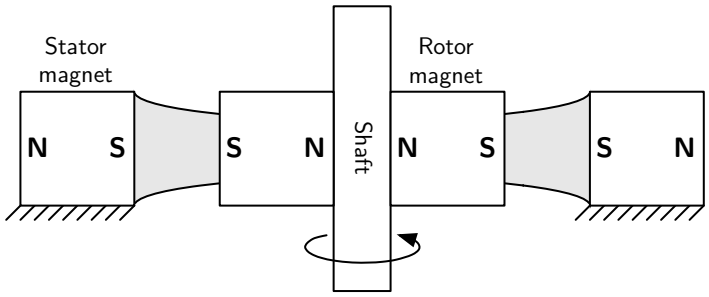

FIGURE 1.9: The cross-section of two radially magnetised ring magnets in a radial bearing.

Backers [24] developed an early active magnetic bearing similar to that shown in Figure 1.10 which used a control system with variable current electromagnets to stabilise the rotor in the unstable axial direction for completely non-contact support. The multipole nature of this bearing will be more closely examined in Chapter 4 on page 129.

In the early decades of magnetics research, it was not feasible to solve the magneto-static forces of these systems completely analytically. Magnetic bearings could be modelled using a two dimensional field solution, simplifying the solutions. In such a way, Yonnet [301] showed that the forces between axially- and radially-magnetised bearings are equal (Fig. 1.11). However, this equality of forces for both orthogonal- or parallel-magnetised magnets should not be taken as a general result; it comes about due to modelling the two-dimensional model of the geometry [13], and it will be shown later that this is in fact not true for cube magnets (see Section 3.2.2 on page 82). Yonnet [302] described how such axial and radial magnetic bearings may be re-arranged to suit different applications, showing a complete taxonomy of simple magnetic bearing designs. Varying geometrical parameters of these magnetic bearings can significantly affect the force and stiffness characteristics [30].

Magnetic bearings are designed to hold two systems apart; when the magnet design is adapted to hold two systems together the device is known as a magnetic couple or coupling. Rather than isolating components from applied loads, a magnetic coupling serves to transmit the forces and torques to couple two components together without direct contact. They can be used, for example, to transmit torque between two separated rotating shafts. Yonnet [302] highlighted in an early treatment on the topic that, even more so than for magnetic bearings, periodic recurring magnetisation (Fig. 1.10) is required for magnetic couplings to transmit torque satisfactorily. Since then, numerous

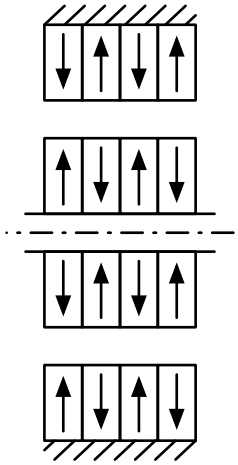

FIGURE 1.10: Cross-section of a multipole radial bearing.

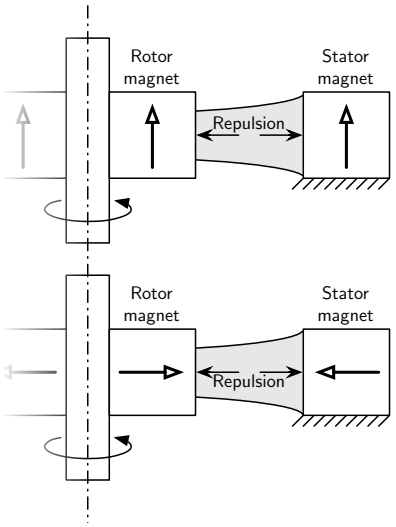

FIGURE 1.11: Two equivalent radial magnetic bearings (with equal forces of repulsion), despite their different directions of magnetisation.

theories have been developed and applied to the analysis of a number of multipole designs of various geometries [62–64, 67, 228, 229].

Magnetic couplings can also be used in transmission systems as non-contact 'gears'; it is by no means a solved research question on how best to design such magnetic gears [233]. While magnetic gears might not always have the torque capacity of a mechanical gear, this is dependent on the device and the design of the gear system. In some cases, magnetic gears can usefully replace mechanical ones in planetary gear trains avoiding typical problems such as tooth wear and chatter [116].

§1.3.3 *Magnets opposing motion*

This section covers areas of the literature in which magnetic forces are used to provide support for load bearing or levitation in which the supported object is intended to remain motionless. Three broad cases are investigated: passive magnetic levitation, which is known to be impossible with regular magnetic fields; diamagnetic levitation, which is not; and actively controlled magnetic suspension.

The impossible passive magnetic levitation

The act of passively levitating a magnet by another is well known as impossible, although popular unlearned opinion is not aware of the fact. Earnshaw [91] proved that objects in the influence of fields that apply forces with an inverse-square relation to displacement cannot form configurations of stable levitation. Approximately one hundred years later, Tonks [279] wrote a paper reminding his contemporaries of the work of Earnshaw by applying the proof specifically to the field of magnetics:

> *... no flexible assemblage of magnetic poles, in which readjustments in position of the poles in the group can occur, can be stable in either a fixed field or in the field from another such assemblage...*

An interesting retrospective on Earnshaw's theorem related to magnetic levitation is given by Bassani [29], and an alternative formulation given by Reusch [234]. A mathematical demonstration of Earnshaw's theorem is conceptually quite simple. Starting with the equation for the magnetic flux density, when there are no external current terms it can be shown to be expressed as Laplace's equation $\nabla \mathbf{B} = 0$, which implies $\nabla^2 \mathbf{B} = 0$.

As the potential energy of a magnet is proportional to the magnetic field it is subjected to, $U = -\mathbf{M} \cdot \mathbf{B}$, when the magnetisation is time-invariant (as in the case of a permanent magnet),

$$\nabla^2 U = \frac{\mathrm{d}^2 U}{\mathrm{d}x^2} + \frac{\mathrm{d}^2 U}{\mathrm{d}y^2} + \frac{\mathrm{d}^2 U}{\mathrm{d}z^2} = 0\,. \tag{1.10}$$

The double derivatives of the energy are the stiffnesses in each direction. For a levitating magnet in a state of stable equilibrium, these three terms must be greater than zero. This requirement cannot satisfy Eq. 1.10 and thus levitation cannot occur.

This situation is easy to visualise by analogy. Figure 1.12 shows a ball balancing on a saddle-shaped curve, which is a two dimensional analogy for the condition of Eq. 1.10. Perturbations on the ball left or right will result in reaction forces keeping it centred and stable, whereas small disturbances into or out from the page will result in increased perturbation as the ball 'falls off' the saddle; that is, a condition of instability. So it is with any permanent magnet arrangement.

Exceptions to Earnshaw

Earnshaw's proof only relates to systems of fixed magnetisation; it does not rule out all forms of 'levitation' unconditionally. Boerdijk [44] reviewed the known methods for levitation, covering levitation by gravitation forces,

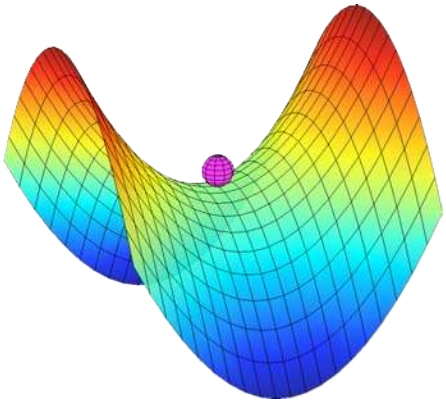

FIGURE 1.12: A ball in unstable equilibrium on a saddle-shaped curve.

pressure reaction forces, radiation field forces, and finally in detail, various magnetic and electromagnetic forces.[9] Bassani [29] revisited Earnshaw's work, in particular to highlight interesting exceptions to the theory against passive levitation.

Because Earnshaw's theorem examines only the case for static equilibrium, cases when the magnetic field is dynamic are not covered. This can occur broadly under three circumstances: when the magnetic field is time-varying; when an unstable permanent magnet arrangement is stabilised with an active control system; and when the system itself is composed of elements with some dynamics associated with them.

To achieve levitation using time-varying magnetic fields, time varying currents create dynamic magnetic fields that induce eddy currents in the levitated object, and it is the interaction of the magnetic fields of these induced currents that causes the levitation [165]. The technique uses a large amount of power, as the levitation forces are entirely generated by the current-carrying coils, and for this reason it is not especially suitable for the purposes of this research.

For an actively stabilised levitation system, the weight-bearing forces are created by permanent magnets (which have time-invariant magnetic fields) and the necessary stabilisation is applied with variable current electromagnets — or some other actuator — with a feedback control system. This system was first implemented by Holmes who levitated a magnetic needle, as cited by Boerdijk [44]. Some more practical examples of these types of

9. 'With an eye to the practical importance of levitation we feel justified here in disregarding those aspects of it associated with magic, spiritualism, and psychic phenomena…' [43].

system are covered in the next section. This summary is fairly brief; Bleuler [41] wrote a more detailed overview. His paper introduced the 'self-sensing active magnetic bearing' [286], which uses back–electromotive force from the controlling electromagnet to sense the position of the floating element. This eliminates the need for a more classical position sensor, but the control system is necessarily more complex and the behaviour not as precise.

Finally, levitation can be achieved in dynamic systems. Bassani [31] levitated a ring magnet above another by using continuous base excitation to find a small zone of stability in the nonlinear dynamics of the system. More well-known, the Levitron toy demonstrates stability of a magnetic spinning top above a ring magnet [39, 40, 88, 264].

Diamagnetic levitation

Levitations involving diamagnetic material are also exempt from Earnshaw's theorem. This was the motivation for the papers of Boerdijk [43] in which he cites Braunbek, who derived that magnetic material is governed by Earnshaw's theorem only because it has a relative magnetic permeability (μ) greater than one — that is, a permeability greater than that of the surrounding medium. A separate analysis of magnetic levitation systems provides a more specific measure for testing the stability of magnetic systems with various boundary conditions [234].

Material with $\mu < 1$ is *not* covered by the theorem since the magnetic flux from the diamagnetic material becomes dependent on the displacement of the permanent magnet; this violates the condition of Earnshaw's theorem that fixed magnetic fields be used, and so static levitation involving magnets and such diamagnetic material becomes possible. To demonstrate this, Boerdijk [43] levitated a small cylindrical magnet of dimensions $\varnothing\,1\,\text{mm} \times 0.3\,\text{mm}$. Simon and Geim [262] provide a good background to the area and use modern approaches to levitate a permanent magnet with a variety of magnet/diamagnet geometries, primarily with a vertical diamagnet–magnet arrangement. Kustler et al. [163] examined a horizontal diamagnet configuration (not dissimilar to the 'horizontal spring' introduced in Section 3.3.4) which could stably levitate multiple magnets simultaneously. Other studies on diamagnetic levitation examine the suspension of larger objects including strawberries and frogs [40, 111, 112, 263] and (widely reported in the media) mice [180] with superconducting electromagnets (on the order of 10 T).

Unfortunately, none of these diamagnetism-based approaches are suitable for large load bearing. Even the element with the strongest diamagnetism in its natural state, bismuth, has a relative permeability $\mu \approx 0.999\,83$ — hardly

different than that of 'free space'.[10] The forces exchanged via magnetic flux between magnetic and diamagnetic materials, therefore, are incredibly small and not suited at all to the purposes of this research.

Superconducting material, on the other hand, behaves ideally diamagnetic with $\mu = 0$, so the forces produced between a superconductor and a magnet are equal to the forces between two permanent magnets themselves (of equal size to the original magnet and separated by twice the distance between the magnet and the superconductor). This allows many exciting possibilities for stable levitation. However, even the so-called 'high temperature' superconducting materials must be cooled to very low temperatures in order to achieve superconductivity. Such a requirement renders this method functionally impractical for this research. A review of work in the area of superconducting levitation has been published by Ma et al. [183].

Single degree of freedom unstable magnetic suspension

A simple variety of magnetic levitation or suspension is the counter-acting of gravity with an active electromagnetic force. The most common form this takes is via an unstable attractive vertical force to directly compensate for gravity; vertically-passive designs are shown in Section 3.3.4 on page 90 and Section 3.3.8 on page 99 which both require active control in the horizontal directions to maintain stability.

The single degree of freedom magnetic system is very popular as an application for control theory, as it is an unstable system in which both the passive and active magnetic forces are nonlinear with displacement. As will be seen later, developing models for magnet and coil forces can be quite involved; for the purposes of control, the closed form expressions introduced in Chapter 2 are too complex to integrate into a control methodology. One way to overcome this issue is to develop a low-order empirical model for the system, with unknown parameters that must be identified; an example of this was shown for a coil-iron suspension by Agamennoni et al. [1].

By contrast, sufficiently advanced nonlinear control can achieve stability and tracking without the use of system identification. As an example, Mahmoud [184] used backstepping with a nonlinear model to provide robust control of a magnetic suspension and Queiroz and Pradhananga [224] similarly used nonlinear control to stabilise a magnetic bearing with pull–pull electromagnets with parameter uncertainties, while also minimising power

10. By contrast, water has $\mu \approx 0.999\,991$, and since living organisms are mostly water, this is the value typical of frogs and mice and humans as well. The strongest diamagnetic material is manufactured pyrolytic graphite, with a permeability of $\mu \approx 0.999\,55$. Permeability numbers all as cited by Simon et al. [263].

consumption of the system. Gentili and Marconi [113] investigated this system with nonlinear feedback control for robust disturbance suppression, and Chang [61] applied nonlinear control to the problem of magnetic levitation, using coupled hybrid magnets (that is, electromagnets biased with permanent magnet cores) that create a magnetic circuit with the levitated table of 20 kg.

However, such advanced control techniques are not always necessary; Li et al. [174] report their success in using simple PID control for suspending a magnetic table using a coupled electromechanical model of the system. Banerjee et al. [28] used a simple cascaded PI and lead controllers to stabilise an electromagnetic suspension. An optimisation technique was used to obtain the control gains necessary to achieve adequate performance over a range of displacement gaps; such control is usually only suitable for fixed-gap systems.

Vibration isolation achieved using magnetic suspensions is addressed later in Section 1.4.1.

§1.3.4 *Magnetic damping*

Henry Sodano completed his Ph. D. in 2005 [265] on eddy current damping for flexible structures and has published several papers based on that work.[11] His work investigates the use of non-contact magnetic (permanent [267–269] or electric [266]) elements to passively [268] or actively [266, 267, 269] add forces to a structure via induced eddy currents. His work investigates the potential for use with flexible structures primarily for use in space applications.[12]

The damping effects of magnetic forces has also been examined by Bonisoli and Vigliani [48]. The use of electromagnetic damping can be advantageous in applications where the absorbed energy is converted to electrical energy for re-use and storage, increasing the overall efficiency of the device; a good example is in the automotive industry [118].

Another recent investigation of an eddy current damper using an aluminium plate is shown by Ebrahimi et al. [92]. Damping of levitated permanent magnets with a similar technique was shown by Elbuken et al. [93]. Their emphasis lay on the problem of micro-levitation, where small stiff-

11. I recommend the thesis for the additional context and literature review.
12. Note that not all permanent magnets are created equal for suitability in space: the cheapest and most common class of rare earth magnetic alloy, neodymium-iron-boron, will become demagnetised in the influence of radiation due to localised heating effects. Samarium-cobalt magnets are less susceptible to this problem due to their higher Curie temperature and have been previously used in space applications [65].

nesses (and damping) results in large amplitudes of disturbance. One of the noted advantages in this case is the fact that the eddy current damping does not add other dynamics to the system it is applied to through structural coupling; equilibrium positions and controller designs are unaffected with this technique.

Eddy currents may generate force on a conductor through two mechanisms: change in magnetic field and/or change in velocity. Change in velocity leads to a (possibly noticeably nonlinear) viscous damping force that is dissipative: it can only decrease the energy of the system. However, a change in the magnetic field can generate forces that can be used to apply work to the system. This is the same mechanism used by time varying current levitating devices [165]. It is unclear whether the use of conductive material has significant advantages over ferrous material to generate vibration suppression forces. For the conductive case, a permanent magnet may be used to increase the field strength of the electromagnet at the expense of added viscous damping (which may or may not be desirable according to the application). However, constant and low frequency forces will not be able to be generated without significant control design since eddy current forces are more difficult to model than quasi-static magnetic forces.

The calculation of eddy currents is an involved process, and has not been investigated in detail for this thesis. The eddy current density $\mathbf{J}_{\text{eddy}}$ induced in a conductive sheet moving through a magnetic field at velocity $\mathbf{v}$ is given by

$$\mathbf{J}_{\text{eddy}} = \sigma \left[\mathbf{v} \times \mathbf{B} \right] . \tag{1.11}$$

where σ is the conductivity of the sheet. The force $\mathbf{F}_{\text{eddy}}$ due to these eddy currents is the integral over the conductor volume V,

$$\mathbf{F}_{\text{eddy}} = \int_V \mathbf{J}_{\text{eddy}} \times \mathbf{B} \, \mathrm{d}v = \sigma \int_V \left[\mathbf{v} \times \mathbf{B} \right] \times \mathbf{B} \, \mathrm{d}v \, , \tag{1.12}$$

which is anti-parallel to $\mathbf{v}$. Due to the cross terms, the maximum force is obtained for magnetic fields perpendicular to the motion of the conductor. Associatively, it is only the component of magnetic field in the perpendicular direction that influences the eddy force. This has implications on the arrangement of eddy current dampers for vibrating structures. Two configurations of eddy current dampers are shown in Figure 1.13, which must be designed taking into account the exact shape of the magnetic field and the gap between the magnet and the conductor. The vertical configuration (Fig. 1.13(b)) will exhibit a nonlinear damping force as the gap between the magnet and conductor varies with displacement of the mass. In practice this may not be

a significant problem if the gap is somewhat larger than the motion of the mass.

Experimental results of a magnetically levitated mass show that eddy current damping between permanent magnets is very low (Section 7.3.3 on page 224), making a passive non-contact eddy current damper of potential importance for vibration suppression in systems that require additional passive damping. Optimisation in this area could investigate the size and shape of the magnet or electromagnet used to best create the field that impinges on the conductor to generate maximal eddy current forces. In addition, the formalisation and potential analytical solutions for calculating eddy current forces for a wide range of magnet geometries has not yet been investigated. This avenue of research is not pursued in this thesis.

§1.3.5 *Summary of magnetics*

From brain imaging to maglev trains, magnetic fields can be used for a very wide range of applications. Of particular interest are those areas in which magnetic fields are used to generate translational forces.

The inherent instability of magnetic suspensions has been introduced and methods shown for overcoming the problems associated with this. Basic magnetic suspension, as the basis for many 'levitation platforms' was addressed.

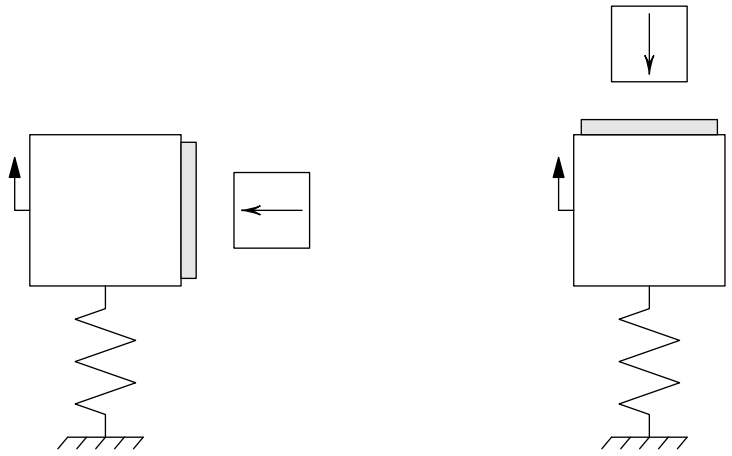

(a) Horizontal configuration; eddy currents induced via axial magnetic flux.

(b) Vertical configuration: eddy currents induced via radial magnetic flux.

FIGURE 1.13: Orthogonal configurations of eddy current dampers for a vibrating (non-magnetic) mass. The shaded section indicates conductive material.

§1.4 Magnets and vibrations

This section explores the overlap between vibration isolation and magnetic actuation systems. For the purposes of this thesis, three broad topics are of interest:

Section 1.4.1 Vibration isolation systems designed using magnetic springs and actuators;

Section 1.4.2 The nonlinear dynamics of magnets in motion; and,

Section 1.4.3 The field of 'quasi–zero stiffness', to which a contribution is made in Chapter 6.

§1.4.1 *Vibration isolation platforms*

Puppin and Fratello [223] demonstrated with a simple system that magnetic springs can be used for vibration isolation. No attempt to achieve contactless suspension was made — the magnets were horizontally constrained in guides. Furthermore, the springs were only used as passive isolators for vibrations in the vertical direction; no active vibration control was used.

Nagaya et al. [209] constructed a non-contact vibration isolation table; they report a high-stiffness spring with transmissibility that 'can be controlled to be nearly zero [*sic*]'. Their table used small magnets in a simple design which could not support large loads. The authors showed later a better control system for their 'perfect [*sic*] non-contact active vibration isolation table' [208].

Watanabe et al. [288] wrote a paper detailing a functional vibration isolator using electromagnetic springs, which could support weights of up to 200 kg. The control system used a combination of two independent control systems for stable levitation and vibration isolation. The magnetic actuator design is not described, however.

§1.4.2 *Nonlinear vibration and/or magnetic systems*

The field of nonlinear dynamics is very large, and surprising results can arise in applications to vibration suppression.

Examples of nonlinear vibration systems

Oueini et al. [213] considered the response of a nonlinear plant with an additional cubic nonlinear feedback law and established that vibration attenuation was possible and that nonlinear phenomena such as chaos existed, which would generally be undesirable for vibration isolation.

A comprehensive review of nonlinear vibration isolation systems for a broad range of techniques was published by Ibrahim [132]. It highlights the importance of nonlinear analysis in this field: in some cases, better results can be achieved using nonlinear spring forces to couple to and absorb vibration energy; in other cases, the behaviour of an isolator cannot be adequately modelled by using linear systems theory. As an example of the former, Starosvetsky and Gendelman [272], with a good review of the literature, introduce the concept of an 'energy sink' in which a nonlinear system provides more effective vibration attenuation over a broader frequency range than a linear absorber alone.

Interesting results have been shown using nonlinear springs to attach the vibration absorber to the structure, such as Jo and Yabuno [145] who use repulsive magnetic springs to produce a tuned absorber with a resonance at double the frequency of the main resonance of the structure. 'Frequency doubling' is a common non-linear effect; it is also seen, for example, in eddy current-based magnetic actuators [267].

Mann and Sims [185] investigated the use of a nonlinear vibration mount for energy harvesting using a magnetic suspension of repulsive magnets to create a Duffing-like oscillator. Large damping ensured that the nonlinear regimes were only realised at large excitation amplitudes, but the idea is that highly nonlinear resonances have a much broader resonance peak through the higher branch around the jump phenomenon.

A similar idea is explored by Shahruz [258] for an energy scavenging cantilever beam that uses an arrangement of attracting magnets to shape the force characteristic of the response. The aim is to achieve a power spectrum of the response to a random excitation that is greater than the predominantly linear response that is obtained without the magnets present.

Zhang et al. [306] use a nonlinear damper to excite the structure at harmonic frequencies of the resonance. This results in less energy at the frequency of vibration, although the resonance peak does remain. While it does not seem likely that this method can compete with the reductions seen with the approach of a vibration neutraliser, this nonlinear damping method does have the advantage that it does not require tuning for a particular frequency and its effectiveness will not change with a time-varying resonance frequency.

Jazar et al. [144] analysed the behaviour of a nonlinear vibration isolation mount in detail, developing analytical models for the jump phenomena of a system with cubic stiffness and quadratic damping. Critical values were illustrated to avoid the ill effects of the nonlinearities; additional damping had the general effect of decreasing the adverse nonlinear response.

Nonlinear magnetic systems

For the purpose of vibration control, augmenting a linear spring system with nonlinear magnetic springs alters the behaviour of the natural frequency of the system to be weakly coupled to the mass of the system. D'Angola et al. [83] analysed the dynamics of a nonlinear system in which a variation of both stiffness and mass by up to 50% resulted in a change in resonance frequency of less than 6%. For an equivalent linear system, the natural frequency variation is ten times greater. This is a very interesting result for loading elements for which the mass to be supported is largely variable, in that the frequency response will vary significantly less than for conventional linear springs. A system with similar characteristics is proposed in this thesis (Section 3.4 on page 107).

However, for weakly nonlinear magnetic springs, variation in the mass will still lead to changes in the resonance frequency. Todaka et al. [277] created a mechanical linkage to support two magnets in repulsion such that as their air gap increased (due to less mass being supported), a horizontal offset between them was created to lower the linearised operating stiffness. This allowed a much smaller variation in resonance frequency than for flush magnets in repulsion. Bonisoli and Vigliani [46] used an experimental apparatus to analyse the nonlinear behaviour of a magnetic and linear spring in parallel, together with further theoretical analysis [47]. They showed a configuration of linear and magnetic springs with the notable feature that the resonance frequency exhibits little dependence on mass loading and nonlinear effects can be seen. A contribution in this area is made in this thesis in Section 3.4 on page 107, in which a purely magnetic device is designed to achieve constant resonance frequency with variations in mass.

§1.4.3 *Quasi–zero stiffness systems*

In a conventional mass–spring system, the static deflection increases as the stiffness of the support is reduced, and a lower limit on the stiffness is imposed by constraints on the allowable displacement. Novel approaches are required to reduce the resonance frequency below that possible with a linear spring. The addition of negative stiffness elements in a design reduces the resonance frequency, which improves vibration isolation. Early examples of such designs using inclined springs were shown by Molyneux [201]. These have an approximately cubic force versus displacement characteristic, which may be tuned to achieve a local region of zero stiffness, which is often termed 'quasi–zero stiffness'. Alabuzhev et al. [8] examined the nonlinear characteristics of such systems, as have several others [55, 57, 160]. The

dynamic response of these systems has been shown to exhibit prominent nonlinearities that distort the frequency response but that do not decrease the vibration isolation efficacy in general. Analysis of the nonlinear dynamics of such systems [160, 161, 169] can be quite involved and is outside the scope of this research.

A variety of mechanical linkages and arrangements can be designed for quasi–zero stiffness [274]. Mechanical quasi–zero stiffness elements, generally using flexible beam supports in a buckling regime, have been used in application for vibration isolation platforms [220], mounts for seismic noise attenuation [59], vibration attenuation from hand-held machinery [270], reduction of aircraft cabin noise [25], and vehicle driver suspension [170]. Friction is a limiting factor in these devices [14, 270]; this particular problem is obviated when non-contact supports are used. As an alternative to the classical helical spring for vibration isolation support, the 'pinched loop' created by clamping both ends of a slender beam at the same location (the shape resembles a droplet) has a wide range of tuning possibilities and offers isolation in two degrees of freedom [285]. Further detail into the field of nonlinear passive vibration isolators is given in the recent review by Ibrahim [132].

Quasi–zero stiffness can also be achieved with magnetic systems. Magnetic configurations with negative stiffness can be used to augment a positive stiffness support (which can be simply a conventional spring) to lower the resonance frequency. For example, Beccaria et al. [32] used this technique (under the term 'magnetic antisprings') to improve the isolation for gravity wave detectors. Others have used attractive magnets in parallel with conventional springs to reduce the resonance frequency of the system [56], or similar hybrid approaches using both magnetic forces and linear springs [294]. Similarly, the negative stiffness of an electromagnetic actuator has been compensated for by embedding the suspended mass within a membrane to achieve a low overall stiffness [252]. Zhou and Liu [309] recently demonstrated an active/passive tuneable quasi–zero stiffness system that used a moving permanent magnet in attraction to soft-iron-core electromagnets as the negative stiffness element in series with a clamped–clamped beam for positive stiffness. A range of stiffness characteristics were demonstrated by varying different system parameters, including the creation of an approximately constant and minimal stiffness over a required displacement range.

Purely non-contact magnetic systems can also be used to similar effect using a repulsive magnet pair in series with an attractive magnet pair both oriented vertically [237, 238], analysed in detail in Section 6.3 on page 191. More recently, multipole systems (see Chapter 4) have been investigated

which use the same general magnet configuration [139]. An alternate design is shown by Hol et al. [127], which uses an axial bearing with 90° rotated magnetisations to bear load in the vertical direction; the force–displacement characteristic is a mirror image of the attraction–repulsion pair. Systems that use such negative stiffness between attracting magnets cannot be brought to a stable quasi–zero stiffness region due to their 'softening spring' characteristic. In these cases the negative stiffness is used to reduce the resonance frequency as much as possible before instability occurs.

Quasi–infinite stiffness systems

For completeness, this section covers the opposite of the quasi–zero stiffness system: with a different combination of spring elements it is possible to create quasi–*infinite* stiffness, shown in a variety of systems over the last decade starting with single-degree of freedom systems [193–197, 199, 211] and later being extended to multi-degree of freedom [130, 198]. The quasi–infinite stiffness effect is produced with a series combination of a positive stiffness and a negative stiffness spring such that the resultant stiffness is given by

$$k_T = \frac{k_1 k_2}{k_1 + k_2} = \infty, \quad \text{when } k_2 = -k_1 \,.$$

Xing et al. [293] formalised the idea of quasi–zero stiffness and quasi–infinite stiffness systems.

Like 'zero stiffness', some qualification is required on the term 'infinite stiffness' in this context. To achieve 'true' infinite stiffness, a control system is required to stabilise the negative stiffness element of the plant. This control system will impart its own dynamics on the system such that the frequency response of the system will only approach the behaviour desired. In the case of the aformentioned studies, the static behaviour of the systems does converge to an infinite stiffness property, but *dynamically* there are still dynamics associated with the connection. These are shown explicitly in the frequency response functions of such systems [199], which exhibit significant resonance peaks for both direct and ground-borne disturbance.

§1.4.4 *Measuring nonlinear vibrations: the variance gain*

The transmissibility $T(\omega)$ of a system characterises response of a system to inputs that are broadband in frequency. It is usually calculated using a transfer function approach, given by

$$T(\omega) = \frac{P_{mb}(\omega)}{P_{bb}(\omega)} \,, \tag{1.13}$$

where $P_{mb}(\omega)$ is the cross power spectral density between the input and output signals and $P_{bb}(\omega)$ is the power spectral density of the input signal [37]. This formulation is generally only useful for linear systems as it is specifically designed to reject nonlinear signals that may arise due to nonlinearities in the system.

One metric to evaluate the response of a nonlinear system in the frequency domain is known as the 'variance gain' V [253], which can be calculated as a ratio of the root-mean-square output to input signals:

$$V = \sqrt{\tfrac{1}{T}\int_0^T \bar{x}_2(t)^2 \,\mathrm{d}t} \Big/ \sqrt{\tfrac{1}{T}\int_0^T \bar{x}_1(t)^2 \,\mathrm{d}t}\,, \tag{1.14}$$

where T is the time interval over which the variance gain is calculated, and $\bar{x}_2$ and $\bar{x}_1$ are the mean-zero output and input displacements of the vibration isolator, respectively. For linear systems, this expression simplifies to the standard formulation for transmissibility. For nonlinear systems, Eq. 1.14 describes the ratio of output to input energy for a given excitation. For a tonal input disturbance, the variance gain at the frequency of excitation ω_e is

$$V(\omega_e) = \frac{1}{A_e}\sqrt{\frac{2}{T}\int_0^T \bar{x}_2(t)^2 \,\mathrm{d}t}. \tag{1.15}$$

The variance gain allows the nonlinearity of the system to be visualised on a familiar transmissibility–like plot for a range of resonance frequencies and equilibrium positions.

The variance gain technique is useful for broadly quantifying the behaviour of nonlinear systems. For measuring the frequency response function of a predominantly linear system that is contaminated by nonlinear signals whose effects should be discarded, other techniques are available [for example, 254]. There are generalisations of the frequency response function for certain classes of nonlinear systems [166, 216], but with nonlinear analysis different techniques focus on examining different behaviours in the response and there is no single approach that is suitable for all cases. For example, Peng et al. [217] compare two methods, one of which captures 'jump phenomena', and the other which shows superharmonic behaviour. But there is not one general method for classes of nonlinear system, nor perhaps can one exist. For the purposes of this thesis, the variance gain is useful as it demonstrates the frequency-dependent behaviour in a manner similar to that which would be measured in a linear system under broadband disturbance. An example of using the variance gain for analysing the response of a nonlinear quasi–zero stiffness system is demonstrated in the next section.

Quasi–zero stiffness is not zero stiffness

It has been established that the goal of a 'zero stiffness' device is to reduce the resonance frequency of the system to as low a value as possible. In the limiting case, if the system is stable and the nominal force of the spring indeed matches the weight of the mass, then the gradient of the force at the operating point will equal zero.

However, it is necessary to use a nonlinear spring to achieve this zero stiffness condition, and the dynamic behaviour of a nonlinear oscillator varies considerably from that of the classic linear spring. Most obviously, the shape of the frequency response is not independent of the amplitude of the forcing disturbance. Consider the stable single degree of freedom system

$$m\ddot{x}(t) + c\dot{x}(t) + k_3\left[x(t) + p(t)\right]^3 = 0, \tag{1.16}$$

where x is displacement and p is an induced displacement disturbance. At the operating position $x = 0$, the nonlinear spring stiffness is $3k_3x^2|_{x=0} = 0$. For a disturbance p, the spring is perturbed and generates a reaction force of k_3p^3 on the mass. The stiffness here is $3k_3p^2$; that is, dependent on the amplitude of disturbance. The ramifications of this nonlinear force on the vibratory response of the system are not exactly straightforward.

Tentor [275] analysed a spring generated by repulsion magnets which behaved as a Duffing oscillator for large amplitude vibrations:

$$F_{\text{Duffing}} = kx + k_3x^3. \tag{1.17}$$

The nonlinear dynamics only affected the response of the system when the nonlinear term dominated over the linear term. For a quasi–zero stiffness spring $k = 0$ and the nonlinear dynamics are more significant.

Carrella et al. [57], for example, use the 'harmonic balance' method to analyse the nonlinear frequency response of a Duffing oscillator model of an inclined spring based quasi–zero stiffness system, showing the typical jump-up and jump-down phenomena of such nonlinear systems. For the purposes of broadband vibration isolation, however, it is instructive to simply examine the power spectra produced with a range of spring stiffnesses and modelling the disturbance input as Gaussian.

A comparison between the linear transmissibility and the variance gain of the system for p and x is shown in Figure 1.14, where p is a white noise signal of variance S_w. Parameters used in the simulation are shown in Table 1.3. It can be seen that since the linear transmissibility attempts to reject non-correlated linear signals, as the input amplitude increases its response

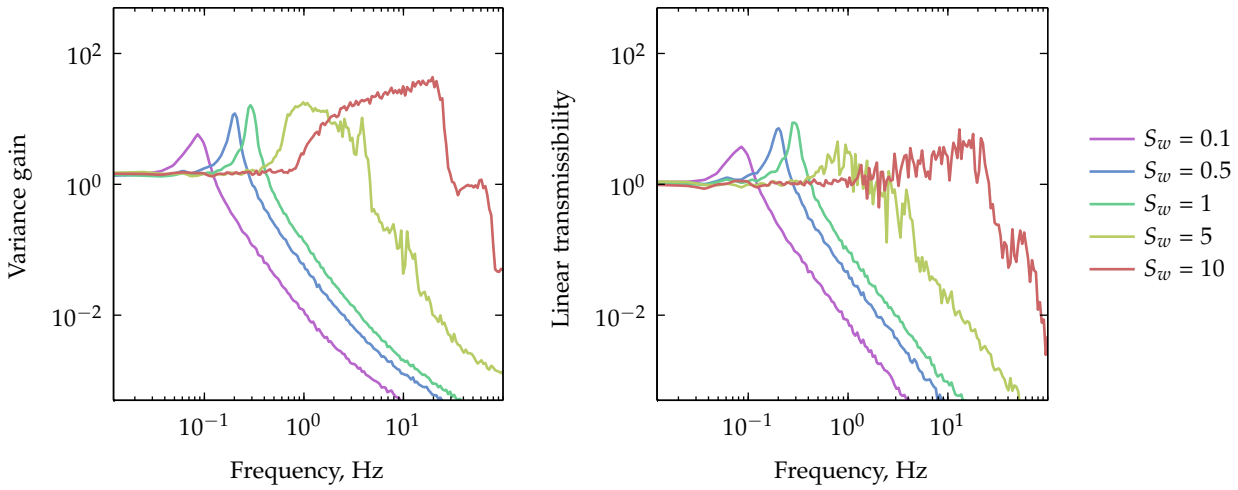

FIGURE 1.14: Frequency response simulations of nonlinear dynamic system Eq. 1.16 with cubic stiffness with random noise inputs of varying variance S_w.

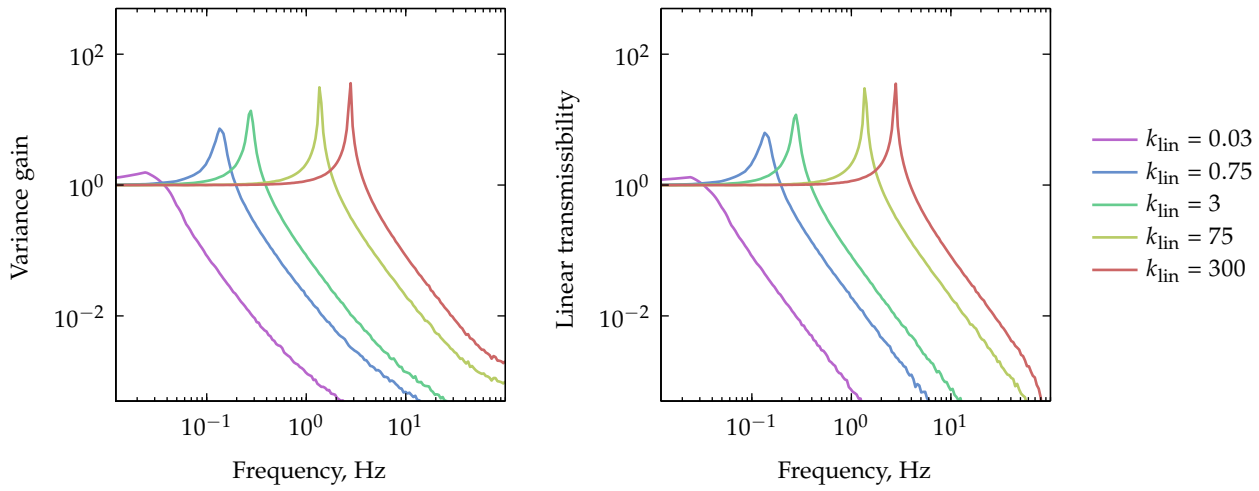

FIGURE 1.15: Equivalent simulations to Figure 1.14 using linearised Eq. 1.18. Note the two methods of showing the transmissibility are equivalent for the linear system, although significant differences are seen as the frequency approaches the maximum measurable frequency according to the sampling parameters.

Table 1.3: Parameters used to simulate the dynamics of Eq. 1.16 (Fig. 1.14).

Simulation time		5000 s
Sample time		0.005 s
FFT size		2^{14}
Mass	m	1 kg
Nonlinear stiffness coefficient	k_3	$1\,\mathrm{kg/m^3}$
Damping	c	$0.1\,\mathrm{kg/s}$

becomes noisier and much of the shape of the power spectrum is lost due to this. Note that the resonance peak changes frequency with input amplitude.

The results of the nonlinear simulation can be compared with a linearised equivalent of the same system given by

$$m\ddot{x}(t) + c\dot{x}(t) + k_{\mathrm{lin}}\left[x(t) + p(t)\right] = 0, \tag{1.18}$$

which has a linear stiffness $k_{\mathrm{lin}} = 3kS_w^2$ equivalent to the stiffness of the nonlinear spring at the variance displacement. Frequency response simulations of this linearised system are shown in Figure 1.15.

When comparing against the nonlinear response, the linearised system response is smaller than the quasi–zero stiffness response in some cases, but especially as the input amplitude increases and the nonlinearities become stronger. This potentially restricts the use of nonlinear springs for vibration isolation application to achieve low resonance frequencies: only when it becomes infeasible to decrease the stiffness of a conventional linear system any further should a nonlinear system be chosen instead. Conversely, the broader 'resonance peaks' of the type seen in Figure 1.14 have been shown to be useful for energy harvesting purposes, especially for wandering narrowband excitation [225].

§1.4.5 *Summary of vibrations and magnetics literature*

The interesting static and dynamic force characteristics exhibited by magnetic systems has suggested their use in a variety of vibration control applications. Of particular research interest is the nonlinear regimes that such systems can operate within; in some cases, these nonlinearities can be detrimental to vibration isolation, while in others they can help improve vibration suppression. For this thesis, the particular use of magnetic systems as softening springs allows them to overcome some limitations seen with linear mechanical springs, the desirable focus in these cases being the 'quasi–zero stiffness' regime to minimise the resonance frequency.

§1.5 Structure of this thesis

This chapter has introduced the themes of this thesis; at this point it is prudent to suggest where the following chapters will lead.

The first half of this thesis is focused specifically on the analysis and design of purely magnetic systems, beginning in Chapter 2 with the theory on calculating forces and torques between magnets of various shape and geometry. Chapter 3 then discusses and analyses load bearing systems composed of various arrangements of singular magnets, culminating in the analysis of a novel magnetic support that uses inclined magnets to achieve a load-invariant resonance frequency. These studies conclude in Chapter 4 with a discussion and analysis of the use of multipole or 'Halbach' arrays, which are composed of many variously-oriented magnets, for improving the load bearing capabilities for magnetic supports.

The thread of the second half of the thesis is the realisation of an experimental apparatus to demonstrate the concepts for a magnetic spring design. Since all forms of unguided magnetic levitation require some degree of active control, Chapter 5 develops theory for calculating quasi-static forces of electromagnets, and performs an optimisation of an electromagnetic actuator suitable for such a task. In discussing quasi–zero stiffness systems for vibration isolation, Chapter 6 begins with a planar analysis of a typical spring-based design from the literature. It is subsequently shown that a magnetic system can be more flexible for adaptive tuning. In the analysis of this quasi–zero stiffness magnetic system, emphasis is made on the small region in which stable operation is achieved. Finally, a prototype based on this magnetic system is presented in Chapter 7 with results demonstrating low frequency vibration isolation and the ability of active vibration control to improve the vibration transmissibility. Chapter 8 summarises the main findings from the preceding chapters, and suggests a list of possible future directions for subsequent research.

Much of the work in this thesis is publicly available for use in the research community under the principles of reproducible research [159]. This can be found in the code repository ⟨`http://www.github.com/wspr/magcode`⟩, which is a compilation of code for calculating the forces between magnets and magnetic systems. A discussion of the philosophy behind this effort and a summary of the reproducible work in this thesis are discussed in Appendix A.

§1.6 Publications arising from this thesis

The following first-authored articles have been published over the course of this Ph. D. research. In one form or another, most of these works have been incorporated into this thesis and are highlighted herein where appropriate.

[236] *A multipole array magnetic spring*; IEEE Transactions on Magnetics, 2005.

[237] *Zero-stiffness magnetic springs for active vibration isolation*; Proceedings of the Sixth International Symposium on Active Noise and Vibration Control, 2006.

[238] *Nonlinear control of a one axis magnetic spring*; Proceedings of the 14th International Congress on Sound and Vibration, 2007.

[244] *Theoretical design parameters for a quasi-zero stiffness magnetic spring for vibration isolation*; Journal of Sound and Vibration, 2009.

[240] *Parameters for optimizing the forces between linear multipole magnet arrays*; Magnetics Letters, IEEE, 2010.

[239] *Maximising the force between two cuboid magnets*; IEEE Magnetics Letters, 2010.

[241] *A simplified force equation for coaxial cylindrical magnets and thin coils*; IEEE Transactions on Magnetics, 2011.

[243] *Theoretical analysis of a non-contact spring with inclined permanent magnets for load-independent resonance frequency*; Journal of Sound and Vibration, 2012.

[242] *Axial force between a thick coil and a cylindrical permanent magnet: Optimising the geometry of an electromagnetic actuator*; IEEE Transactions on Magnets, 2012.

[246] *Planar analysis of a quasi-zero stiffness mechanism using inclined linear springs*; Proceedings of Acoustics 2013.

[245] *Experimental results of a 1D passive magnetic spring approaching quasi-zero stiffness and using active skyhook damping*; Proceedings of Acoustics 2013.

The following conference papers were co-authored:

[101] *Development of a magnetic levitation vibration isolator using inclined permanent magnet springs*; Proceedings of Acoustics 2011.

[310] *The development of a 6 degree of freedom quasi-zero stiffness maglev vibration isolator with adaptive-passive load support*; 15th International Conference on Mechatronics Technology, 2011.

CHAPTER 2

Magnetic and electromagnetic forces

The work presented in Section 2.7 is based on material that has been published as a journal paper [241].

§2.1 Introduction

In this chapter, a summary of various electromagnetic theories used in the remainder of this thesis is presented. The first section covers the basic terminology and physics behind magnetic fields, followed (§2.3) by a discussion of the properties of permanent magnets. Section 2.4 introduces the methods for calculating the force and torque between permanent magnets and coils, followed by an extensive review (§2.6) on analytical equations for forces and torques between cuboid magnets. The chapter concludes on the forces between cylindrical magnets (§2.7), in which a new expression for the force between coaxial cylindrical magnets is presented.

§2.2 Whence magnetic fields

The following is a brief introduction to the physics behind magnets, largely to introduce the notation used later in the thesis.

Magnetic fields are created by moving electrons. A long straight wire will create a cylindrical-like magnet field, and a small loop will create a magnetic dipole. Thus, an electron orbiting a proton is the smallest magnetic element. This is a hydrogen atom. In nature, however, hydrogen exists as H_2, two protons orbited by two electrons — and it happens that the two electrons orbit in opposite directions and the magnetic fields of each cancel each other out. Most material is like this: basically, not magnetic. However, there are a number of compounds that do retain an asymmetry in their electron composition, and this allows them to act magnetically under the right conditions.

§2.2.1 *Magnetic parameters*

The magnetic dipole is designated as the microscopic quantity $\mathbf{m} = I\mathbf{A}$, for a current I and a vector area $\mathbf{A}$ (direction normal to plane). For a collection of magnetic dipoles (as in a permanent magnet) in a vanishingly small volume V, their net effect may be quantified with the macroscopic magnetisation of the material, $\mathbf{M}$:

$$\mathbf{M} = \lim_{V \to 0} \frac{\sum \mathbf{m}}{V} . \tag{2.1}$$

Permanent magnets are generally analysed under the assumption that their magnetisation $\mathbf{M}$ is homogeneous throughout the volume. Inside the magnet itself (with no other external fields present), the magnetic field, $\mathbf{B}$, is given by the relation [54]

$$\mathbf{B} = \mu_0 \mathbf{M} , \tag{2.2}$$

where the proportionality constant μ_0 is known as the permeability of the vacuum.

The equivalence of the magnetic field produced by a current-carrying coil and a permanent magnet is well established. Therefore, it is possible to consider the magnetisation of a permanent magnet to be the result of an (abstract) surface current density $\mathbf{J}_m$ defined by

$$\mathbf{J}_m = \nabla \times \mathbf{M} . \tag{2.3}$$

This is a good starting point for describing the magnetic effects of an external current density $\mathbf{J}$ acting on a magnet. To differentiate between such an induced magnetic field and that caused spontaneously by the magnetic material $\mathbf{M}$, the induced magnetic field is denoted $\mathbf{H}$, defined equivalently as

$$\mathbf{J} = \nabla \times \mathbf{H} . \tag{2.4}$$

These three terms involving magnetic field can now be related to account for both internal and external forms of magnetisation (that is, magnetic field caused by permanent magnets or by current carrying conductors) as [54]

$$\mathbf{B} = \mu_0 (\mathbf{M} + \mathbf{H}) , \tag{2.5}$$

in which $\mathbf{B}$ is referred to as the magnetic flux density, $\mathbf{H}$ is the magnetic field strength, and $\mathbf{M}$ is the magnetisation.[1]

Equation 2.5 may now be used to describe the situation at all points in space (Fig. 2.1). Even in the presence of an external magnetic field, the

1. The names of these terms are not always consistent in the literature. $\mathbf{M}$ is also known as polarisation (often used to avoid statements such as 'magnetisation of the magnet'), and $\mathbf{B}$ and $\mathbf{H}$ are both sometimes known as the magnetic field in different contexts.

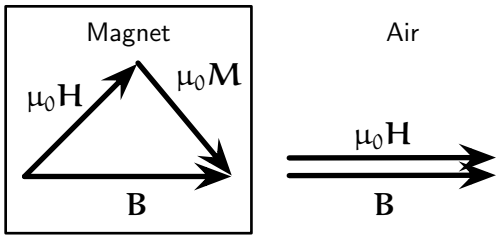

FIGURE 2.1: The magnetic field and its components, both inside and outside a magnet.

magnetic flux density **B** inside a permanent magnet is the vector sum of **H** and **M**, whereas outside the magnet, the magnetisation **M** = 0 and the magnetic flux density **B** is related to the magnetic field strength **H** by a constant. This results in **B** being continuous everywhere, and both **M** and **H** being discontinuous.

§2.2.2 *Relationship between magnetic parameters*

The relationship established by Eq. 2.5 is true only for ideal permanent magnets whose own internal composition is not affected by an applied magnetic field, nor does it provide information about other materials in the presence of a magnetic field. Within such materials, there may be some relationship between the applied magnetic field strength and the resultant magnetic flux density, which is described by the permeability μ of a material where

$$\mu = \frac{\mathbf{B}}{\mathbf{H}}\,. \tag{2.6}$$

The permeability of materials with a non-negligible magnetic interaction will not necessarily be constant with applied field strength or temperature, and for anisotropic materials the permeability will be direction-dependent. It is often convenient to express permeability as a relative measure $\mu_r = \frac{\mu}{\mu_0}$, known as the relative permeability.

The relative permeability of the vacuum is unity, and materials considered 'non-magnetic' such as air, wood, water, and so on, have permeabilities very close to unity (within 1×10^{-5}) as a result. (The consequences of permeability less than unity, diamagnetism, has been discussed on page 30.) Materials which are more strongly affected by magnetic fields have greater permeabilities; for example, within the soft iron core of an electromagnet, current in the coil generates an applied magnetic field on the core, which induces its own internal magnetic field as a result, and which increases the overall strength of the electromagnet (until the core saturates). The larger

the permeability, the larger this 'amplification' effect. Despite having strong remanence and coercivity values, rare earth magnets can be modelled as having a relative permeability of around $\mu_r = 1.05$ under most circumstances (see later discussion on the second quadrant of Figure 2.2(a)), and for most published analytical expressions for field strength the difference from unity is neglected [162].

Refering to Eq. 2.5, in free space where $\mathbf{M} = 0$ the relationship between $\mathbf{B}$ and $\mathbf{H}$ is quite simple, which is essentially the reason that there is a historical terminological confusion between the two. It can be seen that within a magnet, however, their relationship is more complex and important. Consider a magnetic material which has not yet been magnetised. As an external magnetic field is applied to it, the magnetic dipoles within the material begin to align along the direction of the applied field. If the external magnetic field is sufficiently large, the material becomes completely magnetised (such that most of its dipoles are in alignment) and this magnetisation will be retained even once the applied magnetic field is removed. If the magnetic field is increased further, the magnitude of magnetisation of the magnet cannot increase, and it is thus said to be 'saturated'; this saturation magnetisation is denoted M_{sat}. This process is conducted under high temperatures; once the magnetic material cools (with the applied magnetic field still in place) the magnetisation 'sets' and the magnet is formed. This magnetisation is retained unless a large demagnetisation field (which is simply a magnetic field applied in the opposite direction to its magnetisation) is applied to it or the magnet is heated sufficiently to allow its magnetic dipoles to lose their alignment due to thermal effects.

The performance of a magnet is linked to its behaviour under demagnetisation, as a strong magnet that demagnetises easily is of little use in practical application. The behaviour is shown by the BH curve of the magnetic material, an example of which is shown for an ideal strong and weak magnet in Figure 2.2. The BH curve of a magnetic material describes how the magnetic flux density generated by the magnet changes according to applied magnetic field. For the case of using magnetic fields for doing work (such as generating forces), only the second quadrant of the BH curve is considered.

Two important features are shown in Figure 2.2. First, the remanence of the magnet, $B_r = \mu_0 M_{\text{sat}}$, is the value used to indicate the 'strength' of the magnet alone corresponding to its saturation magnetisation. The remanence refers to the amount of magnetic flux density that is measured in the absence of an applied external magnetic field, and it is a common term in practice since the internal magnetisation of a magnet M_{sat} cannot be measured directly.

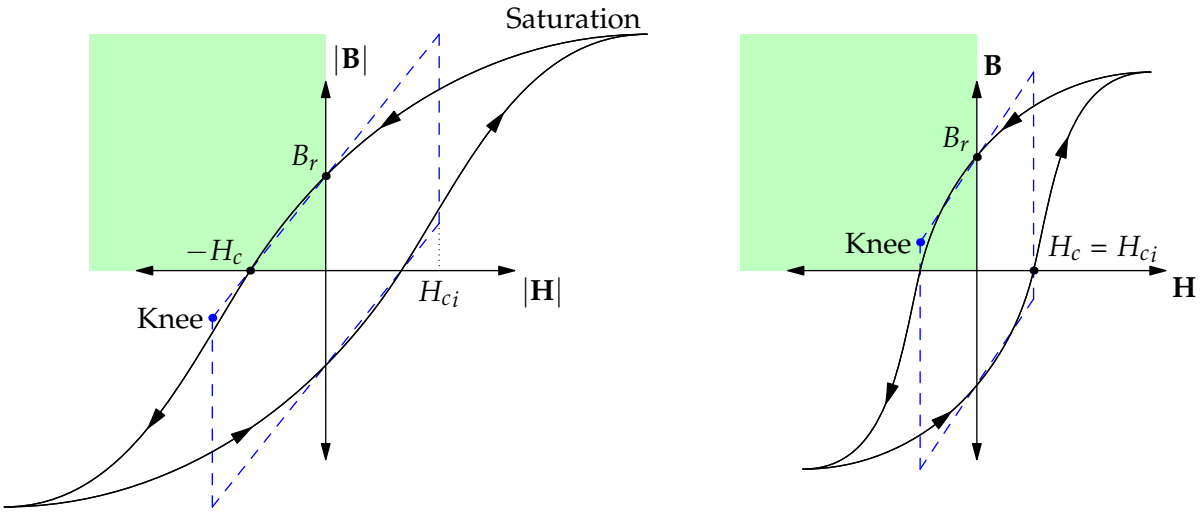

(a) Strong magnet with 'linear' second-quadrant.

(b) Weak magnet with its knee in the second quadrant.

FIGURE 2.2: Characteristic BH curves for a strong magnet and a weak magnet. Dashed lines show the 'idealised' shapes. The second quadrant, in which the magnet is doing work, is shaded.

The second feature of interest on the BH curve is the coercivity, H_c, which is the amount of magnetic field strength required to reduce the magnetic flux density within the magnet to zero. The larger the coercivity, the greater the ability of a permanent magnet to resist demagnetisation due to the influence of external magnetic fields. For the purposes of this thesis, rare earth magnets will be considered which have sufficiently large coercivities to avoid demagnetisation effects.

As well as the remanence B_r and coercivity H_c, two other parameters are often used to describe the 'strength' of a permanent magnet. The first is known as the 'maximum energy product' $\left[BH\right]_{\max}$, relating to the amount of potential energy that can be supplied by the magnetic field in the second quadrant of the BH curve. In an ideal magnet with a BH curve that is linear in the second quadrant, the maximum energy product is directly related to its saturation magnetisation via [54]

$$-\left[BH\right]_{\max} = \mu_0 \left[\frac{M_{\text{sat}}}{2}\right]^2 . \tag{2.7}$$

It can be seen in Figure 2.2(a) that for strong permanent magnets the region of the curve in the second quadrant does indeed approximate a linear function.

For theoretical magnetic force analysis (covered in Section 2.4 and later), the 'strength' value to model the permanent magnets is defined in practice by the remanence of the magnet. When using finite element analysis to model rare earth magnets that can be assumed to have a BH curve that is linear in the second quadrant, it can be necessary to instead define the permeability and coercivity of the magnets. These three terms are related in this case using the relation

$$H_c = \frac{B_r}{\mu\mu_0}\,. \tag{2.8}$$

The final term of interest in the BH curve is known as 'intrinsic coercivity' H_{ci}, which is the magnetic field strength required to completely magnetise a magnetic domain (that is, a collection of dipoles) or to completely reverse the polarity of magnetisation for the same.[2] For weak magnetic material, the intrinsic coercivity is low enough such that the 'knee' of the BH curve enters the second quadrant as shown in Figure 2.2(b), causing the magnet to be easily demagnetised.

§2.2.3 *Properties of magnetic flux*

The previous section introduced **B**, the magnetic flux density. 'Magnetic flux' derives its name from archaic models of magnetism, whose proponents believed in the literal flow of a magnetic fluid called the 'luminiferous æther' [91]. Nowadays, scientists tend toward more modern interpretations using electromagnetic fields involving quantum theory. Nonetheless, the name sticks. Magnetic flux, $\mathbf{\Phi}$, is therefore defined as the amount of 'magnetic fluid' passing through an area:

$$\mathbf{\Phi} = \mathbf{B} \cdot \mathbf{A} \tag{2.9}$$

This flux is almost analogous to electric current; the only difference being that electric current is constrained by the conductor it is flowing through, whereas while magnetic flux is known to *prefer* areas of greater permeability, it occasionally can deviate from these simple paths.

An analysis of how to derive the paths of magnetic flux is a beyond the scope of this document, but it is important to discuss the flux lines themselves. Typical flux lines for a rectangular cross-section magnet are shown in Figure 2.3. It is more instructive for a basic understanding of how magnets behave to examine the ways their flux lines interact. The following

2. Since a permanent magnet is made up of a very large number of magnetic domains, the magnetic field strength used to initially magnetise a permanent magnet is said to be around $5H_{ci}$ as a rule of thumb.

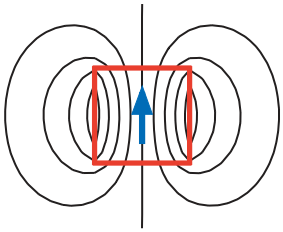

FIGURE 2.3: Lines of magnetic flux of a single magnet.

'magnet design axioms' are adapted from Moskowitz [204], whose book covers permanent magnet design for a wide range of uses.

1. Flux lines follow the path of least resistance. This means that they will travel through the shortest path possible, through the material with the *greatest* permeability — so they will travel more readily through magnetic or ferrous material than air, and more readily through air (although only slightly) than diamagnetic material.
2. Flux lines travelling in the same direction repel each other. This means flux lines will never cross.
3. Flux lines enter (non-saturated) ferrous material at right angles in a low-permeability surrounding.
4. Permeability of ferrous material is 'used up' by flowing flux; when the material reaches saturation, flux lines travel as easily though air as through the saturated material. Saturation is the limiting factor for the design of magnetic shielding.
5. Considering a unit magnetic dipole, flux lines travel from north to south magnetic poles in closed loops.
6. Permanent magnets are made up of a very large number of unit magnetic dipoles.

From these axioms, one can generate incorrect, yet applicable, theories how and why magnets attract and repel each other. For example, two magnets in repulsion have flux lines opposing each other. It can be imagined that the reason forces occur between them is due to a 'squashing' of the flux lines which the magnets try to oppose — but theories like this only help visualising magnetic behaviour, *not* for explaining the reasons behind it.

§2.3 MAGNET PROPERTIES AND SELECTION

There are several materials from which permanent magnets can be made. Short attention will be placed on the cheaper, legacy magnetic materials such as ferrite magnets and alnico magnets due to their poor performance. Rare-earth neodymium magnets are now readily available and rather inexpensive, and have more desirable properties than these old fashioned magnets.

Magnet price is approximately linear with the volume of magnetic material, as shown in the cost graph from a typical magnet supplier shown in Figure 2.4. Prices for permanent magnets have increased dramatically in recent years with greater demand for rare-earth metals in the global market [78].

Table 2.1 shows some approximate ranges comparing the properties of the various magnet types available. Clearly, rare earth magnets are capable of much greater energy output, and their high coercivity precludes them from losing their magnetisation through physical impact or proximity with other magnets — unlike the older ferrite and alnico magnets. The main disadvantage of rare earth magnets is their low maximum operating temperatures. In particular, this could be inconvenient when using rare earth magnets for biased, or hybrid, electromagnets, in which a current carrying coil uses a permanent magnet core to increase the magnitude of the magnetic flux density and provide force even with zero current. At high loads, the coil could

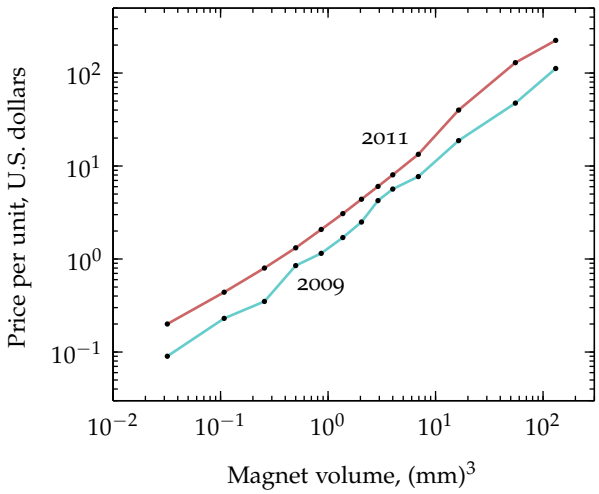

FIGURE 2.4: Magnet price versus magnet volume for rare earth magnets. Data obtained from K&J Magnetics [157] for cube magnets of magnetisation grade N42. 2012–2013 prices have stabilised slightly lower than those shown for 2011.

Table 2.1: Typical values for various permanent magnets. Adapted from information from `http://www.magtech.com.hk/`.

	Magnet type		
Property	Ferrite	Alnico	Neodymium
Max. temperature (°C)	400–500	800–900	80–200
Remanence (T)	0.2–0.4	0.5–1.3	1–1.3
Coercivity (kA/m)	100–200	50–160	800–900
Max. energy product (kJ/m^3)	6–33	10–80	200–300

potentially overheat the magnet past its maximum operating temperature and demagnetise it.

Permanent magnets are graded according to their maximum energy product (Eq. 2.7 on page 51); for example, a magnet with grade N42 has $\left[BH\right]_{\max} = 42\,\mathrm{MG\,Oe}$. Since the conversion to metric for the units of $\left[BH\right]_{\max}$ is $1\,\mathrm{MG\,Oe} = 100/\left[4\pi\right]\,\mathrm{kJ/m^3}$, the metric remanence B_r (units Tesla) of a grade N magnet can be calculated with

$$B_r = 2\sqrt{\mu_0\left[BH\right]_{\max}} = 2\sqrt{N/100}\,, \tag{2.10}$$

which corresponds to $B_r = 2\sqrt{0.42} = 1.3\,\mathrm{T}$ for an N42 grade magnet. The analyses performed in this thesis are generally normalised by magnet strength; that is, the remanence magnetisations for theoretical calculations are usually assumed to be $B_r = 1\,\mathrm{T}$.

Magnets of grade N52 have an approximately 12% increase in magnetic flux density over N42 grade, which corresponds to a force increase of 25%, for an average cost increase of around 40% (prices from K & J Magnetics [157]). As an aside, the highest-known theoretically achievable remanence magnetisation for a permanent magnet is around 2.4 T [256], corresponding to a force increase of 236% over N42 grade magnets. No permanent magnetic material has yet been discovered to achieve anywhere near this magnetisation strength.

§2.3.1 *Homogeneity of magnetisation*

When deriving the equations for the forces between magnets in Section 2.4, it was assumed that each magnet had a constant and uniform magnetisation and a relative permeability of unity. To be fabricated, a homogeneous permanent magnet requires a very strong magnetic field of constant direction and magnitude, and the larger the cross-section of the magnet the harder such a

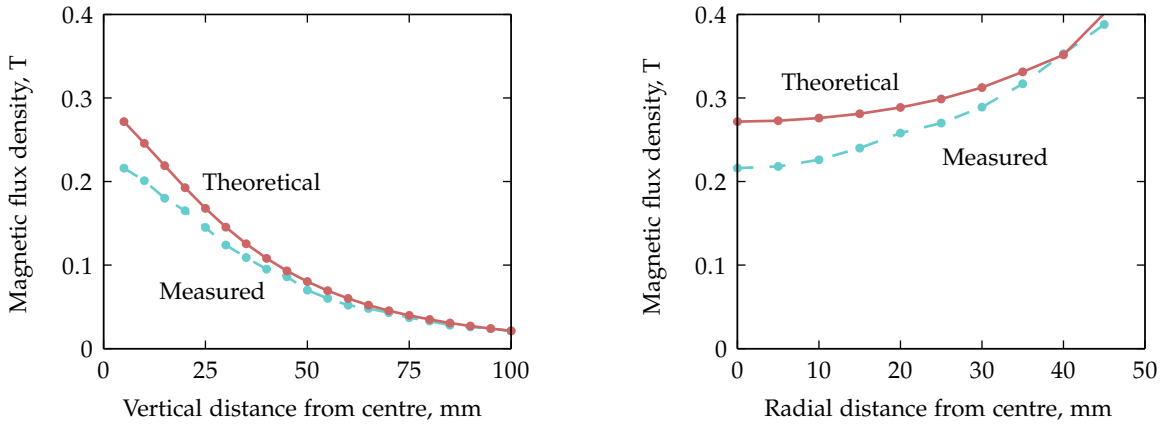

(a) Axial displacement down the centreline.

(b) Radial displacement with a 5 mm offset.

FIGURE 2.5: Magnetic flux density measurements of an N35 neodymium ∅100 mm × 30 mm cylindrical permanent magnet. The origin of the measurements is 5 mm from the face of the magnet.

field is to obtain. For larger permanent magnets, care must be taken when using the force equations presented in the previous chapter. For example, the magnetic field of a neodymium grade N35 cylindrical magnet with diameter 100 mm and thickness 30 mm was compared against theoretical calculations (performed with ANSYS) [51]. While the BH curve of the magnet is unknown, for rare earth magnets it can be assumed that they have a linear relationship in the second quadrant of the BH curve.

To perform these measurements, a gauss meter (Hirst Magnetic Instruments GM07 Gaussmeter) was used to manually sample the magnetic flux density at a number of locations relative to the centre of the top face of the magnet. The results are shown in Figure 2.5. While the comparison across axial position (Fig. 2.5(a)) only shows that the measured magnetic field is lower than expected in the near field, the lateral position results (Fig. 2.5(b)) indicates why: the magnetic field is lower than expected closer to the centre of the magnet. While some of this discrepancy will be caused by the assumption of unity relative permeability [162], this cannot account for the large difference between theory and measurement seen in Figure 2.5. One possibility may be that the magnet is not uniformly magnetised due to its large radius. As a result of this discrepancy in field strength, smaller forces than predicted were measured when using this magnet in repulsion with another large magnet.

§2.4 General techniques for calculating forces between magnets

A general technique for finding the forces between two magnets is simple to describe. The first magnet creates a magnetic field in the region of the second magnet; the force is calculated due to the interaction of the first magnet's field and the internal field of the second magnet.

There are two methods that will be outlined here for calculating the magnetic field of a permanent magnet, known as the charge and current models. Respectively, these consist of modelling the magnets as having two surfaces of 'magnetic charge', or modelling the magnet as being circumscribed of an equivalent surface current density. In the expressions to follow, the magnetisation of each magnet has been assumed to be homogeneous and constant, which is usually a reasonable assumption for modern rare earth magnetic material; hence terms involving $\nabla \cdot \mathbf{M}$ and $\nabla \times \mathbf{M}$ equate to zero and have been omitted from Eqs 2.11 and 2.12.

In the first step, the integration takes place over the surface of the first magnet S_1, which is written for the charge model as

$$\mathbf{B}_1(\mathbf{x}_2) = \frac{\mu_0}{4\pi} \oint_{S_1} \left[\mathbf{M}_1 \cdot \hat{\mathbf{n}}_{s_1}\right] \frac{\mathbf{x}_2 - \mathbf{x}_1}{\left|\mathbf{x}_2 - \mathbf{x}_1\right|^3} \mathrm{d}s_1 \,, \tag{2.11}$$

and for the current model as

$$\mathbf{B}_1(\mathbf{x}_2) = \frac{\mu_0}{4\pi} \oint_{S_1} \left[\mathbf{M}_1 \times \hat{\mathbf{n}}_{s_1'}\right] \times \frac{\mathbf{x}_2 - \mathbf{x}_1}{\left|\mathbf{x}_2 - \mathbf{x}_1\right|^3} \mathrm{d}s_1' \,, \tag{2.12}$$

where $\hat{\mathbf{n}}$ is the normal vector from the differential surface of integration $\mathrm{d}s$.

In the second step, the integration of the function of the magnetic field of the first magnet takes place over the surface of the second magnet S_2, and the integral for the charge model is

$$\mathbf{F} = \oint_{S_2} \left[\mathbf{M}_2 \cdot \hat{\mathbf{n}}_{s_2}\right] \mathbf{B}_1(\mathbf{x}_2) \, \mathrm{d}s_2 \,, \tag{2.13}$$

and for the current model is

$$\mathbf{F} = \oint_{S_2} \left[\mathbf{M}_2 \times \hat{\mathbf{n}}_{s_2'}\right] \times \mathbf{B}_1(\mathbf{x}_2) \, \mathrm{d}s_2' \,. \tag{2.14}$$

Equations 2.13 and 2.14 are general recipes for deriving equations to calculate the forces between permanent magnets of arbitrary geometry, and a similar formulation allows for the modelling of electromagnetic coils as well. In certain circumstances, the geometry of the permanent magnet can

dictate which integral expression should be used; for example, triangular magnets lend themselves towards the charge model [141]. In other cases is not always clear before attempting a solution to the integrals which of Eqs 2.13 and 2.14 will be more suitable in a given situation. For example, a comparison between the current and charge models for calculating the magnetic field for radially-magnetised arc-shaped magnets was made by Ravaud and Lemarquand [226], who stated:

> *The problem is thus to guess what model is the most appropriate for calculating the three components of the magnetic field produced by permanent magnets. It does not seem to be more difficult to use the Amperian current model rather than the Coulombian ['charge'] model for calculating the magnetic field created by parallelepiped magnets. [...] For arc-shaped permanent magnets, it seems to be more difficult to guess what model is the most appropriate.*

One important consideration to bear in mind for deriving force equations is that charge model precludes having overlap between the two volumes, such as when a magnet slides within an outer coil. As an example, the theory of Akoun and Yonnet [5] for calculating the force between two cuboid permanent magnets was derived by modelling each magnet using the charge model; whereas Rovers et al. [248] used the current model for calculating the force between a rectangular cross section coil and a permanent magnet. Since a permanent magnet can be modelled as a thin coil, the two expressions can be compared numerically and they only give equivalent results when the two volumes do not overlap.

Equations 2.13 and 2.14 cannot be solved analytically for complex geometries as the integrals become intractable; numerical integration must be used in this case [63]. When this is necessary, the integrals are generally simplified as much as possible before numerical integration is applied to the remaining terms; for this reason this technique is often called a 'semi-analytical' approach, and is capable of obtaining results in a more straightforward and efficient manner than finite element analysis.

An alternative method to the numerical integration approach is proposed by Furlani [106] in which a magnetic source is discretised into a large number of 'point charges' and the analytical expression for force between each pair combination is summed through superposition. In this case, a general equation for calculating the force between two magnets using the surface charge method can be written as: [105]

$$\mathbf{F} = \frac{B_r^2 \mu_0}{2\pi} \sum_{A_2} \left[\sum_{A_1} \left[\frac{\mathbf{x}_2 - \mathbf{x}_1}{|\mathbf{x}_2 - \mathbf{x}_1|^3} \right] \Delta A_1 \right] \Delta A_2 \,, \tag{2.15}$$

where A_1 and A_2 are the areas of surface charge in the two magnets, and $\mathbf{x}_1$ and $\mathbf{x}_2$ are the position vectors of each surface charge in the interactive pair. While this method does allow the modelling of arbitrary geometries, care must be taken to use a fine enough discretisation mesh to achieve convergence of the solution, and as the mesh becomes finer the algorithm increases in solution time at a rate approximately square to the number of point charges in the model. This discretisation method is avoided in this thesis due to the limited advantage it has over using the semi-analytical approach that uses numerical integration directly.

§2.5 Equations for calculating the magnetic flux density

For the purposes of this work, the analytical calculation of the magnetic flux density $\mathbf{B}$ is largely overlooked in favour of analytical force calculations, which will be addressed in the next section. However, since an analytical formulation for $\mathbf{B}$ is a requirement for then calculating the force, a short literature review will be covered here for different magnet geometries.

The magnetic field for cuboid shaped magnets has a concise solution and has been known for some time for magnetisation in a direction orthogonal to the magnet face [5]. Much more recently, expressions were presented for calculating the magnetic field from a cuboid magnet with magnetisation in an arbitrary direction [227].

Expressions for calculating the magnetic field due to magnetic prisms with triangular faces [79, 141, 249] can be used using superposition to find the magnetic field from magnets with the shape of a quadrilateral pyramidal frustrum, which is a six-sided solid with two parallel faces and four non-orthogonal faces. Such magnet shapes can be stacked to form efficient planar multipole arrays [140] (see also Chapter 4 on page 129).

The geometry of cylindrical magnets and coils results in elliptic integrals in the solution to their field equations. For a cylindrical magnet, the field solutions have been published for both axial magnetisation [231] and radial magnetisation [108]. It is interesting from a historical perspective that new publications on the analytic magnetic field equation for a 'thick coil' (or toroidal conductor with rectangular cross section, more precisely) appear to be being published at an accelerating rate [17, 18, 84, 164, 215, 230, 283, 307]. The newer equations tend to be more general and/or robust.

§2.6 FORCES BETWEEN CUBOID MAGNETS

In this section, the literature for forces between cuboid magnets is introduced in detail as this theory is used extensively in this work. The theory for combining the force equations between parallel and orthogonal cuboid magnets is formalised for the purpose of calculating the forces between arbitrarily magnetised cuboid magnets.

§2.6.1 *(Anti-)parallel alignment*

A variety of analytical solutions have been developed to calculate the force between cuboid-shaped magnets with parallel/anti-parallel magnetisations [5, 48, 207]. More complex geometries can be realised through superposition of the solutions [27].

The notation for the models to calculate the forces between cuboid magnets is as follows, with the geometry of the system depicted graphically in Figure 2.6. The first magnet has dimensions $[2a_1, 2b_1, 2c_1]^\mathsf{T}$ and the second magnet has dimensions $[2a_2, 2b_2, 2c_2]^\mathsf{T}$. The distance between their centres is given by $\mathbf{d} = [d_x, d_y, d_z]^\mathsf{T}$. The force calculated is that acting on the second magnet; for this reason the first magnet is refered to here as the 'fixed' magnet and the second the 'floating' one. The magnetisations of the magnets are assumed to be constant and aligned in the $\hat{z}$ direction ('facing up'). Anti-parallel magnets ('negative magnetisation') corresponds to the secondary

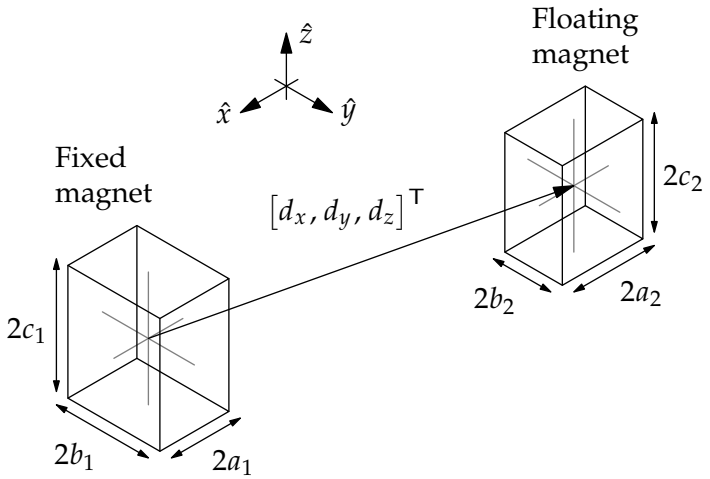

FIGURE 2.6: Geometry for Eq. 2.16 to calculate the forces between two parallel cuboid magnets with magnetisations in the vertical direction, distance between their centres $\mathbf{d} = [d_x, d_y, d_z]^\mathsf{T}$, and magnet sizes as shown.

magnet 'facing down' and results in forces of reversed sign.[3]

The force vector $\mathbf{F}_{z,z}$ between two parallel or anti-parallel magnets with remanences B_{r1} and B_{r2} and geometry defined previously is compactly written as six nested summations of intermediate expressions in the $\hat{x}$, $\hat{y}$, and $\hat{z}$ directions:

$$\mathbf{F}_{z,z} = \frac{B_{r1}B_{r2}}{4\pi\mu_0} \sum_{i,j,k,l,p,q\in\{0,1\}^6} \boldsymbol{\phi}_{z,z}\left(\delta_{i,j,k,l,p,q}\right) \cdot \left[-1\right]^{i+j+k+l+p+q}, \tag{2.16}$$

where $\boldsymbol{\phi}_{z,z}(\delta) = \left[\phi_x(\delta), \phi_y(\delta), \phi_z(\delta)\right]^\mathsf{T}$ will be given later. The (z,z) subscript refers to the directions of magnetisation of the magnets. Force calculations between magnet pairs both oriented in the $\hat{x}$ or $\hat{y}$ directions can be found using a coordinate system transformation on Eq. 2.16.

This form of Eq. 2.16 arises as it is derived from six nested direct integrals. Rather than expanding the limits of each integral, the following summation notation is used instead; say f integrates to F:

$$\int_{-a}^{a} f(x)\,\mathrm{d}x = F(a) - F(-a) = \sum_{i\in\{0,1\}} F\left(a\left[-1\right]^i\right) \cdot \left[-1\right]^i. \tag{2.17}$$

For multiple integrations the summation becomes

$$\int_{z_0}^{z_1}\int_{y_0}^{y_1}\int_{x_0}^{x_1} f(x,y,z)\,\mathrm{d}x\,\mathrm{d}y\,\mathrm{d}z = \sum_{i,j,k\in\{0,1\}^3} F\left(x_i, y_j, z_k\right) \cdot \left[-1\right]^{i+j+k}. \tag{2.18}$$

For N nested integrals, in which f is integrated over variables x_i from $u_i(0)$ to $u_i(1)$:

$$\begin{aligned}&\int_{u_n(0)}^{u_n(1)} \cdots \int_{u_2(0)}^{u_2(1)} \int_{u_1(0)}^{u_1(1)} f(x_1, x_2, \dots)\,\mathrm{d}x_1\,\mathrm{d}x_2 \cdots \mathrm{d}x_n \\ &= \sum_{e_1,e_2,\dots,e_n\in\{0,1\}^N} F(u_1(e_1), u_2(e_2), \dots, u_n(e_n)) \cdot \left[-1\right]^{\sum_{n=1}^{N} e_n}\end{aligned} \tag{2.19}$$

As the limits of the integral occur at the corners of the cuboid magnets, $\boldsymbol{\phi}_{z,z}$ is an intermediate function acting between each combination of corners between the first and second magnet. Bancel [27] used this fact to invent an abstraction for these expressions known as 'magnetic nodes' calling the term $\boldsymbol{\phi}_{z,z}\left(\delta_{i,j,k,l,p,q}\right) \cdot \left[-1\right]^{i+j+k+l+p+q}$ in Eq. 2.16 the 'force' between two magnetic nodes (i,k,p) and (j,l,q). Summing the magnetic node forces between every

3. This relationship is only true of high-coercivity magnets; for magnets such as ferrites whose own magnetic fields can demagnetise each other, an approximation can be made that the repulsive force between two magnets will be approximately 40% of the attractive force between them [204].

combination of corners of the first and second magnet yields the total force between them. This abstraction allows a reduction in the number of calculations required when magnetic nodes overlap; that is, when calculating the forces between arrays of touching magnets.

The distance between two corners/nodes of two respective magnets, $\boldsymbol{\delta}_{i,j,k,l,p,q} = [\delta_{x(i,j)}, \delta_{y(k,l)}, \delta_{z(p,q)}]^\mathsf{T}$, is given by the distance between the magnet centres, $\mathbf{d} = \left[d_x, d_y, d_z\right]^\mathsf{T}$, minus and plus the distance between the magnet centre and corner position for the fixed magnet, $\mathbf{r}$, and for the floating magnet, $\mathbf{R}$, respectively:

$$\boldsymbol{\delta}_{i,j,k,l,p,q} = \mathbf{d} - \mathbf{r}_{i,k,p} + \mathbf{R}_{j,l,q}\,, \tag{2.20}$$

where

$$\mathbf{r}_{i,k,p} = \begin{bmatrix} a_1 \left[-1\right]^i \\ b_1 \left[-1\right]^k \\ c_1 \left[-1\right]^p \end{bmatrix}, \qquad \mathbf{R}_{j,l,q} = \begin{bmatrix} a_2 \left[-1\right]^j \\ b_2 \left[-1\right]^l \\ c_2 \left[-1\right]^q \end{bmatrix}. \tag{2.21}$$

Complete expressions for the corner distances are therefore:

$$\boldsymbol{\delta}_{i,j,k,l,p,q} = \begin{bmatrix} \delta_{x(i,j)} \\ \delta_{y(k,l)} \\ \delta_{z(p,q)} \end{bmatrix} = \begin{bmatrix} d_x - a_1 \left[-1\right]^i + a_2 \left[-1\right]^j \\ d_y - b_1 \left[-1\right]^k + b_2 \left[-1\right]^l \\ d_z - c_1 \left[-1\right]^p + c_2 \left[-1\right]^q \end{bmatrix}. \tag{2.22}$$

The $\boldsymbol{\phi}_{z,z}$ terms required for calculating the 'force between nodes' can now be written, where $r = \sqrt{\delta_x^2 + \delta_y^2 + \delta_z^2}$, as:

$$\boldsymbol{\phi}_{z,z}(\boldsymbol{\delta}) = \begin{bmatrix} \frac{1}{2}\left[\delta_y^2 - \delta_z^2\right]\ln(r-\delta_x) + \delta_x\delta_y\ln\left(r-\delta_y\right) + \delta_y\delta_z\arctan\left(\frac{\delta_x\delta_y}{r\delta_z}\right) + \frac{1}{2}r\delta_x \\ \frac{1}{2}\left[\delta_x^2 - \delta_z^2\right]\ln\left(r-\delta_y\right) + \delta_x\delta_y\ln(r-\delta_x) + \delta_x\delta_z\arctan\left(\frac{\delta_x\delta_y}{r\delta_z}\right) + \frac{1}{2}r\delta_y \\ -\delta_x\delta_z\ln(r-\delta_x) - \delta_y\delta_z\ln\left(r-\delta_y\right) + \delta_x\delta_y\arctan\left(\frac{\delta_x\delta_y}{r\delta_z}\right) - r\delta_z \end{bmatrix} \tag{2.23}$$

Note that when evaluating these functions, two numerical singularities must be accounted for:

$$\lim_{x\to 0} x\log x = 0, \qquad \lim_{x\to 0}\arctan(x/x) = 0. \tag{2.24}$$

The stiffness characteristics can be derived by differentiating Eq. 2.16 with respect to displacement in each respective direction, resulting in

$$\mathbf{K}_{z,z} = \frac{B_{r1}B_{r2}}{4\pi\mu_0}\sum_{(i,j,k,l,p,q)\in\{0,1\}^6} \boldsymbol{\kappa}_{z,z}\left(\delta_{x(ij)}, \delta_{y(kl)}, \delta_{z(pq)}, r\right)\cdot\left[-1\right]^{i+j+k+l+p+q}, \tag{2.25}$$

in which $\boldsymbol{\kappa}_{z,z} = \left[\kappa_x, \kappa_y, \kappa_z\right]^\mathsf{T}$ where

$$\kappa_x = -\frac{\delta_y \delta_x^2}{\delta_x^2 + \delta_z^2} - r - \delta_y \ln\left(r - \delta_y\right) , \tag{2.26}$$

$$\kappa_y = -\frac{\delta_x \delta_y^2}{\delta_y^2 + \delta_z^2} - r - \delta_x \ln(r - \delta_x) , \tag{2.27}$$

$$\kappa_z = \frac{\delta_y \delta_x^2}{\delta_x^2 + \delta_z^2} + \frac{\delta_x \delta_y^2}{\delta_y^2 + \delta_z^2} + 2r + \delta_x \ln(r - \delta_x) + \delta_y \ln\left(r - \delta_y\right) . \tag{2.28}$$

Note that the sum of the stiffness components $\kappa_x + \kappa_y + \kappa_z = 0$ follows from Earnshaw's theorem [91] following from the solution to Laplace's equation.

§2.6.2 *Forces between orthogonal cuboid magnets*

Two groups of researchers simultaneously published, in the same journal, equivalent methods to calculate the force between orthogonal cuboid magnets [10, 137]. The expressions of Allag et al. [10] are slightly simpler and are reproduced here for completeness and consistency. The signs of their equations have been reversed for consistency with Eq. 2.16 in which the equations calculate the force on the second magnet.

The force on a magnet magnetised in the $\hat{y}$ direction due to its interaction with a magnet magnetised in the $\hat{z}$ direction is [10]

$$\mathbf{F}_{z,y} = \frac{B_{r1} B_{r2}}{4\pi\mu_0} \sum_{i,j,k,l,p,q \in \{0,1\}^6} \boldsymbol{\phi}_{z,y}(\boldsymbol{\delta}) \cdot \left[-1\right]^{i+j+k+l+p+q} \tag{2.29}$$

Again, the distance between the 'corner nodes' of each magnet is given by

$$\boldsymbol{\delta}_{i,j,k,l,p,q} = \mathbf{d} + \mathbf{R}_{j,l,q} - \mathbf{r}_{i,k,p} , \tag{2.30}$$

where $\mathbf{r}_{i,k,p}$ and $\mathbf{R}_{j,l,q}$ were defined in Eq. 2.21. The $\boldsymbol{\phi}_{z,y} = \left[\phi_x, \phi_y, \phi_z\right]^\mathsf{T}$ terms required for calculating the 'force between nodes' for orthogonal magnets are

$$\begin{aligned}
\phi_x(\boldsymbol{\delta}) &= \delta_y \delta_z \ln(r - \delta_x) - \delta_x \delta_y \ln(r + \delta_z) - \delta_x \delta_z \ln\left(r + \delta_y\right) + \\
&\qquad \tfrac{1}{2}\delta_x^2 \arctan\left(\tfrac{\delta_y \delta_z}{r \delta_x}\right) + \tfrac{1}{2}\delta_y^2 \arctan\left(\tfrac{\delta_x \delta_z}{r \delta_y}\right) + \tfrac{1}{2}\delta_z^2 \arctan\left(\tfrac{\delta_x \delta_y}{r \delta_z}\right) , \\
\phi_y(\boldsymbol{\delta}) &= -\tfrac{1}{2}\left[\delta_x^2 - \delta_y^2\right] \ln(r + \delta_z) + \delta_x \delta_z \ln(r - \delta_x) + \delta_x \delta_y \arctan\left(\tfrac{\delta_x \delta_z}{r \delta_y}\right) + \tfrac{1}{2} r \delta_z , \\
\phi_z(\boldsymbol{\delta}) &= -\tfrac{1}{2}\left[\delta_x^2 - \delta_z^2\right] \ln\left(r + \delta_y\right) + \delta_x \delta_y \ln(r - \delta_x) + \delta_x \delta_z \arctan\left(\tfrac{\delta_x \delta_y}{r \delta_z}\right) + \tfrac{1}{2} r \delta_y .
\end{aligned} \tag{2.31}$$

The stiffness characteristics can be derived by differentiating Eq. 2.29 with respect to displacement in each respective direction, resulting in

$$\mathbf{K}_{z,y} = \frac{B_{r1} B_{r2}}{4\pi\mu_0} \sum_{(i,j,k,l,p,q) \in \{0,1\}^6} \boldsymbol{\kappa}_{z,y}\left(\delta_{x(ij)}, \delta_{y(kl)}, \delta_{z(pq)}, r\right) \cdot \left[-1\right]^{i+j+k+l+p+q} , \tag{2.32}$$

in which $\boldsymbol{\kappa}_{z,y} = \left[\kappa_x\,,\,\kappa_y\,,\,\kappa_z\right]^\mathsf{T}$ where

$$\begin{aligned}
\kappa_x &= \frac{\delta_x^2\delta_y}{\delta_x^2+\delta_y^2} + \frac{\delta_x^2\delta_z}{\delta_x^2+\delta_z^2} - \delta_x \arctan\left(\frac{\delta_y\delta_z}{\delta_x r}\right) + \delta_z \ln\left(\delta_y + r\right) + \delta_y \ln(\delta_z + r)\ , \\
\kappa_y &= -\tfrac{1}{2}\delta_y + \tfrac{\delta_x^2\delta_y}{\delta_x^2+\delta_y^2} - \tfrac{\delta_x\delta_y\delta_z}{\delta_y^2+\delta_z^2} - \delta_x \arctan\left(\tfrac{\delta_x\delta_z}{\delta_y r}\right) + \delta_y \ln(\delta_z + r)\ , \\
\kappa_z &= -\kappa_x - \kappa_y\,.
\end{aligned} \tag{2.33}$$

§2.6.3 *Simplified force and stiffness expression for cube magnets*

The function F_s is the simplication of the force between parallel magnets, Eq. 2.16, for equal-size coaxial cube magnets, where a is the side length, $l = d_z/a$ is the normalised vertical displacement, and B_{r1} and B_{r2} are the remanence magnetisations of the two magnets:

$$F_s = a^2 f_s\,, \tag{2.34}$$

where

$$f_s = \frac{B_{r1}B_{r2}}{\pi\mu_0}\bar{f}_s\,, \tag{2.35}$$

and

$$\begin{aligned}
\bar{f}_s = {} & \left[-2+l\right]\cdot\left|-2+l\right| - 2l\left|l\right| + \left[2+l\right]\cdot\left|2+l\right| + 4l\sqrt{4+l^2} - 2l\sqrt{8+l^2} \\
& + \left[4-2l\right]\sqrt{8-4l+l^2} + \left[-2+l\right]\sqrt{12-4l+l^2} + \left[-4-2l\right]\sqrt{8+4l+l^2} \\
& + \left[2+l\right]\sqrt{12+4l+l^2} + 2\left[4\arctan\left(\frac{4}{l\sqrt{8+l^2}}\right) + 2\arctan\left(\frac{4}{\left[2-l\right]\sqrt{12-4l+l^2}}\right)\right. \\
& - 2\arctan\left(\frac{4}{\left[2+l\right]\sqrt{12+4l+l^2}}\right) + 2l\ln\left(-2+\sqrt{4+l^2}\right) - 2l\ln\left(2+\sqrt{4+l^2}\right) \\
& - 2l\ln\left(-2+\sqrt{8+l^2}\right) + 2l\ln\left(2+\sqrt{8+l^2}\right) + 2\ln\left(-2+\sqrt{8-4l+l^2}\right) \\
& - l\ln\left(-2+\sqrt{8-4l+l^2}\right) - 2\ln\left(2+\sqrt{8-4l+l^2}\right) + l\ln\left(2+\sqrt{8-4l+l^2}\right) \\
& - 2\ln\left(-2+\sqrt{12-4l+l^2}\right) + l\ln\left(-2+\sqrt{12-4l+l^2}\right) + 2\ln\left(2+\sqrt{12-4l+l^2}\right) \\
& - l\ln\left(2+\sqrt{12-4l+l^2}\right) - 2\ln\left(-2+\sqrt{8+4l+l^2}\right) - l\ln\left(-2+\sqrt{8+4l+l^2}\right) \\
& + 2\ln\left(2+\sqrt{8+4l+l^2}\right) + l\ln\left(2+\sqrt{8+4l+l^2}\right) + 2\ln\left(-2+\sqrt{12+4l+l^2}\right) \\
& \left. + l\ln\left(-2+\sqrt{12+4l+l^2}\right) - 2\ln\left(2+\sqrt{12+4l+l^2}\right) - l\ln\left(2+\sqrt{12+4l+l^2}\right)\right]
\end{aligned} \tag{2.36}$$

The stiffness K_s is calculated by differentiating Eq. 2.16 before simplifying, as with the force terms, to

$$K_s = ak_s\,, \tag{2.37}$$

where

$$k_s = -\frac{2B_{r1}B_{r2}}{\pi\mu_0}\bar{k}_s\,, \tag{2.38}$$

and

$$\begin{aligned}\bar{k}_s = {} & |-2+l| - 2\,|l| + |2+l| + 4\sqrt{4+l^2} - 2\sqrt{8+l^2} - 2\sqrt{8-4l+l^2} + \sqrt{12-4l+l^2} - 2\sqrt{8+4l+l^2} \\ & + \sqrt{12+4l+l^2} + 2\ln\left(-2+\sqrt{4+l^2}\right) - 2\ln\left(2+\sqrt{4+l^2}\right) - 2\ln\left(-2+\sqrt{8+l^2}\right) \\ & + 2\ln\left(2+\sqrt{8+l^2}\right) - \ln\left(-2+\sqrt{8-4l+l^2}\right) + \ln\left(2+\sqrt{8-4l+l^2}\right) \\ & + \ln\left(-2+\sqrt{12-4l+l^2}\right) - \ln\left(2+\sqrt{12-4l+l^2}\right) - \ln\left(-2+\sqrt{8+4l+l^2}\right) \\ & + \ln\left(2+\sqrt{8+4l+l^2}\right) + \ln\left(-2+\sqrt{12+4l+l^2}\right) - \ln\left(2+\sqrt{12+4l+l^2}\right)\end{aligned} \tag{2.39}$$

These simplified equations are reproduced here to emphasise the a^2 relationship for the force shown in Eq. 2.34 and the a relationship for the stiffness in Eq. 2.37. This is interesting because it is not evident from Akoun and Yonnet's original equations that such a simplification is possible. These equations, particularly Eq. 2.35, are useful in Section 6.3 for the analysis of a magnetic system in which the magnet size can be factored away from consideration.

§2.6.4 *Cuboid magnets with arbitrary magnetisations*

Most force expressions are derived from magnetic field equations that are assumed for magnets with magnetisation parallel to one of their sides. Superposition can then be used to combine the expressions for orthogonal magnets to generate the force from a magnet with arbitrary magnetisation. Ravaud and Lemarquand [227] instead show the magnetic field equations for a cuboid magnet with arbitrary magnetisation; their work is still to be extended to calculate the forces between such magnets. Since their equation for calculating the magnetic field is necessarily more complex, it is not clear whether an equation derived using analytical integration to calculate the force directly (if the integral is even tractable) will be more efficient than the superposition approach outlined in the following.

The geometry of the two-magnet system is shown in Figure 2.6, in which the magnets have sides of length $\mathbf{s} = [2a_1, 2b_1, 2c_1]^\mathsf{T}$ and $\mathbf{S} = [2a_2, 2b_2, 2c_2]^\mathsf{T}$ respectively and the distance between their centres is given by $\mathbf{d} = [d_x, d_y, d_z]^\mathsf{T}$. The calculations always assume that the first magnet is fixed and force is acting on the second magnet. The signs must be reversed to obtain the forces acting on the first magnet.

As shown earlier in Eq. 2.16, Akoun and Yonnet [5] provide the force expressions for magnets with vertical magnetisations. This force is now denoted $\mathbf{F}_{z,z}(\mathbf{s}, \mathbf{S}, \mathbf{d}, B_{r1}, B_{r2})$ as a function of the magnet sizes, the distance between

them, and their magnetisation magnitudes B_{r1} and B_{r2}. From Eq. 2.29, Allag et al. [9] provide the force expressions for the first magnet with vertical magnetisation and the second magnet with magnetisation in the horizontal $\hat{y}$ direction. This force is denoted $\mathbf{F}_{z,y}(\mathbf{s}, \mathbf{S}, \mathbf{d}, B_{r1}, B_{r2})$.

The force between a vertically-magnetised magnet and one with magnetisation in the horizontal $\hat{x}$ direction can be calculated by applying a rotational transformation to $\mathbf{F}_{z,y}$ around the $\hat{z}$ axis. That is,

$$\mathbf{F}_{z,x}(\mathbf{s}, \mathbf{S}, \mathbf{d}, B_{r1}, B_{r2}) = \mathbf{R}_z\left(-\tfrac{\pi}{2}\right)\mathbf{F}_{z,x}(\mathbf{s}_{z,x}, \mathbf{S}_{z,x}, \mathbf{d}_{z,x}, B_{r1}, B_{r2}), \tag{2.40}$$

where

$$\mathbf{s}_{z,x} = \left|\mathbf{R}_z\left(\tfrac{\pi}{2}\right)\mathbf{s}\right|, \tag{2.41}$$

$$\mathbf{S}_{z,x} = \left|\mathbf{R}_z\left(\tfrac{\pi}{2}\right)\mathbf{S}\right|, \tag{2.42}$$

$$\mathbf{d}_{z,x} = \mathbf{R}_z\left(\tfrac{\pi}{2}\right)\mathbf{d}, \tag{2.43}$$

for which $|\cdot|$ is the *element-wise* absolute value function and $\mathbf{R}_z(\theta)$ is the rotation matrix around the $\hat{z}$ axis:

$$\mathbf{R}_z(\theta) = \begin{bmatrix} \cos\theta & -\sin\theta & 0 \\ \sin\theta & \cos\theta & 0 \\ 0 & 0 & 1 \end{bmatrix}. \tag{2.44}$$

Using the force expressions $\mathbf{F}_{z,x}$, $\mathbf{F}_{z,y}$, and $\mathbf{F}_{z,z}$ in superposition allows the force to be calculated between a vertically magnetised magnet and another magnet with arbitrary magnetisation direction. By applying coordinate system transformations to these expressions, arbitrary magnetisation directions can be achieved for the first magnet as well.

For horizontal $\hat{x}$ direction magnetisation,

$$\mathbf{F}_{x,\{x,y,z\}}(\mathbf{s}, \mathbf{S}, \mathbf{d}, B_{r1}, B_{r2}) = \mathbf{R}_y\left(\tfrac{\pi}{2}\right)\mathbf{F}_{z,\{z,y,x\}}(\mathbf{s}_x, \mathbf{S}_x, \mathbf{d}_x, B_{r1}, B_{r2}) \tag{2.45}$$

where

$$\mathbf{s}_x = \left|\mathbf{R}_y\left(-\tfrac{\pi}{2}\right)\mathbf{s}\right|, \qquad \mathbf{S}_x = \left|\mathbf{R}_y\left(-\tfrac{\pi}{2}\right)\mathbf{S}\right|, \qquad \mathbf{d}_x = \mathbf{R}_y\left(-\tfrac{\pi}{2}\right)\mathbf{d}, \tag{2.46}$$

and $\mathbf{R}_y(\theta)$ is the rotation matrix around the $\hat{y}$ axis:

$$\mathbf{R}_y(\theta) = \begin{bmatrix} \cos\theta & 0 & \sin\theta \\ 0 & 1 & 0 \\ -\sin\theta & 0 & \cos\theta \end{bmatrix}. \tag{2.47}$$

Similarly, for horizontal $\hat{y}$ direction magnetisation,

$$\mathbf{F}_{y,\{x,y,z\}}(\mathbf{s}, \mathbf{S}, \mathbf{d}, B_{r1}, B_{r2}) = \mathbf{R}_x\left(-\tfrac{\pi}{2}\right)\mathbf{F}_{z,\{x,z,y\}}\left(\mathbf{s}_y, \mathbf{S}_y, \mathbf{d}_y, B_{r1}, B_{r2}\right) \tag{2.48}$$

where

$$\mathbf{s}_y = \left|\mathbf{R}_x\left(\tfrac{\pi}{2}\right)\mathbf{s}\right|, \qquad \mathbf{S}_y = \left|\mathbf{R}_x\left(\tfrac{\pi}{2}\right)\mathbf{S}\right|, \qquad \mathbf{d}_y = \mathbf{R}_x\left(\tfrac{\pi}{2}\right)\mathbf{d}, \tag{2.49}$$

and $\mathbf{R}_x(\theta)$ is the rotation matrix around the $\hat{x}$ axis:

$$\mathbf{R}_x(\theta) = \begin{bmatrix} 1 & 0 & 0 \\ 0 & \cos\theta & -\sin\theta \\ 0 & \sin\theta & \cos\theta \end{bmatrix}. \tag{2.50}$$

From Eqs 2.16, 2.29, 2.40, 2.45 and 2.48, the force between two cuboid magnets of arbitrary magnetisation can be written as

$$\mathbf{F}(\mathbf{s}, \mathbf{S}, \mathbf{d}, \mathbf{B_{r1}}, \mathbf{B_{r2}}) = \sum_{i,j\in\{x,y,z\}^2} \mathbf{F}_{i,j}\left(\mathbf{s}, \mathbf{S}, \mathbf{d}, B_{r1_i}, B_{r2_j}\right) \tag{2.51}$$

where

$$\mathbf{B_{r1}} = \left[B_{r1_x}, B_{r1_y}, B_{r1_z}\right]^\mathsf{T}, \qquad \mathbf{B_{r2}} = \left[B_{r2_x}, B_{r2_y}, B_{r2_z}\right]^\mathsf{T}. \tag{2.52}$$

Although it is well known that the principle of superposition can be used in this way, this is the first formalisation of this theory to decompose a diagonal magnetisation into its orthogonal components for calculating the forces between diagonally-polarised magnets.

§2.6.5 *Forces between magnets with relative rotation*

In 1999, a number of papers were published by researchers at *Laboratoire d'Electrotechnique et de Magnétisme de Brest* investigating the forces between non-contact magnetic rotational force couplings. These are of interest to this work because they use an analytical expression for the forces between two cuboid magnets under arbitrary translation, with one inclined at any angle around the $\hat{x}$ axis. A side-view schematic of this geometry is shown in Figure 2.7.

Three papers were published [62, 64, 95] that all contain the force expression of interest, with a fourth [94] containing just the force expression in a single direction. Their expressions are re-written here because each separate publication contains different typographical errors. The equations here have been reconstructed by comparing the differences and similarities between the equations in the different papers, and re-written in a more compact form. Given two magnets located in three dimensional space, of sizes $[2a_1, 2b_1, 2c_1]^\mathsf{T}$ and $[2a_2, 2b_2, 2c_2]^\mathsf{T}$, with the plane of the second rotated by θ around the $\hat{x}$ axis and their centres separated by a distance $\left[d_x, d_y, d_z\right]^\mathsf{T}$,

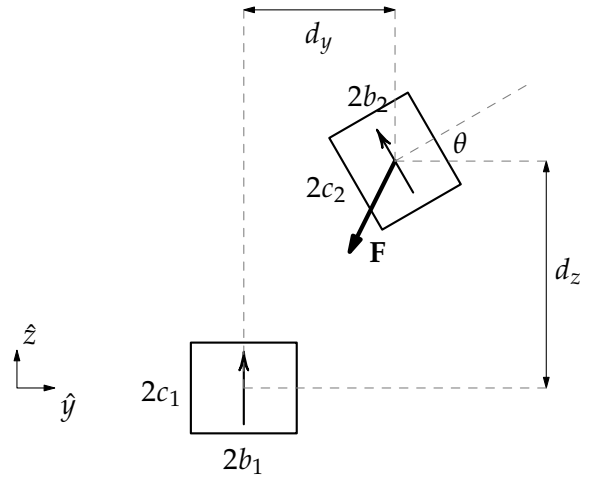

FIGURE 2.7: Geometry for calculating the force between rotated magnets.

the forces in the $\hat{y}$ and $\hat{z}$ directions (F_y and F_z) between the two magnets can be calculated using the following equations:

$$F_y = \frac{B_{r1}B_{r2}}{4\pi\mu_0} \sum_{i,j,k,l,p,q\in\{0,1\}^6} f_{y_2} \cdot \big[-1\big]^{i+j+k+l+p+q}\,, \tag{2.53}$$

$$F_z\Big|_{\theta\neq k\pi} = \frac{-B_{r1}B_{r2}}{4\pi\mu_0} \sum_{i,j,k,l,p,q\in\{0,1\}^6} f_{z_2} \cdot \big[-1\big]^{i+j+k+l+p+q}\,, \tag{2.54}$$

where

$$f_{y_2} = f_3\big(u_0, d_y, d_z, \theta, c_1k, c_2q\big)\,, \tag{2.55}$$

$$f_{z_2} = \frac{f_3(u_1, v_1, w_1, -\theta, 0, 0)}{\sin\theta} + \frac{f_3(u_2, v_2, w_2, \theta, 0, 0)}{\tan\theta}\,, \tag{2.56}$$

and

$$u_0 = d_x - a_1 i + a_2 l\,, \qquad u_1 = u_0 - 2d_x\,, \tag{2.57}$$

$$v_1 = -v_2\cos\theta - w_2\sin\theta\,, \qquad w_1 = v_2\sin\theta - w_2\cos\theta\,, \tag{2.58}$$

$$v_2 = d_y - c_2 q\sin\theta\,, \qquad w_2 = d_z - c_1 k + c_2 q\cos\theta\,. \tag{2.59}$$

The following auxiliary function is used in the above. All dashed variables are local to this function.

$$\begin{aligned} f_3\big(u', v', w', \theta', c', C'\big) = {} & u' f_5\left[\ln\big(f_4 - u'\big) - 1\right] + \tfrac{1}{2}\left[f_6^2 - u'^2\right]\ln(f_4 + f_5) \\ & + \tfrac{1}{2}u'\pi\,\mathrm{sgn}(f_5)\,|f_6| + u' f_6 \arctan\left(\frac{u' f_4 - u'^2 - f_6^2}{f_5 f_6}\right) + \tfrac{1}{2} f_4 f_5\,, \end{aligned} \tag{2.60}$$

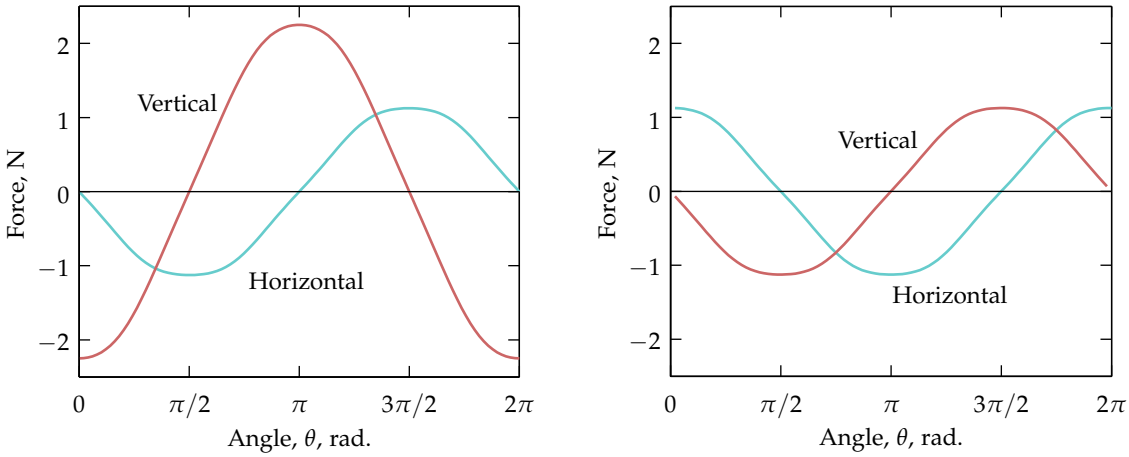

(a) 20 mm vertical displacement.

(b) 20 mm horizontal displacement.

FIGURE 2.8: Vertical and horizontal forces on a rotating magnet due to a fixed one versus rotation angle for fixed horizontal and vertical displacements. The two magnets are 1 T 10 mm cubes.

with

$$f_4 = \sqrt{u'^2 + f_5^2 + f_6^2}\,, \tag{2.61}$$

$$f_5 = \left[v' - b_1 j\right] \cos\theta' + \left[w' - c'\right] \sin\theta' + 2b_2 p\,, \tag{2.62}$$

$$f_6 = -\left[v' - b_1 j\right] \sin\theta' + \left[w' - c'\right] \cos\theta' + C'\,. \tag{2.63}$$

If the second magnet is not rotated around its axis, the force is calculated using Eq. 2.16 since f_{z_2} has a numerical singularity at $\theta = k\pi$.

Although these rotated-magnet force equations permit displacements in the $\hat{x}$ direction, there is no published equation for calculating the component of force in this direction. Numerical integration techniques are currently the best known method if this force must be calculated [63].

Theoretical simulations

As an example of using these equations to calculate forces as a function of magnet rotation, Figure 2.8 shows the forces produced between two 1 T 10 mm cube magnets as a function of rotation angle θ of the second magnet, with a 20 mm offset between their centres. Two cases are shown: in the first, the magnets are displaced vertically; in the second, the magnets are displaced horizontally.

Figure 2.8 shows that the maximum force between two magnets is exhibited when the direction of displacement is in the same direction as their

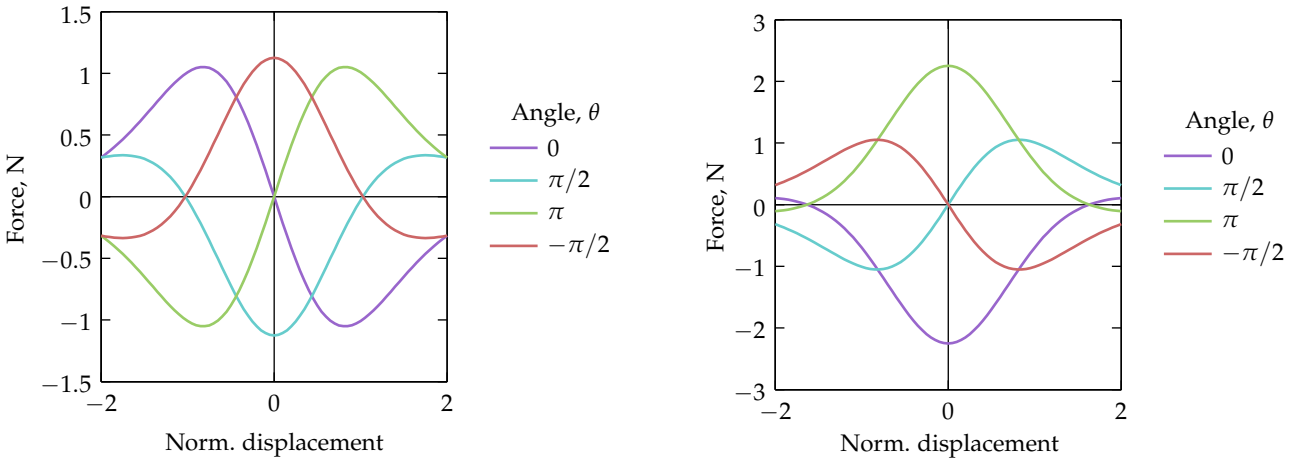

(a) Horizontal forces.

(b) Vertical forces.

FIGURE 2.9: Vertical and horizontal forces on a rotating magnet situated 20 mm above another and displaced horizontally for a range of magnet angles. The two magnets are 1 T 10 mm cubes.

magnetisations. For displacements perpendicular to the direction of magnetisation of the fixed magnet, forces of equal magnitude are obtained for rotation of the second magnet $\theta = k\pi/2$ for $k \in \{0, 1, 2, \dots\}$.

In the second set of simulations, the second magnet is held at a constant height (of a separation distance of one magnet height) and moved from left to right over a range of twice the magnet width symmetrically above the first magnet. Four such displacements are made with four different rotations for the second magnet: 0, $\frac{1}{2}\pi$, π and $-\frac{1}{2}\pi$. Figure 2.9 shows the forces in the horizontal $\hat{y}$ direction and vertical $\hat{z}$ direction, respectively. It can be seen that the opposite rotations result in symmetric force curves, as is expected.

Experimental verification

A series of experiments were performed on a custom built rotating magnet assembly to verify that the re-written equations matched physical measurements.[4] An apparatus for the work of an honours project [52] was constructed to position two magnets relatively to each other with some fixed rotation and horizontal offset with unconstrained vertical motion (Fig. 2.10). The vertical displacement was measured with a Wenglor CP35MHT80 laser sensor, and the base magnet was mounted to an ATI Mini85 SI-950-40 load cell to measure the reaction forces generated by the magnets.

4. Thanks to Mr Callan Byfield for his assistance with the experimental measurements.

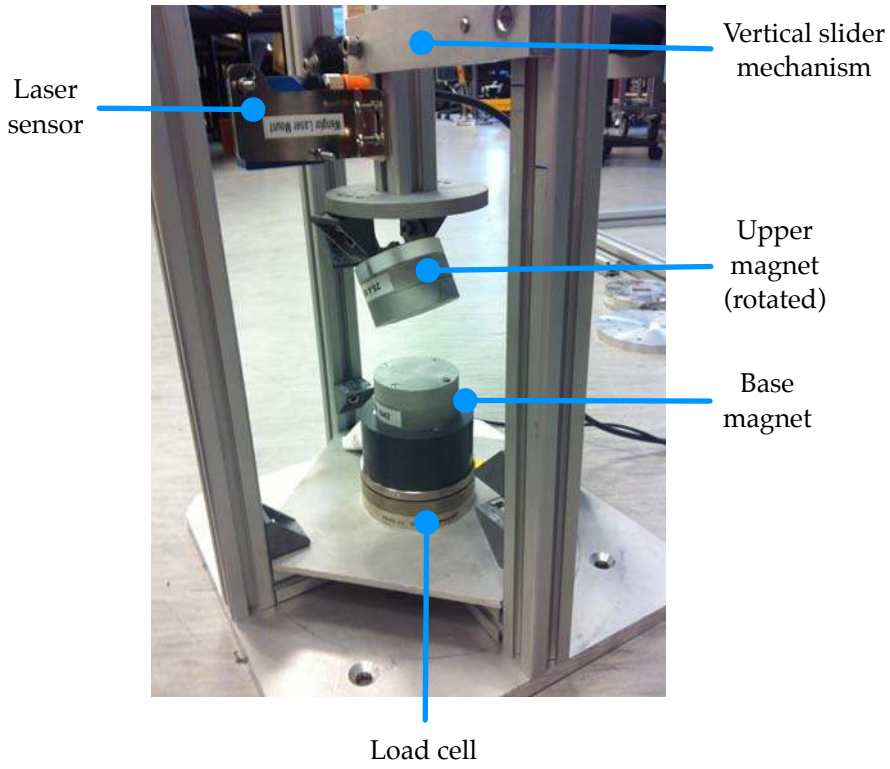

FIGURE 2.10: Photo of the experimental apparatus to measure magnet forces.

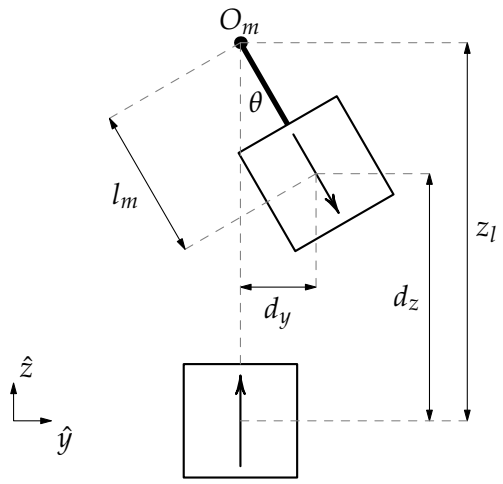

FIGURE 2.11: Geometry of the rotational assembly to determine magnet centre offsets. Upper magnet rotates on a lever arm around point O_m of length $z_l = 53\,\text{mm}$ to the magnet centre.

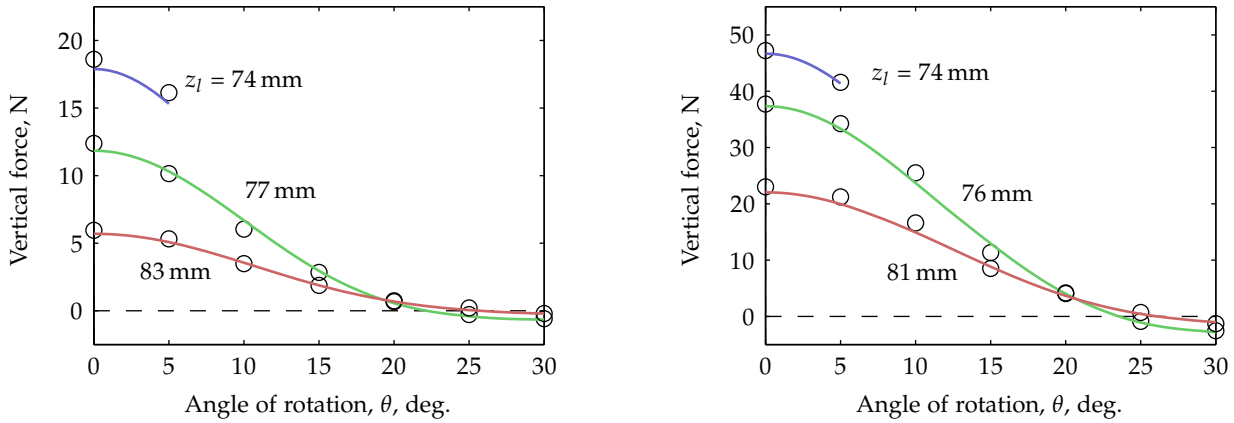

(a) 15 mm × 20 mm × 10 mm N45 cuboid magnets.

(b) 25 mm × 25 mm × 10 mm N52 cuboid magnets.

FIGURE 2.12: Measured forces versus angle of rotation for a rotating magnet assembly showing a set of lever arm displacements, z_l, labelled. Solid lines show theoretical calculations using Eq. 2.54 and circles show experimental measurements. As the magnets become closer together, the cases of the magnets hinder their rotation, limiting their maximum angle.

The geometry of the rotational assembly is shown in Figure 2.11. A number of vertical force versus vertical displacement measurements were taken for a discrete set of rotations θ. Of the tests performed, two sets of results are shown in Figure 2.12:

- N45 15 mm × 20 mm × 10 mm cuboids, and
- N52 25 mm × 25 mm × 10 mm cuboids.

Experimental results match well with theoretical calculations performed using Eq. 2.54. Larger errors with smaller displacements are believed to be caused due to misalignment between the magnets, which would cause larger force discrepancies in the near-field of the magnetic interactions.

§2.6.6 *Torques between cuboid magnets*

Allag and Yonnet [11] have proposed a method, corrected later [303], using the magnetic nodes approach to calculate the torques between cuboid magnets. It is interesting to analyse their approach used to derive their equations, as it is not intuitive from the physics of the situation that their algorithm is valid.

The assertion given by Allag and Yonnet is that since the 'forces' between the nodes of the magnets can be calculated, these corner forces can be used to calculate the applied torque on the magnets. Their expression for the torque (on the second magnet) can be written as per the previous style in the

following form:

$$\mathbf{T}_{z,z} = \frac{B_{r1}B_{r2}}{4\pi\mu_0} \sum_{i,j,k,l,p,q\in\{0,1\}^6} \boldsymbol{\psi}_{i,j,k,l,p,q} \cdot \big[-1\big]^{i+j+k+l+p+q}\,, \tag{2.64}$$

$$\boldsymbol{\psi}_{i,j,k,l,p,q} = \mathbf{R}_{j,l,q} \times \boldsymbol{\phi}_{z,z}\big(\boldsymbol{\delta}_{i,j,k,l,p,q}\big)\,, \tag{2.65}$$

where $\mathbf{R}_{j,l,q}$ is the vector of magnet side lengths as defined in Eq. 2.21. The interpretation of Eq. 2.64 and Eq. 2.65 is that the inner terms of the summation represent the torque applied on the second magnet due to the influence of one corner of the first magnet and one corner of the second magnet. Allag and Yonnet write this slightly differently in terms of the total torque applied from the entire first magnet on each corner of the second:

$$\mathbf{T}_{z,z} = \sum_{j,l,q\in\{0,1\}^3} \mathbf{R}_{j,l,q} \times \mathbf{f}_{j,l,q}, \tag{2.66}$$

where $\mathbf{f}_{j,l,q}$ is the summed force on a corner of the second magnet due to every corner of the first magnet, given by

$$\mathbf{f}_{j,l,q} = \tfrac{B_{r1}B_{r2}}{4\pi\mu_0} \sum_{i,k,p\in\{0,1\}^3} \boldsymbol{\phi}_{z,z}\big(\mathbf{d}_{i,j,k,l,p,q}\big) \cdot \big[-1\big]^{i+j+k+l+p+q}\,. \tag{2.67}$$

In other words, written in this form the 'corner torque' for each node of the second magnet is given by

$$\boldsymbol{\tau}_{j,l,q} = \mathbf{R}_{j,l,q} \times \mathbf{f}_{j,l,q}. \tag{2.68}$$

It is easily seen that Eq. 2.66 and Eq. 2.67 are equivalent to Eq. 2.64 since the inner summation in the former can be migrated out from inside the cross product.

In the interests of clarity, it should be noted that what has been referred to until now as a corner force is in fact not actually a force; rather, it is simply a mathematical abstraction (namely, the bound of an integral). Two examples will be given to highlight this fact. First, consider two geometrically-symmetrical cases from the previous example with zero horizontal displacement:

- nodes $(0,0,0) \to (1,0,0)$, and
- nodes $(1,0,0) \to (0,0,0)$,

where the interaction between two corners is written as $(i,k,p) \to (j,l,q)$. These two interactions are depicted in Figure 2.13(a). The magnetic node force calculated in these two cases are not the same, violating symmetry.

Second, consider a fixed magnet of size $[2a, 2b, 2c]^\mathsf{T}$ reacting with another magnet of some fixed vertical distance away. Compare two cases for

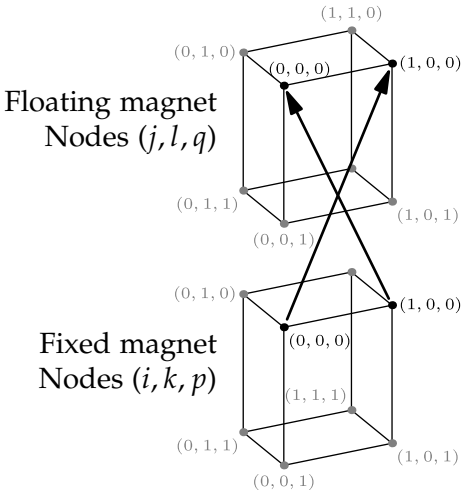

(a) Two geometrically-symmetrical node interactions.

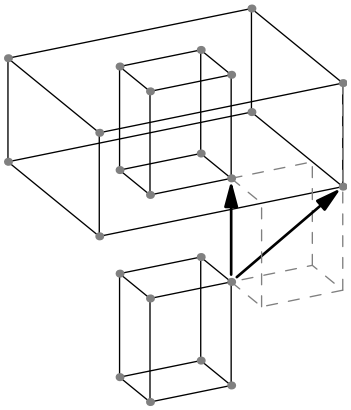

(b) Two node interactions for a smaller magnet and a larger magnet.

FIGURE 2.13: Two examples of interacting magnetic nodes.

the second magnet: the first of equal size as the first with $[2A, 2B, 2C]^{\mathsf{T}} = [2a, 2b, 2c]^{\mathsf{T}}$, and the second of greater size with $[2A, 2B, 2C]^{\mathsf{T}} = [6a, 6b, 2c]^{\mathsf{T}}$. These two cases are shown in Figure 2.13(b) highlighting the interaction between two equivalent corners. The magnetic node force calculated for these cases show that the interaction between the further-apart nodes produces greater magnetic node forces than for the closer nodes. This result violates the well-known inverse-displacement relationship that magnetic forces have.

Despite these two results that show that 'node forces' do not behave like classical forces, the magnetic nodes approach proposed by Yonnet and Allag [303] gives consistent results as the theory by Janssen et al. [142], who separately published a more general equation which derives analytical torque equations from first principles. (Their generalisation allowed the centre of rotation to be located at an arbitrary point rather than the centre of the cuboid magnet.) The same group later published analogous equations for the force between orthogonally-magnetised cuboid magnets [143]. The theory formalising the superposition of magnetic interations outlined in Section 2.6.4 can be used directly to calculate the torques between arbitrarily magnetised cuboid magnets.

§2.7 Forces between cylindrical magnets

The force equations between cylindrical magnets are more difficult to derive than for cuboid magnets since their integrals require a cylindrical coordinate system. In early work in this field, Cooper et al. [81] presented an integral expression for calculating the force between two cylindical magnets. Nagaraj [207] investigated and compared the force between cuboid and cylindrical magnets with arbitrary displacements using numerical integration to calculate his results; Furlani [105, 107] calculated the force between radially-aligned ring magnets using a numerical discretisation of the magnet volume. Hull and Cansiz [131] presented integral equations for calculating the radial and axial forces between a cylindrical magnet and a superconductor, which is equivalent to the force between two cylindrical magnets, and Bassani [30] presented integral equations for calculating the radial and axial forces between ring magnets. The forces between non-coaxial cylindrical magnets were considered by Agashe and Arnold [2], Vokoun et al. [287], with the recent work of Conway [80] the most efficient solution yet presented. All such integral equations require some degree of numerical integration to evaluate, excepting those of Furlani who uses the discretision method instead.

Babic and Akyel [21] and Ravaud et al. [232] presented closed form expressions for calculating the force between pairs of thin coils (in which there are many turns axially but the coil is modelled as having zero radial thickness). As part of the work of this thesis, a simplification of the force equation of Ravaud et al. has been developed [241]. This simplification, Eq. 2.69 on the next page, results in a faster execution time and more convenient calculation with numerical software.

The equation for the force between cylindrical magnets can also be used to calculate the force between thin coils with many axial turns, as both magnet and coil can be modelled as a surface current density around a cylinder (see Figure 2.14). In related work, Kim et al. [151] presented a different integral

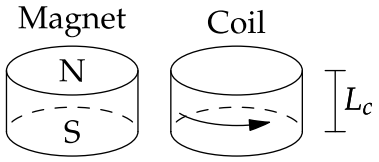

Figure 2.14: The equivalence between a permanent magnet of magnetisation $J = B_r$ (left) in the positive vertical direction, and a current-carrying coil (right) with equivalent magnetisation $J_{\text{eq.}} = \mu_0 NI/L_c$ for current I shown flowing anti-clockwise from the top through N axial turns across length L_c.

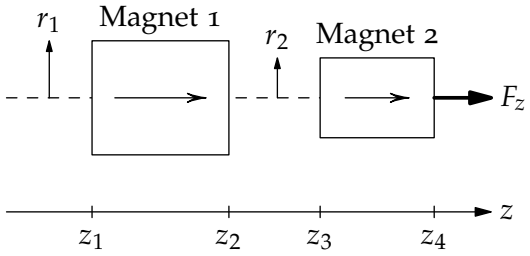

FIGURE 2.15: Two-dimensional side view of a system composed of two coaxial cylindrical magnets with a generated force on the second magnet. (While magnets are shown, either or both may be replaced by a thin coil as shown in Figure 2.14.) Axial displacement between the magnets may be positive or negative, and their volumes may overlap in the case of a magnet located inside a coil. Arrows within the magnets indicate direction of magnetic polarisation.

equation for the radial force between (single-turn) circular coils with eccentric radial displacement, for which further application of their results is required to calculate the forces between coils with many turns. Little attention has been paid to the forces between rotated cylindrical magnets; Babic and Akyel [22] presented equations for calculating the forces between rotated and eccentric (single-turn) circular coils. These expressions can be used with superposition to calculate the forces between rotated and inclined thin-wall solenoids or permanent magnets.

Coaxial magnet force simplification

The magnetic system of interest here consists of two coaxial cylindrical magnets or current-carrying coils which have a relative axial displacement between them, as shown in Figure 2.15. After simplification of the work of Ravaud et al. [231], the equation for calculating axial force F_z is given by [241]

$$F_z = \frac{B_{r1} B_{r2}}{2\mu_0} \sum_{i=1}^{2} \sum_{j=3}^{4} m_1 m_2 m_3 f_z \left[-1 \right]^{i+j}, \tag{2.69}$$

where the intermediate expression f_z is defined in terms of complete elliptic integrals of the first, second, and third kind ($K(m)$, $E(m)$, and $\Pi(n \,|\, m)$, respectively)

$$f_z = K(m_4) - \frac{1}{m_2} E(m_4) + \left[\frac{m_1^2}{m_3^2} - 1 \right] \Pi\left(\frac{m_4}{1 - m_2} \,|\, m_4 \right), \tag{2.70}$$

with parameters

$$m_1 = z_i - z_j\,, \qquad m_2 = \frac{\left[r_1 - r_2\right]^2}{m_1^2} + 1\,, \tag{2.71}$$

$$m_3^2 = \left[r_1 + r_2\right]^2 + m_1^2\,, \qquad m_4 = \frac{4r_1r_2}{m_3^2}\,, \qquad 0 < m_4 \leq 1\,. \tag{2.72}$$

This equation is particularly efficient to calculate as the complete elliptic integrals of the first, second, and third kind can all be calculated simultaneously with a single iteration of the arithmetic-geometric mean approach [90, §19.8(i)]. Additionally, with the use of the complete elliptic integrals this equation is straightforward to implement in numerical software (such as Matlab) that does not have in-built support for the incomplete elliptic integrals.

§2.7.1 *Numerical evaluation of the axial force*

Numerical singularities occur when an expression is mathematically continuous and terms within the expression approach infinity; care must be taken when evaluating such expressions numerically. There are two numerical singularities in Eq. 2.69. The first occurs when the radii are equal such that $m_2 = 1$ and the following term disappears as $\Pi(\pm\infty \,|\, m) = 0$:

$$\left[\frac{m_1^2}{m_3^2} - 1\right] \Pi\left(\frac{m_4}{1 - m_2} \,|\, m_4\right) = 0, \quad m_2 = 1\,. \tag{2.73}$$

The second numerical singularity occurs when the magnets/coils have coincident faces such that $m_1 = 0$ for some values of i and j in the double summation. In this case, the parameter m_2 contains the coefficient $1/m_1^2 = 1/0$. This singularity can be avoided entirely since coincident faces generate no component of force between them, and hence the entire intermediate expression within the summation $m_1 m_2 m_3 f_z'$ can be defined as zero when $m_1 = 0$.

§2.7.2 *Implementation efficiency*

Evaluated in Mathematica v6 (including branching to avoid singularities), Eq. 2.69 took an average of 0.26 ms on a notebook computer to calculate the force at a single location (10000 samples with random input variables). The original equation by Ravaud et al. in the same configuration evaluated in 2.2 ms on average, which is over eight times slower than the new equation. For researchers performing design optimisations with variations over a large number of parameters, such an efficiency improvement is useful in minimising the total computation time of the optimisation process.

TABLE 2.2: Summary of the quasi-static magnetic theory presented in the literature.

Geometry	Expression	Reference
Parallel cuboid	$\mathbf{F}_{z,z}$	[5]
	$\mathbf{F}_{z,y}$	[10, 137]
	$\mathbf{T}_{z,z}$	[142]
	$\mathbf{T}_{z,y}$	[143]
Cuboid rotated around $\hat{x}$ axis	F_y, F_z	§2.6.5
Circular current loops, rotated	F_z, F_r	[22]
Coaxial cylindrical magnet/coil	F_z	[241]
Non-coaxial cylindrical magnet/coil	F_z, F_r	[80]

§2.8 SUMMARY OF THE MAGNETIC THEORY

A brief introduction to the theory and terminology used in the analysis of magnetic systems has been presented. An overview of the literature has highlighted solutions for calculating the forces, torques, and stiffnesses between permanent magnet configurations of various geometries. The closed form solutions that have been presented are summarised in Table 2.2; this theory is used extensively in the remainder of this work.

CHAPTER 3

Magnetic springs

The material presented in Section 3.4 is based on material that has been published as a journal paper [243].

§3.1 Overview

The force created between combinations of permanent magnets can be used in various ways for supporting load. This chapter investigates a number of different configurations for such magnetic springs, of which some have been studied to various degrees in the literature and of which some are novel. Varieties in design lend themselves for different purposes, such as optimising for static load force, low stiffness, number of directions of instability, and low variability in resonance frequency.

Single-axis magnetic springs are discussed in Section 3.2, comparing cuboid and cylindrical magnets. A variety of magnetic spring designs are considered in Section 3.3, especially in regard to the stability of different designs; it is shown that it is possible in theory to design a rotationally-stable magnetic spring.

The chapter concludes with a theoretical (§3.4) and experimental (§3.5) analysis of a new magnetic spring design using inclined permanent magnets that decouples load bearing and resonance frequency.

§3.2 Single-axis magnetic spring

Two magnets with faces aligned in repulsion create a simple spring with a nonlinear 'stiffening' force versus displacement characteristic; as the magnets become closer together the change in force becomes larger. When bearing load at equilibrium, for small displacements such an arrangement closely approximates a classic spring–mass–damper system which can be used for vibration isolation [223].

An example of such a magnetic spring can be seen in Figure 3.1, with one fixed and one floating magnet arranged vertically. With like poles facing, the two magnets repel each other and will hold the system at equilibrium with an air gap between them. Displacement towards each other is restored by the repulsive magnetic force, and displacement away is restored by gravity. The

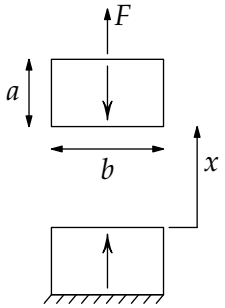

FIGURE 3.1: Schematic of a repulsive magnetic spring. The magnets have square facing sides and extend a distance b in the direction toward the reader. When $x = 0$ the magnet faces are touching.

floating magnet must be constrained in both horizontal directions by guides. If the constraint is removed, it will be naturally unstable horizontally due to Earnshaw's theorem (§1.3.3).

A natural question for magnet selection in such cases is 'what size should the magnets be?'. As magnet price scales with volume (Fig. 2.4), it is often desirable to minimise the magnet volume for a required force, and the question then becomes what magnet *shape* to choose. Permanent magnets in two different shapes are examined here: square-face cuboid and cylindrical.

§3.2.1 *Square-face cuboid magnets*

Consider the basic magnetic spring shown in Figure 3.1, consisting of two magnets separated by a displacement, x (measured between the near faces), and generating a repulsive force, F, between them. The magnets have square facing sides, a height-to-width ratio of $\gamma = a/b$, and a fixed volume V_m; the height of each magnet and the face size width (and length into the page) is, respectively,

$$a = \left[V_m \gamma^2\right]^{1/3}, \qquad b = \left[\frac{V_m}{\gamma}\right]^{1/3}. \tag{3.1}$$

The magnetic force between the magnets can be calculated by applying the theory of Akoun and Yonnet [5], where the force $F = \mathbf{F}_{z,z}(V_m, \gamma, x)$ is Eq. 2.16 as a function of magnet volume V_m, size ratio γ, and displacement x. Such forces were calculated for a magnet volume $V_m = \left[10\,\text{mm}\right]^3$ over a displacement x from 0 mm to 10 mm and a magnet size ratio γ from 0.1 to 1. Note that the forces were calculated with a magnetisation of 1 T for both magnets, normalising the output forces by the magnetisation strength.

In order to compare the force versus displacement characteristics for a range of magnet size ratios, the forces were normalised by the force for cube magnets $F_s = \mathbf{F}_{z,z}(V_m, 1, x)$. Figure 3.2 shows the normalised force F/F_s as a function of displacement x over a range of magnet size ratios γ. The figures are drawn as separate graphs in order to avoid overlap of the curves; size ratio γ varies from 0 to 0.4 in Figure 3.2(a) and from 0.4 to 0.8 in Figure 3.2(b). It can be seen from the two graphs that a magnet size ratio γ of around 0.4 produces the greatest forces; for values both smaller and greater than 0.4, the normalised force curves decrease.

Some overlap in the force curves for $\gamma = 0.4$ and $\gamma = 0.5$ is seen in Figure 3.2(b). This indicates that the optimum magnet size ratio (to maximise the force) is dependent on the displacement between the magnets. Figure 3.4(a) shows the magnet force varying as a function of magnet size ratio γ with a set of curves corresponding to fixed displacements from 1 mm to 10 mm. For each curve, there is a local maxima in the force; this corresponds to the magnet size ratio that produces the greatest force at that displacement. While the magnet size ratio that produces the greatest forces varies somewhat with displacement, the graph shows that the optimum magnet size ratio remains around $\gamma \approx 0.4$. This is consistent with the work of Anderson and Salter [13], who instead performed a series of numerical optimisations to find the maximum magnet force between square-face cuboid magnets. A similar result was shown by Cooper et al. [81] to optimise the forces between magnetic cylinders, using a numerical integration method for the calculations.

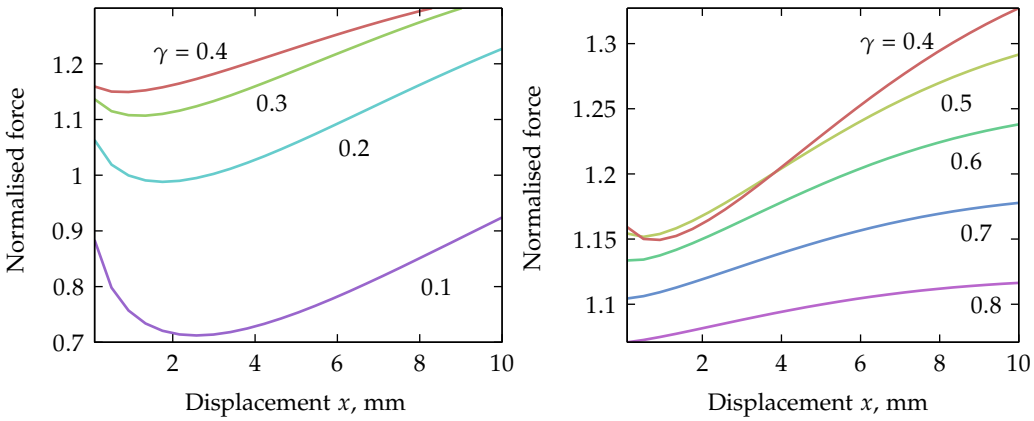

(a) Magnet ratios $\gamma = \{0.1, 0.2, 0.3, 0.4\}$ (b) Magnet ratios $\gamma = \{0.4, 0.5, 0.6, 0.7, 0.8\}$

FIGURE 3.2: Normalised force F/F_s for square-faced cuboid magnets as a function of displacement x.

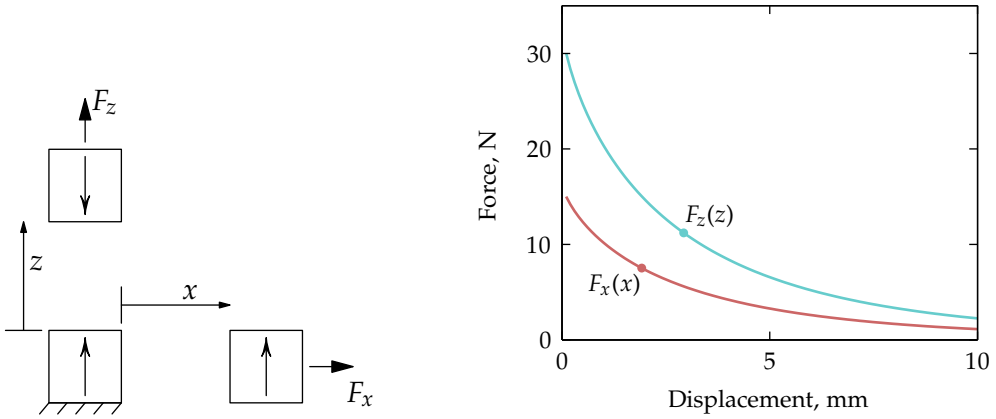

(a) Schematic of the two magnet orientations.

(b) Forces in two directions versus displacement.

FIGURE 3.3: Force/displacement curves between two cube magnets in two orientations with side lengths of 10 mm and a magnetisation of 1 T.

§3.2.2 *Cube magnets in two orientations*

As stated in the introduction in Section 1.3.2, by taking a two dimensional solution for analysing the forces between ring magnets (that is, assuming the curvature of the magnets has negligible effect), Yonnet [301] showed that axially- and radially-magnetised ring magnets produce the same reaction forces. This is an important result for ring magnets, as it is more difficult to magnetise a ring in the radial direction than in the axial direction. There might be considered to be an analogous result for cube magnets. To investigate this, the force versus displacement characteristic between two cube magnets was calculated for displacement perpendicular and orthogonal to the magnetisation directions, as shown in Figure 3.3(a). The results shown in Figure 3.3(b) show that these forces are not equal; in fact, for cube magnets it can be seen that the forces for displacement orthogonal to the magnetisation are exactly half those for magnets which are parallel. Similar results were shown in the discussion of cuboid magnet forces due to rotations (§2.6.5).

§3.2.3 *Cylindrical magnets*

A similar analysis can be performed with cylindrical magnets using a cylindrical magnet ratio defined as the ratio between magnet length and radius $\alpha = L_m/R_m$. Accordingly, the magnet length and radius are calculated using,

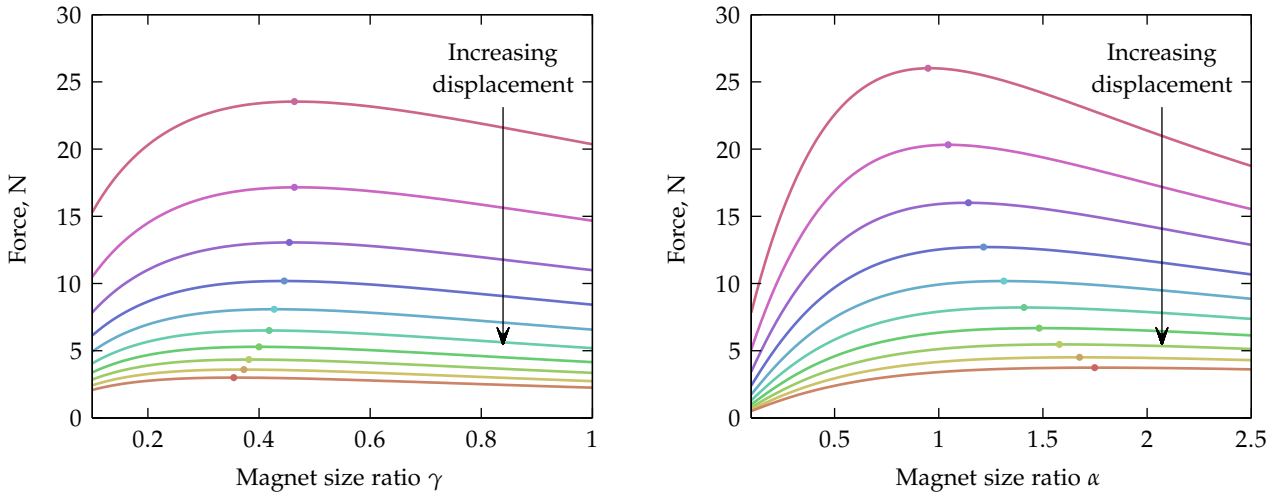

(a) Square-faced cuboid magnets.

(b) Cylindrical magnets. Note the greater force peaks compared to the cuboid magnets.

FIGURE 3.4: Force between two $V_m = \left[10\,\text{mm}\right]^3$ magnets as a function of magnet ratio for a set of fixed displacements from 1 mm to 10 mm. Dots mark the positions of maximum force.

respectively,

$$L_m = \left[\frac{V_m}{\pi\alpha^2}\right]^{1/3}, \qquad R_m = \left[\frac{\alpha V_m}{\pi}\right]^{1/3}, \tag{3.2}$$

with a fixed magnet volume V_m over a range of magnet ratios α. The force is calculated using Eq. 2.69 for a magnet volume of $V_m = \left[10\,\text{mm}\right]^3$ with force versus magnet ratio over a range of displacements shown in Figure 3.4(b). Interestingly, the behaviour for cylindrical magnets shows a different trend than for cuboid shaped magnets; additionally, these results suggest that the force per unit volume is slightly larger for cylindrical magnets due to the closer proximity of the elemental volumes.

§3.2.4 *Comparing cuboid and cylindrical magnets*

In the previous section it was shown that cylindrical magnets appear to achieve a slightly larger force per unit volume in their optimum magnet ratio. The two different magnet shapes cannot be directly compared for a particular value of their magnet ratios, however, so a comparison between the two volumes is difficult. By reformulating the magnet ratio to incorporate face surface area, it is possible to directly analyse the two magnet shapes over a range of alternative aspect ratios to make a definitive comparison.

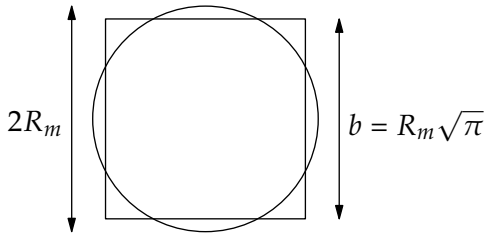

(a) Equal face area for the cuboid and cylindrical magnets.

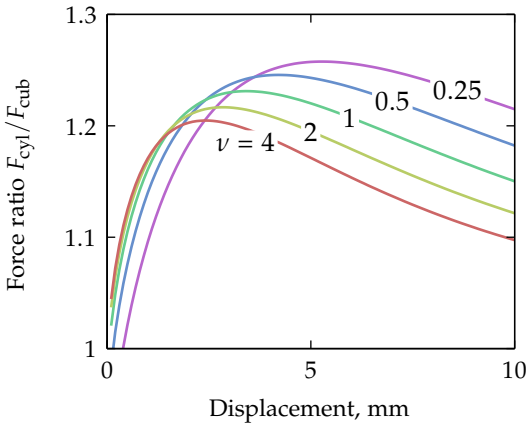

(b) Ratio of cylindrical force to cuboid force versus displacement for a range of magnet ratios ν.

FIGURE 3.5: For magnets with equal volume and face area to length ratios, cylindrical magnets produce greater force.

The alternative magnet ratio ν is defined to be the ratio of magnet length squared to face area. For square-face cuboid magnets and cylindrical magnets the magnet ratio is therefore, respectively,

$$\nu_{cub} = a^2/b^2 = \gamma^2, \qquad \nu_{cyl} = \frac{L_m^2}{\pi R_m^2} = \alpha^2/\pi. \tag{3.3}$$

In other words, for equal ν a cylindrical and cuboid magnet will have the same face area as shown in Figure 3.5(a).[1] Calculating the force versus displacement characteristics across magnet ratio ν between cylindrical and cuboid magnets (F_{cyl} and F_{cub}, respectively) shows that the cylindrical magnets produce greater forces across almost the entire ranges of displacement and magnet ratio (Fig. 3.5(b)).

This particular method for demonstrating the force comparison between cylindrical and cuboid magnets is new work; however, Nagaraj [207] performed a more extensive comparison between cuboid and cylindrical magnets including an analysis of eccentric displacements.

§3.2.5 *Force coupling between degrees of freedom*

A magnetic suspension has inherent dynamic coupling between its degrees of freedom because the magnetic force is a function of displacement in both horizontal and vertical displacements. This is essential to consider for the

1. Relating to a geometrical problem of historical interest known as 'squaring the circle' [125].

purpose of vibration isolation because disturbances from the ground can be transmitted via all six degrees of freedom. Lateral vibrations will cause vertical vibrations; due to symmetry of the forces in the horizontal directions, vertical disturbances will only couple to horizontal forces if the magnets are not vertically aligned.

A numerical simulation was performed to investigate these effects. A vertical, planar, two-magnet system was defined, shown in Figure 3.6(a), in which the lower magnet was horizontally oscillated and the resulting motion of the upper suspended magnet was investigated. The upper magnet was defined to bear a load with a vertical force due to gravity, and stabilised in the horizontal direction with the addition of active positive stiffness.

This simulation was performed on a magnetic system with 10 mm cubes in vertical repulsion, with a floating mass of 0.5 kg and damping ratio of 5 %. The base magnet was excited with a sinusoidal input p at the vertical resonance of the system with a magnitude of 1 mm. The dynamics were defined in the horizontal and vertical directions, respectively, as

$$m\ddot{y} + c\left[\dot{y} - \dot{p}\right] - F_y(0, y - p, z) + g_k\left[y - p\right] = 0\,, \tag{3.4}$$

$$m\ddot{z} + c\dot{z} - F_z(0, y - p, z) + mg = 0\,, \tag{3.5}$$

where $F_y(x, y, z)$ and $F_z(x, y, z)$ are the planar magnetic forces calculated with Eq. 2.16 due to displacement $[x, y, z]^\mathsf{T}$, and g_k is the feedback gain on the relative horizontal displacement term. The (unstable) horizontal stiffness for this system was calculated as around $-200\,\mathrm{N/m}$ and the displacement feedback gain was chosen as $g_k = 250$ to overcome the instability due to this.

A numerical time-domain differential equation solver (Mathematica 7.0's `NDSolve`) was used to simulate the dynamics of this system from initial relative position $(0, 0)$ at which the force due to gravity was balanced by the magnetic force. The displacement trace of the numerical solution is shown in Figure 3.6(b), where the system can be seen to initially follow a non-regular path until reaching a steady state figure-eight limit cycle.

In the equilibrium position, the vertical forces are strongest and the horizontal forces are weakest. The vertical force varies little with horizontal displacement, as shown in Figure 3.7(a), implying that the coupling between horizontal displacement and vertical force will be small. The coupling can be quantified by analysing the ratio between horizontal disturbance displacement range and vertical reaction displacement range. The larger the horizontal displacement range, the larger the coupling ratio as shown in Figure 3.7(b).

While not investigated further in this study, the coupling ratio requires careful attention in the design of a magnetic isolation device with three or

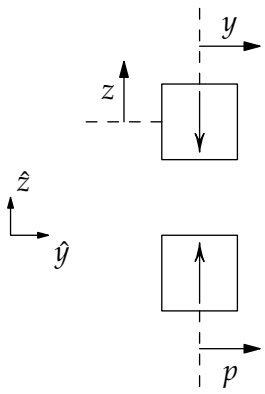

(a) Schematic.

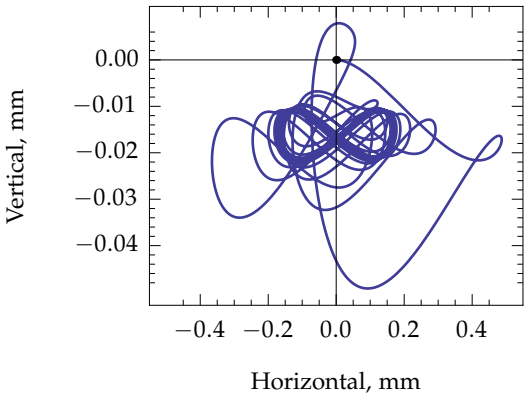

(b) Relative displacement trace.

FIGURE 3.6: Oscillations over time of the displacement of a suspended magnet that is excited through horizontal vibrations of the base magnet. Starting from $(0, 0)$, the resulting figure-eight trajectory shows that the horizontal vibration couples to the vertical forces.

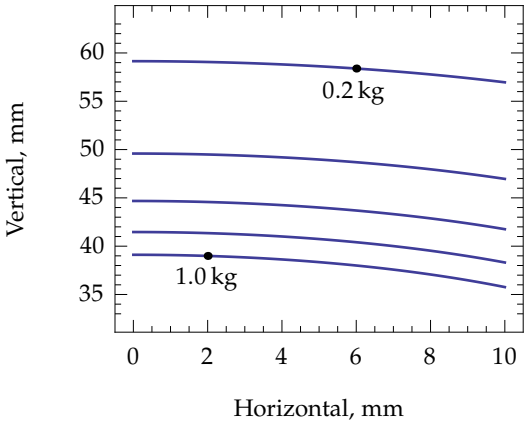

(a) Equilibrium positions of a suspended magnet bearing a range of masses varying with horizontal displacement.

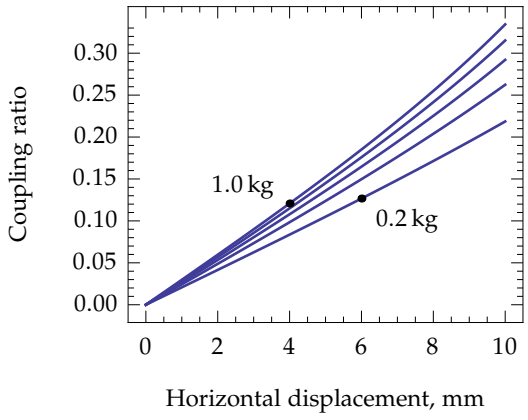

(b) Ratio of vertical to horizontal displacement ('coupling ratio') of a suspended magnet bearing a range of masses varying with horizontal displacement.

FIGURE 3.7: Magnetic coupling between horizontal offset and vertical forces.

more degrees of freedom. Depending on the ratios of vertical to horizontal resonance frequency (and this will be dependent on the control used, as well), improving the horizontal isolation performance may come as a detriment to the vertical isolation. As shown in Figure 3.7(b), however, for small displacement regimes any coupling problems may be negligible compared to the other sources of disturbance. Regardless, this is a factor that should be considered for all practical levitation devices. The coupling between vertical and horizontal directions can be amplified in magnetic systems composed of multipole or Halbach arrangements, which is discussed further in Section 4.4.3 on page 149.

§3.3 Simple magnetic springs using cuboid magnets

The aim of this section is to introduce a variety of simple magnetic springs, demonstrating possibilities in force behaviour that can be achieved. It is implicit in Earnshaw's theorem [91, 279] that all permanent magnet suspensions must be unstable, so one of the main factors involved in analysing the efficacy of a magnetic spring is its type and degree of stability.

Via Earnshaw, for purely magnetic systems the translational stiffesses in each direction sum to zero

$$K_x + K_y + K_z = 0\,, \tag{3.6}$$

although, as discussed in Section 3.3.9, no such relation exists between the rotational stiffnesses. Introducing soft iron, which only attracts permanent magnets, into the system changes Eq. 3.6 to $K_x + K_y + K_z < 0$, reducing the stability of the system [211, App. A]. For this reason, it is rare to see ferrous material featured as part of the design of magnetic springs. This is in contrast with magnetic circuit design (which includes magnetic fasteners in application) which often uses ferrous material to guide and constrain magnetic flux.

Magnetic spring systems can be created with different arrangements of magnets and combinations thereof, influencing the stiffness characteristics in various ways. In the following sections (§3.3.1–§3.3.6), six different magnetic spring configurations are introduced based around cuboid magnets. These are compared with each other in Section 3.3.7 with Figures 3.15 to 3.20 showing for each design their contours of force versus displacement in each direction. These plots allow a qualitative assessment of the complexity of the force fields of each spring design.

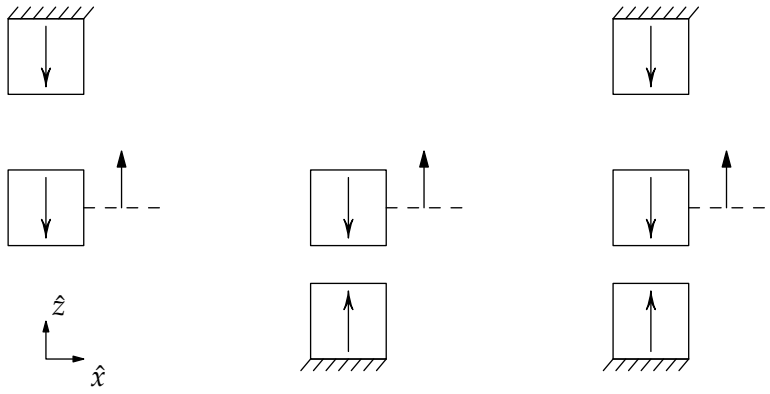

FIGURE 3.8: Three magnetic springs for load bearing in the vertical $\hat{z}$ direction with magnetic force indicated with the solid arrowhead.

§3.3.1 *Unstable vertical spring*

The first three spring designs, Figure 3.8, are variations on using vertically-aligned magnets for load bearing. The 'unstable' arrangement consists of a fixed upper magnet which applies a gravity-cancelling force on a lower magnet in attraction. This configuration is discussed in the literature review in the context of active control methods (§1.3.3), and is the most common magnetic suspension for demonstrating nonlinear control design.

The stability criteria for this system are

$$K_z < 0, \quad K_x = K_y = -\tfrac{1}{2}K_z > 0\,, \tag{3.7}$$

and although this arrangement is unstable in only a single degree of freedom, it is inconvenient to bear loads with a negative stiffness spring.

§3.3.2 *Stable vertical spring*

The 'stable' vertical spring is the opposite of the unstable vertical spring; it consists of a fixed lower magnet supporting a floating upper magnet in repulsion. Its stability criteria are

$$K_z > 0, \quad K_x = K_y = -\tfrac{1}{2}K_z < 0\,. \tag{3.8}$$

The vertical force optimisation for this arrangement has already been analysed in detail in Section 3.2. Since this configuration experiences instability in both horizontal directions, its stabilisation requires active control or constraint in multiple degrees of freedom.

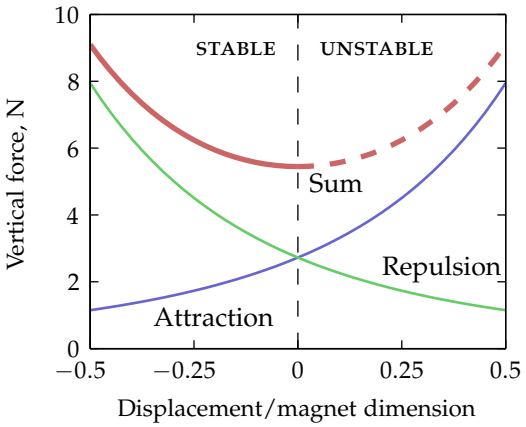

FIGURE 3.9: Quasi–zero stiffness vertical spring forces versus vertical displacement from the centred position. The magnets are 20 mm cubes with 1 T magnetisation, and there is 80 mm between the top and bottom magnet centres. Dashed region for the summation of forces corresponds to negative (unstable) stiffness.

§3.3.3 *Quasi–zero stiffness spring*

First introduced by Nijsse [211], the quasi–zero stiffness magnetic spring uses equal and opposite magnet pairs to create a force–displacement relationship that has a region of zero slope, shown in Figure 3.9 for 1 T 20 mm magnet cubes. With a positive vertical stiffness in series with a negative stiffness, the local minimum in the force/displacement curve creates a marginally stable point of quasi–zero stiffness in all three translational degrees of freedom. If the magnet positions are chosen such that the operating point is midway between the fixed magnets, the stability criteria for this spring are

$$K_x = K_y = K_z = 0\,. \tag{3.9}$$

While the quasi–zero stiffness magnetic spring cannot be passively operated at this centred position of zero stiffness (as it has only marginal stability there), the upper attractive magnet can be considered to simply *reduce* the natural frequency of the system without necessarily having to drive it all the way to zero. In this case, the operating position of the floating magnet is situated closer to the lower magnet, which is as depicted in Figure 3.8. This improves vibration isolation characteristics without altering the stability of the system (given bounded displacements), and this system is analysed in detail in Section 6.3. This configuration has also been used for a tunable vibration energy harvesting device [60], since the resonance frequency can be adjusted by varying the positions of the outer magnets.

§3.3.4 *Horizontal spring*

Unlike the vertical magnetic springs discussed previously, a horizontal arrangement of magnets in attraction, Figure 3.10, provides stability in the vertical direction with only a single degree of horizontal instability. The stability criteria here are

$$K_x < 0, \quad K_y > 0, \quad K_z > 0\,. \tag{3.10}$$

Note this configuration of magnets adds stability in the out-of-plane ($\hat{y}$) direction.

The force–displacement behaviour for the horizontal spring, Figure 3.11, is more complex than for the vertical springs as the vertical forces are dependent on the horizontal placement of the magnets. Figure 3.11 includes the force curve of the vertical spring for comparison; magnets for the simulation were 20 mm cubes with 1 T magnetisation. The vertical spring force occurs as the magnet displaces vertically downwards, which spring force will increase with distance only for a certain range. Beyond this range, the force will begin to decrease as the floating magnet displaces further from the fixed magnets — until the spring stiffness turns negative and the system becomes unstable.

The effect of varying the gap between the fixed and floating magnets for the horizontal spring also varies this behaviour; the further away the fixed magnets are, the weaker the forces are but the larger the displacement range before instability. The inflection point where the horizontal spring force reaches its peak is a quasi–zero stiffness point; careful tuning of such a spring could yield similar advantages to the vertical quasi–zero stiffness spring introduced in Section 3.3.3.

§3.3.5 *Combination spring*

There is a degree of compromise with the horizontal spring in relation to its load bearing ability. It is possible to offset this by augmenting the horizontal spring with an additional vertical magnet in repulsion to increase its load bearing capacity (Fig. 3.12). There are now three fixed magnets: one below, which provides the majority of the stiffness of the spring, and two aside, for stabilising one degree of freedom in the out-of-plane direction, creating stability criteria of

$$K_z > 0, \quad K_x > 0, \quad K_y < 0\,. \tag{3.11}$$

An alternative double-stable spring is discussed in Section 3.3.8.

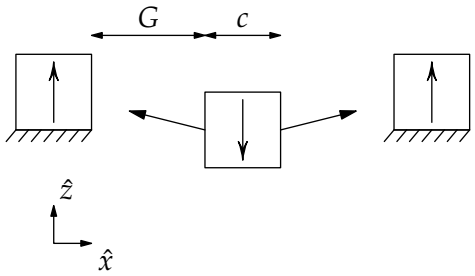

FIGURE 3.10: A horizontal spring with attracting magnets to create positive vertical stiffness.

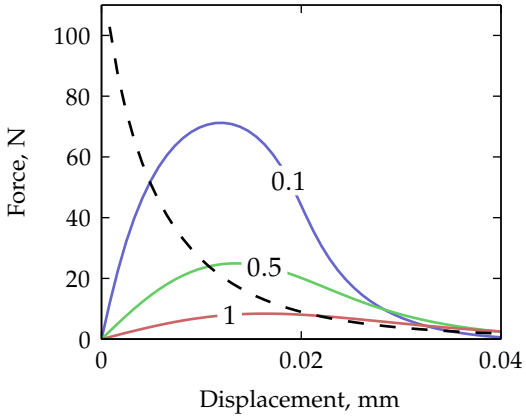

FIGURE 3.11: Vertical forces of the stable vertical (dashed) and horizontal (solid) springs with cube magnets with side length $c = 20\,\text{mm}$. The horizontal spring has a magnet face gap of $G/c \in \{0.1, 0.5, 1\}$.

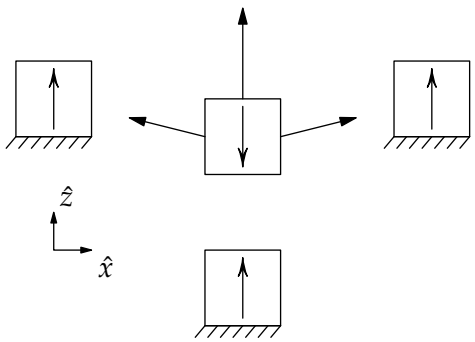

FIGURE 3.12: Combination magnetic spring, with the strength of the vertical spring and the stability of the horizontal spring. Solid arrows indicate magnetic forces.

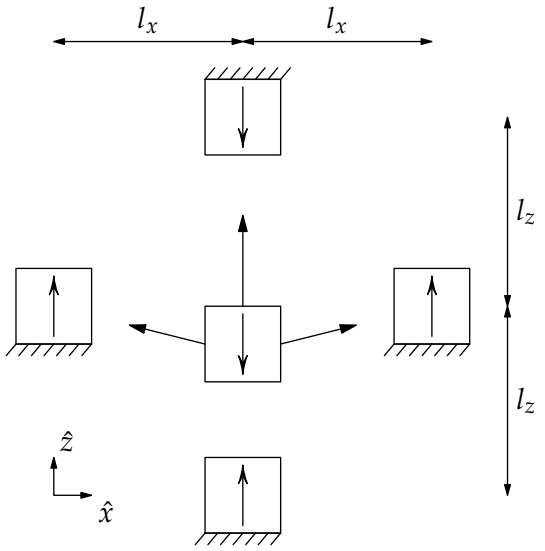

FIGURE 3.13: The combination quasi–zero stiffness magnetic spring with horizontal magnets for stabilisation.

§3.3.6 *Combination quasi–zero stiffness spring*

Lastly, one additional attractive magnet can be added to this system to produce a quasi–zero stiffness effect (Fig. 3.13). This system can approach zero stiffness in the vertical direction with a small positive stiffness in one horizontal direction and an equal negative stiffness in the other:

$$K_z = 0, \quad K_y = -K_x > 0\,. \tag{3.12}$$

A demonstration of the force–displacement curves for this spring is shown in Figure 3.14, for a system with 20 mm cube magnets with 1 T magnetisation and a nominal gap of 30 mm between the centres of the floating magnet and the horizontal magnets and 40 mm nominal gap for the vertical magnet centres. The addition of the horizontal magnets produces an asymmetry in the total vertical force characteristic of the system, yet it still retains a quasi–zero stiffness inflection point.

§3.3.7 *Isoforces and isostiffnesses for magnetic springs*

As the magnetic springs become composed of more elements, analysing their force–displacement characteristics becomes quite challenging. As the three dimensional forces vary with displacement in three degrees of freedom, it is not possible to directly visualise the behaviour of these systems under arbitrary displacement. An attempt to do so here highlights the difficulties

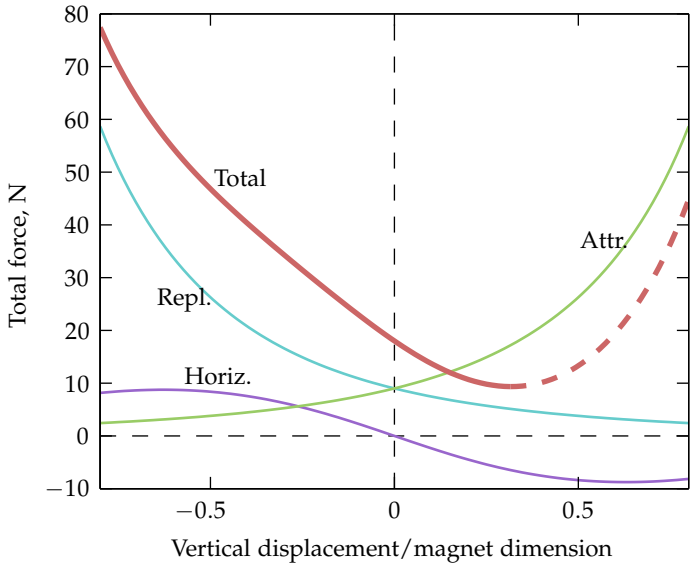

FIGURE 3.14: Individual and total vertical forces on the combination quasi–zero stiffness spring for displacement in the $\hat{z}$ direction. Dashed line for the total forces shows the region of instability.

involved. In this case, representative force component contours are plotted against displacement in each direction separately; these contours are termed 'isoforces' as they trace contours of equal force (Figures 3.15 to 3.20) and 'isostiffnesses' with contours of stiffness (Figures 3.21 to 3.26).

The simple magnetic systems of a pair of magnets in either attraction (§3.3.1) or repulsion (§3.3.2) will be treated first as their qualitative analysis is straightforward; consider their isoforces shown in Figures 3.15 and 3.16, respectively. Each figure shows three plots which correspond to each component of force: F_x, F_y, F_z. The plots are three dimensional, and partially transparent contours represent the magnitude of the respective force component under three dimensional displacement. The colour scale goes through the spectrum from orange to purple as the normalised forces/stiffnesses range from negative to positive.

The vertical components are easiest to comprehend. Figure 3.15(c) shows that as the floating magnet is displaced upwards, the magnitude of the vertical force increases (becoming more blue). Contrariwise, Figure 3.16(c) shows an increase in vertical force with negative displacement for the spring with magnets in repulsion. Despite the magnitude of the forces being vertically upwards, the stiffnesses in Figures 3.21(c) and 3.22(c) shows the negative (orange) stability in the former case and positive (blue) stability in the latter.

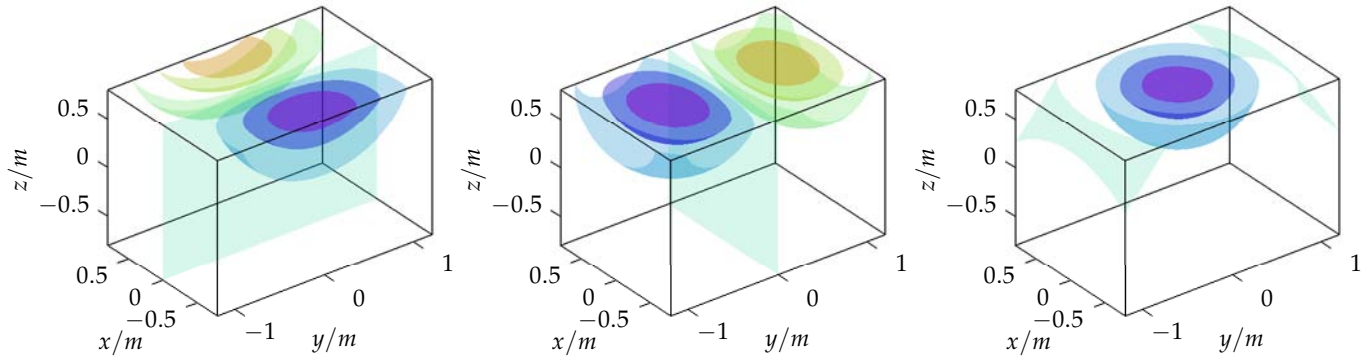

(a) $\hat{x}$ forces. (b) $\hat{y}$ forces. (c) $\hat{z}$ forces.

FIGURE 3.15: Isoforces of the unstable vertical spring (§3.3.1).

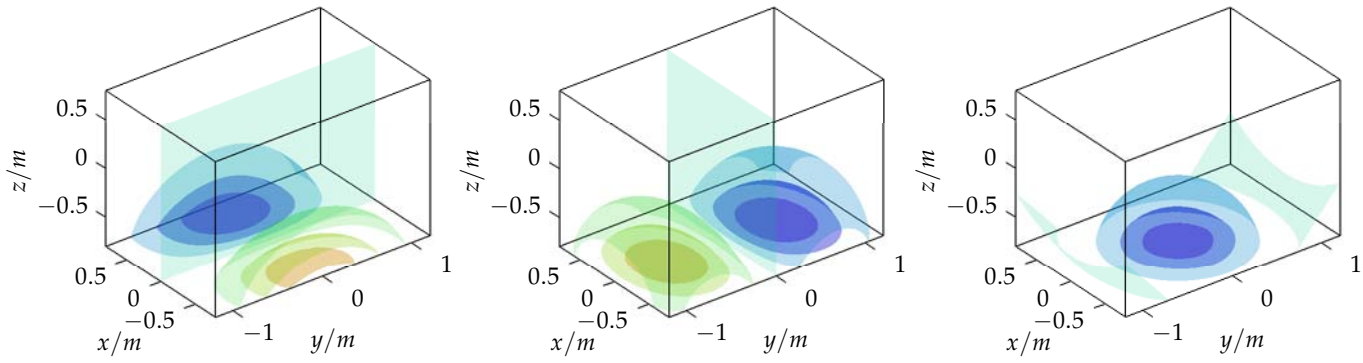

(a) $\hat{x}$ forces. (b) $\hat{y}$ forces. (c) $\hat{z}$ forces.

FIGURE 3.16: Isoforces of the stable vertical spring (§3.3.2).

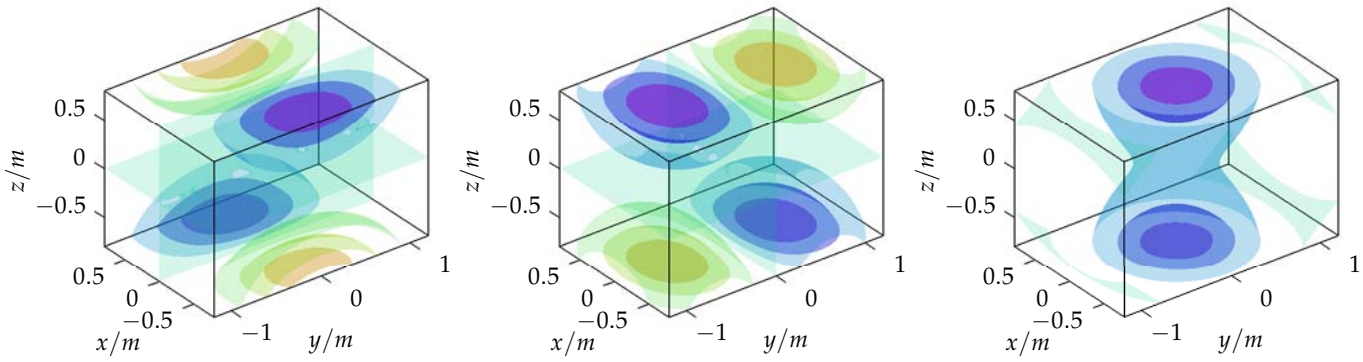

(a) $\hat{x}$ forces. (b) $\hat{y}$ forces. (c) $\hat{z}$ forces.

FIGURE 3.17: Isoforces of the quasi–zero stiffness spring (§3.3.3).

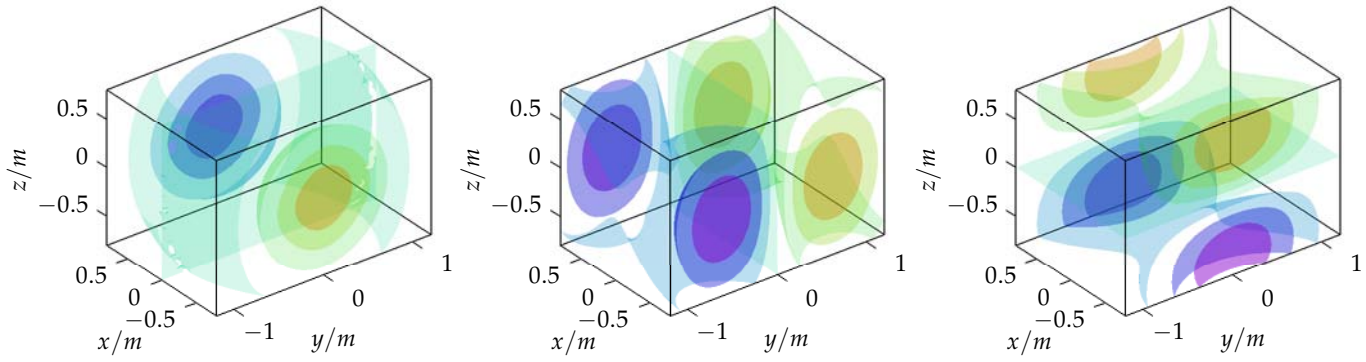

(a) $\hat{x}$ forces. (b) $\hat{y}$ forces. (c) $\hat{z}$ forces.

FIGURE 3.18: Isoforces of the horizontal spring (§3.3.4).

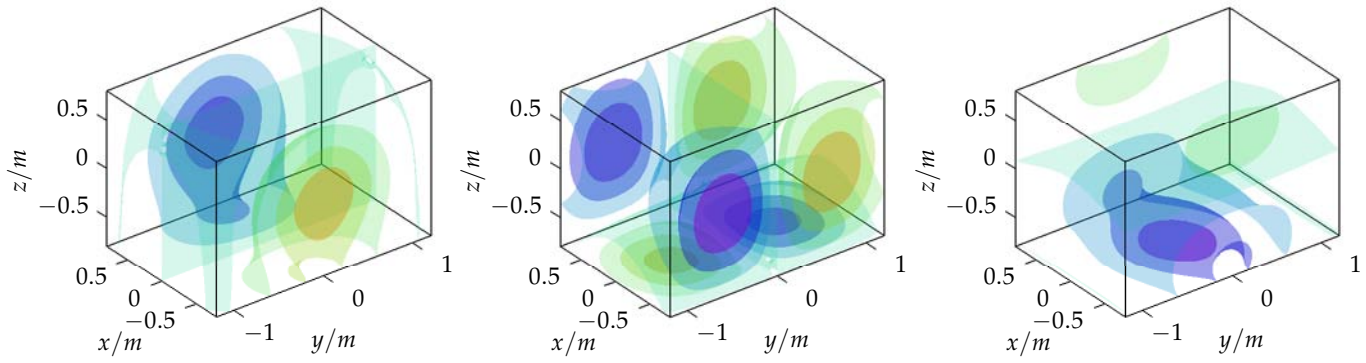

(a) $\hat{x}$ forces. (b) $\hat{y}$ forces. (c) $\hat{z}$ forces.

FIGURE 3.19: Isoforces of the combination spring (§3.3.5).

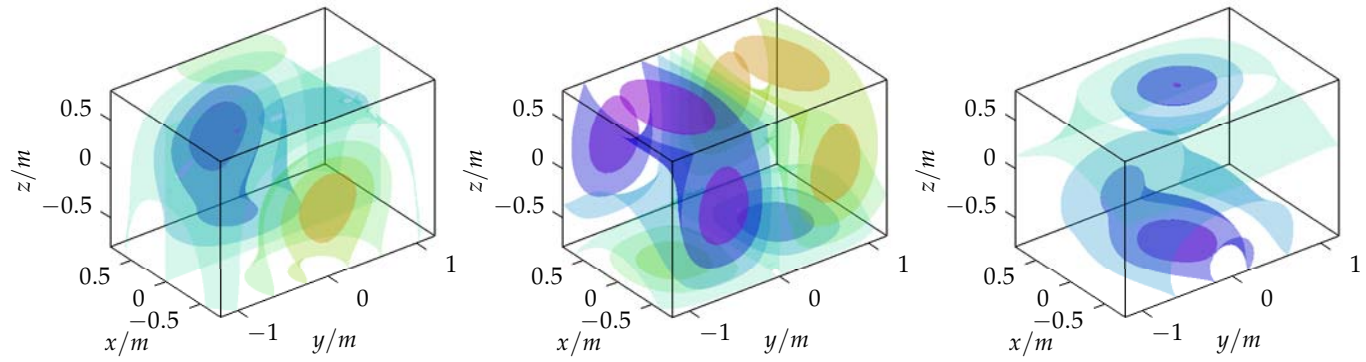

(a) $\hat{x}$ forces. (b) $\hat{y}$ forces. (c) $\hat{z}$ forces.

FIGURE 3.20: Isoforces of the combination quasi–zero stiffness spring (§3.3.6).

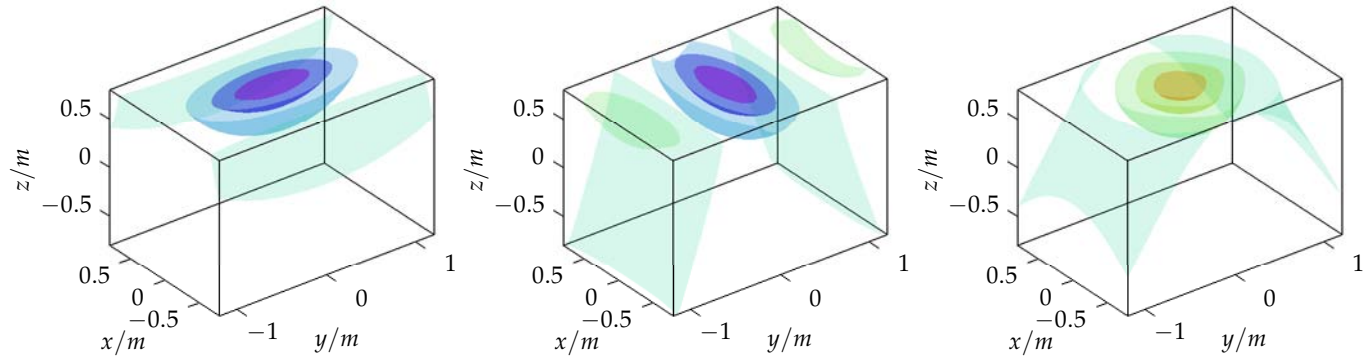

(a) $\hat{x}$ stiffnesses. (b) $\hat{y}$ stiffnesses. (c) $\hat{z}$ stiffnesses.

FIGURE 3.21: Isostiffnesses of the unstable vertical spring (§3.3.1).

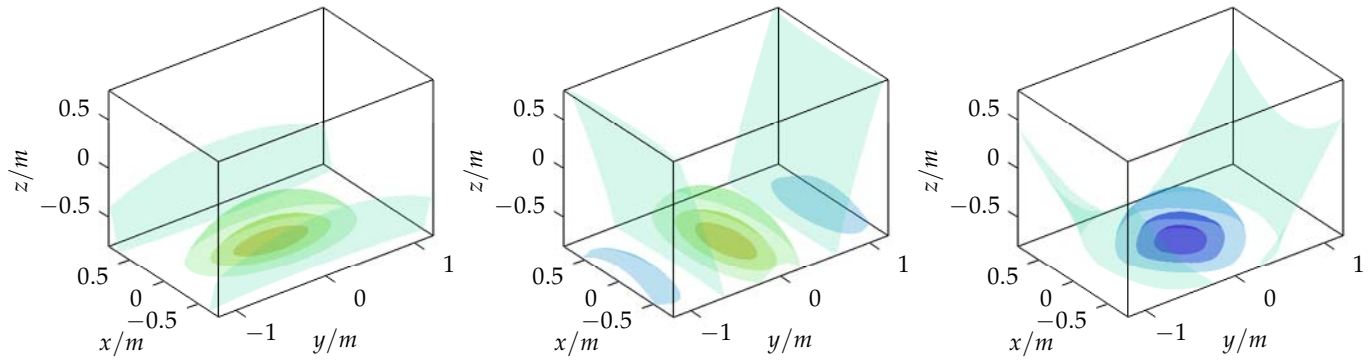

(a) $\hat{x}$ stiffnesses. (b) $\hat{y}$ stiffnesses. (c) $\hat{z}$ stiffnesses.

FIGURE 3.22: Isostiffnesses of the stable vertical spring (§3.3.2).

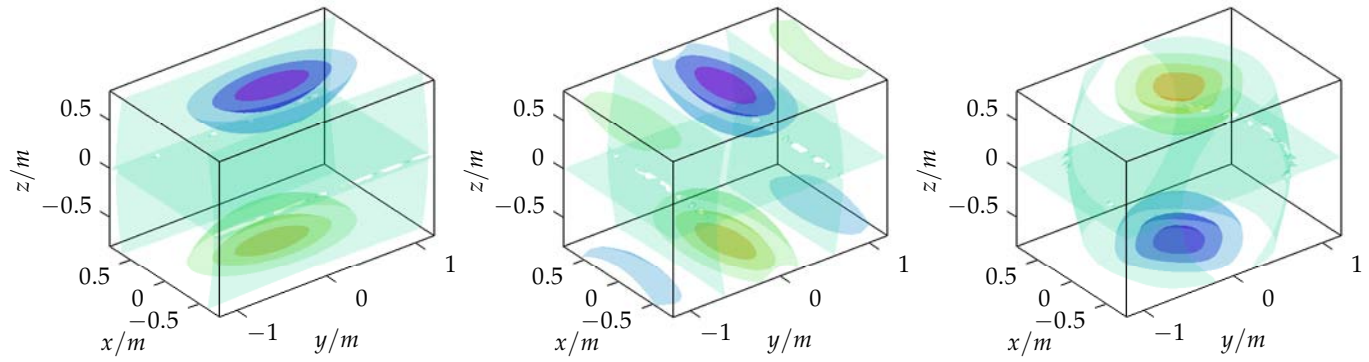

(a) $\hat{x}$ stiffnesses. (b) $\hat{y}$ stiffnesses. (c) $\hat{z}$ stiffnesses.

FIGURE 3.23: Isostiffnesses of the quasi–zero stiffness spring (§3.3.3).

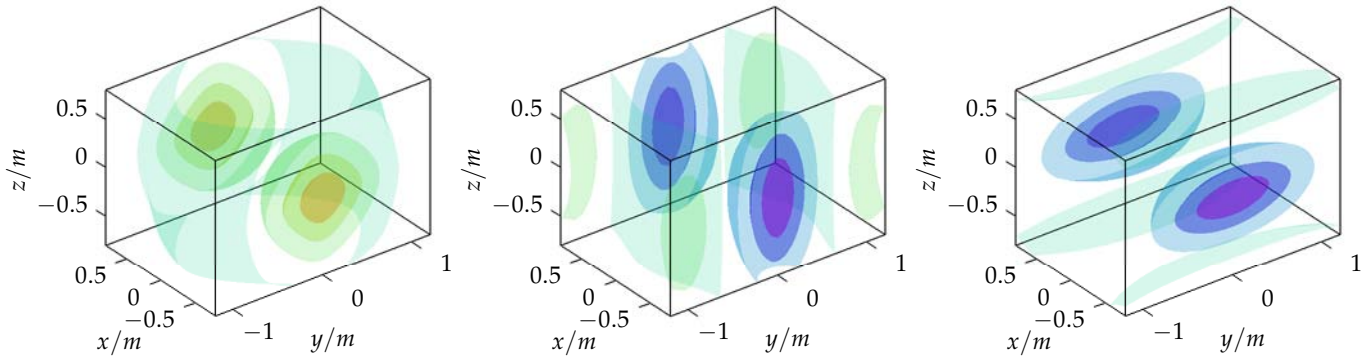

(a) $\hat{x}$ stiffnesses. (b) $\hat{y}$ stiffnesses. (c) $\hat{z}$ stiffnesses.

FIGURE 3.24: Isostiffnesses of the horizontal spring (§3.3.4).

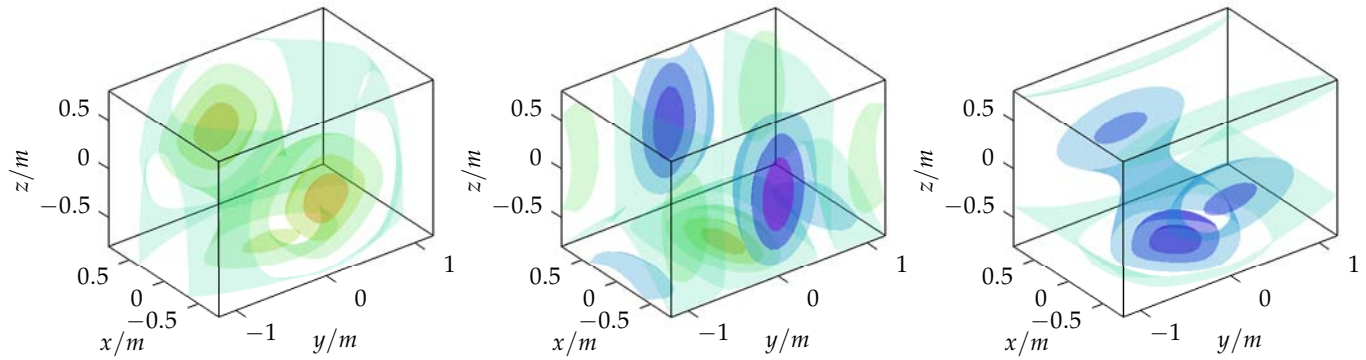

(a) $\hat{x}$ stiffnesses. (b) $\hat{y}$ stiffnesses. (c) $\hat{z}$ stiffnesses.

FIGURE 3.25: Isostiffnesses of the combination spring (§3.3.5).

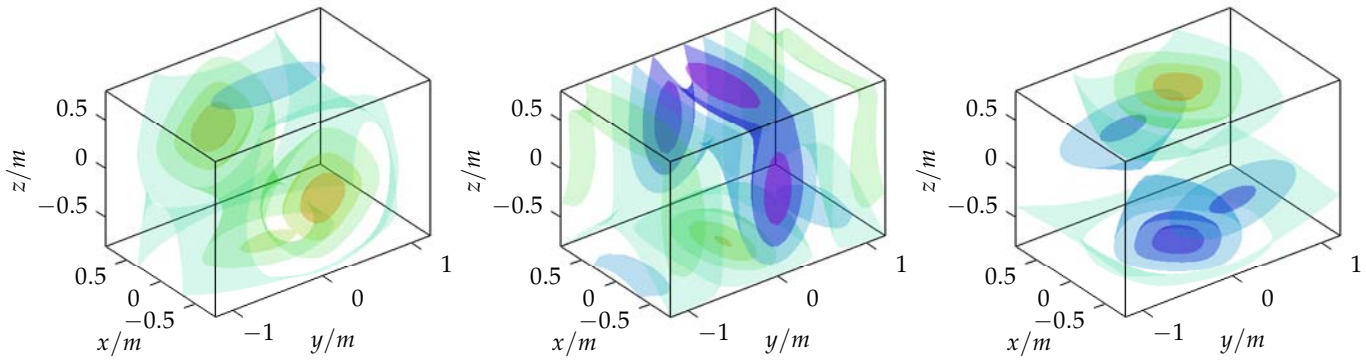

(a) $\hat{x}$ stiffnesses. (b) $\hat{y}$ stiffnesses. (c) $\hat{z}$ stiffnesses.

FIGURE 3.26: Isostiffnesses of the combination quasi–zero stiffness spring (§3.3.6).

For symmetrical cases like the forces in the $\hat{x}$ and $\hat{y}$ directions, pale green-blue is the colour of zero force. Thus, for the vertical attracting spring Figures 3.15(a) and 3.15(b) demonstrate horizontal stability, while for the vertical repelling spring Figures 3.16(a) and 3.16(b) demonstrate horizontal instability. The stiffnesses, positive for Figures 3.21(a) and 3.21(b) and negative for Figures 3.22(a) and 3.22(b) emphasise this behaviour.

The vertical quasi–zero stiffness spring (§3.3.3) retains this simplicity of representation in Figure 3.17, noting particularly the 'switching-stability' horizontal behaviour with vertical displacement. Above the centred position, the spring dynamically behaves as the vertically attracting spring, and below it behaves as the repulsive spring.

The isoforces of the horizontal spring (Fig. 3.18, §3.3.4) show similar shapes to the vertical quasi–zero stiffness spring (Fig. 3.17), albeit rotated ninety degrees. Note, however, that due to the differences in magnetisation direction between the magnets, a different stability pattern is seen; increases in $\hat{y}$ and $\hat{z}$ displacement respectively both result in restoring forces (note the stiffnesses, Fig. 3.24, which are positive in two axes).

The final isoforce graphs are the two 'combination' springs, Figures 3.19 and 3.20, involving superposition of isoforces seen previously. As more magnets are used, the more complex the isoforce patterns become. For the first combination spring (§3.3.5), in which the stable vertical spring is combined with the horizontal spring, the isoforces are very similar to the horizontal spring (Fig. 3.18) with the exception in the vertical forces where the increased load bearing ability can be seen in the centred blue region.

The second combination spring involves the superposition of the quasi–zero stiffness and horizontal spring, with the intention of stabilising one degree of freedom. As this stability regime is the same as for the previous combination spring, the isoforces are similar in the horizontal directions. In the vertical $\hat{z}$ direction, the quasi–zero stiffness behaviour with positive displacements is more clearly seen; the secondary vertical forces added by the horizontal spring can be seen to add a 'bulge' for negative displacements.

In conclusion, combining simple magnets with a variety of geometries can lead to a wide selection of magnet spring types. Only a preliminary analysis of these has been conducted here; in Section 3.4 a different spring type using inclined magnets is covered in detail, and later in Section 6.3 the design characteristics of the zero stiffness spring are examined in more detail.

§3.3.8 *Stability in two degrees of freedom*

In the previous section a number of magnetic designs have been proposed; here the arrangement of Choi et al. [75] is examined. It is an interesting design as it has a single unstable degree of freedom both translationally and rotationally. This design consists of two fixed vertical magnets with some horizontal offset between them, with a floating magnet that levitates halfway between and above the fixed magnets (Fig. 3.27(a)). The work by Choi et al. [75] was focussed on active control of this system in one degree of freedom to achieve stability; with the theory developed for modelling the forces between magnets in Chapter 2, this design can be analysed in more detail. The stability and force characteristics of this design are strongly related to the geometry of the system; the sizes and aspect ratios of each magnet can be varied, along with the distance separating the fixed base magnets. Verification of the translational stability of the system is shown in Figure 3.27(b), which shows the stiffness in each direction as a function of vertical displacement for an example system using 20 mm 1 T cube magnets and $G = 20$ mm separation between the fixed magnets. It can be seen that for a certain range of vertical displacement, both the $\hat{x}$ and $\hat{z}$ stiffnesses are positive, indicating a single degree of instability. When four such devices (or any other symmetric pair configuration) are arranged in a plane, the rotational degrees of freedom can all be stabilised [75].

The design of such a device has not been analysed until now; while Choi et al. [75] demonstrated the concept, their work did not investigate the

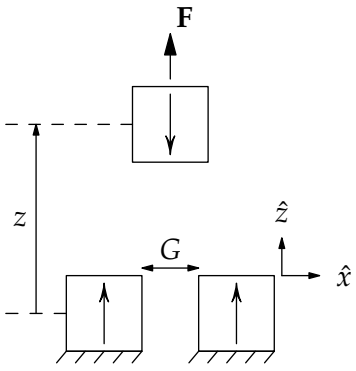

(a) Schematic of the magnetic spring.

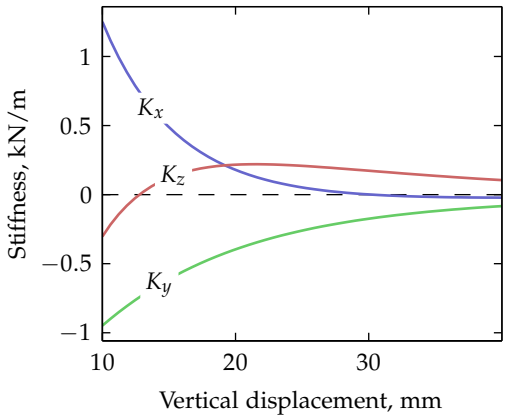

(b) Stiffnesses in each direction as a function of vertical displacement for a fixed magnet gap $G = 20$ mm.

FIGURE 3.27: The singularly-unstable magnetic spring proposed by Choi et al. [75]. 20 mm, 1 T cube magnets are used to demonstrate the concept.

influence of varying the design parameters. An example of the variability of characteristics seen is shown here for the simple case of using cube magnets with side length 20 mm and magnetisation strength 1 T. The variable parameter in this case is the gap G between the fixed magnets; Figure 3.28 shows the effect on the vertical and horizontal stiffnesses due to varying the magnet gap as a function of vertical displacement z; the out-of-plane stiffness is not shown as it is always negative. It can be seen from the figure that the magnet gap has a large effect on the stiffness characteristics of the system, and across vertical displacement there are regions of both positive and negative stiffness in each direction.

The intention of the spring is to load the system such that positive stiffness is achieved in both directions; this displacement region can be found by taking only the positive regions of the curves shown in Figure 3.28. Finding these regions and plotting the vertical force versus displacement curves against magnet gap (Fig. 3.29) demonstrates the useable ranges of the device. By adjusting the magnet gap in the design phase, the system can be tuned to achieve either large force and large stiffness or low force and low stiffness; the lower the load bearing capacity of the system, the larger the permissible displacement range becomes.

This idea of tuning the magnet characteristics to achieve certain stiffness properties is explored in more detail in Section 3.4 using inclined magnets.

§3.3.9 *Rotational degrees of freedom*

It becomes more difficult to examine the behaviour of these systems in six degrees of freedom. Equilibria of a system that have rotational instabilities can be stabilised by coupling together identical systems. An example is the vertically stable spring, which is unstable around both horizontal directions. By rigidly connecting a multiple of these springs, the system can be stabilised around these directions due to the addition of lever arm moments. This is depicted for a planar case in Figure 3.30.

Delamare et al. [86] demonstrated this concept for a radial magnetic bearing by adding a weaker, axial bearing to the system with a larger radius. The coupling of the axial and radial bearings eliminated the rotational instability, while the strength of the radial bearing was such that the effects of the axial bearing were minimised for normal operation. This design is simpler for a bearing system due to the rotational symmetry of the ring magnets and the assumption that the bearing will enable free rotation around one axis. In this section, a cuboid magnet design with similar principles is shown to demonstrate that it is possible to eliminate rotational instability for a

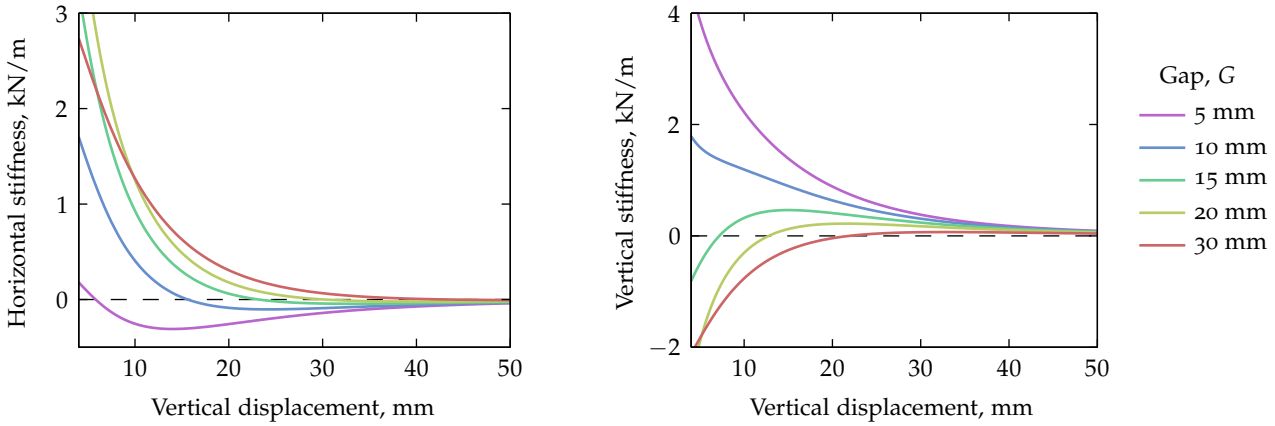

(a) $\hat{x}$ direction. (b) $\hat{z}$ direction.

FIGURE 3.28: Stiffnesses as a function of vertical displacement across a range of fixed magnet gaps. Both can be seen to have positive and negative regions. Out-of-plane stiffness is always negative.

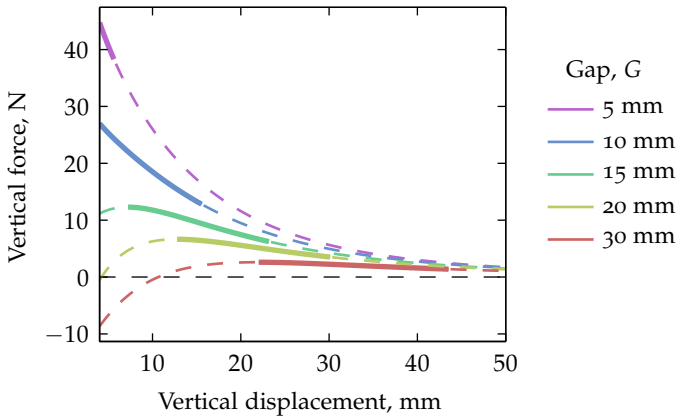

FIGURE 3.29: Force versus vertical displacement across a range of magnet gaps. Regions of positive stability are indicated with thick solid lines; dashed lines indicate regions of negative stiffness in the vertical and/or horizontal directions.

magnetic spring application (also see Section 3.3.8).

As with the bearing system of Delamare et al. [86], the method of eliminating one of these rotational instabilities involves adding supplementary weak magnets that apply small translational forces to the structure with large lever arms, such that the added translation stiffness is negligible but the added rotational stiffness is significant and stabilising.

A rotationally-stable magnet spring based on the 'horizontal spring' (§3.3.4) is presented in Figure 3.31(a), which shows a top-down view. The translational stability of the system can be assessed using the theory between parallel cuboid magnets (Eq. 2.16). In order to model the rotational stability, the torque on the spring due to rotations around each axis must be calculated. Forces in three directions can only be calculated for parallel magnets, and while there are expressions in the literature to calculate the torques between cuboid magnets [142], these expressions also only apply for parallel magnets (that is, magnets that have no relative rotation between them). Furthermore, the moments produced by the magnets at their lever arms around the centre of the platform are likely to dominate over the torque induced between each pair of magnets, since the rotations will be small but the lever arms will be (relatively) large. Finally, if small rotations of the spring are assumed, then the effect of this rotation on the forces and torques between the magnets can be neglected; the assumption is that for the purposes of force calculation, the magnets will remain parallel to each other.

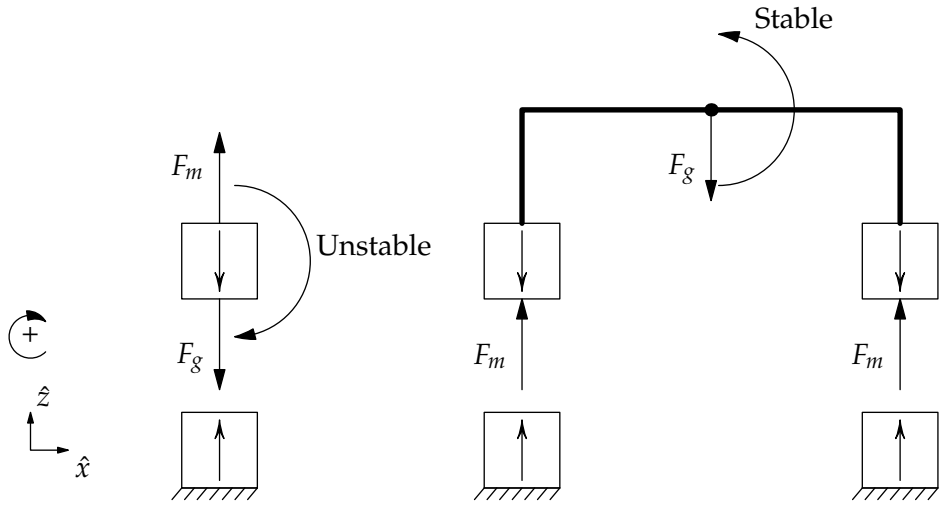

FIGURE 3.30: An example of stabilising rotationally-unstable springs. Forces due to magnets and gravity, F_m and F_g, are depicted. The rotationally unstable case is shown on the left; the right schematic shows the stabilised coupling.

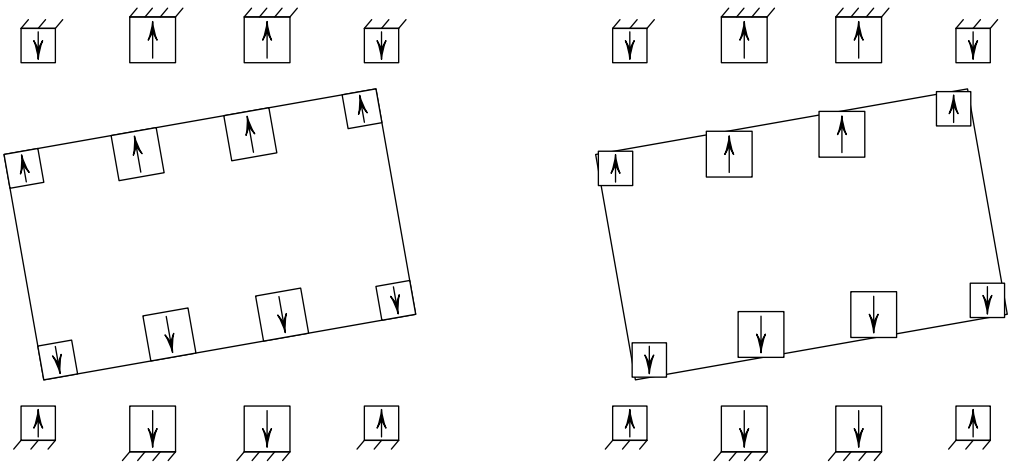

(a) After rotation around $\hat{z}$.

(b) Small-angle approximation for calculating forces and moments.

FIGURE 3.31: Top-view schematic of a single unstable degree of freedom concept.

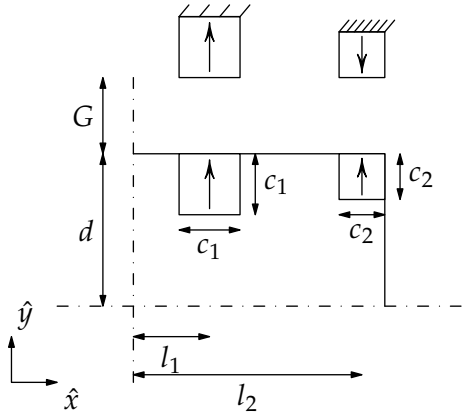

l_1	100 mm
l_2	300 mm
d	100 mm
G	10 mm
c_1	10 mm
c_2	5 mm
z_{eq}	−4 mm

FIGURE 3.32: Top view of geometry used for analysing the magnetic spring with stable rotation. Equilibrium displacement z_{eq} is into the page and not shown. Magnet remanence was normalised at 1 T.

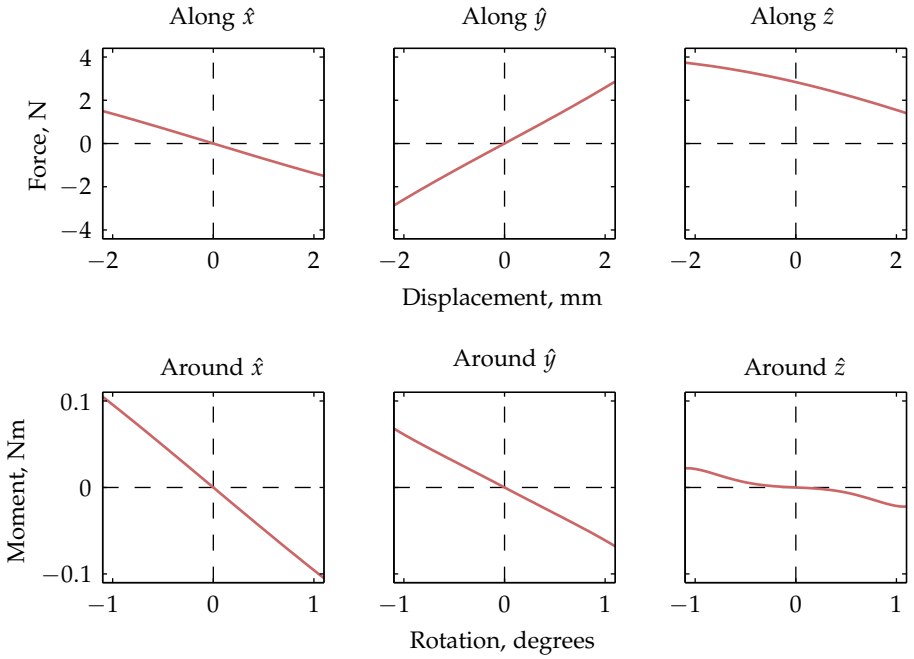

FIGURE 3.33: Demonstration of single degree of freedom instability. The gradients of all forces and torques are negative (infering stability) except for the force along the $\hat{y}$ direction.

The total torque on the system is therefore calculated by neglecting the torques between the magnets and by neglecting the effects of rotation on the forces between the magnets (Fig. 3.31(b)). A static analysis of forces and torques created in this magnetic spring was performed using the geometry shown in Figure 3.32. For this analysis, cube magnets were used for simplicity and the magnet gaps in the centred position are defined to be equal between the strong and the stabilising magnets.

The spring is chosen to have an equilibrium position at z_{eq} from the height of the fixed magnets due to the weight being supported. Spring parameters (shown in Figure 3.32) are chosen to illustrate the concept of having a single degree of instability, with forces and moments shown in Figure 3.33. In this figure, the stabilities for displacement and rotation in each degree of freedom are illustrated with the associated forces and torques due to each perturbation. The spring is in equilibrium at some displacement below the fixed outer magnets such that the force from the magnets balances the load force on the spring; forces in the vertical $\hat{z}$ direction are given in relative difference terms to this equilibrium force. In Figure 3.33 negative gradient indicates stability, as the force or torque acts in opposition to the displacement or rotation that

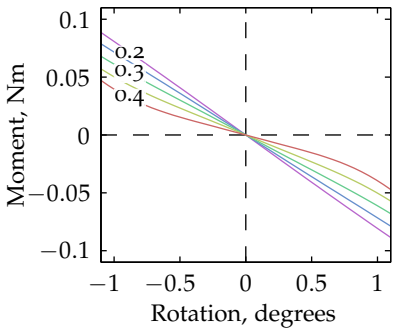

(a) Around the $\hat{y}$ axis. Stability decreases with increased lever arm but does not become unstable in the range shown.

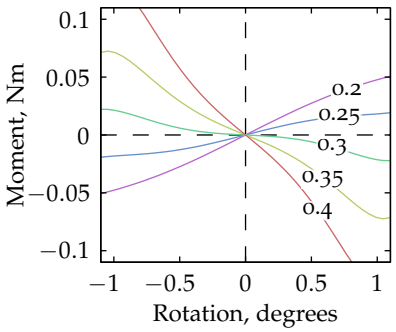

(b) Around the $\hat{z}$ axis. Stability ranges from unstable to stable as the lever arm increases.

FIGURE 3.34: Moment of the magnetic spring as it rotates around the $\hat{y}$ and $\hat{z}$ axes with a varying lever arm for the stabilising magnets. (The moment around the $\hat{x}$ axis does not vary with lever arm and remains stable.) Plots are labelled in terms of the lever arm ratio l_1/l_2.

caused it. The figure shows that only the translatory $\hat{y}$ direction is unstable, and thus in theory only a single actuator would be required to control this system in a non-contact levitating state.

The stability is created by the lever arm of the smaller outer magnets. The influence of this lever arm on the rotational stiffness of the spring is shown in Figure 3.34, where the lever arm varies from twice to four times the centre distance of the strong magnets. In this range, the rotation stiffness begins negative (as it is without any stabilising magnets) and as the lever arm is increased the stability is increased until it becomes positive between 2.5 and 3 times the lever arm of the centre magnets. (The moment around the $\hat{y}$ axis does not vary with spring depth and remains stable.)

There is a trade-off between the size of the stabilising magnets and the effectiveness of the main force-providing magnets. The large lever arm of the stabilising magnets will also affect the stability of the spring in the rotational direction around the $\hat{y}$ axis; if the stabilising magnets are too large then an added instability will be created, counteracting the added stability around the $\hat{z}$ axis. This is illustrated in Figure 3.35 with spring parameters as shown in Figure 3.32 but with a stabilising magnet size varying from 0.4 to 0.8 of the side length of the main magnet. The relative sizes of the magnets is critical to achieving passive stability around the $\hat{y}$ and $\hat{z}$ directions.

Finally, the depth of the spring (size in $\hat{y}$) also affects the stability of this design. Again using the illustrative parameters of Figure 3.32, but with spring depth d varying from 100 mm to 400 mm, the forces and moments are

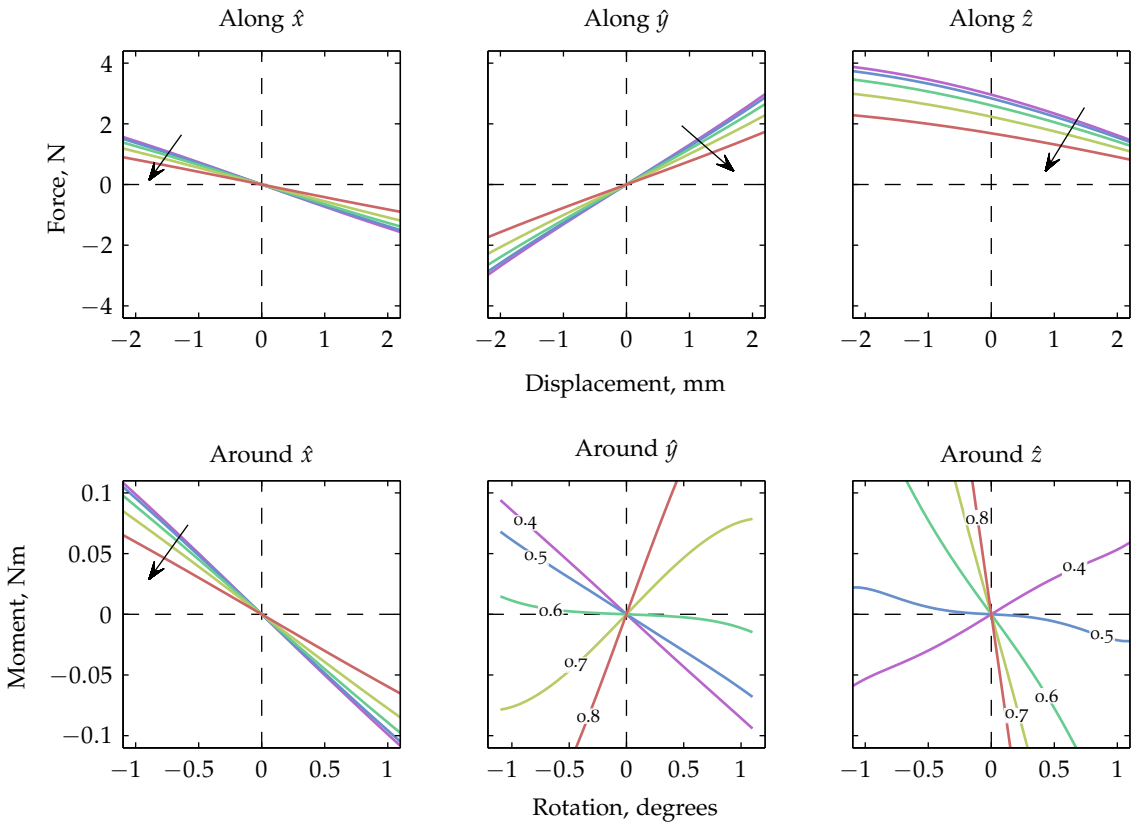

FIGURE 3.35: Varying the size of the stabilising magnets for the conceptual single degree of freedom magnet spring. Magnet size ratios c_2/c_1 are labelled on each plot or indicated in increasing directions with an arrow. The lever arm remains constant, in contrast to Figure 3.34.

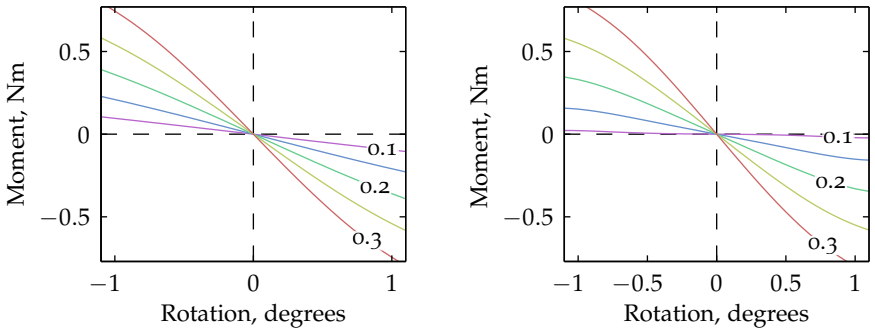

(a) Around the $\hat{x}$ axis. (b) Around the $\hat{z}$ axis.

FIGURE 3.36: Moment of the magnet spring as it rotates around the $\hat{x}$ and $\hat{z}$ axes with a varying spring depth d, labelled in metres. In both cases, the stability increases with greater spring depths.

calculated and shown in Figure 3.36. As the spring depth increases, the lever arms in both $\hat{y}$ and $\hat{z}$ directions increase, thus increasing the magnitude of the moments produced by a given rotation. This result indicates that increasing the spring depth does not affect the stability of the spring.

Variation of the magnetic spring parameters in this case indicates that it is possible to increase the load-bearing ability of such a design without compromising the stability of the system. In this section one particular magnetic system has been shown that has a single degree of instability, and the literature has a small number of other examples [75, 86]. To conclude, there are a plurality of magnet designs that can take advantage of mechanical lever arms to stabilise rotational degrees of freedom even if low-order magnet systems exhibit rotational instability. Optimisation of such systems is an open question that will require a large amount of ingenuity; it is likely that different requirements will yield varying solutions in this area.

§3.4 Inclined magnetic spring design

In comparison to using springs with a linear force–displacement relationship for vibration isolation, using permanent magnets for load bearing can be advantageous due to the smaller variation in resonance frequency seen with increased load as a result of a corresponding increased stiffness. However, two permanent magnets in direct repulsion will not completely eliminate the variability in resonance frequency due to load, only reduce it.

Often, vibration isolation systems are tuned to a narrow-band frequency range and are only effective for a given mass being supported (§1.2.6). A resonance frequency that varies little with load force is desirable due to the resulting predicability of the vibratory behaviour; for example, changes in load force over time will not affect the resonance frequency of the support, which simplifies the system modelling and possible control scenarios. In this section, an arrangement of magnets is investigated with the aim to design a nonlinear spring such that varying the applied load $F = mg$ results in a change in stiffness k such that the natural frequency $\omega_n = \sqrt{k/m}$ remains approximately constant.

A similar idea using permanent magnets has been mentioned previously by Todaka et al. [277], who suggested using a mechanical linkage with two vertically-oriented magnets such that the floating magnet moved in an arc around a fixed magnet due to the effects of the linkage. However, the parameters governing this design were not investigated at that time; their paper primarily investigated the relationship between resonance frequency and horizontal/vertical displacement between the two permanent magnets.

Other work proposed coupling a magnetic spring with a linear elastic spring, for which a nonlinear analysis and experimental results were shown [46, 47]. Such coupled elastic–magnetic systems have been investigated by several authors to various degrees [32, 56, 280, 309], especially in the design of quasi–zero stiffness devices (§1.4.3).

In contrast to quasi–zero stiffness systems, introduced in Section 3.3.3 and analysed in more detail later in Chapter 6, which attempt to reduce the stiffness as much as possible, in this section magnetic forces are used in such a way as to yield a larger region of low stiffness. As with all magnetic springs, positive stiffness in the vertical direction infers negative stiffness or instability in at least one horizontal direction (§1.3.3). This instability may be countered with a linear bearing (or some other physical constraint) or with an active control system.

This section consists of three main parts: Section 3.4.1 defines the geometry of the system and presents the theory for analysing its behaviour; Section 3.4.2 uses this theory to demonstrate the advantages of this magnet design, specifically in terms of its natural frequency versus applied load; and Section 3.4.3 extends the model to analyse rotations and torques to investigate the planar stability of the system.

§3.4.1 *Inclined spring geometry and theory*

A schematic of the inclined magnetic spring is shown in Figure 3.37. Cuboid magnets are used that extend a distance b into the page such that their facing sides are square. The magnet angle θ can range from 0° to 90°, where $\theta = 0°$ has horizontally-oriented magnets and $\theta = 90°$ has vertically-oriented magnets. The spring is composed of two symmetric pairs of inclined magnets; this ensures the horizontal forces cancel when the spring is centred and force is produced in the vertical direction only.

Note that opposing magnets have parallel sides and anti-parallel magnetisations; hence, the force calculations by Akoun and Yonnet [5] (Eq. 2.16) may be applied to this system.

Two dimensions are used to describe the relative displacement between adjacent magnet pairs. The magnet offset d, fixed during operation, is the horizontal face gap in the centred position, and the displacement y can be considered as the vertical face gap in the centred position, designed to vary as the load on the spring changes. With displacement $y = 0$, the facing magnets are horizontally aligned, and with magnet offset $d = 0$ also, the magnet faces are touching. The force and stiffness characteristics of the spring can be affected by adjusting the magnet angle θ and the magnet offset d.

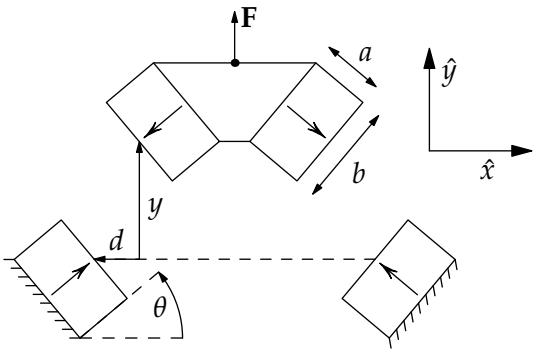

FIGURE 3.37: Schematic of the inclined magnet spring. When magnet offset $d = 0$ and displacement $y = 0$, the magnet faces are aligned and touching. Displacements x and z (not shown) are in the horizontal and out-of-plane directions, respectively.

An assumption is made that there are no magnetic interactions between magnets from one side of the spring to magnets on the other side. This can be ensured in practice with a large enough separation between the pairs on opposite sides. Accordingly, the total force of the spring is given by the superposition of forces for each magnet pair:

$$\mathbf{F} = \mathbf{F}_1 + \mathbf{F}_2. \tag{3.13}$$

To calculate $\mathbf{F}_1$ and $\mathbf{F}_2$ a local coordinate system is defined for each magnet pair at the base magnet, aligned in each respective direction of magnetisation. Then $\mathbf{F}_1 = \mathbf{R}_z(\theta)\mathbf{G}_1$ and $\mathbf{F}_2 = \mathbf{R}_z(\theta')\mathbf{G}_2$, where $\theta' = \pi - \theta$, $\mathbf{G}_1$ and $\mathbf{G}_2$ are the forces between the magnet pairs in the local coordinate systems of the base magnets, and $\mathbf{R}_z(\cdot)$ is the planar rotation matrix given in Eq. 2.44 on page 66.

These forces $\mathbf{G}_1$ and $\mathbf{G}_2$ are calculated with $\mathbf{G}_i = \mathbf{F}_{z,z}(\mathbf{s}_i)$ where $\mathbf{F}_{z,z}(\cdot)$ is the force between parallel cuboid magnets (Eq. 2.16) and $\mathbf{s}_1$ and $\mathbf{s}_2$ are the displacement vectors between the magnet centres in the local coordinate system of the magnets given by

$$\mathbf{s}_1 = \mathbf{R}_z(-\theta)\begin{bmatrix} d+x \\ y \\ z \end{bmatrix} + \begin{bmatrix} a \\ 0 \\ 0 \end{bmatrix}, \qquad \mathbf{s}_2 = \mathbf{R}_z\big(-\theta'\big)\begin{bmatrix} -d+x \\ y \\ z \end{bmatrix} + \begin{bmatrix} a \\ 0 \\ 0 \end{bmatrix}, \tag{3.14}$$

where a and d are parameters defined in Figure 3.37, and $[x, y, z]^\mathsf{T}$ are displacements in the horizontal, vertical, and out-of-plane directions, respectively. In Section 3.4.3 this model will be extended with a small angle approximation to calculate forces and torques due to rotation around the $\hat{z}$ axis.

§3.4.2 *Influence of design parameters*

From Section 3.4.1, it is possible to calculate total force **F** in terms of displacement. This section will outline the influence of the various design parameters on the force, stiffness, and natural frequency characteristics of the system. To begin, vertical force as a function of vertical displacement $F_y(y) = F_y(0, y, 0)$ will be considered (with other displacements $x = z = 0$).

Magnet shape

For this entire analysis, a magnet size ratio of $\gamma = a/b = 0.4$ is used. Depending on the exact desired displacement range, values around this magnet ratio produce the maximum force between two opposing cuboid magnets for a fixed magnet volume (§3.2.1). For the analysis to follow directly, the magnet volume is fixed at $V = ab^2 = \left[10\,\text{mm}\right]^3$. A 'unit length' is defined, $u = \sqrt[3]{V} = 10\,\text{mm}$, and in the subsequent analysis the 'magnet offset ratio' is defined as d/u. The effects of increasing the magnet volume are addressed subsequently.

Magnet angle

Having chosen the magnet size ratio, there are two parameters that influence the force and stiffness characteristics of the spring; these are the magnet angle θ and the magnet offset d. Variations in the magnet angle affect the force characteristics to a greater extent and will be examined first.

The theory outlined in Section 3.4.1 was used to calculate force versus displacement curves over a range of magnet angles from 0° to 90°. These are shown in Figure 3.38, which shows a dramatic effect on the force and stiffness characteristics due to changes in the inclination angle of the magnets. Of particular interest are the low-stiffness regions in the force curves in Figure 3.38; these are potential areas for improved vibration isolation.

Figure 3.38 is difficult to use for design purposes because the required load force will affect the dynamic stiffness as the system sits in equilibrium at a given displacement. However, this equilibrium displacement is not a parameter of particular interest provided the magnetic spring is still levitating. Therefore, for interpreting the operating conditions of the system it is more useful to consider the relationship between load force and natural frequency.

The vertical stiffness k_y was obtained for convenience by numerical differentiation of the vertical force F_y:

$$k_y(y) \approx -\tfrac{1}{2}[F_y(y+\delta) - F_y(y-\delta)]/\delta, \tag{3.15}$$

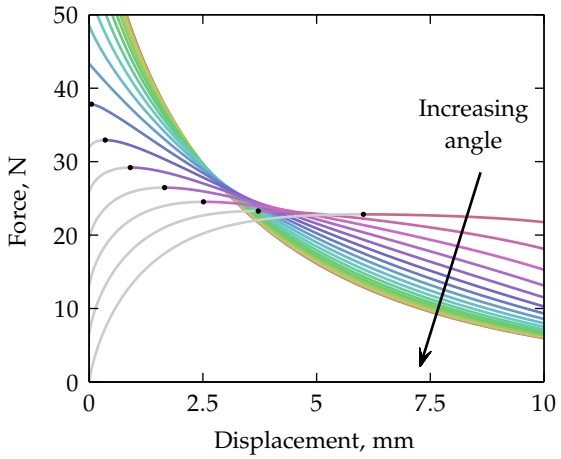

FIGURE 3.38: Vertical force versus displacement y of the inclined magnet spring for magnet angles from 0° to 90° in 5° increments. Offset d between the magnets is zero. Light grey lines indicate negative stiffness (instability) and markers show the position of quasi–zero stiffness.

where δ is a small displacement increment. The natural frequency $\omega_n(y)$ as a function of displacement was calculated in terms of this vertical stiffness k_y with

$$\omega_n(y) = \sqrt{\frac{k_y(y)}{m_{\text{eq}}}} = \sqrt{\frac{k_y(y)}{F_y(y)/g}} \tag{3.16}$$

where the equivalent mass $m_{\text{eq}} = F_y(y)/g$ is the mass required to load the spring such that its equilibrium position lies at the displacement y. The force corresponding to this equivalent mass is referred to as the 'load force'.

By plotting natural frequency as a function of load force in Figure 3.39, it is possible to choose a magnet angle based on a certain load to satisfy a desired natural frequency. Specifically, for the case of zero offset between the magnets $d = 0$ (Fig. 3.39(a)), it can be seen that at a magnet angle of $\theta = 35°$ the natural frequency is almost independent of force for a large range of applied load (approximately $30\,\text{N} \pm 10\,\text{N}$).

Magnet offset

Figure 3.39(a) shows the natural frequency versus load curve for a magnet offset ratio d/u of zero. Increasing the magnet offset d changes the force and stiffness relationships of the spring; Figure 3.39(b) shows the same plot with a magnet offset ratio $d/u = 0.25$. The difference in the shape of the curves is not great, but Figure 3.39(b) shows that a greater magnet offset results in smaller load forces and a smaller range in load force. Also, the angle

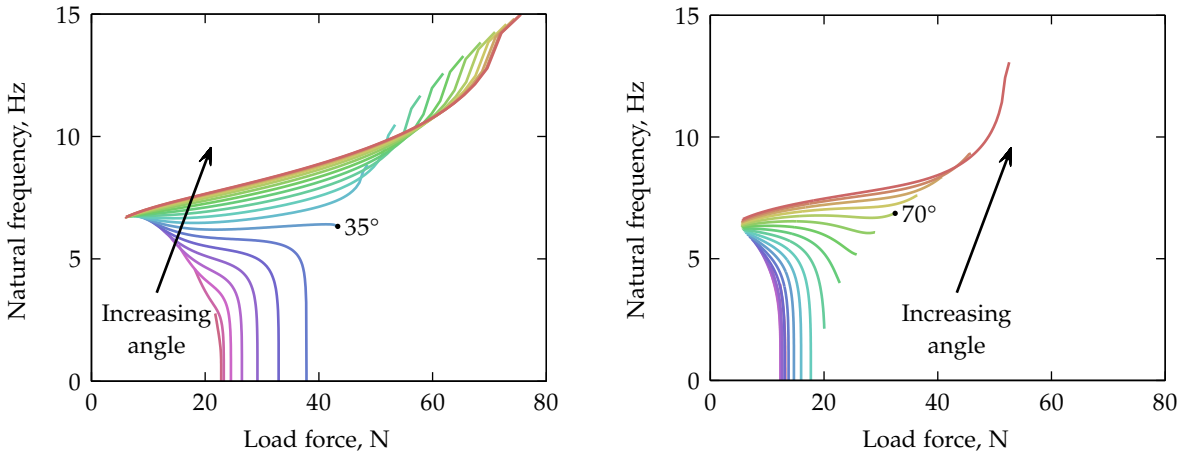

(a) Zero offset d between the magnets. At 35° the natural frequency is near-constant for a wide range of load forces.

(b) Magnet offset ratio $d/u = 0.25$. Near-constant natural frequency occurs at 70°.

FIGURE 3.39: Natural frequency versus load force for magnet angles from 0° to 90° in 5° increments.

which corresponds to the almost-flat natural frequency curve has changed to $\theta = 70°$.

The natural frequency versus load force is redrawn in Figure 3.40 for a fixed magnet angle of $\theta = 45°$ over a range of magnet offset ratios d from zero to 0.5. At this angle, it can be seen that the region of mostly-flat natural frequency occurs at a offset ratio of $d/u = 0.05$. This indicates that the magnet angle should be chosen only after the tolerances of magnet displacement are decided and a minimum offset ratio established.

Horizontal and out-of-plane stability due to vertical displacement

In Figures 3.39 and 3.40, design curves were presented under the assumption that the vertical stiffness only was under consideration. Due to the inclination of the magnets, however, the horizontal and out-of-plane stiffness will also vary as the magnet spring parameters are changed. If active control is used to constrain the floating magnets, it may be desirable to minimise the horizontal instability of the magnet spring in order to reduce the number of sensors and actuators required to stabilise the system.

The horizontal stiffness is calculated with a numerical gradient of the forces when the magnets are centred and when a small horizontal displacement x is applied. In this case, the horizontal force F_x will be considered as a

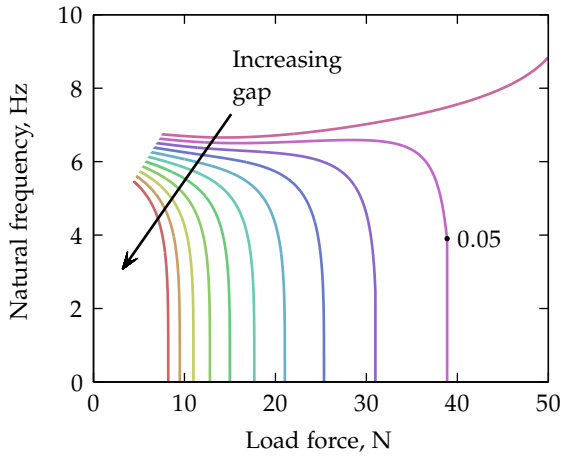

FIGURE 3.40: Natural frequency versus load force for magnet offset ratios from zero to 0.5 in increments of 0.05 and a magnet angle of 45°.

function of vertical displacement y, with horizontal stiffness calculated as

$$k_x(y) = -\frac{1}{\delta}\Big[F_x(\delta, y, 0) - F_x(0, y, 0)\Big] = -\frac{1}{\delta}F_x(\delta, y, 0)\,. \tag{3.17}$$

An equivalent formulation can be used to calculate the out-of-plane stiffness due to a vertical displacement based on the out-of-plane force F_z:

$$k_z(y) = -\frac{1}{\delta}\Big[F_z(0, y, \delta) - F_z(0, y, 0)\Big] = -\frac{1}{\delta}F_z(0, y, \delta)\,. \tag{3.18}$$

An example of spring parameters that achieve positive stability in both the vertical and horizontal directions is shown in Figures 3.41(a) and 3.41(b). This is possible as the stiffness in the out-of-the-page direction of Figure 3.37 is always negative (Fig. 3.41(c)), and as a consequence of Earnshaw's theorem (Section 1.3.3 on page 28) the stiffnesses in each direction must sum to zero; that is, $k_x(y) + k_y(y) + k_z(y) = 0$.

The drawback of achieving minimal instability is a reduction in the achievable low-stiffness regions of the spring. Figure 3.42 shows a plot of natural frequency versus load force for a magnet angle of 40° and for a variety of magnet offsets. In this graph, regions of negative horizontal stiffness have been de-emphasised by drawing those sections of the curves in light grey. It can be seen here that the 'flat' sections of the curve (that correspond to configurations of largely-flat natural frequency against load force) occur largely in the regions of horizontal instability. Figure 3.42 also demonstrates that when designing the system for horizontal stiffness, a larger magnet

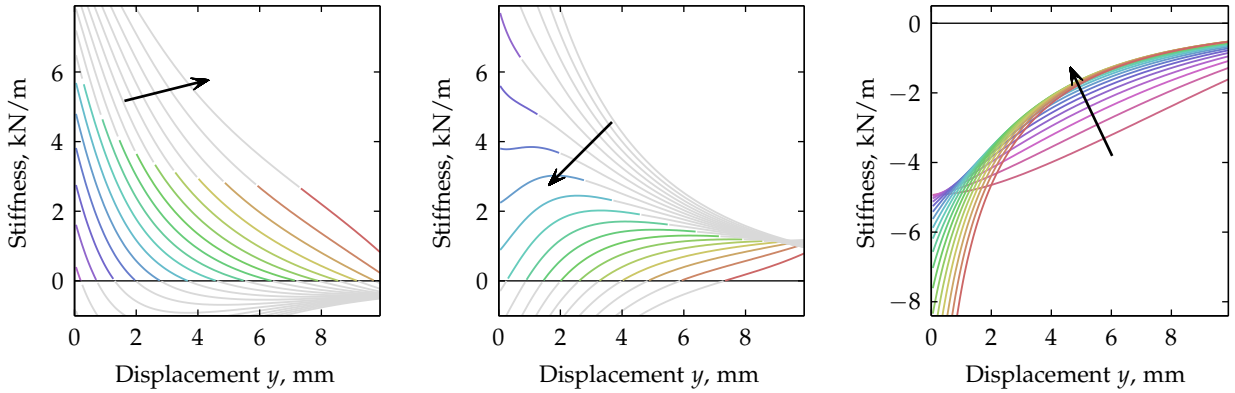

(a) Vertical stiffness. (b) Horizontal stiffness. (c) Out-of-plane stiffness.

FIGURE 3.41: Stiffness in three directions versus vertical displacement for a magnet offset ratio of $d/u = 0.2$ and magnet angles from 0° to 90° in 5° increments (arrows indicate increasing magnet angle). For the horizontal and vertical stiffness plots (a) and (b), regions of positive stiffness for both directions are coloured; regions of grey indicate that either the vertical and/or horizontal stiffness is negative in that position for that magnet angle.

offset increases the displacement range of the magnetic spring, albeit with a decrease in possible load force.

A more detailed investigation on the planar stability of the system is performed in Section 3.4.3.

Magnet volume

Having examined the influence of magnet angle and magnet offset on the natural frequency and load force characteristics, it is essential to confirm that this arrangement is scalable for arbitrary loads by increasing the magnet volumes. With fixed magnet offset ratio of $d/u = 0.2$ and magnet angle of $\theta = 40°$, the natural frequency versus force characteristic with volumes from $V = [10\,\text{mm}]^3$ to $V = [50\,\text{mm}]^3$ is shown in Figure 3.43, which shows that larger magnet sizes permit larger load forces while also retaining a low natural frequency. In fact, the natural frequency decreases with larger magnet sizes. This shows that the inclined magnet spring system is suitable for bearing large loads with low stiffness, and fits into the category of springs that exhibit 'high-static–low-dynamic' stiffness [e.g. 56].

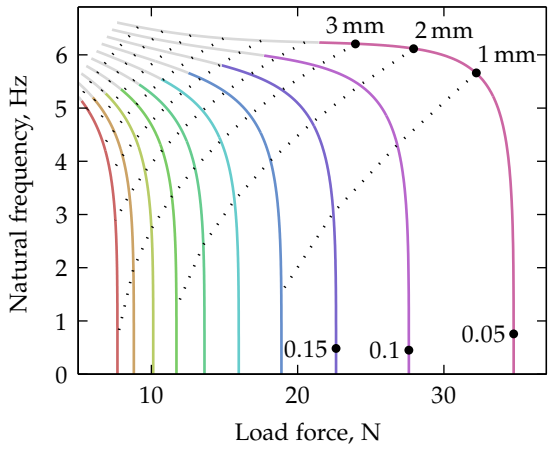

FIGURE 3.42: Natural frequency versus load force for offset ratios from 0.05 to 0.5 in 0.05 increments and a magnet angle of 40°. Regions of negative horizontal stiffness are drawn in light grey, and displacements are labelled with dotted lines for every change in displacement of 1 mm.

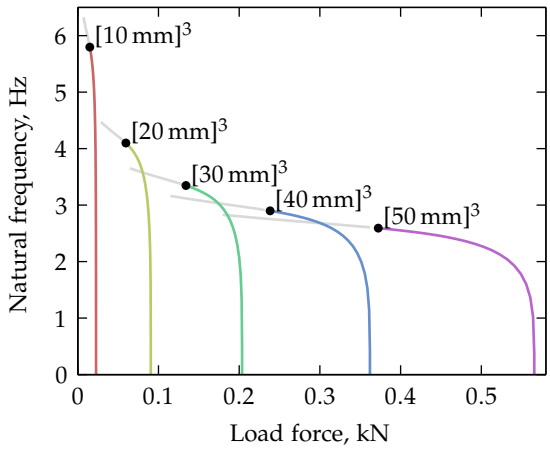

FIGURE 3.43: Natural frequency versus load force for a magnet offset ratio of 0.2 and a magnet angle of 40° over a range of magnet volumes from $\left[10\,\mathrm{mm}\right]^3$ to $\left[50\,\mathrm{mm}\right]^3$. The displacement ranges are proportional to the magnet size such that the system with magnet volume $\left[10\,\mathrm{mm}\right]^3$ undergoes displacement from 0 mm to 10 mm and so on. Regions of negative horizontal stiffness are drawn in light grey.

Design based on these results

Clearly there is a large space of design possibilities for such a magnet arrangement. Using these results requires an iterative approach based around the following constraints:

1. Magnets are large enough to bear the required load variance, which will inform a maximum and minimum magnet clearance;
2. Stiffness at the equilibrium point is satisfied by varying the magnet offset and angle;
3. Load variation is modelled and natural frequency remains within acceptable limits.

Generally, a larger magnet size will permit a larger range of approximate natural frequency invariance (Fig. 3.43). Only by evaluating a number of trial solutions for magnet angle and magnet offset can an acceptable design be found to satisfy a specified amount of load variability.

§3.4.3 *Investigation into planar stability*

In Section 3.4.2, the translational stiffness of the system in three directions was discussed in terms of a change in the vertical equilibrium position of the spring (for example, corresponding to a variation in applied load). However, this is not enough to establish the global stability of the system due to cross-axis coupling and rotational effects that were not included as part of the model. Here, the planar stability of the system will be investigated to attempt to provide some picture of the complex kinetics seen due to planar translation and rotation; the system is assumed to be constrained in a single plane for this analysis with geometry shown in Figure 3.44.

An analytical formulation for calculating the torques between two cuboid parallel magnets has recently been presented by Janssen et al. [142]. The torque equations have not been reproduced here but they follow a similar (albeit more complex) form than that of Eq. 2.16 for force. Note that, with reference to Figure 3.44, the torques are *not* calculated by using the already-calculated force terms (the vectors $\mathbf{F}_1$ and $\mathbf{F}_2$ in that figure); the torque is calculated using a separate integral equation that takes the lever arm into account.

Note, however, that the force and torque equations do not permit a relative rotation between the two interacting magnets (their sides must remain parallel). Therefore, in order to analyse the rotational stability of the magnetic system a small angle approximation must be made, which is illustrated in Figure 3.45: due to overall rotation φ of the spring the moving magnets will

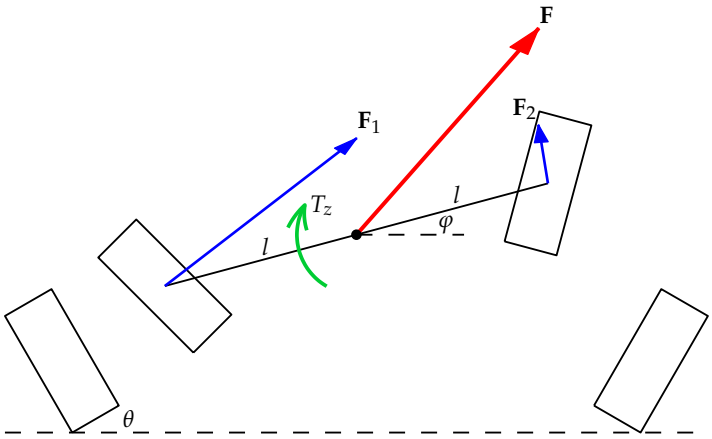

FIGURE 3.44: Geometry of the planar system in which forces and torques due to rotation φ are calculated. The system is shown with $\varphi = 15°$, lever arm ratio $l/u = 2$, magnet angle $\theta = 30°$ and magnet offset ratio $d/u = 0.5$.

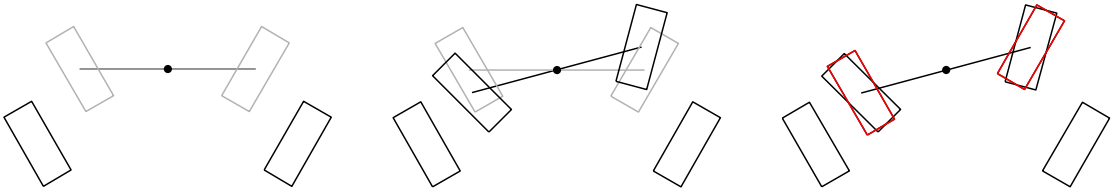

(a) Without rotation.

(b) With rotation shown in black; the unrotated position, as in (a), is shown in light grey.

(c) With small angle approximation of zero magnet rotation shown in colour; the rotated magnets, as in (b), are shown in black.

FIGURE 3.45: Visual representation of the small angle approximation in which the magnet structure rotates but the magnets themselves are assumed to remain parallel to their respective partner.

translate around their lever arms l (the centre of rotation is here assumed to be the mid-point between the magnet centres) but their angle to the horizontal remains fixed. Calculating the force and torque in this way is only valid for small rotations, but is sufficient to establish relationships regarding rotational stability and cross-coupling with translational forces.

Theory for planar force and torque calculations

The model developed for this system in Section 3.4.1 is here extended to calculate torques and allow (small) rotations, both around the $\hat{z}$ axis only. The vector equations for this new geometry require an additional term to ac-

commodate rotation. First define two lever arm vectors for each magnet with respect to a centre of rotation denoted by $\mathbf{l}_1 = [-l, 0, 0]^\mathsf{T}$ and $\mathbf{l}_2 = [l, 0, 0]^\mathsf{T}$ in the local coordinate system of the spring (although other centres of rotation are certainly possible). These lever arms define additional translations of the magnets $\mathbf{p}_1$ and $\mathbf{p}_2$ due to rotation of the system:

$$\mathbf{p}_1 = \mathbf{R}_z(\varphi)\mathbf{l}_1 - \mathbf{l}_1, \qquad \mathbf{p}_2 = \mathbf{R}_z(\varphi)\mathbf{l}_2 - \mathbf{l}_2. \tag{3.19}$$

The displacement vectors between the magnet pairs (again in the coordinate system of the base magnets) are then given by

$$\mathbf{s}_1 = \mathbf{R}_z(-\theta)\left[\mathbf{p}_1 + \begin{bmatrix} d+x \\ y \\ z \end{bmatrix}\right] + \begin{bmatrix} a \\ 0 \\ 0 \end{bmatrix}, \quad \mathbf{s}_2 = \mathbf{R}_z\left(-\theta'\right)\left[\mathbf{p}_2 + \begin{bmatrix} -d+x \\ y \\ z \end{bmatrix}\right] + \begin{bmatrix} a \\ 0 \\ 0 \end{bmatrix}. \tag{3.20}$$

Also, the displacement vectors in the coordinate system of the magnets from the spring magnet centres to the centre of rotation (required for torque calculation) are given by

$$\mathbf{t}_1 = \mathbf{R}_z(-\theta)\left[-\mathbf{R}_z(\varphi)\mathbf{l}_1\right], \qquad \mathbf{t}_2 = \mathbf{R}_z\left(-\theta'\right)\left[-\mathbf{R}_z(\varphi)\mathbf{l}_2\right]. \tag{3.21}$$

As before, the total force is

$$\mathbf{F} = \mathbf{F}_1 + \mathbf{F}_2 = \mathbf{R}_z(\theta)\mathbf{F}_{z,z}(\mathbf{s}_1) + \mathbf{R}_z\left(\theta'\right)\mathbf{F}_{z,z}(\mathbf{s}_2), \tag{3.22}$$

where $\mathbf{F}_{z,z}(\cdot)$ is the magnet force equation given in Eq. 2.16. The torque is not affected by the coordinate system rotations (recall it is around the $\hat{z}$ axis only) and is given by the sum of torques between the magnet pairs as

$$T_z = T_{x,x_z}(\mathbf{s}_1, \mathbf{t}_1) + T_{x,x_z}(\mathbf{s}_2, \mathbf{t}_2), \tag{3.23}$$

where T_{x,x_z} is $\hat{z}$ component of the magnetic torque equation given by Janssen et al. [142] transformed for magnets magnetised in the $\hat{x}$ direction.

Planar stability results

The system is not expected to be completely stable due to cross-axis coupling. For example, after horizontal translation the magnetic force will become asymmetric and a torque will result. Similarly, after a rotation the reverse will occur and a horizontal force will be produced, which can be seen from the resultant vectors in Figures 3.44 and 3.47. Due to the large number of possible magnet parameter combinations, only a select number of cases will be analysed in detail here.

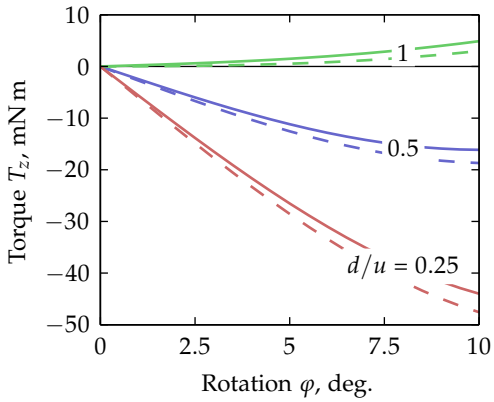

FIGURE 3.46: Torque versus rotation for three spring configurations shown in Figure 3.47 with parameters $u = y = 10\,\text{mm}$, $\theta = 30°$, and $l/u = 2$. Dashed lines show verification torques calculated by using the magnetic forces around their lever arms only (Eq. 3.24).

The torsional stability due to rotation is affected by the geometric parameters of the system as shown by example in Figure 3.46, in which varying the magnet offset ratio changes the rotational stiffness from stable ($d/u = \{0.25, 0.5\}$) to unstable ($d/u = 1$). Scaled vector diagrams to illustrate these are ideas are shown in Figure 3.47. Further torque variations can be effected by varying the lever arm and the position of the centre of rotation. The validity of the torque calculations can be assessed by comparing the torques calculated with the magnet forces only using the equation

$$T_z \approx l(-\mathbf{F}_1 + \mathbf{F}_2) \cdot \begin{bmatrix} -\sin\varphi \\ \cos\varphi \\ 0 \end{bmatrix} \tag{3.24}$$

where the dot product extracts the component of force perpendicular to the lever arm. Torques calculated in this manner are shown in Figure 3.46 as dashed lines and it can be seen they match closely for small angles of rotation.

Stability results will be shown using perturbations of a dynamic simulation of the system in a small number of variations of design parameters. The equations of motion are defined as

$$m\ddot{x} = F_x(x, y, \varphi) - c_x\dot{x}\,, \tag{3.25a}$$
$$m\ddot{y} = F_y(x, y, \varphi) - c_y\dot{y} - mg\,, \tag{3.25b}$$
$$I_m\ddot{\varphi} = T_z(x, y, \varphi) - c_\varphi\dot{\varphi}\,, \tag{3.25c}$$

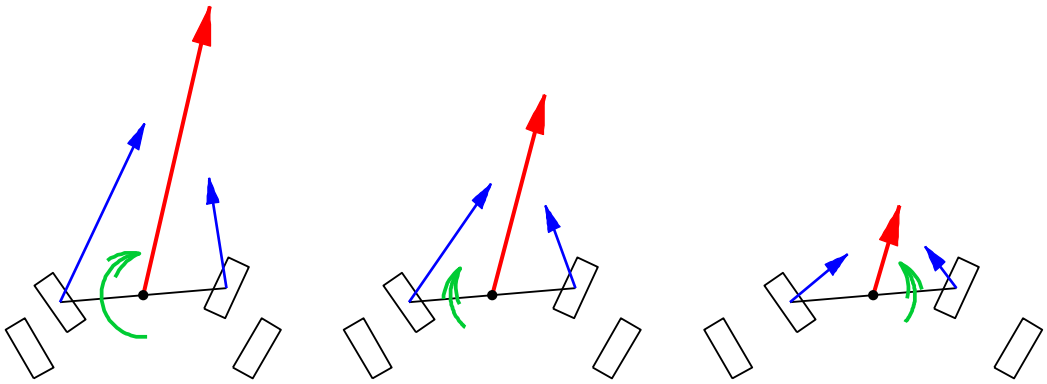

(a) $d/u = 0.25$ (b) $d/u = 0.5$ (c) $d/u = 1$

FIGURE 3.47: Visual representation of the forces and torques at a rotation of $\varphi = 10°$ corresponding to the stability results shown in Figure 3.46. Force vector lengths are proportional to their magnitude, but torque arc lengths are not.

TABLE 3.1: Parameters used for dynamic simulations of the inclined magnetic spring.

Explicit parameters			Implicit parameters		
Mass	m	3 kg	Equilibrium position	y_0	14.04 mm
Damping ratio	ζ	0.2	Moment of inertia	I_m	0.4 g m^2
Magnetisation	B_{r1}, B_{r2}	1 T	Horizontal stiffness	k_x	15.43 N/m
Unit length	u	20 mm	Vertical stiffness	k_y	170.5 N/m
Magnet angle	θ	45°	Rotational stiffness	k_φ	31.3 mN m/rad.
Offset ratio	d/u	0.4	Horizontal damping	c_x	9.05 kg/s
Magnet ratio	γ	0.4	Vertical damping	c_y	2.72 kg/s
Lever ratio	l/u	2	Rotational damping	c_φ	2.83 mN m s/rad.

for which a time-domain solution was produced numerically with a Runge-Kutta technique (Matlab's `ode45` function). Viscous damping terms c_x, c_y, and c_φ account for energy loss in the system. The force and torque terms are those defined in Eqs 3.22 and 3.23 respectively.

The parameters shown in Table 3.1 were used for the dynamic simulations. The equilibrium displacement y_0 is found by numerically inverting a static analysis of the magnet forces $F_y(0, y_0, 0) = mg$; a damping ratio of 20 % is assumed to account for eddy current damping and any other energy losses; and the moment of inertia is approximated with $I_m = \frac{1}{3}ml^2$. The parameters have been selected such that the vertical, horizontal, and rotational direct stiffnesses are all positive for this equilibrium displacement.

Assuming that the device is always designed to move freely in the vertical

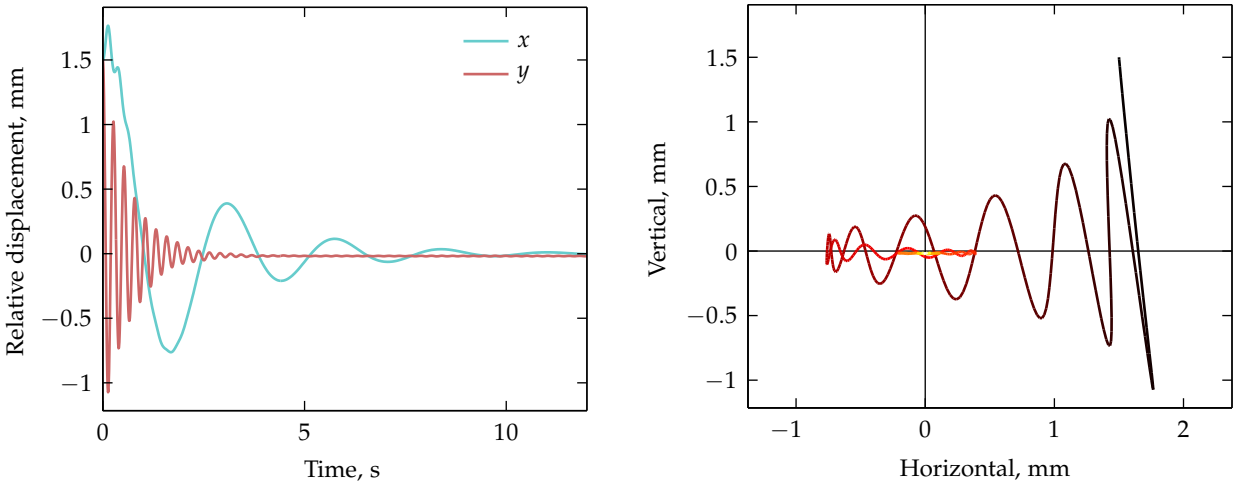

(a) Horizontal and vertical displacement from the equilibrium position.

(b) Displacement map with colour progressing with time from dark to light.

FIGURE 3.48: Dynamic simulation of the rotationally-constrained system defined by Eq. 3.25 with perturbation of $\Delta x = \Delta y = 1.5\,\text{mm}$ and constraint on rotational φ.

direction to accommodate changing load, there are three regimes in which stability could be assessed: constraining rotation, constraining horizontal displacement, and unconstrained. It is evident that the case of constraining both rotation and horizontal displacement will be stable provided the vertical stiffness is positive. The first of the dynamic simulations presented is displacement in the $\hat{x}$–$\hat{y}$ plane with constrained rotation. Given the system described in Equation 3.25 and a perturbation of $\Delta x = \Delta y = 1.5\,\text{mm}$, the resultant dynamics are shown in Figure 3.48 as displacements from the equilibrium position of the spring. While this is close to the maximum perturbation for this system before instability, this example illustrates that there is a region around the equilibrium position within which stability is achieved.

The second stability example constrains horizontal displacement while allowing free rotation of the system. A dynamic simulation was performed with a perturbation of $\Delta y = 1.5\,\text{mm}$ and $\Delta\varphi = 3°$, for which results are shown in Figure 3.49. Again, with one constraint on the system there is a stable region around the equilibrium point. In fact, this arrangement is more stable than the previous as there is less cross-coupling between the vertical and rotational degrees of freedom.

Finally, it might now be expected that since stability was achieved in both x–y and y–φ regimes, an unconstrained system might be similarly stable. Unfortunately this is not the case, as cross-coupling influences are too

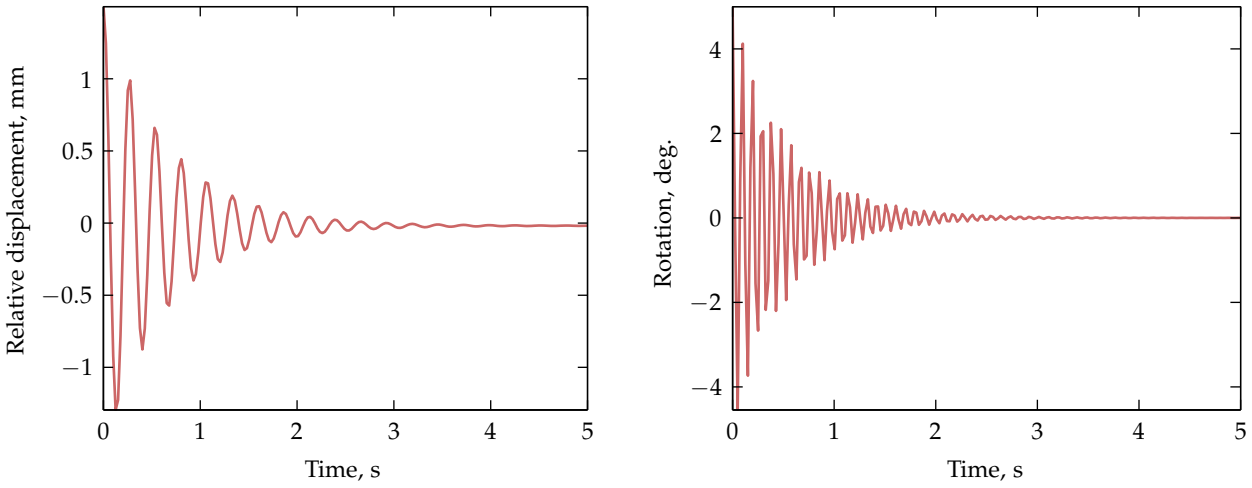

(a) Relative vertical displacement $y - y_0$.

(b) Rotation φ.

FIGURE 3.49: Dynamic simulation with perturbation of $\Delta y = 1.5\,\text{mm}$ and $\Delta\varphi = 3°$ with constraint in horizontal displacement x.

great and even an incremental perturbation eventually leads to instability as shown in Figure 3.50. There is a macroscopic perturbation of $\Delta y = -1\,\text{mm}$ and incremental perturbations of $\Delta x = 1 \times 10^{-9}\,\text{m}$ and $\Delta\varphi = 1 \times 10^{-9}\,\text{deg}$. Despite achieving positive direct stabilities in all three degrees of freedom, some form of control over this cross-coupling instability is required for stable operation; this could take the form of passive bearings or non-contact electromagnetic actuators.

§3.4.4 *Conclusion on inclined magnetic springs*

In this section, a particular magnet geometry was investigated for the purposes of developing a spring for vibration isolation with the goal of a load-invariant natural frequency. The resonance–load relationship was found to have significant flat areas, indicating this goal could be achieved for certain geometries. The load-bearing capacity could be largely increased by scaling the volumes of the magnets; this was shown to have small effect on the natural frequency of the system.

Since the system uses magnetic levitation to achieve its force characteristic, there are various instabilities inherent in its dynamics. Some of these instabilities due to coupling between horizontal and rotational degrees of freedom have been highlighted, but a complete six degree of freedom analysis must await future developments in magnetic torque modelling.

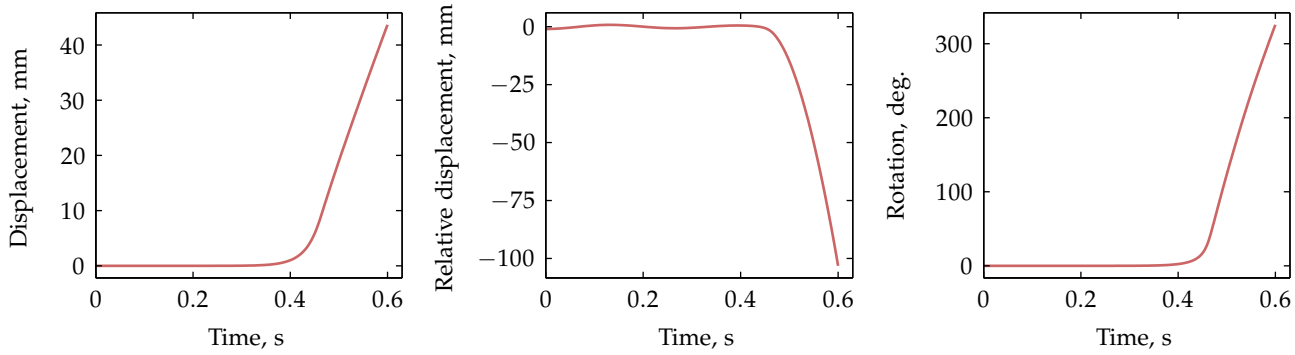

(a) Horizontal displacement x. (b) Relative vert. displacement $y - y_0$. (c) Rotation φ.

FIGURE 3.50: Dynamic simulation without constraint and vertical perturbation only. Despite 'stable' stiffnesses in each direction (seen in Figures 3.48 and 3.49), the unconstrained system is unstable due to cross-axis coupling.

§3.5 PROTOTYPE INCLINED MAGNET SYSTEM

To explore the possibilities raised by the theoretical analysis of the inclined magnetic spring (§3.4), an honours project co-supervised by the author was undertaken in 2011 to design and build a prototype [101, 102].[2]

The prototype was built used Maytec[3] aluminium extrusions to allow modular placement of the inclined magnets with variable magnet angle. A photo of the prototype is shown in Figure 3.51, which shows the main features of the system. Six identical magnet pairs were used; four on the long side of the device and two on the short side. The rare earth magnets of volume 25 mm × 25 mm × 12.5 mm were chosen to generate enough repulsive force to bear a weight of 10 kg with a vertical displacement of around 20 mm depending on the magnet angle. Four electromagnetic actuators were placed at the corners of the device for active vibration control. For the project, passive levitation control was achieved using a linear bearing to constrain the device to vertical displacement, coupled with a rotational bearing to permit rotation around the long horizontal axis. The device was stable even under large displacements and rotations in this partially-constrained configuration, but when analysed for active stabilisation a strong instability around the $\hat{y}$ axis (yaw rotation) was found.

The transmissibility of the system was measured using a custom-built shaker frame using a MB Model 110 shaker. Two Brüel & Kjær Type 4393

2. The members of the project were Mr Yann Frizenschaf, Ms Siobhan Giles, Mr Jack Miller, Mr Thomas Pitman, and Mr Christopher Stapleton.
3. Maytec Australia Pty Ltd, `http://www.maytec.com.au/`

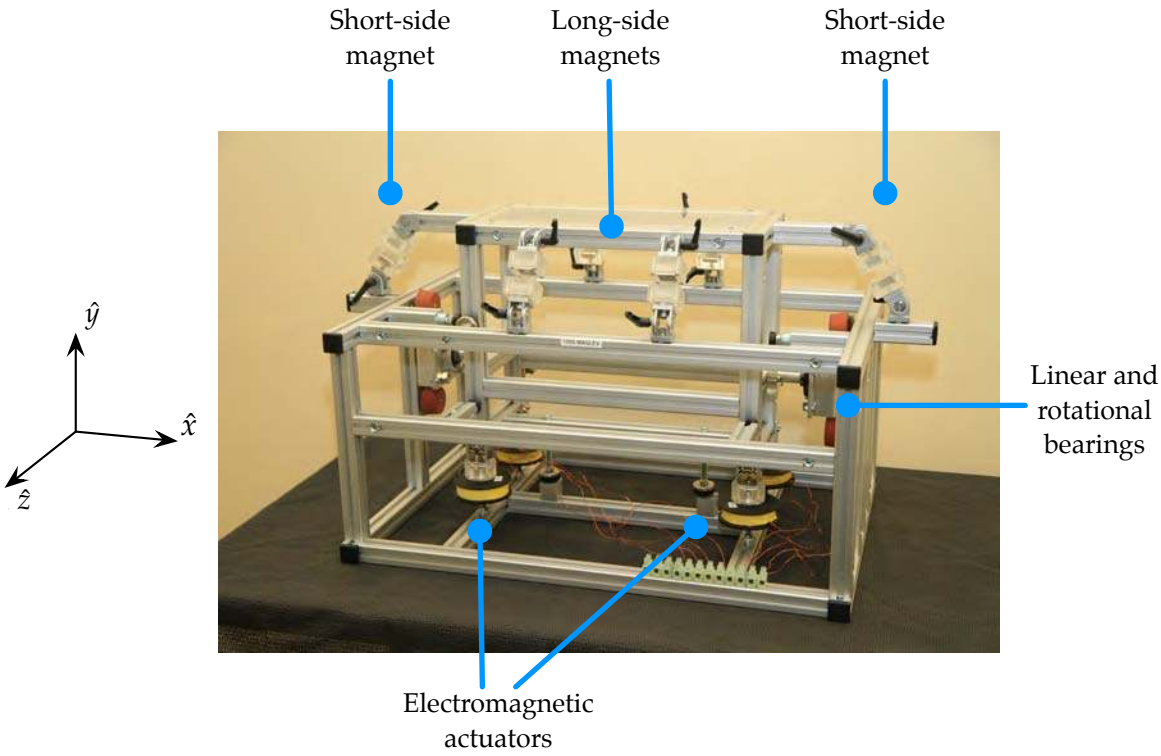

FIGURE 3.51: Prototype inclined magnet isolation device constrained with a linear bearing to translate only in the $\hat{y}$ direction and rotate solely around the $\hat{x}$ axis.

TABLE 3.2: Modelled and measured vibration results for the prototype isolator.

Magnet angle	45°	60°
Resonance frequency, analytical	4.9 Hz	4.0 Hz
Resonance frequency, measured	5.1 Hz	3.8 Hz
Measured damping ratio	4.4 %	9.0 %

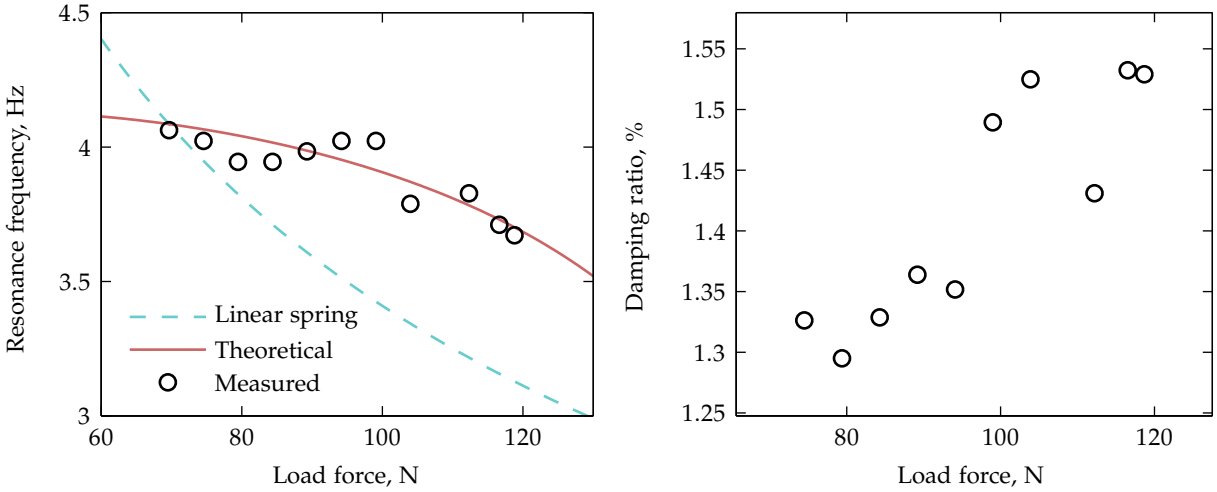

(a) Resonance frequency compared with predicated values and against the response of a linear spring.

(b) Damping ratio.

FIGURE 3.52: Measured values of resonance frequency and damping ratio of the inclined magnet isolation prototype as a function of load force.

accelerometers were used with NVMS charge amplifiers to measure the input vibration and platform response. The frequency analysis was performed using a SignalCalc ACE Signal Analyser with a sample rate of 125 Hz, 1600 spectral lines, 50 % Hanning window overlap, and 30 averages.

The six degree of freedom system was modelled using an extension of the theory developed in Section 3.4.3 for the planar three degree of freedom system [102]. The model predicted the behaviour of the prototype well; Table 3.2 shows the measured and modelled resonance frequency for two magnet angles, which differ by around 5%. The resonance frequencies as a function of load mass are shown in Figure 3.52(a). Due to limitations of the resonance frequency measurements, the measured data is quite noisy but the correspondence with the expected modelled results can still be seen.

It is interesting to compare the significant difference in damping ratio for these two magnet angles (Table 3.2). The strongest contributor to the damping ratio in this system is from induced eddy currents in each permanent magnet by the magnetic field of the other (§1.3.4), as viscous damping in the bearings and due to air resistance can be assumed to be constant. There are two main factors that would cause changes in the magnitude of the induced eddy currents. For a varying magnet angle, the vertical displacement between the magnet pairs would be affected. Secondly, as the angle between the direction of displacement (vertical, in this case) and the direction of magnetisation

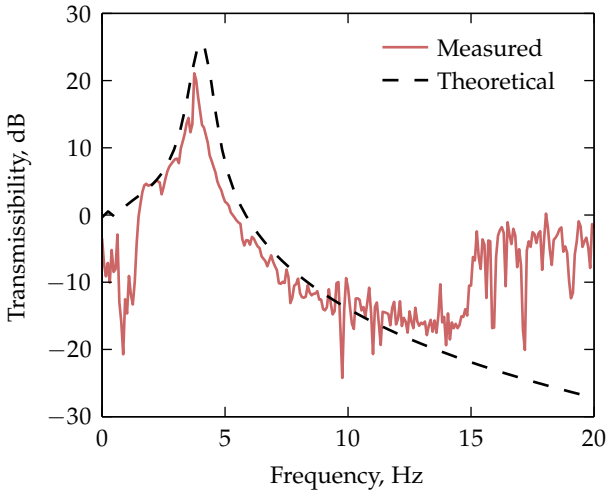

FIGURE 3.53: Measured and modelled transmissibility of the passive inclined magnet isolation prototype with a magnet angle of 60° and a magnet offset ratio of 0.5. Behaviour from 15 Hz is assumed to be due to bearing friction.

increases, the gradient of magnetisation decreases over a certain displacement. The effect on the damping ratio with a variety of load masses is shown in Figure 3.52(b), where it can be seen that as the magnets become closer together, the magnitude of the induced eddy currents are increased and so does the damping ratio. These values were taken in a different configuration than the data shown in Table 3.2, and the damping ratios are not comparable between these two cases.

The theoretical model was also used in a dynamic simulation which predicted the transmissibility of the isolator against ground disturbance. The measured and modelled transmissibility is shown in Figure 3.53, which shows good agreement at low frequencies around the resonance peak. The measured results do not roll off at higher frequencies, however, and this is an important point: due to the inherent friction in the linear bearing at high frequencies, the performance of the isolator is compromised in the passive design. These experimental results indicate that active stability control should be used to achieve non-contact levitation for good high-frequency performance.

The sharp peak in Figure 3.53 is due to the low damping inherent in magnetically levitated systems. Active vibration control was used to improve the vibration transmissibility. Four electromagnetic actuators (custom-built) were driven using a dSpace DS1104 real-time control board. Integrated accelerometer measurements from the platform were used to generate the control signal for 'skyhook damping' (§1.2.3). Measured transmissibility results with

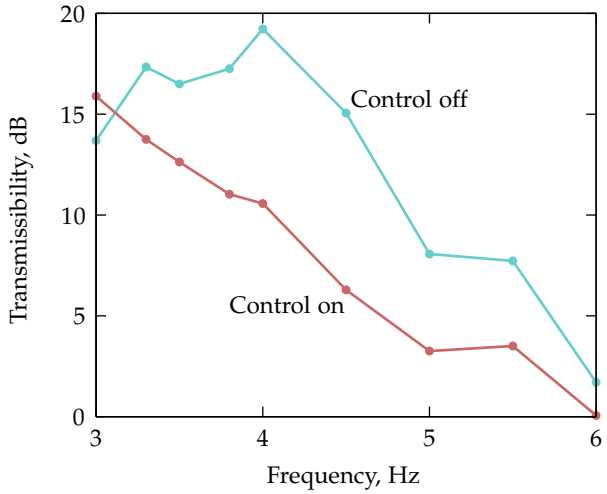

FIGURE 3.54: Measured transmissibility of the inclined magnet isolation prototype with and without active vibration control.

and without active vibration control are shown in Figure 3.54. The skyhook damping method achieves a clear reduction in the resonance peak; around 9 dB in this case. Behaviour at higher frequencies is unaffected, as is expected with this method of vibration control (compare Figure 1.3(b) on page 11).

§3.5.1 *Limitations of the prototype*

This project was unable to achieve active stabilisation of the inclined magnet prototype; a strong instability was found in yaw rotation. For this prototype design, no attempt was made to investigate variation in horizontal stability, but it is unlikely that the yaw rotation would be stabilised by removing the short-side magnet pairs. Indeed, due to the consequences of Earnshaw's theorem it is expected that there will be significant instability in at least one rotational direction unless specific design effort is expended to ensure stability in all rotational degrees of freedom (§3.3.9). Even were this attempted, stabilising all three rotational degrees of freedom could negatively affect the performance of the translational behaviour of the design.

Due to the lightly damped nature of the system and the coupling between different axes for each magnet pair, a significant degree of cross-coupling was observed in the overall vibration behaviour of the system, requiring careful adjustment to excite the structure in the vertical direction only. Active control applied to each corner of the prototype compounded this problem, as imperfections in the coil manufacture led to variations in coil impedance and therefore differences in force–displacement behaviour for each coil. As a

result, the control signals were difficult to tune such that their resultant forces on the system were in a single degree of freedom only. When not perfectly tuned, these unbalanced coils had the tendency to induce cross-coupling motion (generally rotations around the horizontal axes) unless carefully calibrated and monitored.

§3.6 Summary of magnetic spring design

In this chapter, a number of designs for load bearing using individual magnets in a variety of configurations were introduced and discussed. Cuboid and cylindrical magnets were compared, and it was shown that cylindrical magnets produce greater magnetic forces per volume; choosing an equal radius and side length will produce the approximately greatest forces. A number of unique spring designs were demonstrated using cuboid magnets, with a quasi–zero stiffness design of particular interest in future chapters. While each cuboid magnet spring design had different degrees of instability, it was shown that by carefully introducing additional magnets in a design the degree of instability can be minimised in certain cases. Finally, a particular focus was placed on a new spring design using inclined magnets, and this design was experimentally tested; its results tracked well with theoretical calculations and its utility for vibration isolation was explored.

CHAPTER 4

Multipole arrays for improved levitation

The material presented in Section 4.3 is based on work that has been published as a journal paper [240].

§4.1 Background of multipole arrays

The magnetic designs presented in Chapter 3 were based around various configurations of multiple discrete magnets each oriented in specific directions. In this chapter, an analysis is presented on using 'multipole' magnet arrays, which are groups of magnets stacked together with varying directions of magnetisation within the array.

Early work in this area focussed on using multipole stacks for magnetic bearings (see Figure 1.10 on page 27), which continue to see research focus in areas such as artificial hearts [66, 100, 250], and wind power generation [176]. The theory for these magnetic bearings assumed originally that the effect of curvature of the ring magnets to be negligible and analysed the forces between two large flat plates with non-uniform magnetisation as if multiple magnets were stacked together to form a planar structure. In such early cases, it was shown that a North–South alternating magnetisation (that is, 180° rotations between successive magnets) across the plates yields stronger forces than homogeneous magnetisation [24]. Using 90° rotation increments the stiffness can be approximately doubled again while keeping the magnet volume constant [304]; further optimisation of such systems can yield improvements of up to an order of magnitude [202]. Early work by the author of this thesis demonstrated how these ideas could be used when applied to magnetic springs as discussed in Chapter 3 [236].

It was not until the wide-spread availability of the high energy density rare-earth magnets in the late 1970s that more complicated multipole magnetic geometries became feasible. The classic multipole array is a linear array of magnets stacked to approximate a single magnet with sinusoidal

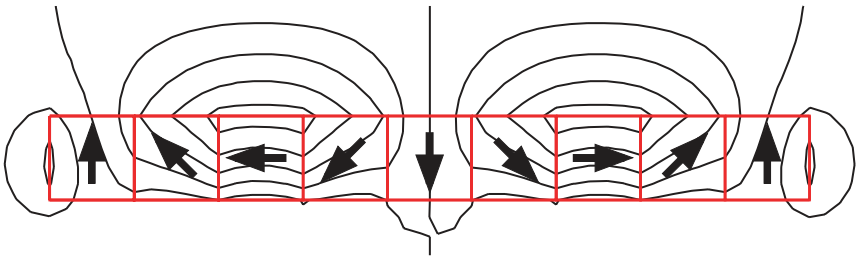

FIGURE 4.1: Magnetic field lines for a multipole array with 45° magnetisation rotations (indicated by the arrowheads). The single-sided nature of the magnet field is evident.

magnetisation, first analysed in the 1970s [120, 261].[1] The main feature of these multipole arrays is to focus the magnetic field, which can increase the magnetic flux density on one side of the array and to reduce or eliminate any need for magnetic shielding on the reverse side. The lines of magnetic flux produced by one such multipole array (calculated with ANSYS) is shown in Figure 4.1, in which the single-sided nature of the magnetic field can clearly be seen. This figure shows magnets with 45° increments of magnetisation, but any integer division of 360° is possible — indeed, irregular magnet shapes may also be used [140, 190].

To emphasise the approximately single-sided nature of these arrays, consider the three multipole arrays shown in Figure 4.2 with contours of magnetic field strength (calculated with ANSYS). The multipole arrays are arranged all in repulsion, but the top pair have their strong sides facing whereas the bottom pair have their weak sides facing. In this static arrangement, the forces between the strong pair are about 200 times stronger than the weak pair. As well as increasing the stength of the magnetic field in the desired area of use, this has the added advantage of 'shielding' external equipment from the field where the magnetic forces are not required, although there are other various possiblities to effect magnetic shielding [33]. Such inherent shielding makes these arrays particularly beneficial in maglev transportation [126], where strong, stray magnetic fields are potentially dangerous to external equipment or personnel.

An examination of the flux lines of various facing Halbach arrays shows how flux interacts between the two separate linear arrays (Figure 4.3). It can be seen that by varying the direction of magnetisation of the first magnet in

1. Multipole magnet arrays are often refered to as 'Halbach arrays' in a system approximating sinusoidal magnetisation such as shown in Figure 4.1. The more generic term 'multipole' is used in this thesis to cover both Halbach arrays and planar arrays with two dimensional magnetisation variation.

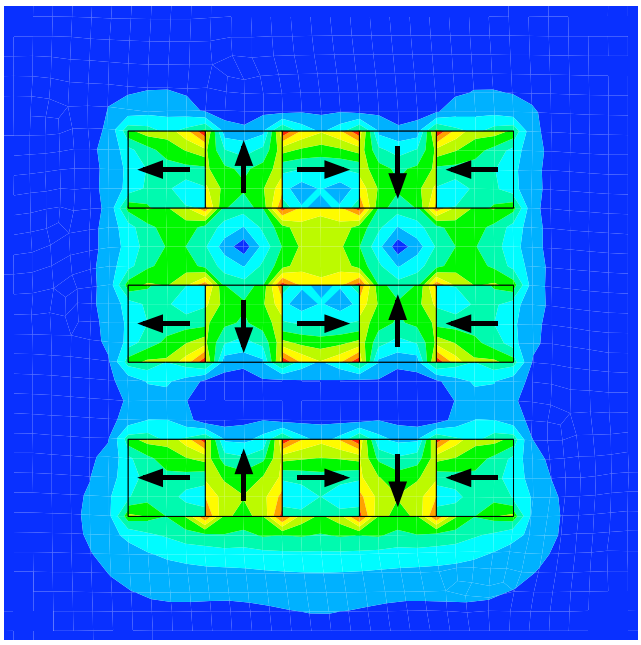

FIGURE 4.2: Opposing Halbach arrays demonstrating magnetic field strength on the strong and weak sides. Magnitude of magnetic field is shown varying from blue (weak) to red (strong).

the second array, a full range of forces can be achieved between the arrays — at the limits, total attraction or repulsion in the vertical direction, as shown in Figures 4.3(a) and 4.3(b) respectively. The variation of vertical force with horizontal displacement must therefore be carefully considered in the design of a levitation system using such multipole arrays.

Multipole arrays have been analysed for a variety of force-producing applications; one particular area that has received significant attention that will not be considered further here is for generating magnetic fields for use in rotary, linear, and planar actuations systems [71, 134, 135, 156, 172, 173, 187, 192, 282, 312]. There are a range of designs also presented for cylindrical and spherical actuator/bearing design [292, 298, 312], which is outside of the work considered in this thesis. Some of these devices use unique multipole arrangements, and in some cases these may be of interest for magnetic levitation as larger magnetic fields will produce larger magnetic forces.

Since multipole arrays usually attempt to emulate a sinusoidal magnetisation with discrete, homogeneous magnets, several authors have studied the use of triangular or trapezoidal magnets to attempt to better emulate such magnetisation [71, 72, 173, 186, 190]. The theory for calculating the magnetic fields and forces between such irregular magnet shapes is beginning

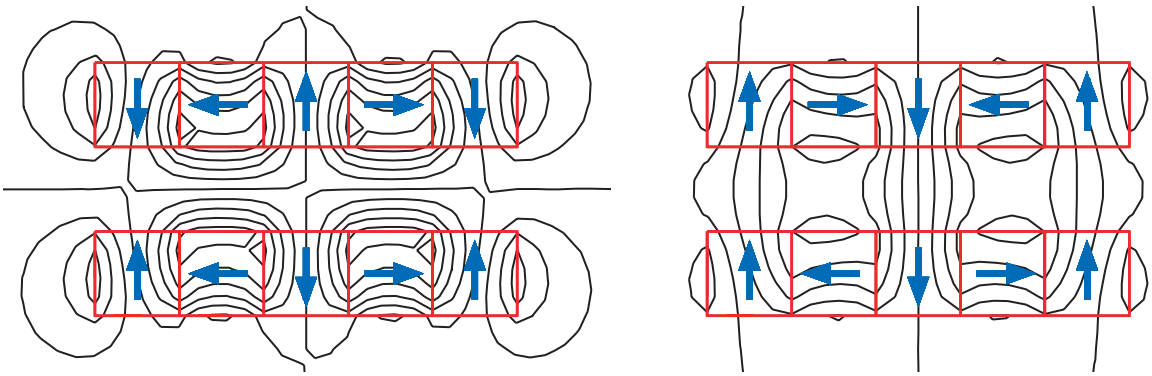

(a) In repulsion. (b) In attraction.

FIGURE 4.3: Magnetic field lines of linear multipole arrays.

to appear in the literature [140], but little work has been done to date on optimising such multipole arrays for levitation purposes.

It bears noting that the construction of these arrays can be quite difficult since the magnets are oriented in various forms of repulsion except in the case of 180° alternation. Few studies have examined the effect of these repulsive forces on the construction of the former required to hold the magnets in place [247].

In the following sections, the magnetic theory presented in Chapter 2 is abstracted for use to analyse linear and planar multipole arrays constructed of cuboid-shaped magnets. It is shown how such systems may be optimised by considering the design parameters for such arrays.

§4.2 GEOMETRY OF MULTIPOLE MAGNET ARRAYS

Having expressed the forces between two magnets with arbitrary magnetisation (§2.6.4), it becomes simple to use this expression iteratively over an array of magnets with varying magnetisation strengths or directions. The force between two arrays is simply the superposition of every combination of forces between the individual magnets in each array. While several authors have used the superposition method presented here [9, 139], this is the most detailed formalisation of the approach to date.

Some abstractions to the manner in which the iteration over each combination of magnets is performed allows us to simplify the terminology necessary to express a variety of configurations of the multiple arrays. This facilitates logical comparisons between different designs.

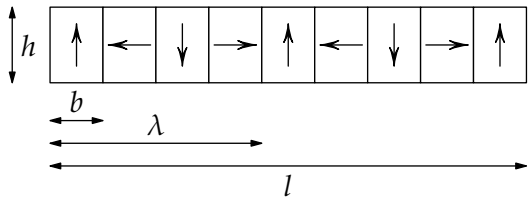

FIGURE 4.4: Geometry of a linear Halbach array with four magnets ($R = 4$) of length b per wavelength of magnetisation λ. This array contains two wavelengths of magnetisation ($W = 2$) with an end magnet for symmetry.

A multipole array can be uniquely defined in terms of several sets of variables. The simplest such description is:

- size of each magnet $[b, d, h]^\mathsf{T}$,
- number of magnets N,
- magnetisation direction of the first magnet ϑ_0 and rotation between successive magnets ϑ, and
- additional gap between adjacent magnet faces G (optional).

Other variables that can also be used to describe the array are:

- length of the array $l = bN$,
- number of magnets per wavelength $R = 2\pi/\vartheta_0$,
- wavelength of magnetisation $\lambda = bR$, and
- number of wavelengths $W = [N - 1]/R$.

Figure 4.4 illustrates the relationship between magnet length, array length, and wavelength for an example linear array. The wavelength of magnetisation is the length required to achieve, with successive magnets, a full rotation of magnetisation direction. As the number of magnets per wavelength of magnetisation R increases, the magnetisation pattern of the array more closely approximates true sinusoidal magnetisation, as shown in Figure 4.5.

Note the presence in Figures 4.1 and 4.4 and in general of an 'end magnet' that adds symmetry to the discretisation of the magnetisation. This extra magnet is necessary to balance the forces in the horizontal direction.

Provided that enough information is specified and it is internally consistent, multipole arrays can be defined in terms of any combination of the magnet and array variables when defining the geometry of each array. Rather than explicitly enumerating the location and magnetic orientation of each magnet, software written to calculate multipole array forces (Appendix A) requires just an axis with which to align the array and the facing direction of its 'strong' side. Input variables can be specified only as necessary by the user, and the unspecified properties of the multitude of magnets in the arrays can be inferred directly.

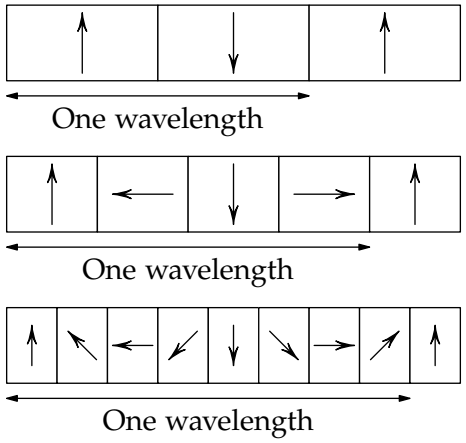

FIGURE 4.5: Three Halbach arrays of equal length, facing up, each with a single wavelength of magnetisation and composed of $R \in \{2, 4, 8\}$ magnets per wavelength respectively.

For the design of such software, however, it is not entirely straightforward to determine how a variety of specified input variables should be processed to define the unspecified ones, since the equations of constraint are not orthogonal. Using a collection of conditional statements becomes cumbersome, since many permutations of possible input variables must be accounted for. Furthermore, additions of variables to the code becomes difficult since each path through the code must be analysed and possibly edited to correspond to the overall changes. For this reason, a mathematical approach to processing input variables and calculating the unspecified ones is presented.

Since the variables considered previously are not all orthogonal, it is useful to express the coupled ones (only) as equations of constraint which need to be solved simultaneously:

$$\lambda = Rl, \qquad l = Nb, \qquad W = N/R, \qquad R = 360°/\vartheta, \tag{4.1}$$

where, for convenience, the additional end magnet (for symmetry) is omitted. Taking logarithms and writing these constraints in matrix form yields

$$\begin{bmatrix} 1 & 0 & 0 & -1 & 0 & -1 & 0 \\ 0 & 1 & 0 & -1 & -1 & 0 & 0 \\ 0 & 0 & 1 & 0 & -1 & 1 & 0 \\ 0 & 0 & 0 & 0 & 0 & 1 & 1 \end{bmatrix} \log \begin{bmatrix} \lambda \\ l \\ W \\ b \\ N \\ R \\ \vartheta \end{bmatrix} = \begin{bmatrix} 0 \\ 0 \\ 0 \\ \log(360°) \end{bmatrix} \tag{4.2}$$

This matrix can be used to compute the variables needed given sufficient inputs to define the problem. For example, say a magnet array was defined in terms of magnetisation wavelength, total length, magnets per wavelength, and number of wavelengths. In this case, the left hand side of Eq. 4.2 is separated into two matrices of specified variables

$$\begin{bmatrix} 1 & 0 & 0 & -1 \\ 0 & 1 & 0 & 0 \\ 0 & 0 & 1 & 1 \\ 0 & 0 & 0 & 1 \end{bmatrix} \log \begin{bmatrix} \lambda \\ l \\ W \\ R \end{bmatrix} = V, \tag{4.3}$$

and unspecified variables

$$\begin{bmatrix} -1 & 0 & 0 \\ -1 & -1 & 0 \\ 0 & -1 & 0 \\ 0 & 0 & 1 \end{bmatrix} \log \begin{bmatrix} b \\ N \\ \vartheta \end{bmatrix} = V^*, \tag{4.4}$$

where

$$V + V^* = \begin{bmatrix} 0 \\ 0 \\ 0 \\ \log(360°) \end{bmatrix}. \tag{4.5}$$

The unspecified variables can then be calculated by solving for V in Eq. 4.3 and for V^* in Eq. 4.5. This process is generalisable provided that the specified variables are defined sufficiently. Furthermore, in the case that more variables are specified than required, the unspecified variables will still be calculated correctly provided that the specified variables are consistent with Eq. 4.1. If the specified variables are not consistent, the solution process will fail, providing a simple method to check the validity of the input.

Using this process yields properties of the multipole arrays as defined in Eq. 4.1. As previously mentioned, it is undesirable to have an integer number of wavelengths of magnetisation in the magnet arrays such that $N = WR$ as the horizontal force between two arrays is non-zero when aligned vertically. It is preferable to achieve zero lateral force by incorporating an additional end magnet such that $N = WR + 1$. However, this equation cannot be represented in the aforementioned linear (after taking logarithms) algebra of Eq. 4.3. Therefore, these corrections are made in a separate step after the solution process has been undertaken.

§4.3 Towards optimising the forces between linear multipole arrays

Having covered the theory for representing the geometry of linear multipole arrays in Section 4.2, this section investigates the optimisation of force characteristics between linear multipole magnet arrays as a function of array size and magnet arrangement using cuboid-shaped magnets.

A linear 'Halbach array' composed of magnets with N magnets aligned along an horizontal axis is considered; planar stacks with multiple magnets in two directions will be considered in Section 4.4.

The magnetic field pattern of a multipole array is dependent on the wavelength of magnetisation λ. As the wavelength of magnetisation decreases, the total number of magnets used in the array increases, for a fixed array length l. The relationship between wavelength, array length, and number of magnets has been shown in Figure 4.4. The volume of magnetic material will be fixed, and the number of magnets will be inferred from the other specified variables. There are therefore only two independent variables to consider when choosing the parameters for a linear Halbach array of a certain size: number of magnets per wavelength R, and total number of wavelengths W in the array. Note the one extra magnet will always be included to balance the forces in the horizontal direction (shown in Figures 4.5 and 4.4) such that the total number of wavelengths $W = [l - b]/\lambda$.

§4.3.1 *Varying magnetisation discretisation and wavelength*

Consider two linear Halbach arrays of equal size with height $h = 10\,\text{mm}$, square cross section, and length $l = 100\,\text{mm}$. Their strong sides are aligned towards each other and their magnetisation pattern is such that there is a repulsive force between them. The vertical displacement between their centres is z, which can be normalised by the height of the arrays; $z/h = 1$ corresponds to the position at which the faces of the two arrays are touching. The forces between the arrays are calculated using superposition of the forces between each permutation of magnet pairs in the two arrays [9]. Results are shown in Figure 4.6 of the force versus normalised vertical displacement for number of magnets per wavelength $R \in \{2, 4, 8\}$ and number of wavelengths $W \in \{1, 2, 4\}$; these multipole forces are compared to the forces generated between a pair of magnets of homogeneous magnetisation which have the same dimensions as the multipole arrays.

For a small number of wavelengths, the discretisation of the magnetisation makes little difference to the force characteristic (Figure 4.6(a)). But as the number of wavelengths increases the number of magnets per wavelength

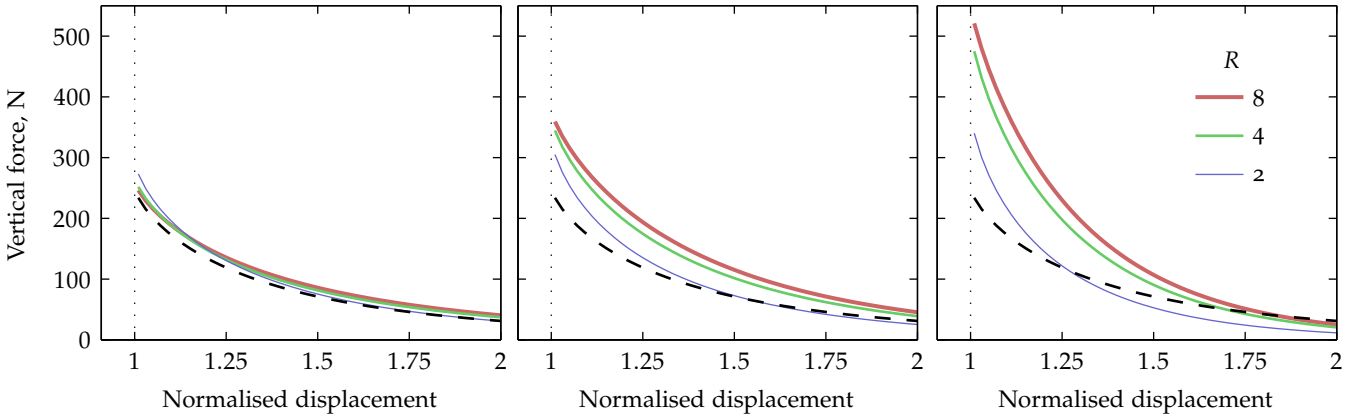

(a) $W = 1$ (b) $W = 2$ (c) $W = 4$

FIGURE 4.6: Vertical force versus displacement normalised by the array height h between two facing linear Halbach arrays with a varying number of magnets per wavelength R and a varying number of wavelengths of magnetisation W. The dashed line is the force between two single magnets of equal size to the arrays.

has an increasing effect. Increasing the number of magnets per wavelength R increases the forces over all values of displacement considered (Figure 4.6(c)).

Therefore, as a general guide, it is only necessary to use a large number of magnets per wavelength if there are at least several wavelengths in total in the array. In the results shown in Figure 4.6, the ratio in forces between $R = 2$ and $R = 4$ is greater than the ratio in forces between $R = 4$ and $R = 8$; most of the benefit of increasing the number of magnets is realised using four magnets per wavelength of magnetisation (that is, 90° rotations between successive magnets such as shown in Figure 4.4). In cases where there are many more wavelengths of magnetisation again (as shown in Figure 4.8 later), there is a greater advantage to using $R = 8$ over $R = 4$. Therefore, the greater number of wavelengths of magnetisation, the greater the force improvement realised by increasing the number of magnets per wavelength.

The use of multipole arrays can significantly affect the useful range of the force/displacement characteristic. As the number of wavelengths increases, the magnetic field of each array becomes stronger but the magnetic field lines exhibit smaller excursions outside the magnet array before returning. Thus, the forces become stronger but over a smaller displacement, and therefore the stiffness of the magnetic spring is increased as well. For some purposes and in some cases, this can be detrimental in that it can increase the resonance frequency of the system, resulting in poorer vibration isolation properties.

§4.3.2 *Constant number of magnets*

The results shown previously have in general indicated that improvements to the force characteristic are seen with a greater number of magnets. However, given a minimum magnet thickness that can be fabricated, and hence for a given array length a maximum total number of magnets, it is not clear how the compromise should be made between maximising the number of wavelengths W and the number of magnets per wavelength R. An illustration of the extremes in this case is shown in Figure 4.7, in which two multipole arrays composed of the same number and size of magnets are displayed. The first has the minimum number of wavelengths of magnetisation ($W = 1$), and the second has minimum number of magnets per wavelength ($R = 2$).

In order to investigate this compromise, consider an array of the same outer dimensions as the previous example (height $h = 10\,\text{mm}$, square cross section, and length $l = 100\,\text{mm}$) composed of magnets each of length $b = 2\,\text{mm}$ and of cross-sectional area $10\,\text{mm} \times 10\,\text{mm}$, such that there are 50 magnets in the array. The force characteristic for two of these arrays in repulsion, again with $R \in \{2, 4, 8\}$, is shown in Figure 4.8. In this extreme example with a large number of wavelengths of magnetisation W, the strong region of the field is close to the surfaces of the arrays and there is considerable difference in the curves for each number of magnets per wavelength R; maximising R produces stronger results providing there are sufficiently many wavelengths of magnetisation along the length of the array. When W is small (say $W < 5$) for a fixed magnet size, these general results do not hold and the design possibilities must be evaluated on a case-by-case basis.

§4.3.3 *Non-equal magnet sizes*

While the force characteristic of an eight-magnet wavelength ($R = 8$) array can outperform the four-magnet ($R = 4$) array, the latter can be improved in some cases by adjusting the relative sizes of the magnets in the array. Consider the four-magnet array shown in Figure 4.9 in which the horizontally-polarised magnets of length b_1 are smaller than the vertically-polarised magnets of length b_2. Magnet size ratio $\gamma = b_1/b_2$ is the measure used here to compare different array configurations, for which $\gamma = 0$ corresponds to an array composed only of vertically-oriented magnets, and $\gamma = 1$ corresponds to equally-sized magnets of both horizontal and vertical magnetisations (as considered previously in this section).

Figure 4.10 compares the force characteristic with a variety of magnet size ratios for arrays composed of nine magnets (that is, two wavelengths of magnetisation with a symmetry magnet), of length $l = 100\,\text{mm}$, and of cross-

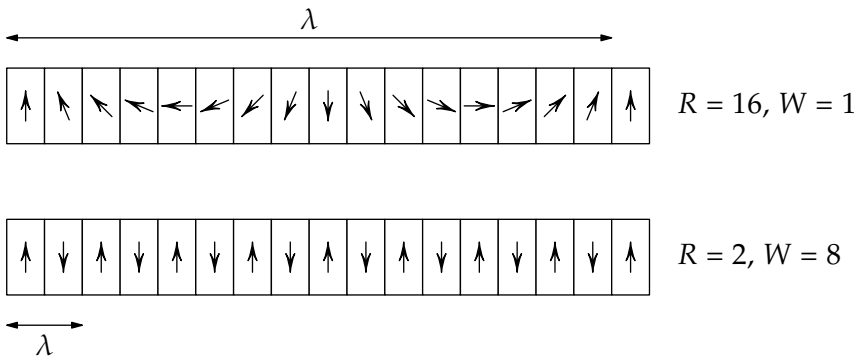

FIGURE 4.7: Two multipole arrays of equal length and number of magnets demonstrating extremes in wavelength of magnetisation W and number of magnets per wavelength R.

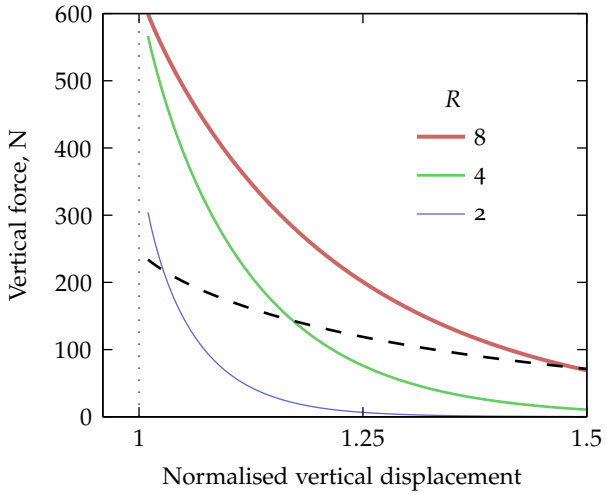

FIGURE 4.8: Force characteristic with arrays each composed of fifty magnets of length $b = 2$ mm, over a variety of number of magnets per wavelength R. The dashed line is the force between two homogeneous magnets of length 100 mm.

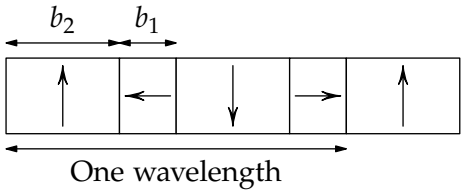

FIGURE 4.9: Schematic of a four-magnet Halbach array with variable magnet sizes. The number of magnets per wavelength $R = 4$ for all arrays of this type except in the degenerate case of $b_1 = 0$, in which $R = 2$.

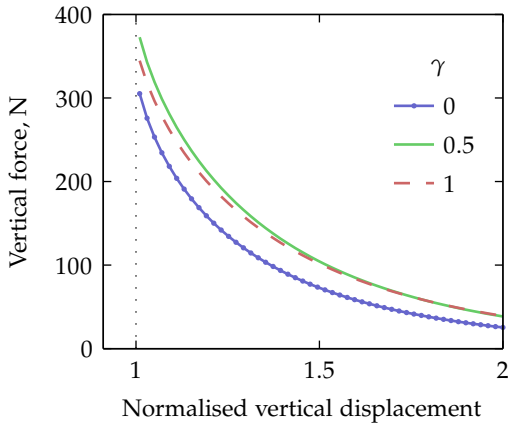

(a) Force–displacement characteristic between arrays with $W = 2$.

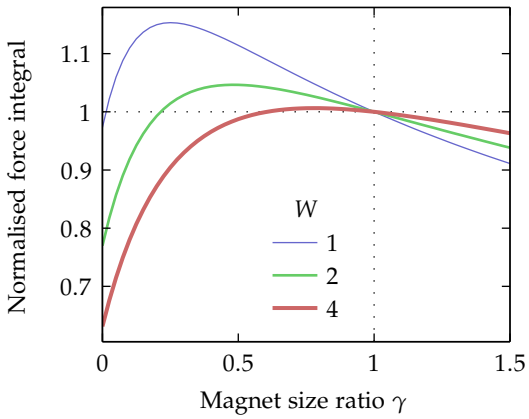

(b) Integral of the force–displacement characteristic versus magnet length ratio γ of two modified Halbach arrays.

FIGURE 4.10: Influence of the magnet length ratio γ on the force characteristics of two modified Halbach arrays in opposition over a displacement range of 10 mm to 20 mm; each array has size 100 mm × 10 mm × 10 mm.

sectional area 10 mm × 10 mm. As expected from the previous results, $\gamma = 0$ results in smaller forces than for $\gamma = 1$; however, $\gamma = 0.5$ results in slightly greater forces again: an increase of 5 % at a displacement of approximately $z = 1.3h$, tapering off as the displacement increases. (This value of γ is close to optimum for this system; see Figure 4.10.) This result can be justified intuitively with the recognition that there is a stronger vertical force between opposing vertically-polarised magnets than between horizontally-polarised magnets (Section 3.2.2 on page 82); dedicating a greater proportion of the magnet volume to the vertical magnets yields an increase in the total force.

However, as the number of wavelengths of magnetisation W increases, there is a decrease in the improvement due to reducing the size of the horizontal magnets. This can be quantified by comparing the integral of force over the displacement range of interest for a variety of magnet length ratios γ. Such results are shown for the same arrays discussed previously in Figure 4.10, comparing the relative difference of the force–displacement integral as a function of the magnet length ratio, normalised by the integral results for $\gamma = 1$. Since the force improvement with adjusting γ is only significant for low numbers of wavelength of magnetisation, this technique is only suitable for increasing the forces when a small total number of magnets are to be used. Otherwise, it is more efficient simply to increase the number of magnets than to change the magnet size ratio.

§4.3.4 *Separation between successive magnets*

In the preceding analysis, all calculations have been performed assuming that there is zero separation between successive magnets in the multipole arrays. By allowing some additional separation between the magnets, it may simplify the construction of the arrays to use a non-magnetic former, in which solid walls are used to locate and hold each magnet in place. The magnets in this case will have a small separation between their faces in the direction in which they are stacked; it is important to evaluate the influence this separation has on the generated forces.

A simulation was performed using opposing multipole arrays constructed of nine 1 T $\left[10\,\mathrm{mm}\right]^3$ cube magnets (Figure 4.11). The magnets were polarised for two wavelengths of magnetisation; additionally, a separation G was added between each successive magnet. The force–displacement characteristic was calculated for the arrays while varying the separation distance G (Figure 4.12). The results are presented in terms of normalised vertical displacement z/h and normalised separation distance G/b.

Even comparatively thin wall thicknesses compared to the magnet size have a noticeable effect on the forces generated at small vertical displacements z between the arrays. The far-field forces are less affected, implying for large multipole array structures it is indeed suitable to add a magnet separation using a nonmagnetic former to set the magnets in place. As shown in the figure, however, once the separation distance becomes large enough, it is better to simply use opposing magnets; the magnet separation is so large that the magnetic interaction between the magnets is limited to the directly opposing pairs. Since the magnetic force between opposing parallel magnets is less than anti-parallel opposing magnets (§3.2.2 on page 82), this arrangement results in smaller forces than having a set of widely spaced magnets all magnetised in the same direction (Figure 4.13).

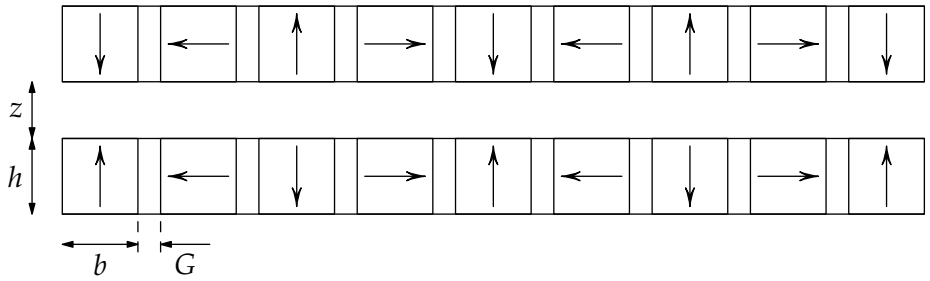

FIGURE 4.11: Opposing multipole arrays with magnet separation G.

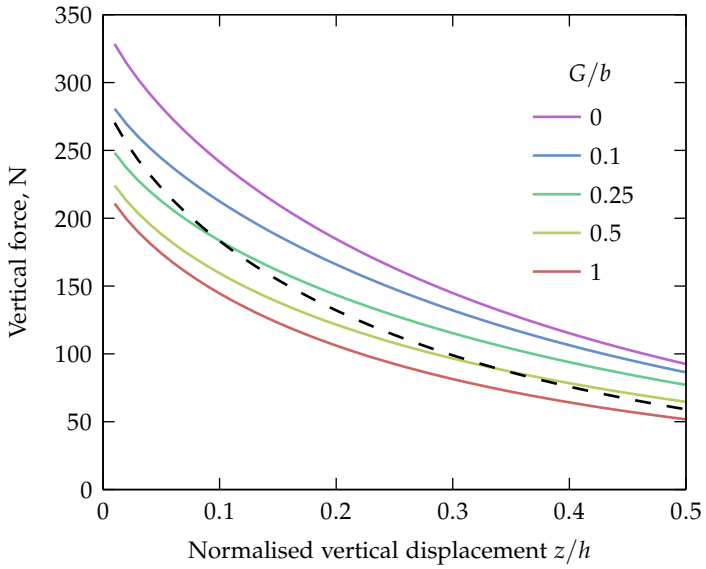

FIGURE 4.12: The effect of magnet separation G on the force characteristic of multipole arrays composed of nine cube magnets (Figure 4.11). The dashed line is the force between an equivalent number of equally-sized and non-interacting pairs of magnets in repulsion (limiting case of Figure 4.13(b) as $G \to \infty$).

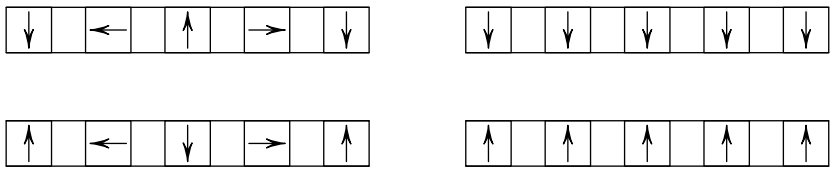

(a) Multipole configuration. (b) Homogeneous configuration.

FIGURE 4.13: Opposing multipole arrays with too large a separation. In this case the second pair of arrays produces the greater forces since the magnets are too widely spaced to obtain the advantages of the multipole configuration.

Conclusion to analysis of linear multipole arrays

In conclusion, in optimising the forces between linear Halbach magnet arrays, it has been shown that there is an effect on the force versus displacement characteristic from both the wavelength of magnetisation and the number of magnets in the array. While keeping the array length constant, decreasing the wavelength of magnetisation increases the number of magnets per wavelength. In order to achieve significantly larger forces over homogeneous magnetisation, a large number of magnets should be used. When only a small number of magnets are used, small increases in the forces can be achieved by using magnets of non-uniform size.

The analysis undertaken in this section has demonstrated some design principles for multipole arrays for a certain aspect ratio. There is still scope for further analysis of the force behaviour between multipole arrays of varying height-to-width (and perhaps height-to-wavelength) aspect ratios.

§4.4 Planar multipole arrays

In Section 4.3, linear multipole arrays were considered in some detail for increasing magnetic spring forces. The term 'linear' is used to indicate that magnetisation is varying as a function of position in a single direction. Using the magnet theory covered in Section 2.6.4 on page 65, it is also possible to calculate the forces between magnet arrays with magnetisation as a function of position in two directions.

Planar multipole arrays consist of a two dimensional stack of magnets that vary in magnetisation as a function of their position. There are a number of different arrangements that have been considered; in the section to follow only those which use cuboid magnets are discussed due to the difficulty in analysing the forces between non-cuboid magnets.

The simplest case is the result of 180° magnetisation rotations in each direction [71, 154]. The resultant magnetisation pattern looks like a checkerboard or 'patchwork' (Figure 4.14(a)). From the analysis performed on linear multipole arrays in the previous section, it can be expected that the patchwork design, with only two magnets per wavelength of magnetisation, will produce smaller forces than could be achieved with an alternate design.

Using cuboid magnets with 0° or 90° magnetisation directions is advantageous in that the magnets are readily available. Several authors have examined the 'quasi-Halbach' planar multipole array, shown in Figure 4.14(b), in which all magnetisation directions are restricted to one of the orthogonal directions of the axes [139, 203, 247]. Due to the symmetry of the pattern,

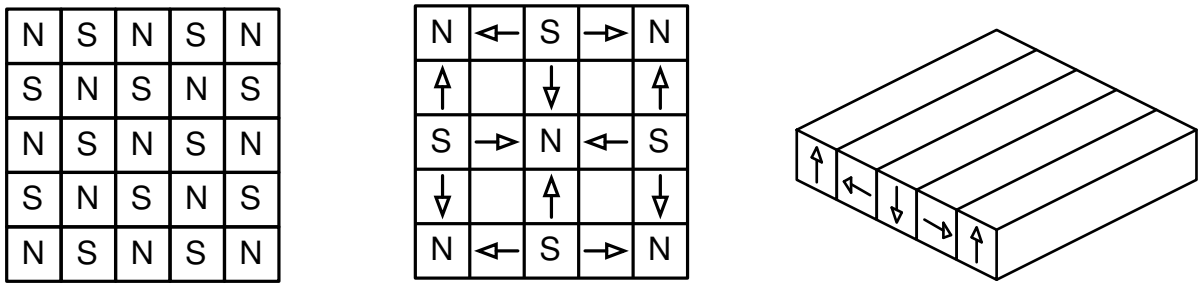

(a) Patchwork array, top view. (b) Quasi-Halbach array, top view. (c) Linear Halbach array.

FIGURE 4.14: Three planar multipole array designs, with strong sides facing 'towards the reader' for the first two and 'up' for the third. Note the (unfilled) areas of zero magnetisation in the quasi-Halbach array.

there are regions within this multipole array of zero magnetisation.

A more complex arrangement can be constructed by using superposition of orthogonal linear multipole arrays [154, Appendix A]. Such a system, called here a 'planar Halbach' array, is shown in Figure 4.15, with five magnets per side and 90° magnetisation rotation in both the $\hat{x}$–$\hat{z}$ and $\hat{y}$–$\hat{z}$ planes between successive magnets. This design requires magnets with 45° magnetisation directions; it is possible to consider superimposing designs with a greater number of magnets per wavelength to achieve even more complex magnetisation patterns.

Recent work in this area has suggested more complex structures for optimising the field strength or repulsion force generated by planar arrays, including using three dimensional variations in magnetisation [72, 73], triangular as well as rectangular cross-section magnets [71], and using pyramidal-frustum-shaped magnets [140, 173] to stack with less empty space than the planar- or quasi-Halbach arrays. A variation on the planar- and quasi-Halbach array has also been suggested [192]. There is insufficient scope in the current study to compare the broad range of possibilities available. An example is shown demonstrating a simple comparison between the more straightforward arrays.

§4.4.1 *Equations describing planar magnetisation patterns*

Planar magnet arrays are composed of $N_x \times N_y$ magnets each with magnetisation vector $\mathbf{M}_{ij}$ for $i \in \{1 \dots N_x\}$ and $j \in \{1 \dots N_y\}$. The planar designs have periodic magnetisations as functions of i and j, which are described in what follows in terms of normalised magnetisation $\hat{\mathbf{M}} = \mathbf{M}/B_r$, where B_r is

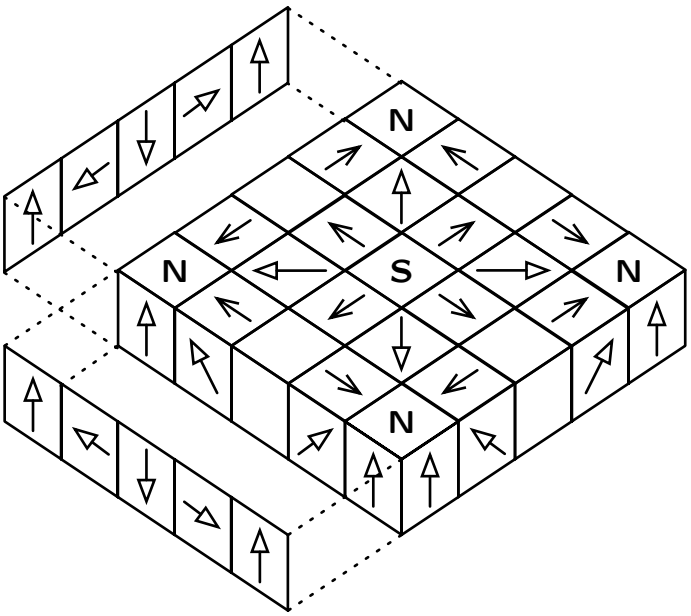

FIGURE 4.15: A planar Halbach array, facing up, with magnetisation directions as the superposition of two orthogonal linear Halbach arrays. Non-filled arrowheads denote diagonal magnetisation and empty magnets have zero magnetisation.

the remanence magnetisation of the magnet. For example, the normalised magnetisation of a homogeneous magnet aligned vertically facing up would be $\hat{\mathbf{M}} = [0, 0, 1]^{\mathsf{T}}$. In the equations to follow, the arrays are assumed to be aligned in the $\hat{x}$–$\hat{y}$ plane with their magnetic field extending largely into the $+\hat{z}$ direction (that is, facing 'up'); for arrays facing down in the $-\hat{z}$ direction, the normalised magnetisation in the $\hat{z}$ direction should have reversed sign.

Patchwork array

The patchwork array is only magnetised in the out-of-plane direction.

$$\hat{\mathbf{M}}(i,j) = \begin{bmatrix} 0 \\ 0 \\ \cos(i\pi)\cos(j\pi) \end{bmatrix} = \begin{bmatrix} 0 \\ 0 \\ [-1]^{i+j} \end{bmatrix}. \tag{4.6}$$

Linear Halbach array

A linear Halbach array has homogeneous magnetisation along one horizontal direction; in this case, the array is chosen to vary magnetisation along the $\hat{x}$

TABLE 4.1: Calculated normalised magnetisation vectors using Eq. 4.7 for the linear Halbach array shown in Figure 4.14(c).

i	$\vartheta_0 + \vartheta\left[i-1\right]$	$\hat{\mathbf{M}}^\mathsf{T}$
1	90°	[0, 0, +1]
2	180°	[−1, 0, 0]
3	270°	[0, 0, −1]
4	0°	[+1, 0, 0]
5	90°	[0, 0, +1]

direction (that is, $N_y = 1$).

$$\hat{\mathbf{M}}(i) = \begin{bmatrix} \cos\left(\vartheta_0 + \vartheta\left[i-1\right]\right) \\ 0 \\ \sin\left(\vartheta_0 + \vartheta\left[i-1\right]\right) \end{bmatrix}, \tag{4.7}$$

where ϑ_0 is the magnetisation direction of the first magnet in the $\hat{x}$–$\hat{z}$ plane and ϑ is the magnetisation rotation per magnet. For example, for the linear Halbach array shown in Figure 4.14(c) where $\vartheta_0 = 90°$, $\vartheta = 90°$, and $N_x = 5$ (and $i = 1$ starts from the left), the normalised magnetisation vectors for each magnet are shown in Table 4.1.

Planar Halbach array

In the planary Halbach array, the *directions* of magnetisation are found from the superposition of two orthogonal linear Halbach array magnetisations,

$$\hat{\mathbf{M}}(i,j) = \begin{bmatrix} \cos\left(\vartheta_{xz} + \vartheta\left[i-1\right]\right) \\ \cos\left(\vartheta_{yz} + \vartheta\left[j-1\right]\right) \\ \sin\left(\vartheta_{xz} + \vartheta\left[i-1\right]\right) + \sin\left(\vartheta_{yz} + \vartheta\left[j-1\right]\right) \end{bmatrix}, \tag{4.8}$$

where ϑ_{xz} and ϑ_{yz} are the directions of magnetisation of the initial magnet in the $\hat{x}$–$\hat{z}$ and $\hat{y}$–$\hat{z}$ planes, respectively. However, as written this results in certain magnets having greater than unity normalised magnetisation, which implies that stronger than regular magnets would be required. Therefore, care must be taken when using this equation to ensure that the magnetisation vectors for each magnet in direction $\hat{\mathbf{M}}(i,j)$ have constant magnitude B_r.

Quasi-Halbach array

Finally, for simplicitly assume for the quasi-Halbach array that the magnetisation vector for the initial magnet is in the $+\hat{z}$ direction as shown in

Figure 4.14(b) (bottom left corresponds to $i = j = 1$). The magnetisation function for each magnet in the array is given by

$$\hat{\mathbf{M}}(i,j) = \begin{bmatrix} \sin\left(\frac{1}{2}\pi i\right)\cos\left(\frac{1}{2}\pi j\right) \\ \cos\left(\frac{1}{2}\pi i\right)\sin\left(\frac{1}{2}\pi j\right) \\ \sin\left(\frac{1}{2}\pi i\right)\sin\left(\frac{1}{2}\pi j\right) \end{bmatrix}. \tag{4.9}$$

§4.4.2 *Example comparison between planar arrays*

When pairs of arrays are faced in opposition, a vertical force is produced between them that can be larger than the corresponding force between two equivalently-sized magnets with homogeneous magnetisation. Each array configuration has a different magnetic field pattern and has a different force/displacement profile. Force–displacement characteristics for the quasi-Halbach array have been shown recently [139] but it should be noted that an analysis of the forces generated between planar Halbach arrays has not yet been shown in the literature. Since the planar Halbach array uses magnetisations in directions non-orthogonal to its axes, the necessary calculations contain more terms than for the quasi-Halbach array.

The vertical force versus vertical displacement characteristics of each array considered (linear Halbach, planar Halbach, patchwork, and quasi-Halbach) are compared in Figure 4.16, all with the same array size and volume. The linear Halbach, planar Halbach, and quasi-Halbach have all been chosen to have a single wavelength of magnetisation with an end magnet for symmetry. The linear Halbach array follows the same arrangement analysed in Section 4.3 with long sides in the axis orthogonal to the plane of magnetisation (Figure 4.14(c)). The forces between two single magnets (of the same size as the arrays) are included for comparison. Each array has the same outer dimensions of 50 mm × 50 mm, thickness 10 mm, and is composed of magnets with magnetisation 1 T, and each magnet is either cube-shaped or, for the linear array, has a square cross-section.

It is interesting that the linear array exhibits the greatest force for a given displacement; this can be explained by the fact that the planar array and the quasi-Halbach array both have regions of zero magnetisation; this degrades their load-bearing ability since there is less inherent magnetic energy in each. These results indicate that for this comparison the linear Halbach array is the most suitable choice for bearing vertical loads; not only are the forces stronger, but the magnetisation arrangement (and hence construction of the array) is simpler as well.

It is also notable that despite the much simpler magnetisation pattern of the quasi-Halbach array compared to the planar Halbach array, the results

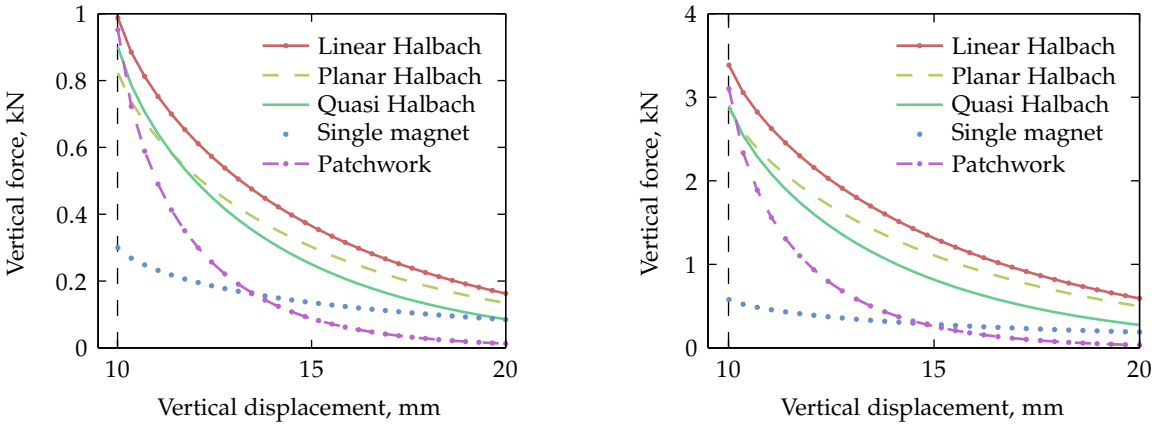

(a) 5 × 5 magnets; face area 50 mm × 50 mm.

(b) 9 × 9 magnets; face area 90 mm × 90 mm.

FIGURE 4.16: Vertical forces versus vertical displacement between the array centres to compare the load-bearing ability of a range of magnet arrays. Two sizes of array are compared, each composed of multiple 10 mm 1 T cube magnets. The dashed vertical line indicates the displacement at which the array faces are in contact.

for these two are quite similar, especially at small displacements. For these two arrays, greater forces can be achieved by reducing the amount of non-magnetised material in the design. For the quasi-Halbach design, this can be performed by using a non-uniform magnet size as analysed for the linear case (§4.3.3). Greater improvements than for the linear case can be expected for the planar array as decreasing the magnet size ratio also decreases the amount of non-magnetic material in the design [139, 247]. For the planar Halbach array, the volume of non-magnetic material can be decreased by using a larger number of magnets per wavelength, albeit with an increase in the number of unique magnetisation directions required for each magnet in the array.

Finally, it is not strictly fair to compare the patchwork array to the others in this manner since the wavelengths of magnetisation differ between the arrays. In all cases, optimisation of the magnet forces for this particular array volume and/or aspect ratio could be considered separately and different results may be seen. Janssen et al. [138] have also shown the advantages of using pairs of magnet arrays in which the floating array is composed of smaller magnets with different magnet separation than in the fixed array.

It must be noted that these results differ from the experimental results of diamagnetic levitation [203] and from another theoretical study which uses an alternate theory for calculating the forces [53]. It is possible that the

effect on the magnetisation of each magnet due to the magnetic field of the other magnets in the array, which is assumed to be negligible, actually has a measureable effect in practice. These differences highlight the need to study these systems in more detail outside of the realm of theoretical analysis.

§4.4.3 *Forces due to horizontal displacement*

The sensitivity of multipole arrays to horizontal displacement, such as shown in Figure 4.17, is an important consideration for levitation purposes. For homogeneous magnets, the coupling between horizontal displacement and vertical force was shown to be relatively small (§3.2.5). For multipole arrays, it is dependent largely on the wavelength of magnetisation; the smaller that it is, the more cross-coupling there will be.

The characteristic of this cross-coupling varies significantly between array designs. An example of this is shown in Figure 4.18 for three multipole arrays under horizontal displacement with total size 50 mm × 50 mm × 10 mm, four 1 T magnets per wavelength of magnetisation, and fixed $z = 15$ mm vertical displacement between the array centres. Since the linear Halbach array is the only array considered which is not symmetrical in the horizontal plane, the vertical forces are considered due to displacements in both $\hat{x}$ and $\hat{y}$ directions (Figures 4.18(a) and 4.18(b)). The planar Halbach and the quasi-Halbach coupling characteristics (Figures 4.18(c) and 4.18(d)) are calculated due to horizontal displacement y in the $\hat{y}$ direction only; the results are identical in the $\hat{x}$ direction.

The horizontal coupling behaviour for the linear Halbach design is significant in that the negative stiffness in the 'out-of-plane' $\hat{x}$ direction (orthogonal to the plane of magnetisation) is less than in the $\hat{y}$ direction. Comparing these results to the planar and quasi-Halbach arrays, the negative stiffness for those (equal in each direction) is approximately mid-way between the two negative stiffnesses in each direction of the linear Halbach array. Relatedly, the horizontal forces for the planar and quasi-Halbach arrays are around half

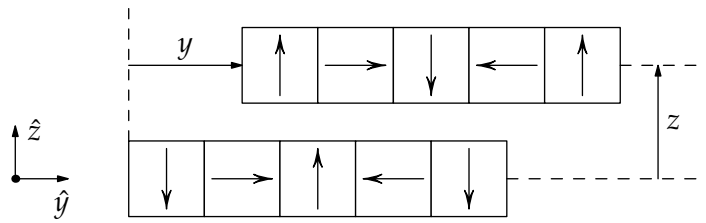

FIGURE 4.17: Linear multipole system with five magnets (end view) depicting horizontal displacement y and vertical displacement z between the array centres.

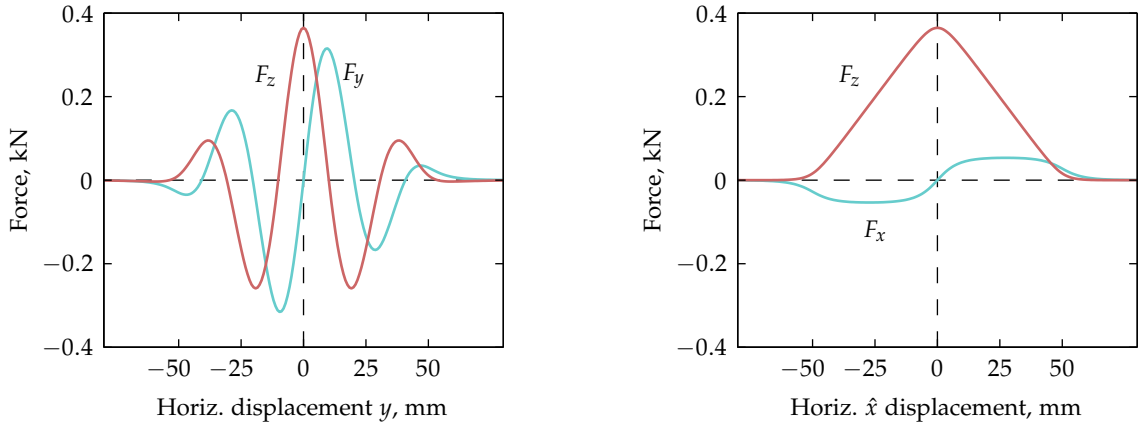

(a) Linear Halbach arrays.

(b) Linear Halbach arrays, $y = 0$ (out-of-plane).

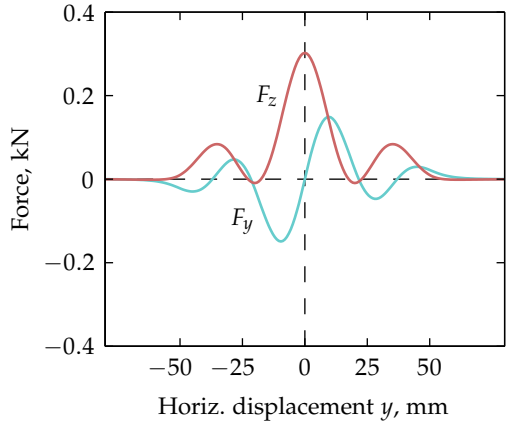

(c) Planar Halbach arrays.

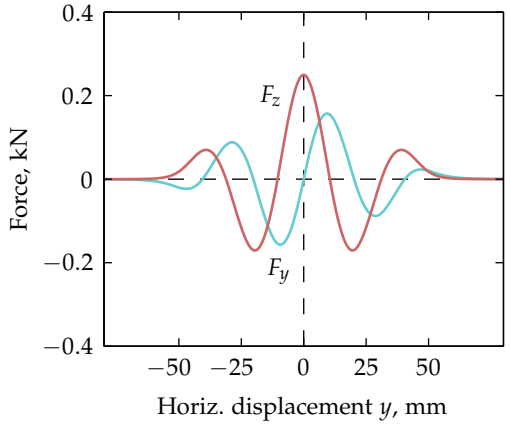

(d) Quasi-Halbach arrays.

FIGURE 4.18: Force versus horizontal displacement results between linear and planar multipole arrays of total size 50 mm × 50 mm × 10 mm. Vertical displacement $z = 15$ mm; the $\hat{x}$ forces are all zero.

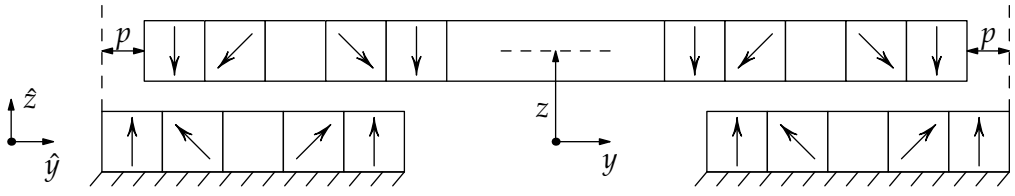

FIGURE 4.19: Double 5 × 5 planar Halbach design in which complementary horizontal offsets p are imposed to decrease the cross-coupling stiffness. Side-view shown; see Figure 4.15 for the isometric view of a single planar Halbach array.

the magnitude of the vertical forces, whereas for the linear Halbach array the forces in the $\hat{y}$ direction are close to the magnitude of the vertical forces.

It is interesting to note that the vertical force for the planar Halbach array is largely positive, even as the arrays shift by half a wavelength, whereas the linear Halbach and quasi-Halbach forces are more symmetric and become significantly negative under a similar displacement. The effect of this is that the vertical force peak for the planar Halbach array is broader than the others, which will therefore be more suitable for cases where some horizontal displacement is expected and the vertical force variation must be minimised.

In fact, since the planar Halbach array has the broadest peak, this suggests that adding multiple pairs of planar Halbach arrays to a system with certain horizontal offsets (Figure 4.19) may allow a decrease in the amount of cross coupling in the system. Force results for such a system are shown in Figure 4.20 for a relative offset of 90% of one magnet width (chosen by trial-and-error in this case but could be chosen using an optimisation routine). With a net doubling of the total magnet volume, the vertical load bearing capacity is unchanged; however, the variation of the load force with horizontal displacement is significantly decreased. Such a system has an increased working range of horizontal displacement before force cross-coupling becomes an issue.

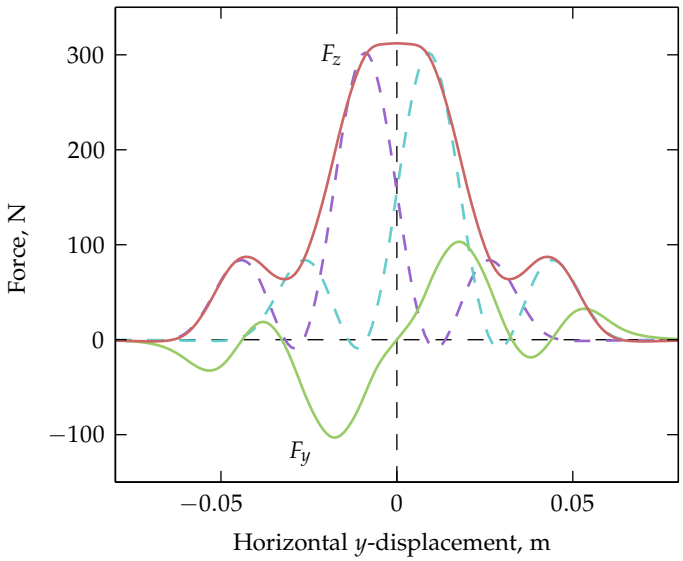

FIGURE 4.20: Force versus horizontal displacement results between a pair of double-Halbach multipole arrays (Figure 4.19) with an offset p of 90 % of one magnet width. Dashed lines show the vertical force contribution by each individual planar Halbach array.

§4.5 Conclusions on multipole arrays

This chapter contains material touching on the diverse field of multipole magnetic arrangements and formalising the theory for calculating forces between multipole arrays using cuboid magnets with arbitrary magnetisations. The theory presented in previous chapters was abstracted for the purposes of analysing multipole arrays, and analysis was performed on linear and planar 'Halbach arrays' for assessing their potential for increasing the load-bearing capacity of a magnetic spring. Differences with results in the literature suggests further experimental work should be conducted to establish shortcomings in the theory used for numerical simulations.

The parameters for designing the multipole arrays are critical in achieving useful improvements, and there are certain caveats with using such designs. Primarily, it must be noted that multipole designs will be more sensitive to lateral displacements, leading to higher levels of cross-coupling instability than homogeneous magnets. Multipole arrays are best used for devices with restricted degrees of freedom or sufficient control authority for stabilising the inherent instabilities in the device. Nonetheless, it has been shown that it is possible to increase the region of useable horizontal mobility using 'offset' pairs of Halbach arrays.

CHAPTER 5

Electromagnetic actuators

The work presented in Sections 5.2.1 and 5.3 is based on material that has been published as a journal paper [242].

§5.1 Introduction

The field of electromagnetic actuators spans a large variety of applications. The oldest of these is the voice-coil loudspeaker, which is an area still undergoing continued refinement. In the introduction of this thesis, a variety of other electromagnetic devices were discussed including planar and multi–degree of freedom actuators (§1.3.2). In Chapter 2 the theory was summarised for calculated forces between permanent magnets; many of these methods used a modelling technique in which a permanent magnet is represented as a surface current density around the circumference of the magnet. This theory also covers, therefore, the case where the force between a magnet and a coil is under investigation, provided that the coil being modelled can also be represented as an infinitely thin current density. This is the case only for 'thin' coils consisting of one (or a small number of) windings deep.

The equivalence of the current surface density model for permanent magnets and thin coils means the same approach can be used to model both systems, as seen in the work for calculating the force between two thin coils or magnets [21, 231, 241] summarised in Section 2.7.

The theory discussed in this section is based around an integral expression with an efficient numerical implementation for calculating the axial force between a coaxial cylindrical magnet and a 'thick' solenoid that consists of many turns both radially and axially. This integral expression is compared against a variety of other methods.

Electromagnetic actuators play an important part in magnetic quasi–zero stiffness systems, as it is common to apply non-contact forces for stiffness tuning, vibration control, and/or stability control. The motivation for this study arose when designing the custom actuator for the prototype quasi–zero stiffness device developed in Chapter 7; it became clear that design guidelines for coil–magnet actuators were scarce or non-existent.

In this chapter, a simple electromagnetic actuator is analysed in detail, using detailed coil force equations that have only recently been available.

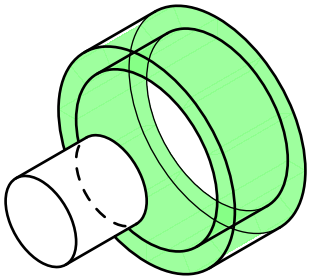

FIGURE 5.1: Three-dimensional sketch of the system composed of a permanent magnet (unshaded, left) and thick coil (shaded, right). The magnet can be modelled as an equivalent cylindrical surface current density, and the coil as a volumetric current density.

The design of a 'sleeve coil actuator' is considered in which a magnet of a certain volume moves inside a fixed coil of a certain impedance, with the objective to optimise the geometric parameters to maximise the peak force of the actuator (although other metrics are also possible). Only the quasi-static force/displacement characteristics are considered; in other words, any effects caused by induced currents from the moving magnet are neglected, which could affect the high-frequency behaviour of the device.

A new equation is developed for calculating the force between cylindrical coils and magnets with eccentric displacement. The analysis herein of a single degree of freedom actuator shows that it can be possible to optimise coil size, magnet size, and wire diameter to achieve a given force maximum. Other cost functions can be used in the design methodology to achieve other metrics, such as linearity [191]. Finally, an example of an alternate 'dual-coil' electromagnet design is provided, which based on the modelling results is shown to achieve greater forces than a single-coil design, all else being equal.

§5.2 CYLINDRICAL MAGNET AND THICK COIL SYSTEMS

The system under investigation is shown in Figures 5.1 and 5.2. In this study there is no restriction on the size or geometry of the magnet or coil. To describe the geometry of the magnet–coil configuration, two aspect ratios are defined for the magnet and coil respectively. The 'magnet ratio' is given by the ratio between length and radius for the magnet, $\alpha = L_m/R_m$, and the 'coil ratio' similarly by the ratio between coil length and inner radius, $\beta = L_c/r_c$. The clearance (or gap) between the inner coil and magnet radii is denoted $r_g = r_c - R_m$.

The coil may have many turns in both axial and radial directions; denote

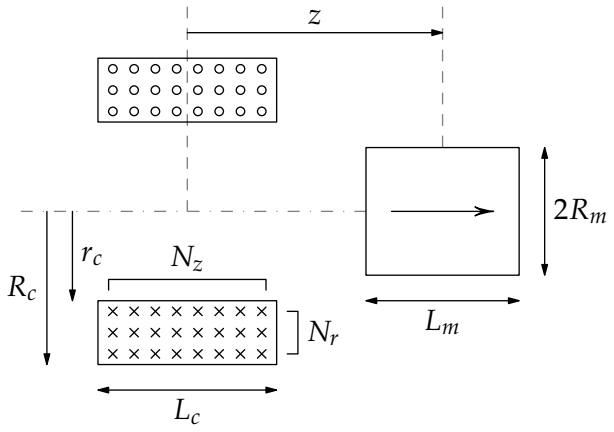

FIGURE 5.2: Schematic of a 'sleeve coil' magnetic actuator. This geometry can be described in terms of magnet ratio $\alpha = L_m/R_m$ and coil ratio $\beta = L_c/r_c$. Circles and crosses represent coil windings out from and into the page, respectively.

N_z the number of turns axially and N_r the number of turns radially. Such a coil will have $N = N_z \times N_r$ turns in total, and assuming the turns are packed equally in both directions the coil will have a volume current density of $NI/\left[L_c\left[R_c - r_c\right]\right]$, where I is the current passing through the coil.

The permanent magnet is assumed to have a sufficiently large coercivity such that its magnetisation strength will not be affected by the magnetic field of the coil. The permanent magnet is also assumed to be homogeneous with a constant magnetisation strength B_r in the axial direction only.

§5.2.1 *Thick-coil/magnet axial force methods*

In this section, the theory for calculating the interaction force between the thick coil and permanent magnet (Fig. 5.1) will be discussed. In the first two force calculation methods, denoted 'filament' and 'shell', the coil and/or magnet are modelled in terms of discrete elements (such as single-turn or thin coils) for which the interaction forces may be summed through superposition of each combination of elements. The final method uses a single integral expression to calculate the force, and two formulations and solutions for this integral are discussed. The shell method and the first integral method were developed as part of the current study; the other two methods are taken from the literature, examined for comparison.

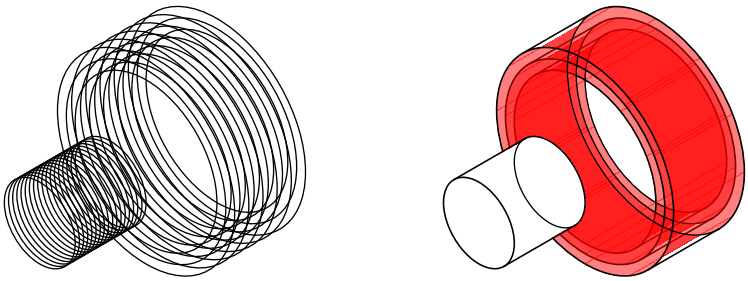

(a) Filament model. (b) Shell model.

FIGURE 5.3: Schematics of the filament and shell models. In the filament model, the magnet and thick coil are modelled with individual current loops. In the shell model, the magnet is modelled as a cylindrical surface current density and the thick coil is modelled as a number of individual concentric surface current densities to represent multiple windings in the radial direction.

The filament method

For two circular coaxial loops (that is, a single turn of a solenoid) carrying currents I_1 and I_2 respectively, the axial force between them is given by [260]

$$F_f(r_1, r_2, z) = \mu_0 I_1 I_2 z \sqrt{\frac{m}{4r_1 r_2}} \left[K(m) - \frac{m/2 - 1}{m - 1} E(m) \right], \tag{5.1}$$

where

$$m = \frac{4r_1 r_2}{\left[r_1 + r_2\right]^2 + z^2}, \tag{5.2}$$

where r_1 and r_2 are the coil radii and z is the axial distance between the coils. The functions $K(m)$ and $E(m)$ are the complete first and second elliptic integrals, respectively, with parameter m. These functions are also referred to elsewhere in the literature with notation $K(k)$ and $E(k)$ in terms of the modulus k, where $m = k^2$.

Using the 'filament method' [for example, 7, 21], Eqs 5.1 and 5.2 can be used to calculate the force between any arrangement of coaxial solenoids by representing each turn of the solenoid as a separate coil, and summing the forces through superposition for every pair-wise combination of coil interaction forces. Figure 5.3 shows such a filament model for the interaction between a thin coil (representing a permanent magnet) and a thick coil. Using this technique, the total force between them is given by

$$F_{c1} = \sum_{n_m=1}^{N_m} \sum_{n_r=1}^{N_r} \sum_{n_z=1}^{N_z} F_f(r(n_r), R_m, z + L(n_m, n_z)), \tag{5.3a}$$

$$r(n_r) = R_c + \frac{n_r - 1}{N_r - 1}\left[R_c - r_c\right], \tag{5.3b}$$

$$L(n_m, n_z) = -\frac{1}{2}\left[L_m + L_c\right] + \frac{n_z - 1}{N_z - 1}L_c + \frac{n_m - 1}{N_m - 1}L_m, \tag{5.3c}$$

where R_m is the magnet radius, r_c and R_c are the inner and outer coil radii, L_m and L_c are the magnet and coil lengths, z is the axial distance between their centres, N_r and N_z are the number of turns in the thick coil in the radial and axial direction, and N_m is the number of turns in the thin coil. The filament current $I_1 = I$ is the current in the thick coil. The arrangement of 'turns' used to model the permanent magnet is related to an equivalent surface current density with current per turn of $I_2 = B_r L_m / \left[N_m \mu_0\right]$ and permanent magnet strength B_r. The number of 'turns' N_m used to model the permanent magnet should be chosen to be sufficiently large such that the resultant force converges to a stable value.

The shell method

In the 'shell method' developed here, a thick solenoid and a magnet may be modelled by representing each radial layer of turns as a separate thin coil with surface current density $1/N_r$, the volume current density. The force between them is calculated by summing the forces through superposition of the forces between each thin coil and the magnet:

$$F_{c2} = \frac{1}{N_r}\sum_{n_r=1}^{N_r} F_z(R_m, r(n_r), L_m, L_c, z) \tag{5.4}$$

$$r(n_r) = r_c + \frac{n_r - 1}{N_r - 1}\left[R_c - r_c\right] \tag{5.5}$$

where $F_z(R_m, r, L_m, L_c, z)$ is the force between a permanent magnet and a thin coil, shown previously in Eq. 2.69 on page 76, in which $B_{r1} = B_r$ is the strength of the permanent magnet and $B_{r2} \equiv \mu_0 N_z I / L_c$, where I is the current in the coil.

An integral method

An integral expression for the force between a solenoid and magnet is derived using the theory of Furlani [106]. Here it has been assumed that the solenoid can be modelled as a volume current density and the permanent magnet is modelled as a surface current density around its circumference. A solenoid

with current volume density $\mathbf{J}$ generates a magnetic field $\mathbf{B}$ at a displacement $\mathbf{d}_1$ given by the integral over the coil volume V_c

$$\mathbf{B}(\mathbf{d}_1) = \frac{\mu_0}{4\pi} \int_{V_c} \frac{\mathbf{J}(\mathbf{d}_2) \times \left[\mathbf{d}_2 - \mathbf{d}_1\right]}{\left|\mathbf{d}_2 - \mathbf{d}_1\right|^3} \, \mathrm{d}v_c \,, \tag{5.6}$$

where $\mathbf{d}_2$ is the distance vector to the differential coil volume $\mathrm{d}v_c$. The vector force $\mathbf{F}$ due to that field on a permanent magnet with magnetisation vector $\mathbf{M}$ is given by the integral over the magnet surface S_m with normal vector $\hat{\mathbf{n}}$

$$\mathbf{F} = \oint_{S_m} \left[\mathbf{M} \times \hat{\mathbf{n}}\right] \times \mathbf{B}(\mathbf{d}_1) \, \mathrm{d}s_m \,, \tag{5.7}$$

where $\mathbf{d}_1$ is the distance vector to the differential magnet surface $\mathrm{d}s_m$. Following the magnetic field expression in polar coordinates shown by Ravaud et al. [230] and taking only the axial component of the force results, Eq. 5.7 is written in full as a function of axial displacement z as

$$\begin{aligned} F_{c3}(z) = \frac{B_r N I}{L_c \left[R_c - r_c\right]} \int_{-L_c/2}^{L_c/2} \int_0^{2\pi} \int_{r_c}^{R_c} \int_{z-L_m/2}^{z+L_m/2} \int_0^{2\pi} \\ \frac{r_1 r_2 \left[r_2 - r_1\right] \cos\left(\phi_2 - \phi_1\right)}{\left|\mathbf{d}_2 - \mathbf{d}_1\right|^3} \, \mathrm{d}\phi_1 \, \mathrm{d}z_1 \, \mathrm{d}r_2 \, \mathrm{d}\phi_2 \, \mathrm{d}z_2 \end{aligned} \tag{5.8}$$

where

$$\left|\mathbf{d}_2 - \mathbf{d}_1\right| = \sqrt{r_1^2 + r_2^2 - 2 r_1 r_2 \cos\left(\phi_1 - \phi_2\right) + \left[z_2 - z_1\right]^2} \,. \tag{5.9}$$

Analytically integrating this equation in variables ϕ_1, ϕ_2, and z_1 yields

$$F_{c3} = \frac{B_r N I}{L_c \left[R_c - r_c\right]} \int_{-L_c/2}^{L_c/2} \int_{r_c}^{R_c} \sum_{e_1}^{\{1,-1\}} \left[e_1 m_6 f_{c_3}\right] \, \mathrm{d}r_2 \, \mathrm{d}z_2 \,, \tag{5.10}$$

where

$$f_{c_3} = \left[1 - \tfrac{1}{2} m_5\right] K(m_5) - E(m_5) \,, \tag{5.11}$$

$$m_5 = \frac{4 R_m r_2}{m_6^2}, \qquad m_6^2 = \left[R_m + r_2\right]^2 + \left[z + \tfrac{1}{2} e_1 L_m - z_2\right]^2 . \tag{5.12}$$

Note that z_2 and r_2 in Eq. 5.12 are variables of integration.

Computing Eq. 5.10 using numerical integration is an efficient means to calculate the axial force between a coaxial magnet and thick solenoid. This method is here referred to as the 'integral' method.

The integral method of Babic et al.

Babic et al. [19] presented a different solution for the integral of Eq. 5.8. Their solution consists of an entirely analytical component with one separate term requiring a single numerical integration. Corrected for a typographical error [20] and rewritten, their expression is shown in Eq. 5.13 and herein is refered to as the 'Babic' method. The sign of the result has been reversed over the original expression to ensure consistency with the results presented in this paper. With parameters as described earlier in this section, the force exerted on a permanent magnet by a thick coil using Babic's method, F_{c4}, is

$$F_{c4} = \frac{NIB_r R_m^3}{6L_c\left[R_c - r_c\right]} \sum_{e_1,e_2,e_3}^{\{1,-1\}^3} \left[e_1 e_2 e_3\, t\, f_{c_4}\right] \tag{5.13}$$

where

$$\begin{aligned}
f_{c_4} &= \psi_1\sqrt{\rho m_1} + \frac{\pi\psi_2}{2\,|t|} + 6\psi_3\,,\\
t &= \frac{z + \frac{1}{2}e_1 L_m + \frac{1}{2}e_2 L_c}{R_m}, \qquad \rho = \frac{r_c + R_c + e_3\left[R_c - r_c\right]}{2R_m}\,,\\
m_1 &= \frac{4\rho}{\left[\rho+1\right]^2 + t^2}, \quad m_2 = \sqrt{t^2+1}\,,\\
\psi_1 &= K(m_1)\left[\frac{m_2+2}{m_2+1}\left[t^2-2\right] + \rho^2 + \rho + 2 - \frac{2}{\rho+1}\right] - \frac{4\rho}{m_1}E(m_1)\\
\psi_2 &= \rho\,\mathrm{sgn}(\rho-1)\left[\rho^2-3\right]\left[\Lambda_0\left(|\xi_1|\,,m_1\right) - 1\right] +\\
&\quad m_2\left[t^2-2\right]\left[\Lambda_0\left(|\xi_2|\,,m_1\right) - 1 + \mathrm{sgn}(\rho-m_2)\left[\Lambda_0\left(|\xi_3|\,,m_1\right) - 1\right]\right]\\
\psi_3 &= \int_0^{\pi/2} \sinh^{-1}\left(\frac{\rho+\cos(2\varphi)}{\sqrt{\sin(2\varphi)^2 + t^2}}\right)\mathrm{d}\varphi\,,\\
\xi_1 &= \arcsin\left(\frac{\rho-1}{\rho+1}\sqrt{\frac{1}{1-m_1}}\right), \qquad \xi_2 = \arcsin\left(\frac{t}{m_2+1}\right),\\
\xi_3 &= \arcsin\left(\frac{t}{m_2+1}\sqrt{\frac{1}{1-m_1}}\right),
\end{aligned}$$

where Λ_0 is the Heuman Lambda function defined by

$$\Lambda_0(\phi,m) = \frac{2}{\pi}\left[F(\phi\,|\,1-m)\left[E(m) - K(m)\right] + E(\phi\,|\,1-m)\,K(m)\right], \tag{5.14}$$

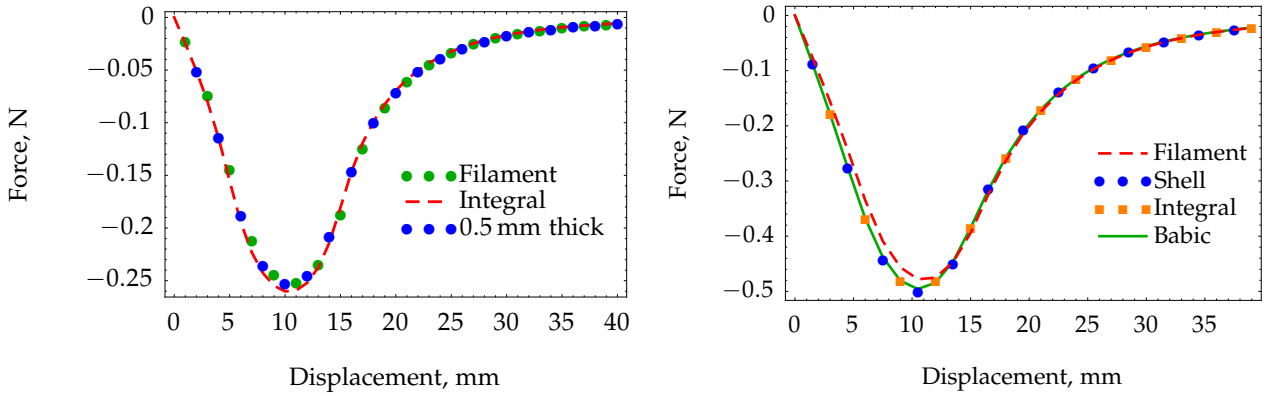

(a) Three methods for a thin coil.

(b) Four methods for a thick coil.

FIGURE 5.4: Results of various methods for calculating the force versus axial displacement between a coaxial coil and magnet.

and $\mathrm{sgn}(\cdot)$ represents the sign function

$$\mathrm{sgn}(x) = \begin{cases} -1 & x < 0, \\ 0 & x = 0, \\ +1 & x > 0. \end{cases} \tag{5.15}$$

When implementing Eq. 5.13, note that $tf_{c_4} = 0$ when $t = 0$ and the inner term f_{c_4} does not need to be evaluated as it otherwise contains a numerical singularity.

Comparison of these methods

The filament model with a single radial turn ($N_r = 1$) can be used to verify the thin coil magnet force, and an initial verification of the integral solution can be performed by comparing the thin coil results for a thick coil with coil thickness equal to the wire diameter. Force versus displacement calculations are performed with these three techniques (Eqs 5.3a, 5.4 and 5.10) using the physical parameters defined in Table 5.1; results of these calculations are shown in Figure 5.4(a) and it can be see that the three models produce comparable results. The results due to the filament model have a small discrepancy around the extremum of the curve due to the discretisation of the magnet into virtual filaments.

Having verified the filament, shell and integral methods for calculating the force between a thin coil and a magnet, the next step is to perform a similar comparison for calculating the force for a thick coil instead. A

Table 5.1: Magnet–coil parameters used for simulation of thin-coil forces (Fig. 5.4(a)). Coil thickness is used for the thick coil equation only.

Magnet radius	R_m	9 mm
Magnet length	L_m	10 mm
Magnet 'turns'	N_m	100
Magnet remanence	B_r	1 T
Coil inner radius	r_c	10 mm
Coil thickness	$R_c - r_c$	0.5 mm
Coil length	L_c	20 mm
Coil turns	N_z	40
Coil current	I	1 A

similar set of calculations were performed, including Babic et al.'s integral approach (Eq. 5.13), using the same set of parameters as in Table 5.1 except with a thick coil instead with a thickness $R_c - r_c = 5\,\text{mm}$ with $N_z = 20$ turns in the axial direction and $N_r = 5$ turns in the radial direction. The force versus displacement results for the thick coil/magnet calculations are shown in Figure 5.4(b), and again the results of the four techniques are in close agreement. In particular, the equation by Babic et al. [19] produces results consistent with the integral expression developed in this chapter. The discrepancy due to the discretisation of the filament model is larger here than for the results of Figure 5.4(a).

The four methods compared in Figure 5.4(b) all use different algorithms, and their execution speed varies significantly as a result. The shell method is more efficient than the filament method, since its execution time is linear with the number of radial layers of turns N_r due to the presence of only a single summation term in its equation. The filament method is the slowest to execute of the four methods, as it has computation time proportional to $N_z \times N_r \times N_m$, which is approximately cubic with the number of turns in total.

Of the integral and Babic methods (Eqs 5.10 and 5.13 respectively), for calculations requiring less stringent accuracy (say, to four significant figures precision) it is more efficient to use the integral method due to the mathematical complexity of the latter, despite it requiring a lesser amount of numerical integration. This is illustrated in Figure 5.5, in which it can be seen that increasing the integration precision when performing calculations using Mathematica causes the time for numerical evaluation of the integral to increase exponentially, whereas the 'Babic' method has a constant execution speed as its single term requiring numerical integration is only

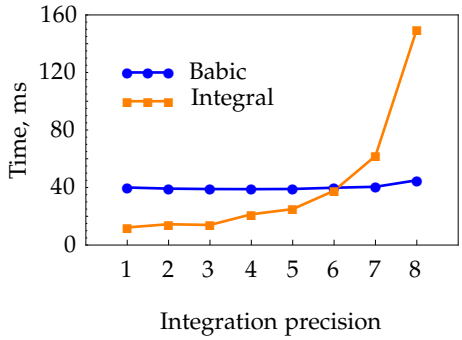

FIGURE 5.5: Illustrative computation times for evaluating the results shown in Table 5.2. Integration precision refers to the minimum number of correct significant figures.

a small component of the overall equation. Nonetheless, as shown in the numerical results (Table 5.2), the integral solution will generally produce results to a sufficient level of accuracy even with low integration accuracy thresholds and therefore may be the preferred solution in some cases, such as for optimisation studies.

In contrast, the shell method is more efficient than either of the integral methods in this case; it executes faster than the Babic method by up to two orders of magnitude. In comparison to the 40 ms time shown in Figure 5.5 for the Babic method, the shell method executes in around 0.26 ms per radial turn with an output result differing by 0.0125 % from the most accurate of Table 5.2. The large improvement in execution speed of the shell method is due to the mathematical simplicity of its solution which does not require numerical integration. Despite the presence of small variations in the results due to the discretisation of the algorithm, this method will be significantly faster and achieve comparable results than the other techniques discussed in this section for analysing thick coils with up to around 100 radial turns.

While the computational times given in this section are specific to the platform used to perform the calculations, their relative differences should be comparable across different computers and numerical implementations.

§5.2.2 *Axial force with eccentric displacement*

The work in the previous sections considered only coaxial forces between a coil and magnet. Certain electromagnetic designs will require the consideration of the effect of eccentric displacement; that is, displacement in the radial direction. An example of such a design is 'pancake coils' [6, 260], which are thin axially but have a large radial face; eccentric displacement is

TABLE 5.2: Numerical output with increasing integration precision. Gray digits indicate inaccuracy in the result after rounding to that many significant figures.

	Method	
Precision	Babic, Eq. 5.13	Integral, Eq. 5.10
1	2.45444**07879895993**	2.**4744006907978187**
2	2.45444**07879895993**	2.45**48594892044457**
3	2.45444**07879895993**	2.45**48594892044457**
4	2.4544438**306124783**	2.4544**392729491915**
5	2.4544438**306124783**	2.45444**10458278520**
6	2.45444382**96675000**	2.45444378**64466280**
7	2.454443830**039190**	2.45444381**75568843**
8	2.45444383009**03315**	2.454443829**9997147**
9	2.45444383009**03315**	2.45444383**01061358**
10	2.454443830090**3230**	2.454443830090**4050**

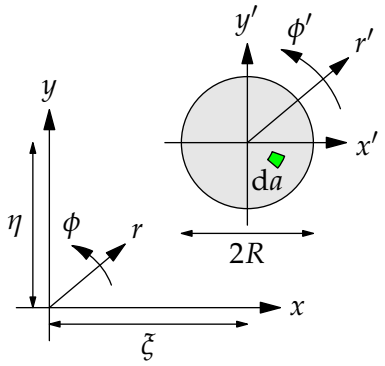

FIGURE 5.6: Region of integration for a radially displaced magnet, shifted by $[\xi, \eta]^\mathsf{T}$ from the original coordinate system.

not constrained and the sensitivity of eccentricity on axial force may be of interest.

The theory for coaxial magnet/coil forces (Eq. 5.8) can be extended for the non-coaxial case. Under eccentric displacement in the radial direction, the limits of integration must be expressed in a translated coordinate system (see Figure 5.6) and the original integral must be modified to include additional terms to take this into account.

In order to incorporate eccentric displacement into the integral, the terms for r_1 and ϕ_1 must be expressed as functions of the terms r_1' and ϕ_1'. The

following transformation can be used to perform this:

$$r_1 = \sqrt{x_1^2 + y_1^2} \qquad x_1 = x_1' - \xi \qquad x_1' = r_1' \cos(\phi_1') \tag{5.16}$$

$$\phi_1 = \arctan(y_1, x_1) \qquad y_1 = y_1' - \eta \qquad y_1' = r_1' \sin(\phi_1') \tag{5.17}$$

Due to the additional complexity introduced by this transformation, the original integral can no longer be easily solved analytically with respect to ϕ_1'. The variable r_1' is not an integration term and therefore $r_1' = R_m$. Accordingly, after rederiving the integral, the axial force due to both axial and radial displacement is now given by

$$F_{c4} = \frac{NIB_r}{\pi L_c \left[R_c - r_c\right]} \int_{-L_c/2}^{L_c/2} \int_{r_c}^{R_c} \int_0^{\pi} \sum_{e_1}^{\{1,-1\}} \left[e_1 m_2 f_{c_4}\right] \, \mathrm{d}\phi_1' \, \mathrm{d}r_2 \, \mathrm{d}z_2 \,, \tag{5.18}$$

where the intermediate term is

$$f_{c_4} = \left[1 - \frac{m}{2}\right] K(m) - E(m) \,, \tag{5.19}$$

with parameters

$$m = \frac{4 r_1 r_2}{m_2^2}, \qquad m_2^2 = \left[r_1 + r_2\right]^2 + \left[z + \tfrac{1}{2} e_1 L_m - z_2\right]^2 . \tag{5.20}$$

Due to the additional numerical integral that must be evaluated when using Eq. 5.18, it is approximately an order of magnitude slower to calculate than Eq. 5.10. The expression is slightly optimised for efficiency; from 0 to 2π around ϕ_1' the integral is symmetric so only the first half is calculated; this approximately halves the execution time of numerical integration.

The filament method can again be used to verify Eq. 5.18. Kim et al. [151] presented an expression for calculating the filamentary force between two non-coaxial circular coils; their equations were corrected for typographical errors and reprinted by Hull and Cansiz [131]. However, it is believed that their work is incorrect as the results produced from Kim et al.'s equation are not consistent with either the coaxial filament force (Eq. 5.1) nor the recently published generalisation by Babic and Aykel [22] for calculating the force between noncoaxial and inclined circular coils.

The non-coaxial filamentary coil force in the axial direction for eccentric (radial) displacement e_r is taken from the third special case given by Babic and Aykel [22], adapted:

$$F_f(r_1, r_2, z, e_r) = \frac{\mu_0}{4\pi} I_1 I_2 r_2 z \int_0^{2\pi} \frac{m_2}{v} \cos(\theta + t) \left[2K(m) - E(m) \frac{2 - m}{1 - m}\right] \, \mathrm{d}t \,, \tag{5.21}$$

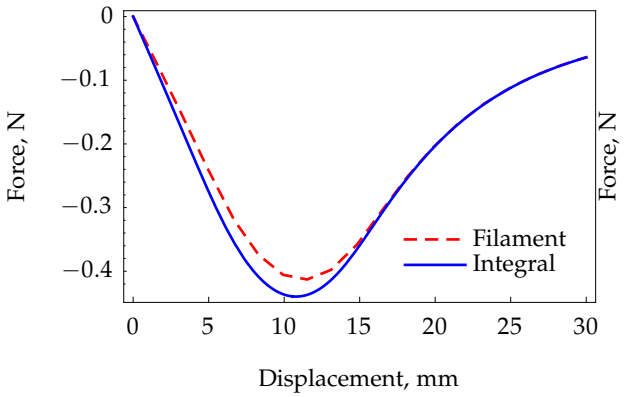

(a) Comparison of the filament and integral methods for calculating eccentric thick coil–magnet forces.

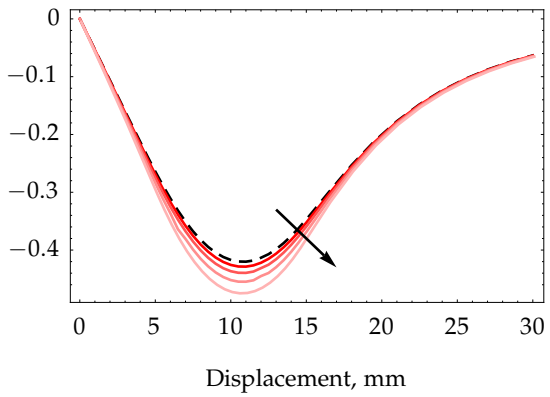

(b) Example thick coil forces in the axial direction versus displacement for increasing eccentricities from 1 mm to 2.5 mm indicated by the arrow. Zero eccentricity is shown dashed.

FIGURE 5.7: Two examples of eccentric thick coil magnet forces calculations.

where

$$m = 4r_1 v m_2^2, \quad m_2 = \left[\left[r_1 + v \right]^2 + z^2 \right]^{-1/2}, \quad \theta = \arctan(y, x)\,,$$
$$v = \sqrt{x^2 + y^2}, \quad x = e_r - r_2 \sin(t)\,, \quad y = r_2 \cos(t)\,. \tag{5.22}$$

Equation 5.21 can be used with the filament method (as in Eq. 5.3a) to calculate thick-coil magnet forces, but this is only useful as a verification as the filament method using a numerical integral is extremely slow to execute (around three orders of magnitude slower than the integral solution of Eq. 5.18). Such a comparison is shown in Figure 5.7(a), which has system parameters as shown in Table 5.1, aside from a larger inner coil radius of 11.5 mm and an eccentric displacement of 1.5 mm. This figure shows that the integral method proposed here gives results in agreement with the filament method.

Eccentricity acts to increase the axial force of a coil/magnet system as the magnetic material comes closer to the region of greater magnetic field strength due to the solenoid (Fig. 5.7(b)). This result indicates that decreasing the air gap between the coil and magnet as much as possible is desirable to maximise the forces obtained for a given input current.

§5.3 Optimisation of a sleeve coil magnetic actuator

In the previous section, methods were presented for calculating coil forces with arbitrary examples used for verification. These equations can be used

for optimisation of a magnetic actuator; for example, to choose geometric parameters for an inertial shaker to maximise the peak force or to maximise the stroke length. In this section, a common 'sleeve coil' configuration is investigated in which a cylindrical magnet moves axially within a hollow coil, such that the inner coil radius is greater than the magnet radius; $r_c > R_m$. A schematic of this system was shown in Figure 5.2.

§5.3.1 *Relationship between coil impedance and outer diameter*

When attempting to optimise the force output of a coil/magnet design, it is important to carefully consider the parameters to be varied so that comparisons between different cases are fair. In the theory developed in Section 5.2.1, the force is calculated using coils of a given current density and coil thickness. When designing a coil, however, it is instead more applicable to fix the coil resistance and wire thickness and calculate the number of turns and outer coil radius from these values. In this way, comparisons between different geometries will be indicative of force for some fixed electrical input power as each coil variation will draw the same amount of current for a given driving voltage.

The resistance of the coil R directly infers the length of the wire winding, l_w, through the relation

$$l_w = Ra_w/\rho, \tag{5.23}$$

for wire of resistivity ρ and cross sectional area a_w, assumed here as having circular cross section $a_w = \pi \left[\frac{1}{2}d_w\right]^2$ where d_w is the wire diameter.

The fixed parameters of the coil are driving voltage, resistance, wire diameter and material, which in turn determine the total length of wire to be used. Given a fixed length of wire, it is possible to derive a relation between the coil length L_c and the coil radii, r_c and R_c. Assuming that each turn of wire sits directly above or adjacent to its neighbours, an approximate expression for the total wire length is given by

$$l_w = N_z \sum_{n=0}^{N_r-1} 2\pi\left[r_c + d_w\left[n + \tfrac{1}{2}\right]\right] = 2\pi N_r N_z \left[r_c + \tfrac{1}{2}N_r d_w\right], \tag{5.24}$$

where $N_r = \left[R_c - r_c\right]/d_w$ and $N_z = L_c/d_w$ are the number of turns in the axial and radial directions respectively. While this relationship does not model any wire coating or the packing effect of how tightly-wound coils will sit,[1] this equation is simple and allows some conservatism in the quality of the

1. Taking into account of the packing factor will reduce the outer radius by around 10% of the thickness of the coil [299].

construction of the electromagnet. Solving Eq. 5.24 for R_c, the outer radius of the coil for a coil of fixed inner radius and fixed total wire length is given by

$$R_c = \sqrt{\frac{l_w d_w^2}{\pi L_c} + r_c^2}\,. \tag{5.25}$$

§5.3.2 *Notation*

From Section 5.2.1, the axial force versus displacement z for a thick-coil/magnet system can be expressed as a function of its gross geometric parameters (defined in Figure 5.1) as

$$F_c\big(B_r, I, N_z, N_r, R_m, L_m, r_c, R_c, L_c|z\big)\,, \tag{5.26}$$

with electromagnetic parameters (B_r, I, N_z, N_r) defined previously and F_c calculated with any of the filament, shell, or integral methods (Eqs 5.3a, 5.4, 5.10 and 5.13, respectively).

The magnet radius R_m can be expressed in terms of the magnet ratio α and magnet volume V_m with

$$R_m = \left[\frac{V_m}{\pi\alpha}\right]^{1/3}, \tag{5.27}$$

from which the magnet length $L_m = \alpha R_m$, coil inner radius $r_c = R_m + r_g$, and coil length $L_c = \beta r_c$ are inferred directly from the geometric ratios and clearance r_g between the coil and magnet.

As discussed in Section 5.3.1, the outer coil radius R_c and the coil turns N_z and N_r can be calculated from the coil resistance R, wire diameter d_w and wire resistivity ρ. Therefore, the force function of Eq. 5.26 can be expressed in terms of the following different set of parameters which are more useful for design optimisation:

$$F_c\big(B_r, I, \rho, V_m, R, d_w, \alpha, \beta, r_g|z\big)\,. \tag{5.28}$$

Of these parameters, the magnet strength is set to be $B_r = 1\,\mathrm{T}$, the radial clearance is fixed at $r_g = r_c - R_m = 0.5\,\mathrm{mm}$, and the resistivity of copper of $\rho = 1.7 \times 10^{-8}\,\Omega\,\mathrm{m}$ is used. Initially the force per unit current $\hat{F}_c$ is considered, which is calculated by evaluating the force for a current of $I = 1\,\mathrm{A}$. Removing these fixed parameters from Eq. 5.28 produces the function for force

$$\hat{F}_c\big(V_m, R, d_w, \alpha, \beta|z\big)\,. \tag{5.29}$$

In the sections to come, the coil-magnet force F_c will be discussed as a function of magnet volume V_m, coil resistance R, wire diameter d_w, magnet

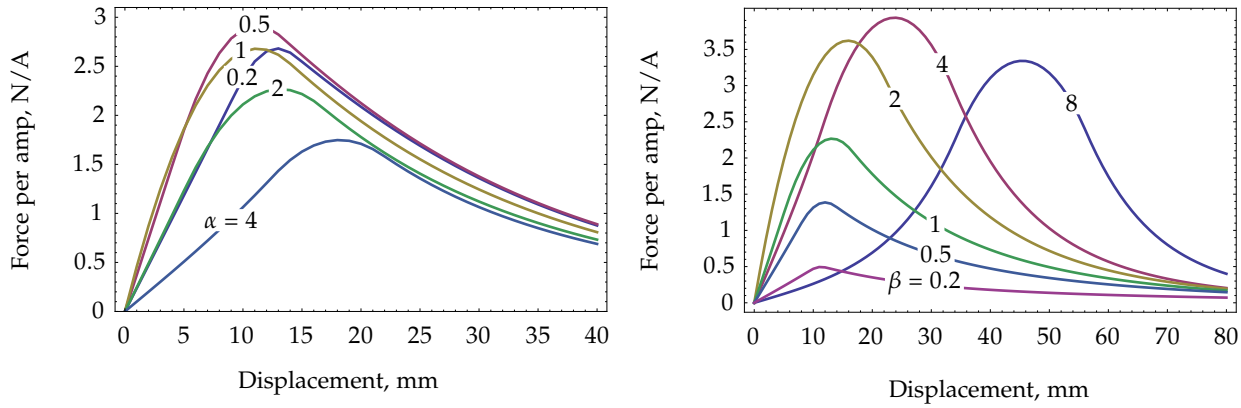

(a) Varying magnet ratio α for a fixed coil ratio $\beta = 1$.

(b) Varying coil ratio β for a fixed magnet ratio $\alpha = 2$.

FIGURE 5.8: Normalised force $\hat{F}_c$ versus displacement calculations for two cases.

ratio α, coil ratio β, and axial displacement z. The goal of the analysis will be to derive optimum values for certain of these parameters.

At the outset it is assumed that increasing the magnet volume V_m will result in greater forces since there will be a greater amount of magnetic energy in the system; this is not then a parameter to be varied but instead to be selected as necessary.

§5.3.3 *Optimisation of magnet and coil geometry*

To perform the optimisation of magnet and coil geometries, the shell method, Eq. 5.4, is used to calculate the force as a function of displacement with varying magnet and coil ratios.

For sake of example, a wire diameter $d_w = 1\,\text{mm}$ was selected to produce the initial results; wire diameter is later varied in Section 5.3.4. The volume of magnetic material is held constant at $V_m = \left[20\,\text{mm}\right]^3$ and the coil impedance at $R = 4\,\Omega$. Therefore the normalised force per unit current is calculated for this case as

$$\hat{F}_c(\alpha, \beta | z) = \hat{F}_c\Big(\left[20\,\text{mm}\right]^3, 4\,\Omega, 1\,\text{mm}, \alpha, \beta | z\Big)\,. \tag{5.30}$$

The effects on the force–displacement characteristic of Eq. 5.30 of varying the magnet ratio α and coil ratio β independently are shown respectively in Figure 5.8. For each it can be seen that the peak force and the shape of the curve varies significantly as the geometry of the magnet and coil changes. It can also be seen that an optimal α and β could be chosen to satisfy a particular cost function such as peak force, integral of force over

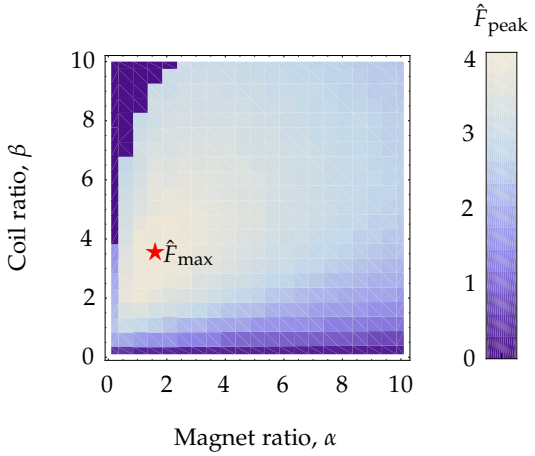

FIGURE 5.9: Peak normalised force $\hat{F}_{\text{peak}}$ as magnet and coil ratios α and β are varied over a 20×20 discrete grid for a specific wire diameter, coil impedance, and magnet volume. Maximum normalised peak force is indicated with a star.

displacement, displacement over which at least 95% of the peak force is achieved, linearity over a certain displacement range, and so on, according to the requirements of the actuator being designed. For simplicity, in the examples to follow the metric to be maximised is chosen to be the peak force but the methodology for design optimisation holds regardless of the cost function.

The magnet and coil ratios α and β were considered over a range from 0.1 to 10 and the normalised peak force over displacement calculated as a function of these two varying parameters. The normalised peak force was calculated as

$$\hat{F}_{\text{peak}}\left(V_m, R, d_w, \alpha, \beta\right) = \max_z \left\{ \hat{F}_c\left(V_m, R, d_w, \alpha, \beta | z\right) \right\}, \tag{5.31}$$

where magnet volume V_m, coil resistance R, and wire diameter d_w were fixed as described earlier.

Figure 5.9 shows an example of the normalised peak force evaluated with Eq. 5.31 over a discretisation of the magnet and coil ratio ranges. This surface can be seen to be concave, and therefore a single value for α and β can be chosen to maximise the normalised peak force for a given magnet volume, coil impedance, and wire diameter.

§5.3.4 *Optimisation of wire diameter*

In Section 5.3.3, the peak force results were normalised against coil current and the effect of wire diameter was not taken into account. However, the wire

diameter is a particularly important parameter, as it directly infers the length of wire to be used but more importantly restricts the current carrying capacity of the coil. A larger diameter wire will produce a lower resistance per unit length, and hence for a given input impedance a longer wire length in total. Depending on the geometry of the coil, having a longer wire length could cause the coil to become unnecessarily thick, moving magnetic energy away from where it is required, which is as close as possible to the permanent magnet. Having shown a method by which an optimal magnet and coil geometry can be chosen (for example, as shown in Figure 5.9) it is now possible to introduce the wire diameter as a variable parameter, which will allow an optimal wire diameter to be chosen.

First consider the case of optimising the normalised peak force per unit of current over magnet and coil ratios and a range of wire diameters using the equation

$$\hat{F}_{\max}(V_m, R, d_w) = \max_{\alpha,\beta} \left\{ \hat{F}_{\text{peak}}\left(V_m, R, d_w, \alpha, \beta\right) \right\}. \tag{5.32}$$

Rather than gridding the parameter space for α and β into discrete values as in Figure 5.9, this optimisation was performed using a two-dimensional local maximum search function (Mathematica's `FindMaximum`). The results from evaluating Eq. 5.32 as a function of wire diameter over a range of coil resistances is shown in Figure 5.10(a). As the wire diameter increases, the resistance per unit length decreases and a larger coil is required; past a certain point, this decreases the amount of force per unit current that the coil can achieve.

Figure 5.10(a) is noisy at small wire diameters due to quantisation errors in calculating the number of turns of the coil. When calculating the outer radius of the coil with Eq. 5.25, a non-integer number of radial turns is required to achieve an exact wire length, and discrepancies result as the number of radial turns in quantised. These errors are greater at lower wire diameters as each individual coil turn contributes a greater proportional of the total coil resistance.

§5.3.5 *Consideration of maximum current rating*

As the wire diameter increases, the amount of force per unit of current decreases. However, as the wire diameter increases the maximum current rating increases as well; larger wire diameters can be driven with a larger input voltage.

There is a general relationship relating wire diameter and its maximum current rating [251], denoted $I_{\max}(d_w)$ and shown in Figure 5.11; note that

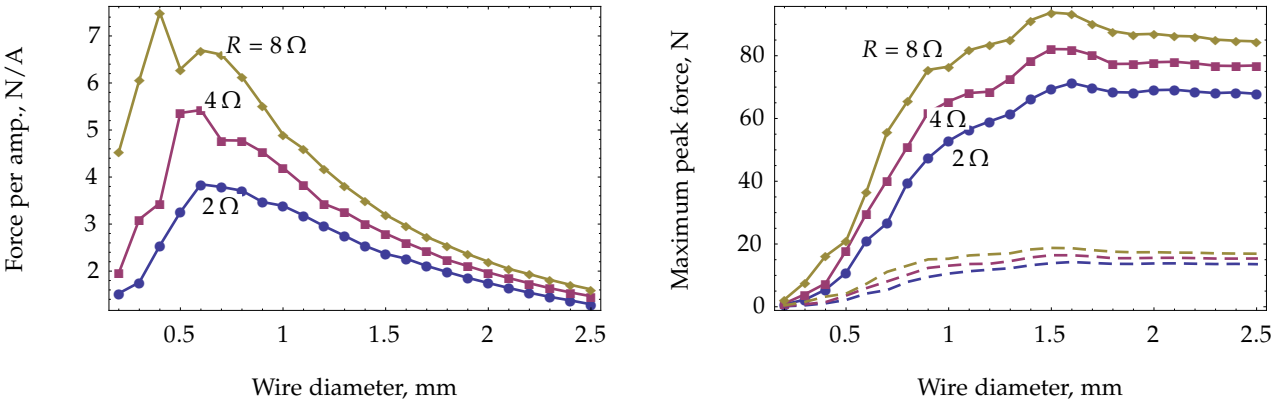

(a) Maximum normalised force per ampere of current.

(b) Maximum peak force $F_{\max}$ versus wire diameter with and without a safety factor.

FIGURE 5.10: Maximum peak and normalised force per ampere of current, optimised by magnet and coil geometry as a function of wire diameter. Results are shown for three values of coil impedance while the magnet volume is fixed at $V_m = \left[20\,\text{mm}\right]^3$. Solid, labelled lines have a safety factor of 100 %; dashed lines represent the same curves using a 20 % safety factor on allowable maximum current; they exhibit the same shape with a proportionally lower peak amplitude.

although this relationship is conservative it does not take into account factors such as thermal loading due to tightly-wound coils or high-frequency current oscillations. As the maximum current rating data is applicable only for bare wire, a safety factor must be used for coils with many turns; a value of 20 % is chosen for illustrative purposes here. Using this data, an estimate of the maximum peak force (after optimising the magnet and coil geometries individually) can be calculated for a range of wire diameters scaled according to their maximum current rating.

An upper estimate of the maximum force obtainable with a coil of certain wire diameter is found by multiplying the normalised maximum peak force by the maximum current rating,

$$F_{\max}\left(V_m, R, d_w, S_f\right) = \hat{F}_{\max}(V_m, R, d_w) \times I_{\max}(d_w) \times S_f\,, \tag{5.33}$$

using a safety factor S_f to account for unmodelled thermal effects. This produces the curves of maximum peak force shown in Figure 5.10(b), which each show a global maximum against wire diameter, although as the wire diameter increases the achievable peak force remains largely flat for wire diameters above the optimum values.

It is important to consider that these results can only be considered an upper limit on the possible forces achievable as the maximum operating

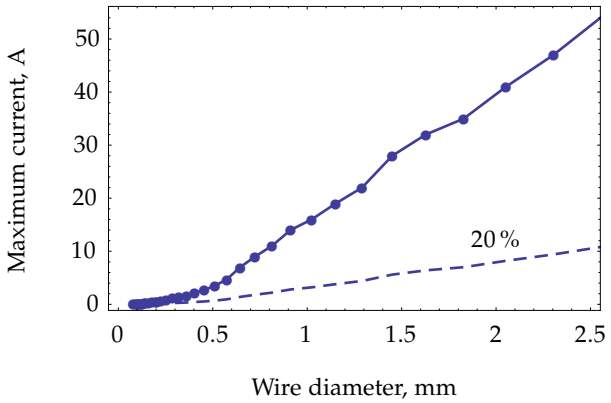

FIGURE 5.11: Typical values for maximum current rating for copper wire of varying diameter [251, adapted], and the same data with a 20 % safety factor (dashed).

temperature will be greatly limited due to thermal effects. Nonetheless, the shape of these curves and hence the value of suitable wire diameter, is not affected by the safety factor chosen. Primarily, the curves in Figure 5.10(b) indicate that increasing the wire diameter is not effective past a certain point for the chosen constraints, being a maximum diameter of around 1 mm to 1.5 mm.

§5.3.6 *Trends in the optimisation results*

It is interesting to consider the parameters chosen for the optimal values of magnet and coil ratios (Fig. 5.12). As discussed earlier, due to quantisation errors in the calculation of radial turns, the optimal magnet and coil ratios are not smooth with wire diameter. Secondly, the accuracy of the numerical methods used to calcute these optimal values introduces numerical error into the results, and improving this accuracy is prohibitive in terms of calculation time.

Despite this, two broad characteristics can be seen. The magnet ratio is bound in most cases by around $1 \leq L_m/R_m \leq 2$. Secondly, as the wire diameter increases so does the coil ratio in an approximately linear relationship. The implication of this trend is that as the wire resistance per unit length decreases and the total length of wire increases (requiring more turns), it is advantageous to extend the length of the coil rather than to extend its outer radius. As shown in Figure 5.10(a), however, as the length of the coil exceeds the magnet length significantly, the normalised amount of force produced quickly decreases; driving the coil with a larger current is the only way to achieve parity with shorter coils with smaller wire diameter.

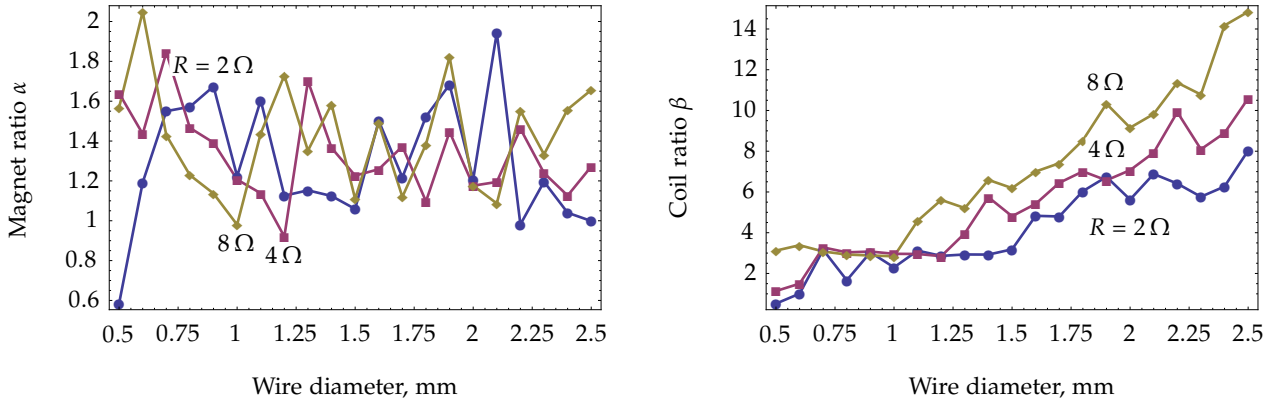

(a) Optimal values of magnet ratio α.

(b) Optimal values of coil ratio β.

FIGURE 5.12: Optimal values found of the magnet and coil ratios at each value of wire diameter investigated, corresponding to the results shown in Figure 5.10.

§5.3.7 *Effects of magnet volume and coil resistance*

Finally, while the results from Figure 5.10(b) indicate that increasing the coil resistance will lead to an increased maximum peak force for a given magnet volume, this increase provides diminishing returns as the resistance increases past a certain point. This is shown in Figure 5.13 as a plot of maximum peak force versus coil resistance over a range of magnet volumes according to the function

$$F_{\max}(V_m, R) = \max_{d_w}\left\{ F_{\max}\left(V_m, R, d_w, S_f\right) \right\}, \tag{5.34}$$

using a safety factor of $S_f = 20\%$ on the maximum current to accommodate unmodelled thermal effects.

Qualitatively, this diminishing return in the maximum peak force can be explained by the fact that the larger the total coil resistance the longer the length of wire needed and the less compact the coil can be, resulting in a movement of the magnet field away from the permanent magnet. Therefore, despite the larger electrical energy input, this can only be achieved with a less efficient geometric design of the electromagnetic system. To add to the disadvantage of increasing the force in this way, the larger the resistance the greater the electrical power required to drive the coil at a certain current, the more windings required to construct the coil, and the greater the chance of thermal difficulties with the cooling of bulkier coils. Increasing the volume of the permanent magnet will generally be a more suitable approach to generating larger forces.

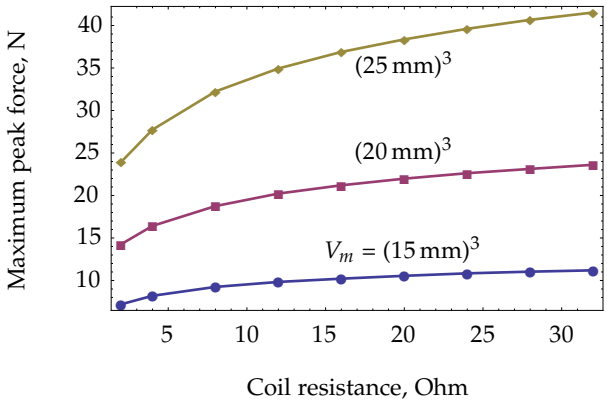

FIGURE 5.13: Maximum peak force as a function of coil resistance over a range of magnet volumes, showing that an increase in coil resistance leads to diminishing returns in peak force. A safety factor of 20% on the maximum current has been applied to obtain these results.

The overall outcome of this modelling is to conclude that after choosing a magnet volume and coil impedance, it is possible to optimise the force–displacement characteristic according to some cost function to choose the wire diameter, magnet shape, and number of coil turns. Designing a device to achieve a certain peak force, say, then requires simply choosing an appropriate magnet size and coil impedance, both of which depend on additional considerations including cost, availability of suitable amplifier specifications, requirements for compact design, and so on.

§5.3.8 *Summary*

In this section the theory has been summarised and compared for analytically calculating the force generated between a thick coil of varying dimensions and a cylindrical permanent magnet with relative displacement in the axial direction. Despite the integral equation for this system being solved by other researchers almost entirely analytically, in some cases such a solution is computationally more expensive than numerical integration. An alternative solution using iteration over 'shells' of infinitely thin surface current densities is computationally cheaper again for coils with a relatively small number of radial turns.

This theory is suitable for optimising a wide range of actuator designs and in particular the general case of designing a magnetic actuator for peak force has been shown to reduce to choosing a coil impedance and magnet volume from which all geometric parameters are implicitly calculated. This

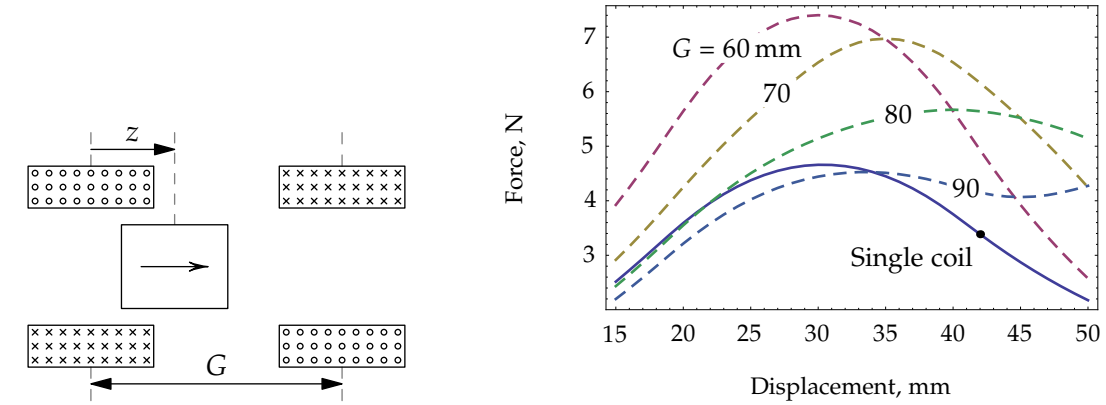

(a) Schematic of the dual-coil system.

(b) Example dual-coil forces (dashed) against an equivalent single coil system of equal resistance (solid).

FIGURE 5.14: Electromagnet system with dual push/pull coils.

design methodology can also be used to optimise the system parameters using other cost functions such as stroke length or linearity.

§5.4 DUAL-COIL ELECTROMAGNET DESIGN

Considering the force equation between a magnet and coil (Eq. 5.8, and other methods), the constant term $NI/\left[R_c - r_c\right]$ is the cause of some subtle considerations when designing electromagnetic actuators. The force created by a single layer coil (that is, $N_r = 1$) cannot be improved upon for a fixed input power by adding more layers radially, because the total length of wire (and hence the resistance, and the inverse of current) will increase faster than the linear gains achieved in the force.

The study in Section 5.3 has outlined an optimisation technique to achieve the maximum peak force given a fixed magnet volume and input resistance. This peak force can be subsequently improved upon by using a different coil design. By wiring two half-resistance coils in series and in opposite winding directions, with the permanent magnet in the gap between them (Fig. 5.14(a)), greater forces can be achieved than with a single coil of equivalent resistance. This design is also better at dissipating heat, as the effective surface area is greater.

For two coaxial coils with a distance G between their centres, superposition can be used to calculate the forces F_{c1} and F_{c2} generated between each and a permanent magnet free to move between them. The axial distances between the permanent magnet and the two coils is denoted by z and $\left[-G+z\right]$

respectively. The two coils are assumed to be the same size, and the total axial force on the magnet is given by

$$F_{c\mathrm{T}}(z, G) = F_{c1}(z) + F_{c2}(-G + z)\,. \tag{5.35}$$

For a fixed dual-coil geometry, this equation allows an investigation of the force versus displacement curves while varying the distance between the coils and the position of the permanent magnet.

The improvement that can be achieved with the dual-coil design is demonstrated via an example. The results from the previous optimisation for coil and magnet aspect ratios (Fig. 5.12) indicate that generally a longer coil than magnet produces larger forces (that is, a larger coil aspect ratio). In such cases, the maximum force experienced by the permanent magnet is seen at a displacement of half the coil length. The dual-coil spacing G should be chosen such that the displacement for peak force aligns for both coils so as to achieve maximum force from both coils; for the case of longer coils than magnets, this spacing becomes equal to the coil length. In other words, there will be zero gap between the adjacent coils. When the separation distance is larger than this, a long stroke actuator can be designed with such a setup by sacrificing maximum force to achieve a wider but lower force peak.

These ideas are shown by example in Figure 5.14, which shows a dual-coil design with varying coil gap G. Simulation parameters for this example are shown in Table 5.3; note that in the dual-coil design the outer radius of the coil is the only difference, corresponding to fewer radial turns to achieve half the coil resistance. The dual-coil design can achieve over 50% greater peak force than the equivalent resistance single coil design; even when some additional gap is added (such as the $G = 80\,\mathrm{mm}$ case), the peak force is still larger but the stroke length is greatly improved. As the coils are separated further, they exhibit a 'double peak' characteristic (shown for $G = 90\,\mathrm{mm}$) which essentially bounds the coil gap where the dual-coil design is advantageous over having a single coil alone. Larger improvement to the forces could be achieved by optimising the shapes of each separate coil in the dual-coil arrangement rather than taking the coil aspect ratio from the original single-coil design.

This analysis does not take into account the effects of coil inductance or eddy current drag on the dynamics of the actuator, and it is possible that the dual-coil system, which exhibits larger quasi-static forces, has longer time constants than a single-coil system. The self-inductance of the coils governs the dynamics of the electric system only (the relationship between current and voltage), and eddy current drag is governed by the mutual inductance of the electromagnetic system. With new developments in this field allowing the

analytical calculation of these parameters for cylindrical geometries [23, 182], it is proposed for future work that these inductance effects be incorporated into the cost function for developing optimum electromagnetic actuator designs.

Table 5.3: Explicit and implicit parameters for the dual-coil example. The dual-coil system has twin coils of half resistance.

Explicit		Implicit	
Magnet ratio	2	Magnet length	21.7 mm
Coil ratio	5	Magnet radius	10.8 mm
Wire diameter	1 mm	Coil inner radius	11.8 mm
Coil resistance (single)	8 Ω	Coil length	59 mm
Magnet volume	$[20\,\text{mm}]^3$	Coil thickness (single)	34 mm
Coil current	1 A	Coil thickness (dual)	22 mm
Magnetisation	1 T		

§5.5 Summary of electromagnetic coil design

In this chapter, theory has been developed for calculating forces between cylindrical coils and magnets; as a contribution to the literature, a much improved method has been demonstrated for calculating the force between thin coils. The use of this equation to efficiently calculate thick-coil/magnet forces has also been detailed. An equation has also been presented for calculating the axial force between a thick coil and permanent magnet with both axial and radial (or eccentric) displacement.

Two electromagnetic systems have been analysed. The first was an optimisation of a 'sleeve-type' electromagnetic actuator, and for this system it was shown that such analysis can yield optimal values for magnet and coil parameters. The outcome from this study is to posit a solution to the inverse problem: given a required electromagnetic force, what magnet sizes and coil windings should be used to achieve this force with minimal space and/or cost?

Secondly, it has been shown that the single-coil system analysed in detail can be further improved by using two equivalent coils in series with half the resistance; the overall effect is to direct the magnetic field of these coils more efficiently than can be done with a single coil alone.

CHAPTER 6

Quasi–zero stiffness design

The work presented in Section 6.3 is based on material that has been published as a journal paper [244]. The work in Section 6.2 has been submitted as a conference paper [245].

§6.1 Introduction to quasi–zero stiffness springs

In a conventional mass–spring system, the static deflection increases as the stiffness of the support is reduced, and a lower limit on the stiffness is imposed by constraints on the allowable displacement. Consider the linear isolator with force balance described by $mg = kx$, and a natural frequency of $\omega_n = \sqrt{k/m}$. The displacement required to support this mass can be written $x = g/\omega_n^2$.

This inverse-quadratic relationship imposes a heavy penalty on the static displacement required to support loads at low frequency (note that this expression is independent of the mass of the object being supported). While a resonance at 5 Hz requires a static displacement of approximately 1 cm, a 1 Hz resonance requires a displacement of almost 25 cm. A different approach is desired for achieving a load bearing relationship that can exhibit a low *dynamic* stiffness without the need for an associated large static deflection.

An example of a system with such behaviour is that of a cubic force versus displacement characteristic; for a dynamic force characteristic of, say, $f(x) = f_0 + x^3$, localised zero stiffness occurs at zero deflection (that is, $f'(0) = 0$), which is termed 'quasi–zero stiffness'. The 'quasi' qualifier is included for two reasons: because the zero stiffness is only valid at a single displacement, and because the relationship is usually infeasible to implement in a physical system. An investigation into the literature yields a variety of such devices, as previously discussed in Section 1.4.3.

This chapter will investigate the quasi-static behaviour of two of these quasi–zero stiffness systems. The first, in Section 6.2, is an 'inclined spring' device that has been studied previously in the literature; here, it is studied from a fresh perspective in order to contrast its behaviour with the second quasi–zero stiffness system examined in Section 6.3: an arrangement of attracting and repelling permanent magnets that allows simpler tuning of the system to adapt to dynamic load bearing.

§6.2 Inclined springs

The spring arrangement shown in Figure 6.1 is a well studied planar quasi–zero stiffness device [8, 55, 57, 201]. It consists of a load bearing vertical spring in parallel with a pair of inclined springs that behave in a buckling regime. Generally, analyses of this device have only considered its stiffness properties in a single degree of freedom, in the direction of the primary load bearing.

This section consists of an analysis of the quasi-static behaviour of this inclined spring system and re-formulates the force and stiffness characteristics in both vertical and horizontal directions, describing in some detail the approach by which low stiffness in both directions can be achieved. Low stiffness in the vertical direction has been previously documented (as cited previously) due to the negative vertical stiffness of a pair of horizontal springs in compression. Low stiffness in the horizontal direction is newly analysed here, which is achieved due to the negative stiffness in the horizontal direction of the load-bearing vertical spring.

A potential drawback of the planar low-stiffness system is observed, which is that large compressions are required from the springs in order to operate at quasi–zero stiffness in both directions simultaneously.

§6.2.1 *Geometry*

Figure 6.1(a) shows the planar inclined spring system without load (that is, with undeflected springs) and Figure 6.1(b) shows the same system after deflection to the position which has the potential of achieving 'quasi–zero stiffness', which is the position of maximum compression of the inclined springs. The overall stiffness of the system must be tuned to support the mass of the load at this position.

At the unloaded state shown in Figure 6.1(a), all springs are considered to be in their uncompressed state; with inclined spring lengths $L_0 = \sqrt{w^2 + h^2}$ and vertical spring length $H_0 = \eta L_0$, where η is denoted the 'length ratio' between the vertical and inclined springs. The inclined springs each have stiffness k_i and the vertical spring has stiffness $k_v = \alpha k_i$, with α denoted the 'stiffness ratio' between the vertical and inclined springs. The stiffness and deflection properties of the springs are summarised in Table 6.1.

The position of maximum compression of the inclined spring, shown in Figure 6.1(b), defines the displacement origin of the system, where z is the displacement in the load bearing direction, and x is the displacement in the non–load bearing direction (this is used later for the derivation of the

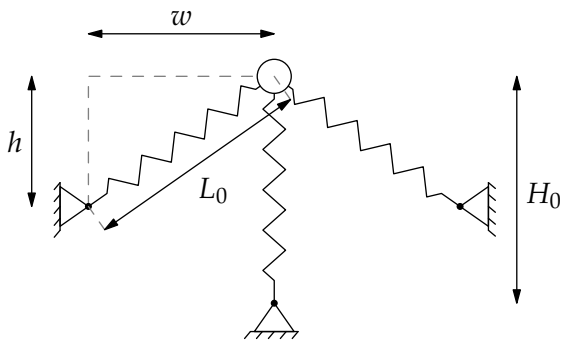

(a) Inclined springs in their unloaded, uncompressed state, corresponding to a vertical displacement of $z = h$.

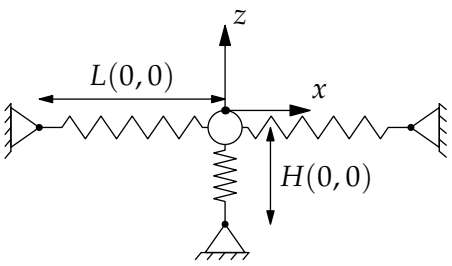

(b) Inclined springs at a position of maximum negative stiffness, corresponding to a vertical displacement of $z = 0$.

FIGURE 6.1: Inclined springs with negative stiffness in the vertical direction in parallel with a positive stiffness vertical spring.

TABLE 6.1: Properties of the springs in the quasi–zero stiffness inclined spring system defining stiffness ratio α and length ratio η.

Spring	Stiffness	Undeflected length
Inclined	k_i	$L_0 = \sqrt{w^2 + h^2}$
Vertical	$k_v = \alpha k_i$	$H_0 = \eta L_0$

horizontal stiffness of the system).

The deflected lengths of the springs from vertical displacement z and horizontal displacement x are $L(x,z)$ for the inclined spring and $H(x,z)$ for the vertical spring. The compressed length of the inclined spring on the left is

$$L(x,z) = \sqrt{\left[w + x\right]^2 + z^2}\,, \tag{6.1}$$

and the vertical spring length is

$$H(x,z) = \sqrt{x^2 + \left[H_0 - h + z\right]^2}\,; \tag{6.2}$$

note that $L(0,h) = L_0$ and $H(0,h) = H_0$.

The geometry that has been chosen uses linear springs that are all arranged to be undeflected in the unloaded state of the device. The use of pretension and nonlinear springs [160] is not explored in this study.

§6.2.2 *Vertical forces*

The forces on the mass are calculated by analysing the components due to each spring individually. The force due to the inclined spring (on the left of Figure 6.1(a)), in the direction of the spring, is given by

$$\begin{aligned} F_i(x,z) &= \left[L_0 - L(x,z)\right] k_i \\ &= \left[\sqrt{w^2+h^2} - \sqrt{\left[w+x\right]^2 + z^2}\right] k_i \,. \end{aligned} \tag{6.3}$$

Assuming only vertical displacement ($x = 0$), the vertical component of this inclined spring force is

$$F_{i_v}(x,z) = F_i(0,z)\frac{z}{L(0,z)} = zk_i\left[\frac{\sqrt{w^2+h^2}}{\sqrt{w^2+z^2}} - 1\right]. \tag{6.4}$$

It is convenient to normalise this result by representing the lengths and displacements as ratios of the uncompressed height of the inclined springs. With the coordinate substitutions $\xi = z/h$ and $\gamma = w/h$, the inclined spring force in the vertical direction can be written in non-dimensional form as

$$\frac{F_{i_v}(\xi)}{hk_i} = \xi\left[\sqrt{\frac{\gamma^2+1}{\gamma^2+\xi^2}} - 1\right], \tag{6.5}$$

where γ is denoted the 'geometric ratio' of the device and ξ the normalised displacement.

This is a different normalisation than used in the literature [55, 57]; note that here $\gamma = 0$ corresponds to unloaded inclined springs at 90° (that is, vertical) before compression, and $\gamma = \infty$ corresponds to unloaded inclined springs at 0° (that is, horizontal). In the coordinate system used here, the displacement origin $z = 0$ corresponds to the position of maximum compression of the inclined springs; that is, when they are horizontal.

Figure 6.2(a) illustrates the force characteristic of Eq. 6.5 versus normalised displacement for a range of geometric ratios γ. The 'snap-through' forces that cause the negative stiffness are especially strong for smaller values of geometric ratio γ (that is, the more vertical the spring angles before deflection in Figure 6.1(a)).

The total vertical force produced by the system, $F_{t_v}(x,z)$, is calculated by combining Eq. 6.4 for each inclined spring with the force due to the vertical spring:

$$F_{t_v}(x,z) = 2F_{i_v}(x,z) + F_{v_v}(x,z)\,. \tag{6.6}$$

For vertical displacements, the force due to the vertical spring is given by

$$F_{v_v}(x,z) = \left[h - z\right] k_v\,, \tag{6.7}$$

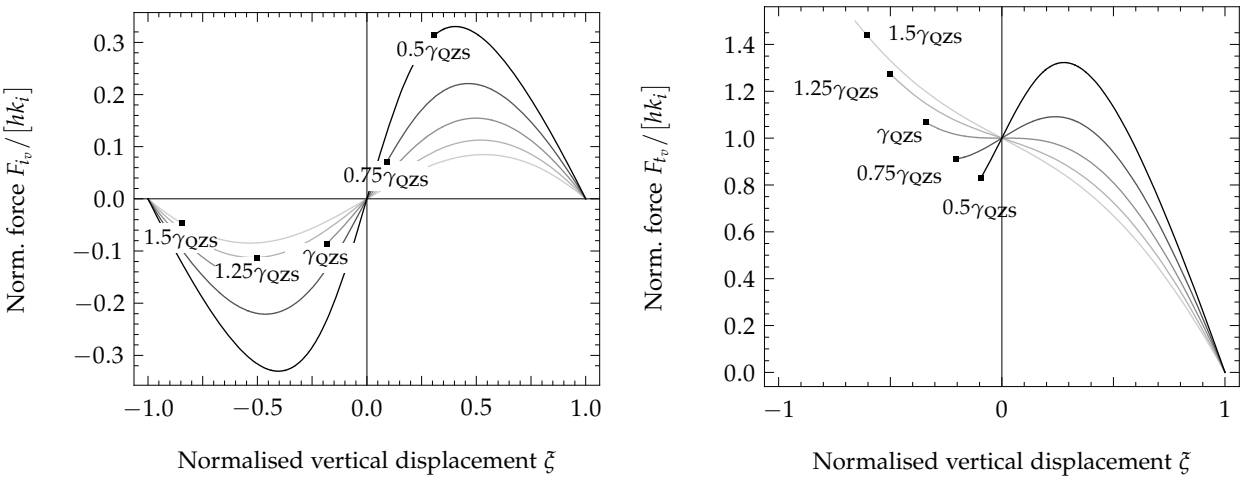

(a) Vertical force due to inclined springs only using Eq. 6.4 for a range of geometric ratios γ.

(b) Normalised vertical force characteristic of the system calculated with Eq. 6.8. Minimum displacements are calculated from Eq. 6.9; these termination points represent the limiting case of the vertical spring being compressed to zero length.

FIGURE 6.2: Vertical forces due to the inclined springs. γ_{QZS} is the value of γ for which quasi–zero stiffness is achieved at $\xi = 0$, calculated from Eq. 6.12.

and the total force in the vertical direction can be nondimensionally represented by

$$\frac{F_{t_v}(x,z)}{hk_i} = -\xi\alpha + \alpha + 2\xi\left[\sqrt{\frac{\gamma^2+1}{\gamma^2+\xi^2}} - 1\right], \tag{6.8}$$

recalling that $\alpha = k_v/k_i$ is the stiffness ratio between the vertical and inclined springs. This equation is depicted in Figure 6.2(b) for a unity stiffness ratio ($\alpha = 1$), where it can be seen that by selecting the geometric ratio γ appropriately it is possible to generate a local region of low stiffness at displacement $\xi = 0$, approaching the quasi–zero stiffness condition under ideal circumstances. The calculation for γ_{QZS}, the value of the geometric ratio γ for which quasi–zero stiffness is achieved, will be shown later in Eq. 6.12.

The force curves in Figure 6.2(b) terminate at a certain point in the negative displacement region, which corresponds to the maximum possible compression of the vertical spring, given by the condition $H(0, z_{\min}) = 0$. In other words, the spring has been compressed to zero length. This condition can be solved for $z_{\min}$ and subsequently normalised for the equivalent $\xi_{\min}$, which are given by

$$z_{\min} = h - H_0\,, \quad \xi_{\min} = 1 - \eta\sqrt{\gamma^2+1}\,. \tag{6.9}$$

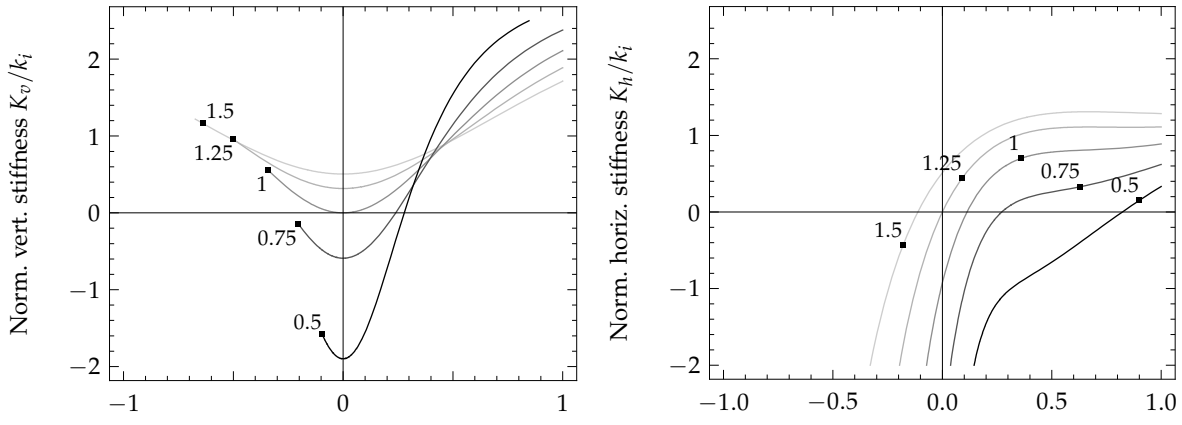

(a) Normalised vertical stiffness of the system calculated with Eq. 6.11.

(b) Normalised horizontal stiffness of the system calculated with Eq. 6.19.

FIGURE 6.3: Vertical and horizontal stiffness characteristics for a range of geometric ratios γ at $\alpha = 1$. Plots are labelled with their ratio to γ_{QZS}, which is calculated for a length ratio of $\eta = 1$.

§6.2.3 *Vertical stiffnesses*

The vertical stiffness characteristic, K_v, of the system is calculated by differentiating the vertical force, Eq. 6.8, with respect to vertical displacement z:

$$K_v = -\frac{\mathrm{d}}{\mathrm{d}z} F_{t_v}(x, z)\,, \tag{6.10}$$

$$\frac{K_v}{k_i} = -2\gamma^2 \sqrt{\frac{\gamma^2 + 1}{\left[\gamma^2 + \xi^2\right]^3}} + \alpha + 2\,. \tag{6.11}$$

Graphs of the normalised vertical stiffness K_v/k_i versus normalised displacement ξ are shown in Figure 6.3(a) together with the associated horizontal stiffness (Fig. 6.3(b)), which will be analysed in Section 6.2.4. The parameter selection required to achieve a quasi–zero stiffness condition in the vertical direction can be found by solving Eq. 6.11 for $K_v = 0$ at $\xi = 0$. This results in the relation

$$\gamma_{QZS} = \frac{2}{\sqrt{\alpha^2 + 4\alpha}} \tag{6.12}$$

which is used as the reference value of the geometric ratio γ for the results shown in Figures 6.2 and 6.3.

Achieving exactly quasi–zero stiffness with this spring is not feasible in practice as the stiffness characteristic becomes negative for $\gamma < \gamma_{QZS}$,

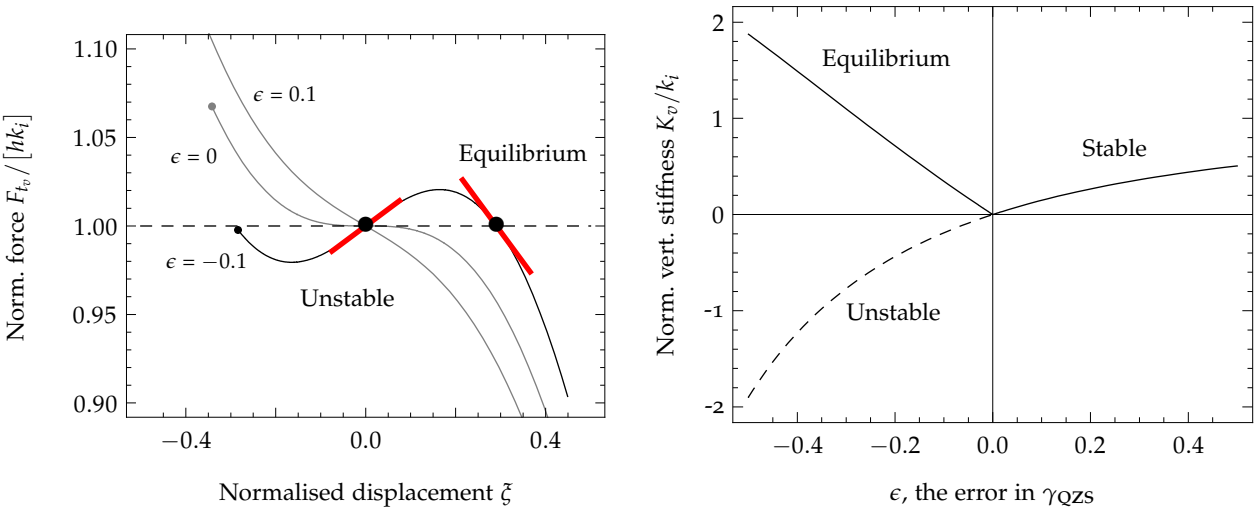

(a) The stable and unstable equilibrium points for $\epsilon \in \{-0.1, 0, 0.1\}$. The rest position will move from the unstable point to the stable point of equilibrium.

(b) The stiffness at equilibrium as ϵ varies; as the stiffness becomes negative, the stiffness shown corresponds to the stable point of equilibrium shown in the figure adjacent.

FIGURE 6.4: Force and stiffness of the inclined spring system near quasi–zero stiffness, showing the effect of unstable equilibrium.

as shown in Figure 6.3(a). This is important as the geometric ratio γ will have some uncertainty in its value due to environmental conditions such as temperature and physical imperfections such as creep. The deviation of γ from γ_{QZS}, ϵ, can be defined by

$$\gamma = \left[1 + \epsilon\right] \gamma_{QZS} \,. \tag{6.13}$$

Figure 6.4(a) shows the total vertical force, $F_{t_v}(x, z)$, of the system for $\epsilon \in \{-0.1, 0, 0.1\}$. It can be seen that negative values of ϵ (that is, a geometric ratio less than that for quasi–zero stiffness) correspond to negative stiffness at normalised displacement $\xi = 0$. A system in this condition is in a position of unstable equilibrium, and will move towards and remain at the position of stable equilibrium indicated in the figure rather than the design point at $\xi = 0$.

Figure 6.4(b) plots the stiffness at this deviated equilibrium point as ϵ varies; in the unstable zone, the system will move to the equilibrium point shown in Figure 6.4(a) away from $\xi = 0$.[1] It can be seen that the stiffnesses in

1. With sufficient excitation the system will 'snap though' from one equilibrium position to another with a resulting displacement profile that is comparatively large given the excitation amplitude; this mechanism has been proposed as a useful phenomenon for energy harvesting purposes [225].

the stable region for $\epsilon > 0$ are smaller than the stiffnesses in the equilibrium region for $\epsilon < 0$. This highlights the importance of never breaching the $\epsilon < 0$ instability condition. Therefore, a chosen value for the geometric ratio γ will approach γ_{QZS} but always be slightly greater in order to retain stability of the equilibrium position.

§6.2.4 *Horizontal stiffness characteristic due to vertical displacement*

Now that the vertical stiffness characteristics of the system have been analysed and a condition derived to achieve quasi–zero stiffness in that direction, the same approach will be taken for the horizontal behaviour. Only vertical displacements will be considered in assessing horizontal stability; for this study, the planar dynamics of the system have not been considered.

In order to calculate the horizontal stiffness of the system, the force from the vertical spring needs to be represented in terms of both vertical and horizontal displacements. This force, aligned in the direction of the nominally-vertical spring, is

$$F_v(x,z) = \left[\eta L_0 - \sqrt{x^2 + \left[-h + z + \eta L_0\right]^2}\right] k_v\,, \tag{6.14}$$

recalling that x is the displacement of the mass in the horizontal direction. Substituting $x = 0$ into Eq. 6.14 yields the previous Eq. 6.7. The horizontal component of this force is

$$F_{v_h}(x,z) = F_v(x,z)\frac{x}{H(x,z)}\,. \tag{6.15}$$

Similarly, the horizontal component of the force from the inclined spring on the left (referring to Figure 6.1(a)) is given by

$$F_{i_h}(x,z) = F_i(x,z)\frac{w+x}{L(x,z)}\,, \tag{6.16}$$

and the horizontal component of the force from the inclined spring on the right is

$$F_{i_h}(x,z)\Big|_{\text{right}} = -F_{i_h}(-x,z)\,. \tag{6.17}$$

The stiffness characteristic in the horizontal direction, K_h, is derived in a similar fashion to the vertical stiffness. The total force in the horizontal direction is

$$F_{t_h}(x,z) = F_{i_h}(x,z) - F_{i_h}(-x,z) + F_{v_h}(x,z)\,. \tag{6.18}$$

Differentiating with respect to horizontal displacement x and evaluating at $x = 0$ gives the horizontal stiffness characteristic as the vertical displacement varies,

$$\frac{K_h}{k_i} = -2\xi^2 \sqrt{\frac{\gamma^2+1}{\left[\gamma^2+\xi^2\right]^3}} + \frac{\alpha\left[\xi-1\right]}{\eta\sqrt{\gamma^2+1}+\xi-1} + 2\,. \tag{6.19}$$

This equation has been previously graphed together with the vertical stiffness in Figure 6.3 on page 184. In these figures, it can be seen that while the vertical stiffness is zero at normalised displacement $\xi = 0$ and geometric ratio $\gamma = \gamma_{\text{QZS}}$ (which is as derived), the horizontal stiffness exhibits separate behaviour, and can even be negative (that is, unstable) for values of γ lower than around $1.25\gamma_{\text{QZS}}$.

Since the vertical stiffness and horizontal stiffness are independent, further analysis into the behaviour of the horizontal stiffness at the vertical quasi–zero stiffness condition is warranted. Substituting the quasi–zero stiffness condition of Eq. 6.12 into Eq. 6.19 at displacement $\xi = 0$ gives the normalised horizontal stiffness as a function of stiffness ratio α:

$$\left.\frac{K_h}{k_i}\right|_{\text{V. QZS}} = 2 - \alpha\left[\frac{\left[\alpha+2\right]\eta}{\sqrt{\alpha\left[\alpha+4\right]}} - 1\right]^{-1}. \tag{6.20}$$

This equation is depicted in Figure 6.5; it can be seen that the horizontal stiffness of the spring may be chosen by varying both the spring stiffness ratio α and the spring length ratio η. Since the length ratio η is not found in Eq. 6.11, the horizontal and vertical stiffnesses may be tuned independently in order to achieve quasi–zero stiffness in both simultaneously.

To obtain zero stiffness in the horizontal direction at the nominal position, Eq. 6.20 is solved for $K_h = 0$, showing a relationship between α and η when the quasi–zero stiffness condition is achieved in both the vertical and the horizontal directions:

$$\alpha_{\text{QZS}}(\eta) = 2\left[\sqrt{\eta^2+1}-1\right], \text{ or } \quad \eta_{\text{QZS}}(\alpha) = \frac{1}{2}\sqrt{\alpha\left[\alpha+4\right]} \tag{6.21}$$

As a consequence, increasing η (say, in order to reduce the compression of the vertical spring) results in an increasing value of the vertical spring stiffness in order to remain at quasi–zero stiffness.

Using α_{QZS} from Eq. 6.21 in the stiffness equations 6.11 and 6.19 allows the stiffness characteristics of the system in the two directions to be compared when both have quasi–zero stiffness simultaneously. Considering the vertical stiffness first in Figure 6.6(a), it can be seen that increasing the length ratio η increases the vertical stiffness gradient, which is an important parameter

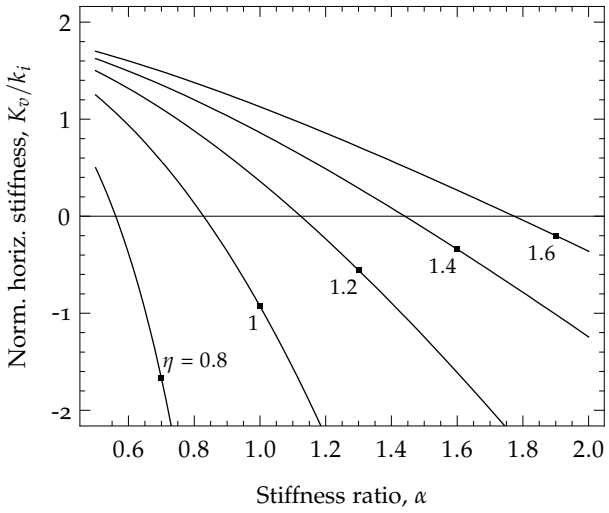

FIGURE 6.5: Horizontal stiffness characteristic at the vertical quasi–zero stiffness condition for varying stiffness ratio α and length ratio η, calculated with Eq. 6.20.

to be kept small in order to mitigate possible nonlinear dynamic effects that may arise due to a large rate of change of stiffness over displacement.

The graph of horizontal stiffness versus vertical displacement is shown in Figure 6.6(b). Note that contrary to the vertical case, the horizontal stiffness curves are not symmetric around zero vertical displacement. This is caused by the effect of the vertical spring; with negative vertical displacement (compression of the vertical spring) a horizontal perturbation results in an unstable horizontal force, whereas with positive vertical displacement (extension of the vertical spring) any horizontal forces act in a restoring sense.

Figure 6.6(b) illustrates that the quasi–zero stiffness condition is always marginally unstable in the horizontal direction since negative vertical displacement will result in negative horizontal stiffness. In practice this requires that the system be tuned slightly away from the quasi–zero stiffness condition in the horizontal direction after accommodating for the maximum disturbance displacement of the isolator. It is possible to do this without compromising the quasi–zero stiffness condition in the vertical direction because the spring length ratio η does not affect the vertical stiffness.

As an example, Figure 6.7 shows the horizontal stiffness for a stiffness ratio detuned by five percent below that required for quasi–zero stiffness (that is, $\alpha = 0.95\alpha_{\text{QZS}}$). In comparison with Figure 6.6(b), the spring has a stable displacement range of approximately $\xi = \pm 0.025$. Provided that the spring length ratio η is large enough, the horizontal stiffness at $\xi = 0$ is still significantly reduced.

Therefore, there is a direct compromise between the nonlinearity of the stiffness in the vertical direction (which increases with η) and the amount of stiffness reduction in the horizontal direction (which decreases with η).

§6.2.5 *Spring compression*

One factor that has not yet been addressed with this particular design is the amount of spring compression required at the equilibrium position of quasi–zero stiffness. The total allowable compression will be limited by the shape and properties of the springs themselves. By adjusting the design parameters of the inclined spring system, the amount of compression in each spring at equilibrium can be selected.

The amount of spring compression can be analysed with a metric here denoted the 'compression ratio' related to the uncompressed spring length. For the inclined and vertical springs, respectively, the compression ratios C_i and C_v are given by

$$C_i = 1 - \frac{L(x,z)}{L_0}\,, \quad C_v = 1 - \frac{H(x,z)}{H_0}\,. \tag{6.22}$$

This metric for the compression ratio was chosen to be zero for a spring in its uncompressed position and unity if it is compressed by its full length.

The compression ratios were evaluated at the quasi–zero stiffness condition in both directions; that is, $(x,z) = (0,0)$, $\gamma = \gamma_{\text{QZS}}$, and $\eta = \eta_{\text{QZS}}$ (see Eqs 6.12 and 6.21), yielding

$$C_i\Big|_{\text{QZS}} = \frac{\alpha}{\alpha+2}\,, \quad C_v\Big|_{\text{QZS}} = \frac{2}{\alpha+2}\,. \tag{6.23}$$

The compression ratios of the vertical and inclined springs at quasi–zero stiffness are shown in Figure 6.8 as functions of varying spring stiffness ratio α. (Recall that quasi–zero stiffness is achieved by adjusting η for each specified value of α with the relationship shown in Eq. 6.21.) These results show that a large compression (greater than fifty percent) in at least one of the springs is required to achieve quasi–zero stiffness.

§6.2.6 *The general applicability of the inclined springs system*

In order to adapt this system to withstand time-varying load conditions, both the anchor positions of the inclined and the vertical springs must be adjusted in order to tune for, first, the required load bearing, and second, the amount of negative stiffness required to achieve quasi–zero stiffness in the vertical direction.

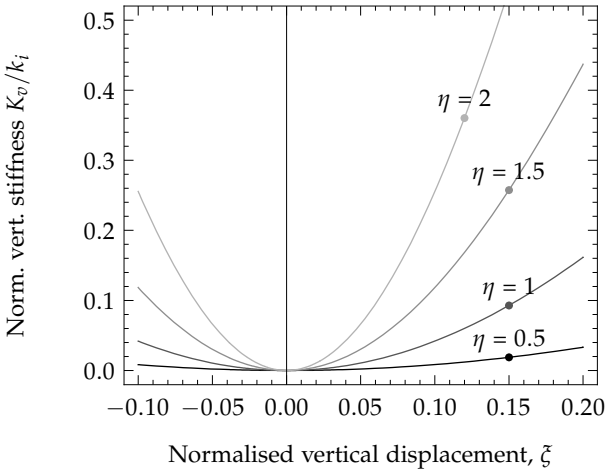

(a) Normalised vertical stiffness of the system.

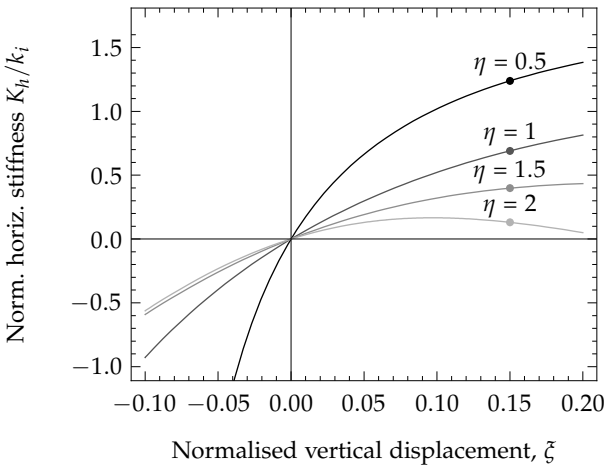

(b) Normalised horizontal stiffness of the system; negative displacement will result in negative stiffness.

FIGURE 6.6: Vertical and horizontal stiffness characteristics at quasi–zero stiffness in both directions, for a range of spring length ratios, η.

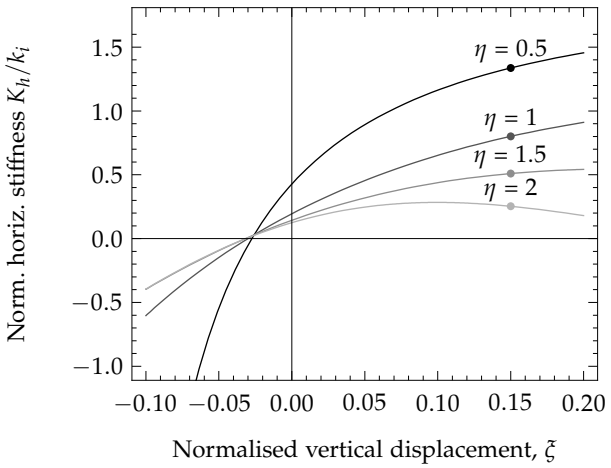

FIGURE 6.7: Normalised horizontal stiffness of the system at $\alpha = 0.95\alpha_{\text{QZS}}$ in order to obtain a small range of displacement around $\xi = 0$ with positive stiffness (compare with Figure 6.6(b) which has negative stiffness for $\xi < 0$). The vertical quasi–zero stiffness condition is unaffected.

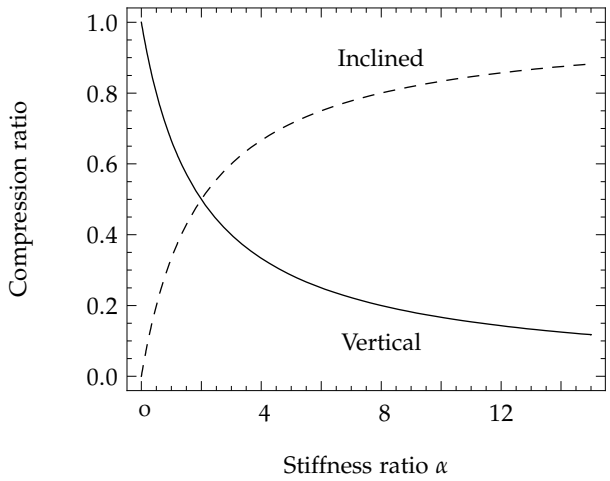

FIGURE 6.8: Compression relationship of the springs for a range of spring stiffness ratios, at quasi–zero stiffness both horizontally and vertically.

Dynamically changing the system for quasi–zero stiffness in the horizontal direction requires that either the uncompressed spring lengths or the spring stiffnesses be adjustable during operation. Spring lengths could be adjusted by mounting the springs on ball-screws or a similarly stiff actuator. Springs stiffnesses could be varied, for example, with magnetorheological fluid springs, or using geometric effects with leaf springs in a four-bar linkage [74].

Note that the principles discussed for horizontal stiffness can be extended to a three-dimensional system, most easily with a rotationally-symmetric structure with horizontally aligned springs in each plane. The main conclusion from the analysis in this section is that quasi–zero stiffness in both vertical and horizontal directions can be achieved with this spring arrangement, which is not generally considered in analyses of this type. However, the tuning required to maintain quasi–zero stiffness for this spring arrangement is difficult to achieve in practice. In the next section, a magnetic system is examined in detail that exploits a similar negative stiffness principle but can be more easily adjusted online.

§6.3 Magnetic quasi–zero stiffness

This section examines a different system that can also exhibit localised zero stiffness. Introduced in Section 3.3.3, this system consists of a pair of fixed magnets that supports a mass against gravity by respectively repelling the mass from below and attracting it from above, as shown in Figure 6.9. This

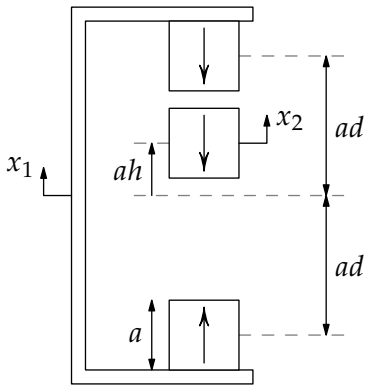

FIGURE 6.9: Schematic of a magnetic spring with quasi–zero stiffness at $h = 0$ to isolate displacement x_2 from ground disturbance vibration x_1. Large arrows indicate direction of polarisation of the magnets. In this section, cubical magnets are used with side length a, distance $2ad$ between the centres of the fixed magnets, and displacement of the floating magnet from the zero stiffness position ah. Rest position at positive h (upwards) corresponds to unstable equilibrium; negative h (downwards) is stable.

arrangement of magnets has seen some previous attention [211, 237, 238], in which the force versus displacement characteristic can be approximated by a quadratic polynomial for small gaps between the magnets.

A 'cubic-like' force curve such as discussed in Section 6.2 can be more useful because it creates a stable inflection point with localised zero stiffness; in contrast, a quadratic-type spring is marginally stable at its quasi–zero stiffness position and must be operated away from this point to avoid moving into the unstable region. For example, the inclined spring system can be tuned such that its force characteristic is very close to the cubic-like quasi–zero stiffness regime (Fig. 6.4(a)) and displacements around the equilibrium point are guaranteed to be stable. On the other hand, for the quasi–zero stiffness magnetic spring, as soon as the mass displaces closer to the top magnet than the bottom the system is now unstable regardless of the tuning of the magnet locations. Nonetheless, the magnet arrangement is worth studying as a mechanism to achieve *low* stiffness, since this device reduces the stiffness in all three translational degrees of freedom in a mechanically simple way compared to the inclined spring system studied in the previous section.

As well as its use to design low frequency isolation mounts, this idea of non-contact magnetic forces can have particular application in support structures where a reduction in stiffness is desired to mitigate a vibration problem that has been discovered after its construction. The noncontact

nature of the force between the magnets allows their easy attachment to an existing structure.

The structure of this section is as follows. The exact equation for the forces between two cubical magnets is presented in Section 6.3.1, which is used to calculate the exact and approximate force versus displacement profiles of the quasi–zero stiffness magnetic spring. In Section 6.3.2, the criteria that govern the behaviour of a vibration isolation device are applied to the magnetic spring and suitable ranges for the design parameters are found to achieve the design goals. Finally, Section 6.3.4 analyses the dynamic behaviour of the spring to ensure that the isolation capabilities are not compromised by the nonlinear characteristics of the magnetic spring.

§6.3.1 *Magnet forces*

For this study, the simplified expressions of Akoun and Yonnet [5] for cubical magnets with a vertical offset are used, as shown in Eq. 2.34 on page 64. The distance between the magnet centres d_z (Figure 2.6 on page 60) with respect to the size of the magnets (side length a) is expressed as a normalised length l:

$$l = d_z/a\,. \tag{6.24}$$

After some manipulation of the original equation given these simplifying assumptions, the force $F_s(a,l)$ on the second magnet in attraction (that is, for magnets with polarisation in the same direction) can be shown to be directly proportional to the facing area of the magnets, a^2, for a fixed normalised displacement, l, between the magnets:

$$F_s(a,l) = a^2 f_s(l)\,. \tag{6.25}$$

For magnets in repulsion, the expression has opposite sign. The derived expression for the normalised force $f_s(l)$ was given in Eq. 2.35 on page 64.

The stiffness between two cubical magnets can be calculated by differentiating the force expression in Eq. 6.25 with respect to vertical displacement $d_z = al$ and can be shown to be proportional to the magnet size a:

$$K_s(a,l) = \frac{\partial}{\partial d_z} F_s(a,l) = \frac{1}{a}\frac{\partial}{\partial l} a^2 f_s(l) = a k_s(l)\,. \tag{6.26}$$

The derived expression for the normalised stiffness $k_s(l)$ is given in Eq. 2.38 on page 65.

A 'quasi–zero stiffness' magnetic spring consists of an attracting magnetic pair above a repelling magnet pair as shown in Figure 6.9, originally introduced in Section 3.3.3. Parameter ad is the gap between the centres of the

magnet pairs at quasi–zero stiffness, and $x_2 = ah$ is the static displacement of the floating mass about the centre line between the magnets. The parameters d and h are referred to as normalised magnet gap and normalised magnet displacement, respectively. The force due to the lower magnet in repulsion is

$$F_{\text{repl}}(a, d, h) = -F_s(a, ad + ah) = -a^2 f_s(d + h)\,, \tag{6.27}$$

and the force due to the upper magnet in attraction is

$$F_{\text{attr}}(a, d, h) = F_s(a, -ad + ah) \tag{6.28}$$
$$= a^2 f_s(-d + h). \tag{6.29}$$

The total force on the floating magnet, $F_T(a, d, h)$, is a superposition of $F_{\text{repl}}(a, d, h)$ and $F_{\text{attr}}(a, d, h)$, yielding

$$F_T(a, d, h) = F_{\text{repl}}(a, d, h) + F_{\text{attr}}(a, d, h) \tag{6.30}$$
$$= a^2 \left[- f_s(d + h) + f_s(-d + h) \right] \tag{6.31}$$
$$\stackrel{\text{def}}{=} a^2 f_T(d, h)\ . \tag{6.32}$$

The stiffness of the system can be similarly expressed as

$$K_T(a, d, h) = a k_T(d, h)\,, \tag{6.33}$$

where

$$k_T(d, h) = -k_s(d + h) + k_s(-d + h)\,. \tag{6.34}$$

The force $f_T(d, h)$ and stiffness $k_T(d, h)$ of the magnetic spring are readily calculated for values of normalised displacement and gap, h and d, from Eqs 2.35 and 2.38. However, these expressions are too complex for use in any calculation where they must be inverted (say, finding a value of d for a certain $k_T(d, h)$). It is therefore necessary to obtain a simpler model of $f_T(d, h)$.

Previously, due to the shape of the force curve, $f_T(d, h)$ has been modelled as a quadratic polynomial [211, 237], with coefficients $q_0(d)$, $q_2(d)$ that vary with magnet gap:

$$f_T(d, h) \approx q_2(d)\, h^2 + q_0(d)\,. \tag{6.35}$$

This has the advantage of simplicity, and over small displacement ranges this approximation yields adequate results, but the coefficients are dependent on the gap between the magnets and the displacement range used to fit the model.

A more accurate result (which is also accurate over larger displacement ranges) can be achieved with a quartic polynomial approximation,

$$f_T(d, h) \approx q_4(d)\, h^4 + q_2(d)\, h^2 + q_0(d)\,, \tag{6.36}$$

but the same criticisms hold as for the quadratic polynomial model: the resulting model is not general; furthermore, if the model approximation is to also represent changes in magnet gap d, the functions $q_0(d)$, $q_2(d)$, and $q_4(d)$ require high-order polynomials to represent the variation sufficiently well.

A simpler approximation of the normalised force between two magnets $f_s(l)$ can be found by numerically fitting the constant coefficients Q_0, Q_1, and possibly n in the empirical approximation

$$f_s(l) \approx \frac{Q_0}{\left[Q_1 + l\right]^n} \,. \tag{6.37}$$

This approximation can be used to calculate the forces in the quasi–zero stiffness magnetic spring. Xu and Tamura [295] used the more complicated empirical approximation

$$f_s(l) \approx Q_3 \left[\frac{Q_0}{Q_1 + l}\right]^n + Q_2 \,, \tag{6.38}$$

but in this case the additional complexity does not justify the slight increase in accuracy this expression may offer.

When applying Eq. 6.37, Bonisoli and Vigliani [46] used $n = 3$, and Piombo et al. [219] recommended either $n = 2$ or $n = 4$. The values for n they selected were based on the best fit curves of the forces for the specific geometry of their magnets in each case. As these are empirical equations, however, n is not restricted to integer values and does not have to be chosen *a priori* to the curve fitting.

An unbounded least squares fit was performed with Eq. 6.37 varying all three parameters Q_0, Q_1, and n over the range $2 \leq h \leq 5$ to achieve an approximation of Eq. 2.35. The quality of the approximation was assessed using percentage error

$$\frac{f_s(l) - \tilde{f}_s(l)}{f_s(l)} \tag{6.39}$$

where $\tilde{f}_s(l)$ is the approximation of $f_s(l)$ for each parameter fit. Over the displacement range used to fit the model, modelling errors of less than 1 % were achieved. (The remanence magnetisation of each magnet, B_r, was taken as unity.) Including displacements outside of this range (especially $1 < h \leq 2$) diminishes the accuracy of the fit, but is less relevant for this work: displacements $1 < h \leq 2$ generate high stiffnesses, and displacements $h \geq 5$ have low supporting forces. Both of these properties are undesirable for a vibration isolator in terms of resonance frequency and adequate load bearing, respectively.

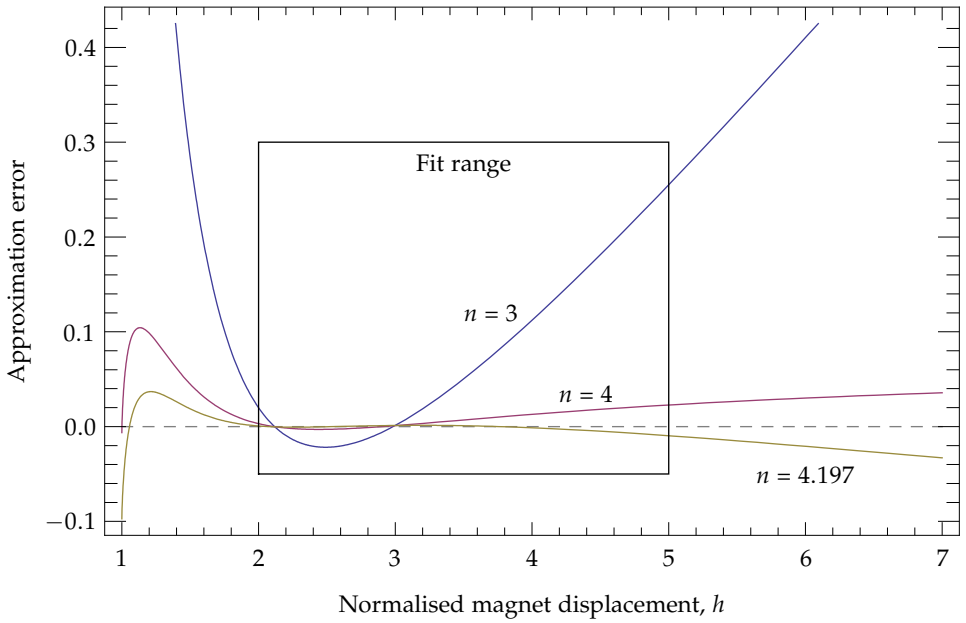

FIGURE 6.10: Modelling errors of Eq. 6.37 compared to the exact Eq. 2.35, for parameters shown in Table 6.2.

Figure 6.10 shows the approximations found with Eq. 6.37 for set values $n = 3$ and $n = 4$ (only coefficients Q_0 and Q_1 are varied); in the third curve, n has also been allowed to range for the least-squared fit. Table 6.2 displays the values for all three calculated parameters in each case. The curves for $n = 2$ and $n = 5$ produce much greater errors than those shown in Figure 6.10 and have been omitted for clarity.

An empirical approximation of Eq. 6.25 for the force between two coaxial cubical magnets is thus given by

$$F_s(a,x) \approx \pm a^2 B_r^2 \frac{6.028 \times 10^5}{\left[0.1883 + x/a\right]^{4.197}} \tag{6.40}$$

TABLE 6.2: Best fit parameters for Eq. 6.37. Fixed integer values of n were chosen for the first two cases, and the latter value best fits the model by varying all three parameters. Note that these constants are unitless.

n	Q_0	Q_1
3	6.580×10^4	-0.5796
4	4.071×10^5	0.0607
4.197	6.028×10^5	0.1883

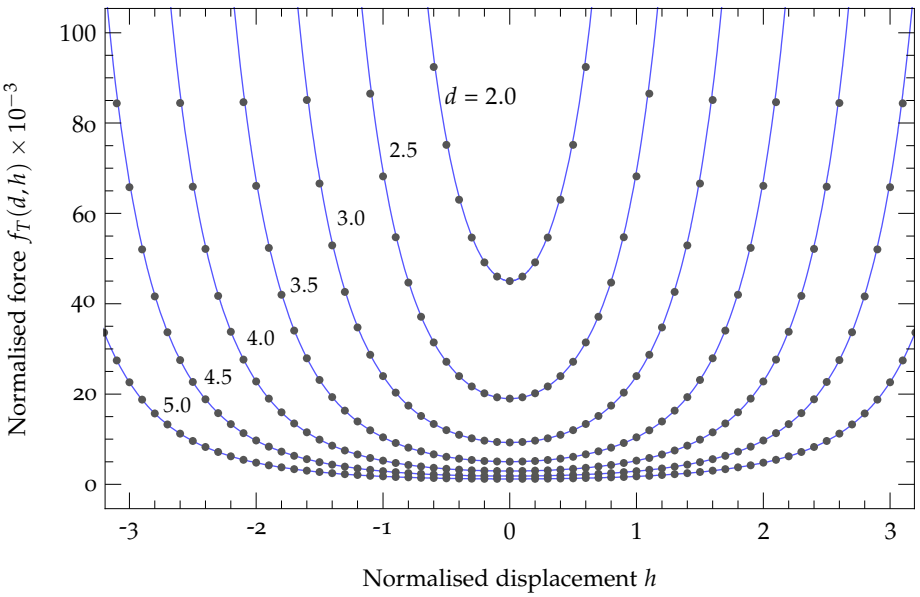

FIGURE 6.11: Normalised force $f_T(d,h)$ versus displacement h curves of a quasi–zero stiffness magnetic system for a range of normalised gap d (the stiffness is zero at $h = 0$). Single points correspond to the exact solution; solid lines correspond to the approximation given by Eq. 6.37.

with force $F_s(a,x)$ in Newtons, magnet size a and centre displacement x both in metres, and remanence magnetisation B_r in Tesla, where the expression is positive for magnets in repulsion and negative for magnets in attraction.

Figure 6.11 shows the model of the magnetic system using Eq. 6.37 to calculate the force due to the repelling and attracting magnets separately:

$$f_T(d,h) \approx Q_0 \left[Q_1 + d + h\right]^{-n} + Q_0 \left[Q_1 + d - h\right]^{-n}, \tag{6.41}$$

where Q_0, Q_1, and n are the best-fit parameters previously discussed. This solution is both simpler in form and more accurate than the polynomial models of Eqs 6.35 and 6.36. It is also much easier to invert numerically than the exact Eq. 6.32, although note that Eq. 6.41 still cannot be algebraically inverted and numerical methods are used instead. The normalised stiffness can be approximated by differentiating Eq. 6.41 with respect to h (as shown previously in Eq. 6.26):

$$k_T(d,h) \approx nQ_0\left[Q_1 + d + h\right]^{-n-1} + nQ_0\left[Q_1 + d - h\right]^{-n-1}. \tag{6.42}$$

In this section, a model of the magnet forces was presented that is accurate over large relative displacements. Despite the fact that the vibration disturbance will occur in small magnitudes relative to the size of the magnet

dimension, it is important to model the magnet forces accurately over a large displacement range so that the design evaluations in the next section may be applied over variations in magnet gap.

§6.3.2 *Design criteria*

In the previous section, a magnetic system was introduced with an exact expression and various approximations for calculating the force versus displacement characteristics for a range of system designs. It is proposed that this system is suitable for a vibration isolation platform due to the possibility of low inherent dynamic stiffness of the design. However, the stiffness is dependent on the load that is being supported, and the magnetic arrangement must be designed for this purpose.

Four constraints were imposed on the system parameters to satisfy the following design criteria:

Strong The magnets are large enough to support the weight of the payload.

Soft The stiffness is small enough to achieve a low natural frequency.

Saturation The magnets will not come into contact under disturbance.

Stability Excessive displacement will not result in instability.

Bounds of normalised force and normalised displacement are depicted graphically in Figure 6.12 to help visualise these constraints, as will be discussed further as each criterion is introduced and defined mathematically.

The normalised equilibrium position of the system h_q can be found by equating the magnet force at equilibrium f_q with the load due to gravity mg and inverting numerically:

$$f_q(a, d, m) = f_T\left(d, h_q\right) = mg/a^2. \tag{6.43}$$

A positive displacement of the mass ($h \geq 0$) is unstable, and so Eq. 6.43 must be solved such that $h_q < 0$. Figure 6.13 shows the equilibrium position h_q varying over a and d for a system of mass $m = 0.5\,\mathrm{kg}$.

The normalised equilibrium position h_q of a mass can be approximated from the polynomial fits of the force curve by equating, for example, Eq. 6.36 with the force due to gravity and solving for h. However, the more accurate approximation Eq. 6.41 cannot be algebraically rearranged to solve for h; hence, solutions based on that equation must be obtained numerically.

The magnet size and gap must be chosen based on h_q to ensure that the spring is of sufficient stiffness to support a desired load but not so stiff

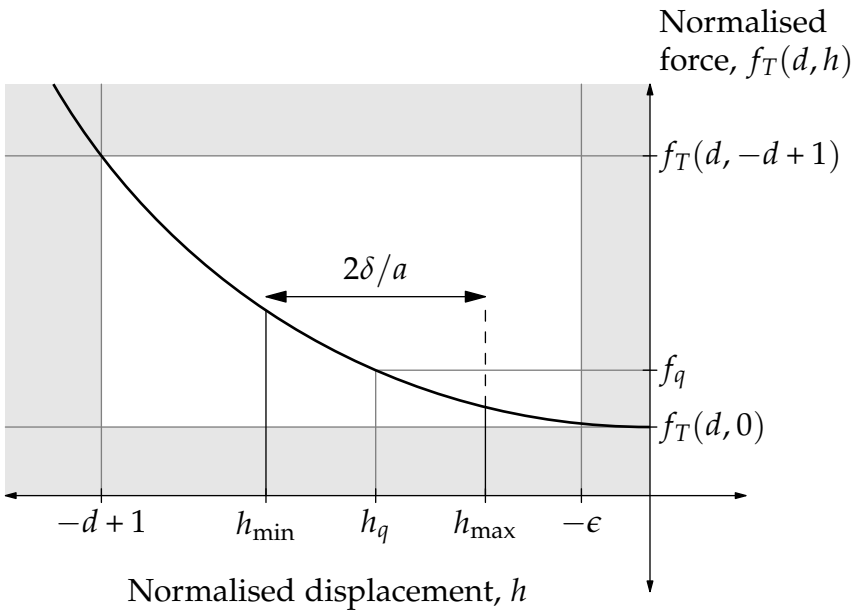

FIGURE 6.12: Normalised force versus normalised displacement curve illustrating the bounds of both allowable load that can be bourne and the displacement range of the magnet; see Eqs 6.44, 6.46 and 6.47 respectively for the mathematical representations. $-d+1$ is the position where the floating magnet is touching the upper face of the lower fixed magnet, $2\delta/a$ is the displacement bound due to the external excitation, and $-\epsilon$ is the closest allowable position to the quasi–zero stiffness position.

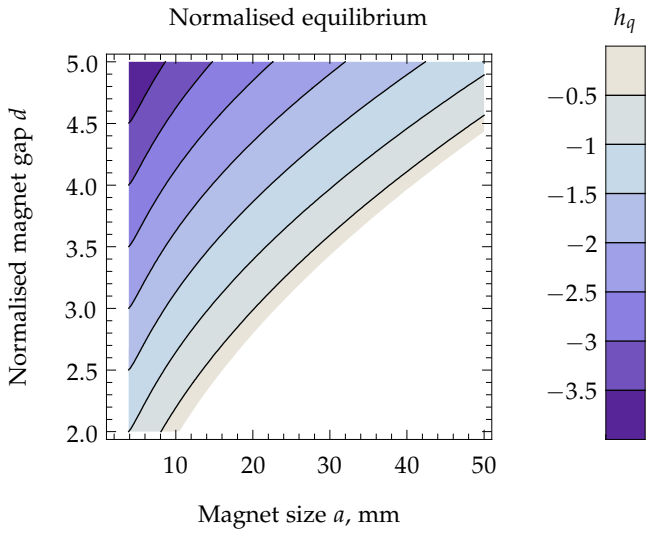

FIGURE 6.13: Map of the normalised equilibrium position h_q over varying magnet size a and normalised magnet gap d for a system with mass $m = 0.5\,\text{kg}$.

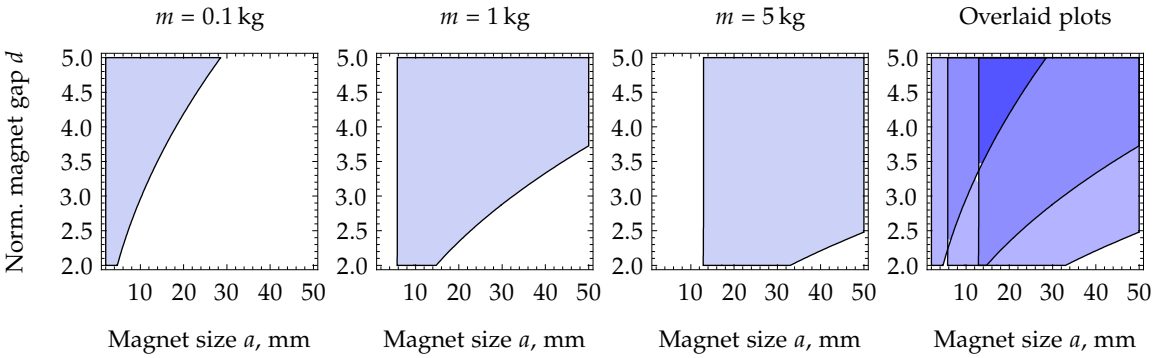

FIGURE 6.14: Regions of a and d satisfying the static deflection criterion of Eq. 6.44 for a range of masses. Larger masses require larger magnet sizes.

that the supported mass cannot be in equilibrium in the stable region of the spring. The 'strong' criterion is defined to achieve these constraints:

$$f_T(d, 0) < mg/a^2 < f_T(d, -d + 1)\,, \tag{6.44}$$

which is shown graphically in the vertical axis of Figure 6.12. This criterion is depicted in Figure 6.14 as a region over the parameters a and d for three different mass loads. The first inequality in Eq. 6.44 corresponds to the curved diagonal boundary in Figure 6.14 and the second inequality corresponds to the vertical boundary. The shape and location of the regions show that for a fixed magnet gap, larger magnets are required to support larger loads.

In Figures 6.14 to 6.17, the individual criteria are plotted with a range of relevant parameters on three separate graphs. The fourth graph in each figure has the three plots overlaid with transparency to demonstrate the trend of the curves due to each criteria. For example, it can be seen in Figure 6.14 that adjusting the mass affects the region for both magnet size and magnet gap.

Assuming that linearisation is appropriate to model the vibration response of the system, the equivalent linear stiffness at equilibrium, K_q, must satisfy the natural frequency criterion: $K_q = K_T\big(a, d, h_q\big) \leq \omega_d^2 m$, where ω_d is the maximum allowable natural frequency. From Eq. 6.42, this stiffness, or 'soft', requirement can be formulated as

$$\big[Q_1 + d + h_q\big]^{-n-1} + \big[Q_1 + d - h_q\big]^{-n-1} \leq \frac{\omega_d^2 m}{anQ_0}. \tag{6.45}$$

This criterion is shown for a range of desired nominal stiffnesses in Figure 6.15. As the natural frequency decreases, larger magnets are required with a larger magnet gap to support the load with a small force gradient.

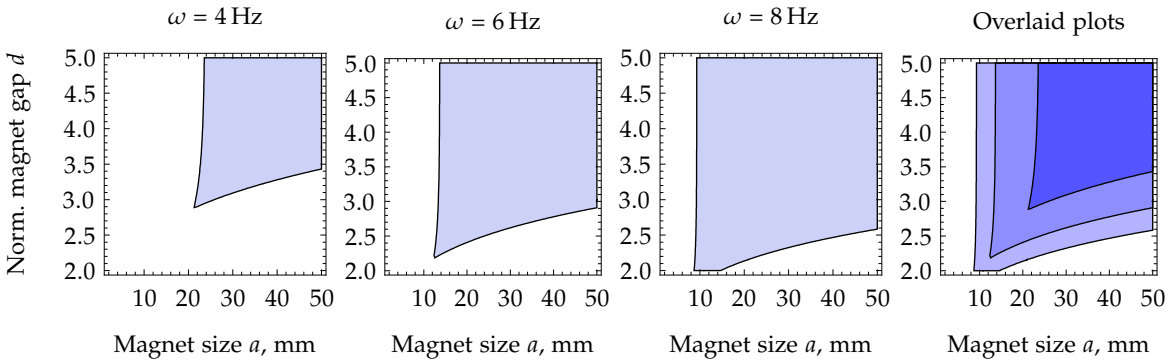

FIGURE 6.15: Regions of a and d satisfying the natural frequency criterion of Eq. 6.45 for a range of allowable natural frequencies and a mass $m = 0.5\,\text{kg}$. A lower natural frequency results in a smaller range of allowable magnet sizes and gaps.

Finally, the amplitude of the input vibration must be smaller than the physical displacement bounds of the system. This can be visualised on a normalised force/displacement plot as shown the horizontal axis of Figure 6.12, which shows a maximum (absolute) displacement, δ, of the mass from its equilibrium position.

Considering first the lower bound of displacement h_{min}, which is required to be high enough such that the floating magnet will not come into contact with the lower base magnet. With reference to Figure 6.12, this 'saturation' criterion is

$$h_{\text{min}} = h_q - \delta/a \geq -d + 1\,. \tag{6.46}$$

The more critical 'stability' criterion considers the upper bound of displacement h_{max}, which must remain below a certain buffer region to ensure that the moving magnet is not perturbed past the quasi–zero stiffness position into the unstable zone. With tolerance $a\epsilon$ as the closest allowable distance to the (marginally stable) quasi–zero stiffness position at which the system can operate, the stability criterion is

$$h_{\text{max}} = h_q + \delta/a < -\epsilon\,. \tag{6.47}$$

Note that in practice the maximum displacement of the spring will not be symmetric with input displacement due to the softening spring stiffness. This analysis is simplified, however, by representing the maximum displacement in the stability and saturation criteria (Eqs 6.46 and 6.47) with the same term.

These latter saturation and stability constraints impose only small limits on the design of the system. The saturation criterion, shown in Figure 6.16 as a region over the parameters a and d for a range of δ, limits the lower size of the magnet.

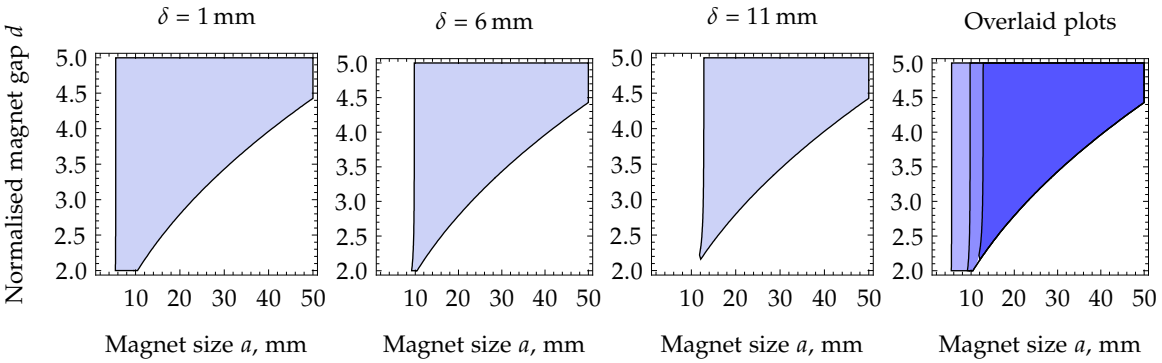

FIGURE 6.16: Regions of a and d satisfying the maximum displacement criterion of Eq. 6.46 for a range of disturbance displacements δ and a mass $m = 0.5\,\text{kg}$. A larger maximum displacement increases the minimum size of the magnets.

TABLE 6.3: Summary of design criteria for quasi–zero stiffness magnetic design.

Criterion	Equation	Figure
Strong	6.44	6.14
Soft	6.45	6.15
Saturation	6.46	6.16
Stability	6.47	6.17

The stability criterion is governed by two parameters, δ and ϵ, which are varied in Figures 6.17(a) and 6.17(b) respectively. Again, this criterion only has a small effect on the constraint region, but it is an important one. Because the stability criterion limits the minimum distance between the quasi–zero stiffness position and the equilibrium position, this can prevent the spring from reaching the very low equilibrium stiffnesses found just below the quasi–zero stiffness position.

The introduced criteria may be simultaneously satisfied for some specified values of mass, natural frequency, and displacement range (m, ω, and δ) by varying the free parameters magnet size a and magnet gap ad. A summary of the criteria introduced previously is shown in Table 6.3. The shared region of the criteria previously introduced (Eqs 6.44 to 6.47) are shown in Figure 6.18 for various combinations of supported mass and natural frequency. This figure presents a complete design map that shows how the techniques presented in this section can be used for speculative design work and optimisation.

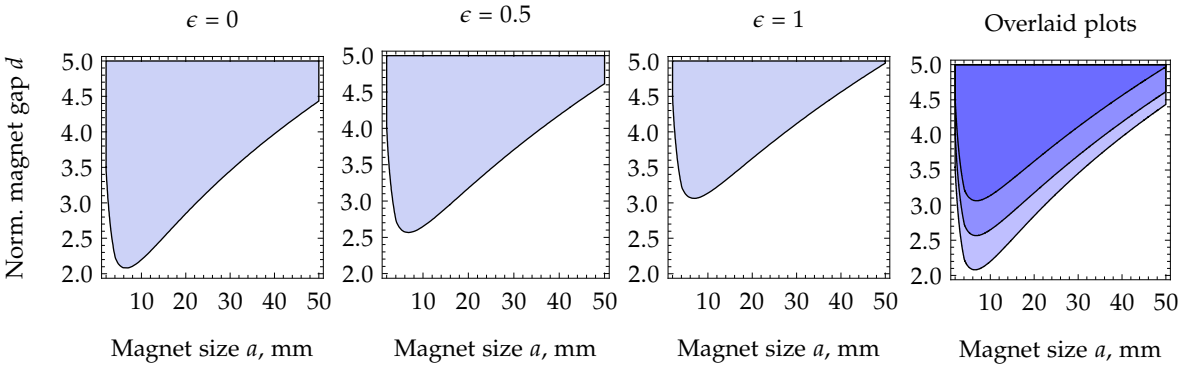

(a) A range of normalised displacement tolerances ϵ and a maximum disturbance displacement of $\delta = 5\,\text{mm}$.

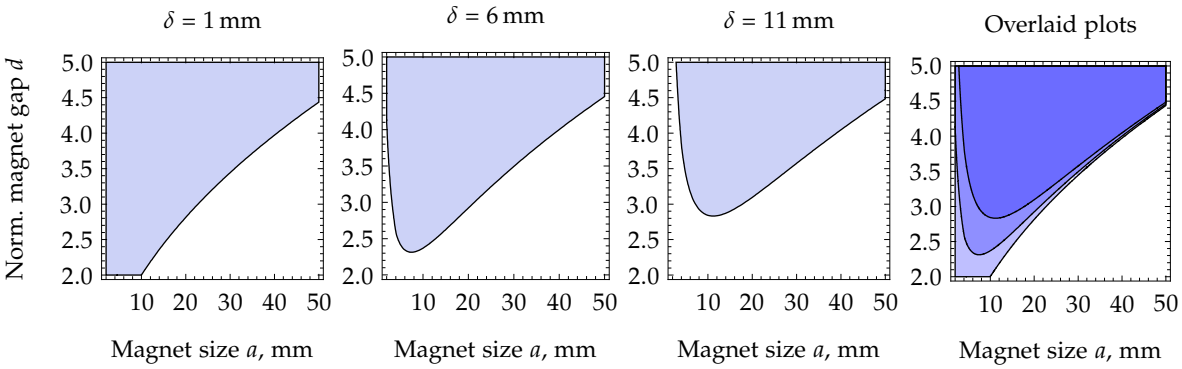

(b) A range of disturbance displacements δ and a normalised displacement tolerance $\epsilon = 0.1$.

FIGURE 6.17: Regions of a and d satisfying the stability criterion of Eq. 6.47 for a range of normalised displacement tolerances ϵ and maximum disturbance displacements. The displacement tolerance has a greater effect on the design constraints.

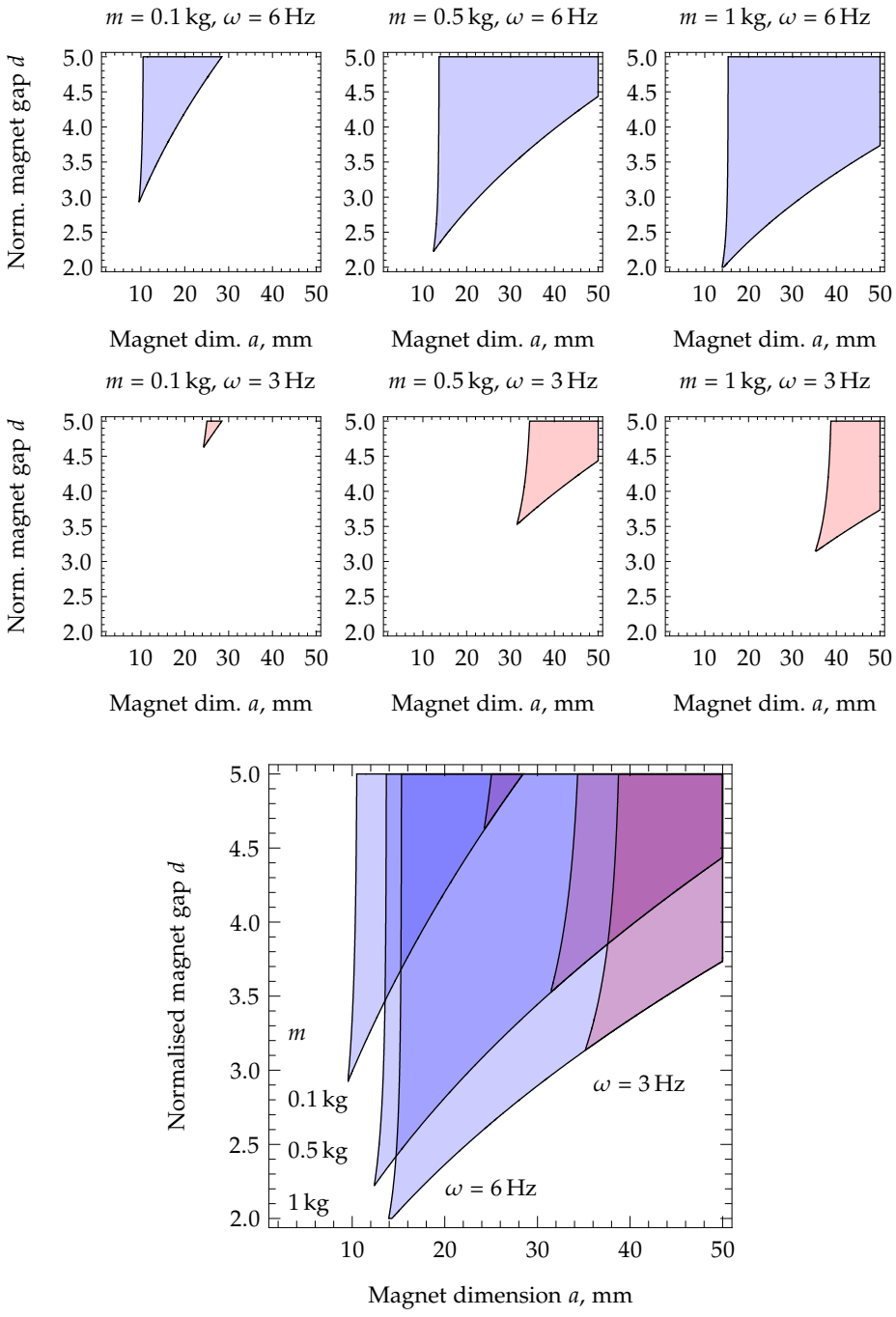

FIGURE 6.18: Regions of a and d satisfying all design criteria, demonstrating the effects of changing the mass m and the natural frequency ω of the desired system.

§6.3.3 *Measure of stiffness reduction*

In the previous section, ranges for magnet size and magnet gap were shown to achieve certain design criteria. It is not impossible, however, that this process could yield a design that behaves acceptably with only a single repulsive magnet: the magnet gap could be so large as to render the effect of the negative stiffness negligible.

The total stiffness characteristic of the magnetic system is given by Eq. 6.34 as the sum of the stiffnesses due to repulsive and attractive magnets respectively. At equilibrium, this can be written as

$$\begin{aligned} K_q(a,d,m) &= K_{\text{repl}}\left(a,d,h_q\right) + K_{\text{attr}}\left(a,d,h_q\right) \\ &= K_{\text{repl}} \cdot \left[1-\kappa\right], \end{aligned} \tag{6.48}$$

where

$$\kappa\left(a,d,h_q\right) = \left|\frac{K_{\text{attr}}}{K_{\text{repl}}}\right|. \tag{6.49}$$

The variable $\kappa\left(a,d,h_q\right)$ can be considered as the ratio of 'stiffness reduction' achieved by the presence of the attractive magnet. For $\kappa = 0$, the upper magnet is providing no negative stiffness to the system; for $\kappa = 1$, the equilibrium position is at quasi-zero stiffness and the system is marginally stable.

Figure 6.19 illustrates the variation of κ over a particular design region; this plot shows that designs achieved with larger magnet gaps have little influence from the stiffness reducing effect of the attractive magnet. As κ tends towards one, the natural frequency drops dramatically as the equilibrium position approaches the quasi–zero stiffness position (compare with Figure 6.13).

§6.3.4 *Nonlinear behaviour*

In Section 6.3.2, constraints were imposed on the design of the magnetic system such that a certain natural frequency was achieved for a given mass loading. The slope of the force versus displacement curve at equilibrium was used as the basis for the natural frequency criterion. However, as the mass is perturbed from equilibrium the stiffness of the spring changes. When designing for vibration isolation, it is important to ensure that this nonlinearity does not produce a significant effect in the response of the system.

As a proxy for the nonlinearity of the system, the change in spring stiffness over its maximum peak-to-peak displacements can be compared to

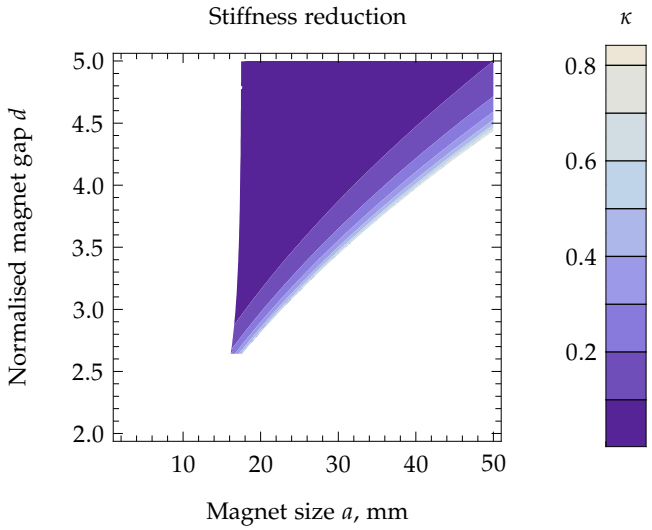

FIGURE 6.19: Contours of stiffness reduction κ due to the negative stiffness of the attractive magnet, shown inside the region of a, d satisfying all design criteria for parameters $m = 1\,\text{kg}$, $\omega = 5\,\text{Hz}$, $\delta = 1\,\text{mm}$, $\epsilon = 0.1$.

its nominal stiffness at equilibrium. This measure will be refered to here as the nonlinearity ratio η_k, given by

$$\eta_k = \frac{K_T\left(a, d, h_q + \delta/a\right) - K_T\left(a, d, h_q - \delta/a\right)}{K_T\left(a, d, h_q\right)}. \tag{6.50}$$

For the quadratic approximation of $f_T(d, h)$ given by Eq. 6.35, η_k is the ratio between the maximum displacement and the equilibrium position:

$$\eta_k \approx \frac{\delta}{a h_q}, \tag{6.51}$$

and since $\delta/a < \left|h_q\right|$ for stability (recall Eq. 6.47), it follows that the degree of nonlinearity is directly related to the amplitude of disturbance vibration. Figure 6.20 demonstrates the manner in which η_k varies over an allowed region of design parameters, with $k_T(d, h)$ given by the exact expression of Eq. 6.34.

The nonlinearity ratio increases both as magnet size and normalised magnet gap decrease. Comparing Figure 6.20 to Figures 6.13 and 6.19, it can also be seen that the nonlinearity ratio increases the closer the equilibrium displacement becomes to the quasi–zero stiffness position, and the greater the effect of the negative stiffness from the attractive magnet.

To analyse these nonlinear effects on the vibration response of the magnetic spring, the system shown in Figure 6.9 is simulated with the dynamics

$$m\ddot{x}_2 + c\left[\dot{x}_2 - \dot{x}_1\right] + F_T\left(a, d, \left[x_2 - x_1\right]/a\right) - mg = 0 \tag{6.52}$$

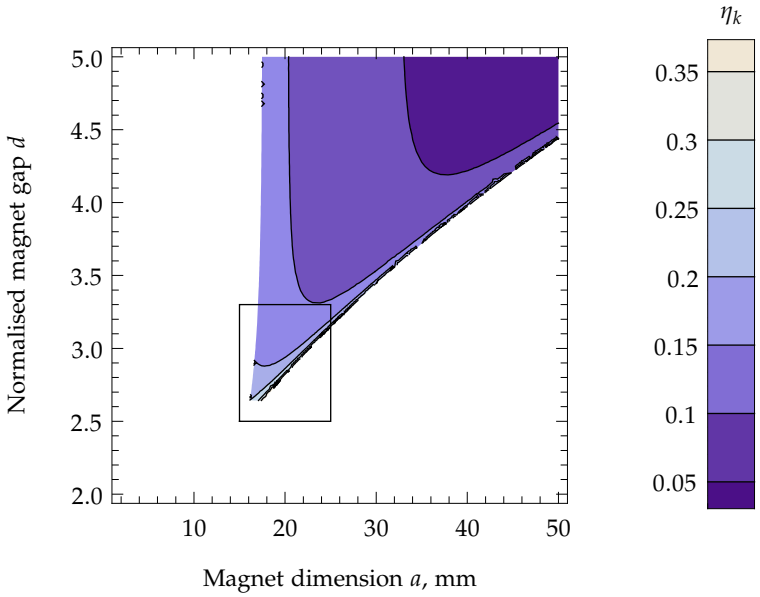

FIGURE 6.20: Contours of nonlinearity ratio η_k shown inside the region of a, d satisfying all criteria for parameters $m = 1\,\text{kg}$, $\omega_d = 5\,\text{Hz}$, $\delta = 1\,\text{mm}$, $\epsilon = 0.1$. A closeup (of the box) is shown in Figure 6.21.

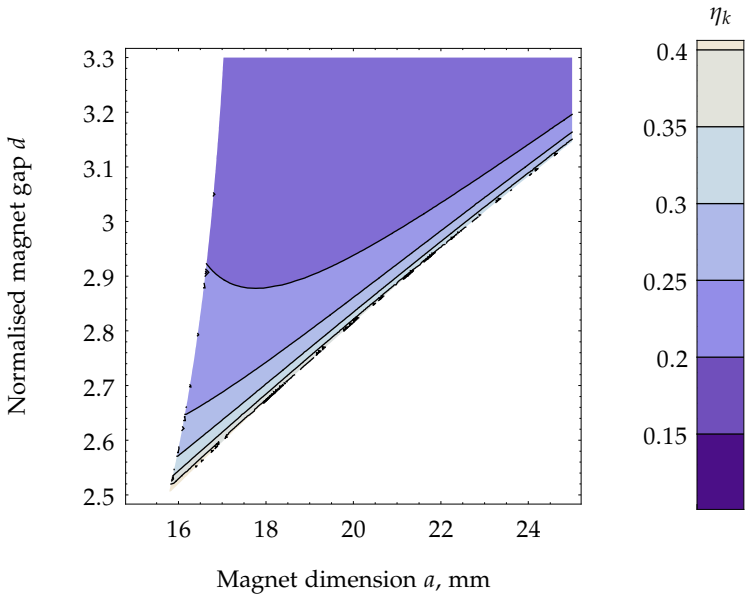

FIGURE 6.21: Zoom of Figure 6.20 to show the behaviour of the nonlinearity ratio in the lower limits of a magnetic design.

where x_2 is the displacement of the isolated mass, x_1 is the displacement of the external disturbance, and c is the viscous damping coefficient. The system is excited tonally at the damped natural frequency of the linearised system ω_d in order to depict the steady state response with the greatest magnitude and therefore greatest nonlinearity ratio. The excitation has amplitude A_e, and is given as a function of time t by

$$x_1(t) = A_e \sin(\omega_n t)\,. \tag{6.53}$$

The system parameters for the simulation are $m = 0.5\,\text{kg}$, $a = 20\,\text{mm}$, $d = 3$, excitation frequency $\omega_n = 3.58\,\text{Hz}$, and with these parameters the equilibrium position h_q is 10.4 mm below the quasi–zero stiffness position. While the exact amount of damping present in the system will be highly model-dependent, the damping ratio $\zeta = 0.5c/\sqrt{K_q m}$ is chosen as 5% based on the small damping forces due to eddy current and air resistance effects [48, 104, 211].

Figure 6.22 shows the steady state response of Eq. 6.52 for a range of peak-to-peak ground disturbance amplitudes in increments of 0.2 mm up to $A_e = 1\,\text{mm}$. Because the excitation is at resonance, the output displacement is greater than the input displacement. The phase plot of the response becomes increasingly skewed as the amplitude of vibration, and hence the nonlinearity ratio, increases. Physically, this is interpreted as the spring being perturbed further into the stiffer region as the mass is moved closer to the repulsive lower magnet, which results in stronger forces as the normalised displacement increases. Conversely, as the mass moves upwards, closer to the quasi–zero stiffness position, the stiffness and force both decrease.

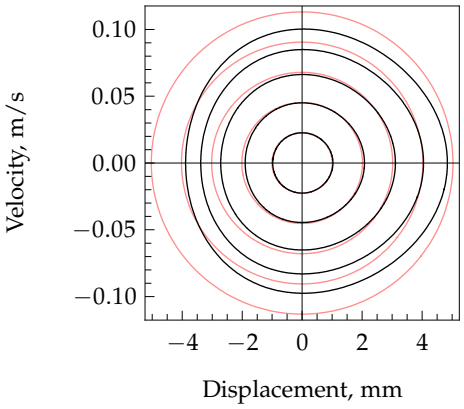

A_e, mm	ΔK_T, N/m	η_k
0.2	68	0.13
0.4	135	0.27
0.6	198	0.39
0.8	253	0.50
1.0	297	0.59

FIGURE 6.22: Phase plot of the magnetic system at steady state resonance for a range of input disturbance amplitudes, shown with respective nonlinearity values η_k. The light line is the equivalent linear response.

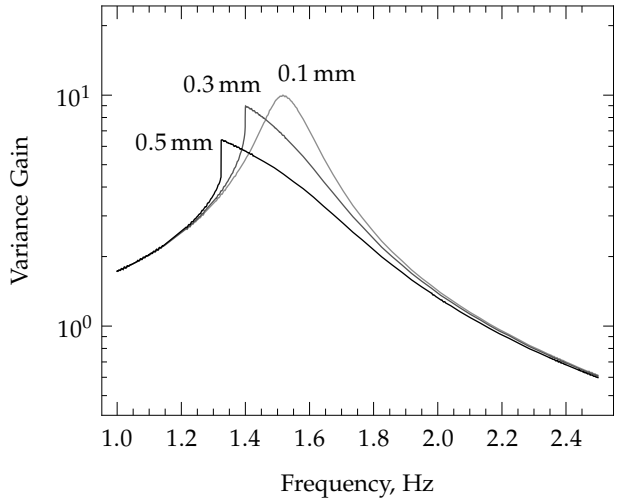

FIGURE 6.23: Variance gain at a position close to quasi–zero stiffness, for a range of excitation amplitudes A_e, as labelled. The spring softening effect at resonance can be clearly seen as the amplitude increases.

The results shown in Figure 6.22 indicate that for small magnitude disturbances the phase plot is very similar to a linear system. As the amplitude increases, the nonlinear system response increases at a slower rate than the linear spring. This slowdown is due to a shifting of the resonance peak as the nonlinearity ratio increases, as will be seen later in this section.

It is important to consider the role of damping in the results shown in Figure 6.22. A low damping coefficient results in a greater displacement response at resonance in the low frequency range. This increase in the displacement response will also increase the nonlinear behaviour of the spring. However, the advantage of low damping is a very fast roll-off in vibration attenuation at frequencies above resonance. Since the damping of the non-contact magnetic spring is very low, either the bandwidth of excitation must lie well above the resonance frequency or active vibration control must be applied in order to reduce the strong effect that the resonance has on the low-frequency response. As previously discussed, skyhook damping is especially suitable for this purpose because the isolation region of the frequency response is not affected §1.2.3 on page 10.

Figure 6.23 shows the variance gain (§1.4.4 on page 39) for a magnetic system with $m = 0.5\,\text{kg}$, $a = 20\,\text{mm}$, and $d = 2.8$ with excitation amplitude ranging from 0.1 mm to 0.5 mm. With these parameters, the equilibrium position is 1.55 mm below the quasi–zero stiffness position. As seen in the figure, the greater the excitation amplitude, the greater the softening nonlinearity of

TABLE 6.4: Nonlinearity values, η_k, and maximum displacements, $x_{\max}$, of the responses shown in Figure 6.23. The equilibrium stiffness is $K_q = 46.6\,\mathrm{N/m}$.

A_e, mm	ΔK_T, N/m	$x_{\max}$, mm	η_k
0.1	29.3	−1.04	0.31
0.3	57.6	−0.47	0.62
0.5	66.3	−0.24	0.71

TABLE 6.5: Nonlinearity values, η_k, and maximum displacements, $x_{\max}$, of the high amplitude responses ($A_e = 0.5\,\mathrm{mm}$) shown in Figure 6.24, for a range of magnet gaps, d.

d	K_q, N/m	ΔK_T, N/m	$x_{\max}$, mm	η_k
2.8	66.3	46.6	−0.24	0.71
2.85	138.8	145.8	−2.72	0.48
3.0	167.6	253.5	−7.80	0.33

the spring. One particular aspect of the nonlinearity which can be seen is the 'snap-through' phenomenon at the resonance peak; this is a common feature of such nonlinear systems in general [83], shown particularly clearly in the experiments of Bonisoli and Vigliani [47] for a magnetic spring exhibiting a hardening nonlinearity.

Table 6.4 shows some data from the simulated responses, including the maximum displacement of the spring towards the quasi–zero stiffness position, and the nonlinearity measures η_k for each amplitude of excitation. The maximum displacement $x_{\max}$ corresponds with the maximum normalised displacement $h_{\max}$ shown in Figure 6.12; as $h_{\max}$ tends towards zero, the motion of the magnetic spring moves closer to the quasi–zero stiffness position. Note that the pronounced nonlinearity seen in Figure 6.23 belongs to a system that is approaching its bounds of stability, reaching 0.24 mm below the quasi–zero stiffness position in its most extreme displacement.

Figure 6.24 shows the variance gain of the same system as the magnet gap d is altered. Results are shown for excitations of both $A_e = 0.1\,\mathrm{mm}$ and $A_e = 0.5\,\mathrm{mm}$. Data for the simulations with $A_e = 0.5\,\mathrm{mm}$, including nonlinearity measure η_k and maximum displacement $x_{\max}$, are shown in Table 6.5. Two related features are important to note from Figure 6.24. The first is the large decrease in resonance frequency as the magnet gap decreases. The second is the corresponding increase in nonlinear behaviour as this occurs, seen with both a snap-through resonance and a superharmonic-like

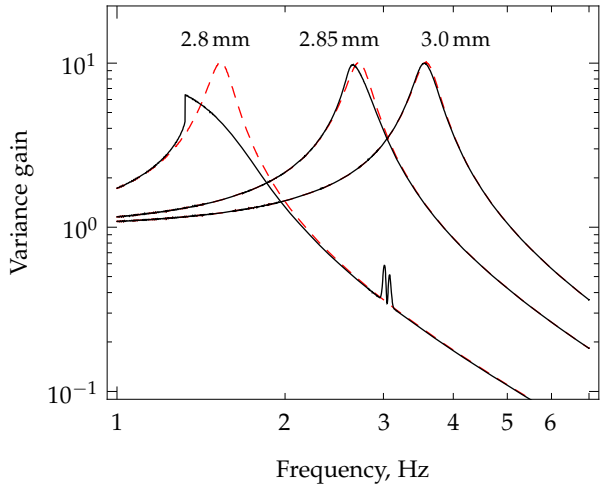

FIGURE 6.24: Variance gain of the magnetic system comparing two excitation amplitudes with varying values of magnet gap d, as labelled. Low amplitude, dashed, is $A_e = 0.1\,\text{mm}$ and high amplitude, solid, is $A_e = 0.5\,\text{mm}$.

behaviour at twice the resonance frequency. As the equilibrium position moves away from the instability at quasi–zero stiffness, the variance gain quickly exhibits linear behaviour.

§6.3.5 *Summary of magnetic quasi–zero stiffness design*

This section has analysed a magnetic spring for the purposes of load bearing with low stiffness. Empirical expressions were derived for cube-shaped magnets for analysing the behaviour of this system, which are simple and accurate over a large displacement range, and may be used for cubical magnets of any size.

Four criteria were imposed on the system in terms of the two variable design parameters: magnet size and gap between the fixed magnets. A technique for explicitly mapping these constraints to a range of valid parameters was shown. Allowable stroke and magnet size availability allow a design to be optimised using this technique based on the required load bearing and natural frequency.

The magnetic isolator is weakly nonlinear with a phase plot that is distorted compared to a linear system; the variance gain shows a resonance peak skewed into the lower frequencies. These nonlinearities only become apparent at larger vibration amplitudes at equilibrium positions that are close to the quasi–zero stiffness position. Provided the system remains stable, the nonlinearities are not detrimental to the frequency response of the system.

The vibration isolator described in this section is therefore suitable for precision applications where low resonance frequencies are required. The design is scalable in that many such isolators may be used in parallel to achieve greater load bearing even if only small magnets are available. The inherent low damping of the system results in good high frequency performance, but low frequency disturbances will result in large outputs due to the high resonance peak. This effect could be mitigated by the application of absolute velocity feedback control ('skyhook damping') to the system, which will be discussed in Chapter 7.

Further research on the practical development of this system is currently being undertaken at The University of Adelaide, with a particular focus on adaptive load balancing, and control for both stabilisation and vibration attenuation in six degrees of freedom [310].

§6.4 Conclusion on quasi–zero stiffness systems

This chapter consisted of separate analyses of two quasi–zero stiffness systems. The first was a mechanical design using linear springs, seen in the literature, and analysed in a planar form herein for the first time. It was shown that quasi–zero stiffness was possible to achieve in both horizontal and vertical directions simultaneously with careful tuning of the parameters of the system.

The second analysis considered a simple magnetic quasi–zero stiffness arrangement and investigated the parameters necessary to design such a system based on desired load bearing and allowable operating parameters. A set of criteria was developed and the solution space for one such design investigated. The nonlinear aspects of using magnetic forces were considered and it was shown that nonlinearities became significant when the spring tended close to its quasi–zero stiffness position.

An important point to emphasise for quasi–zero stiffness systems is that their ideal operating condition cannot be achieved in practice. For the magnetic design with a quadratic-shaped force curve, instability results from displacements that breach the quasi–zero stiffness position since the stiffness becomes negative. For the inclined linear spring design with a cubic-shaped force curve, any slight deviation past the quasi–zero stiffness tuning point results in a spring with greater stiffness and a shifted equilibrium position. In both cases, the operating point of the system must be chosen as close as possible to the quasi–zero stiffness position; the more extreme the operating requirements the finer the tolerances on manufacturing and, if necessary, stability measures.

CHAPTER 7

Prototype low-stiffness magnetic spring

The work presented in this chapter has been submitted in condensed form as a conference paper [246].

§7.1 Overview

In the previous chapter, a single degree of freedom magnetic quasi–zero stiffness system was analysed theoretically. This chapter covers the implementation details, experiments performed, and results obtained from the experimental apparatus built for this project to validate some of the concepts and theory discussed in previous chapters. The behaviour of the open loop transmissibilities are examined in terms of magnet position; in addition, a velocity feedback vibration control system is implemented to improve the vibration isolation performance of the device.

§7.2 Design of the experimental apparatus

The experimental apparatus that was designed and built as part of this study is shown as a schematic in Figure 7.1 and as a photograph in Figure 7.2. The design consisted of one pair of magnets in repulsion for load bearing and one pair in attraction for stiffness reduction. The physical location of the fixed magnets may be moved vertically in order to vary the respective amounts of positive and negative stiffness.

Physical parameters of the design are shown in Table 7.1. The experimental apparatus was built to serve as a platform for investigating the dynamics of a simple system supported by magnets with varying stiffnesses; specifically, for demonstrating a particular case of the concepts underpinning the quasi–zero stiffness arrangement analysed in detail in Section 6.3.

The magnet system is designed to investigate the dynamics in the vertical displacement direction; having stability in this direction implies instability in the horizontal direction (as discussed in Section 1.3.3). In order to remain stable, the magnets require a physical constraint, achieved by placing the floating magnets at the end of a long pinned rigid beam. Small rotations of

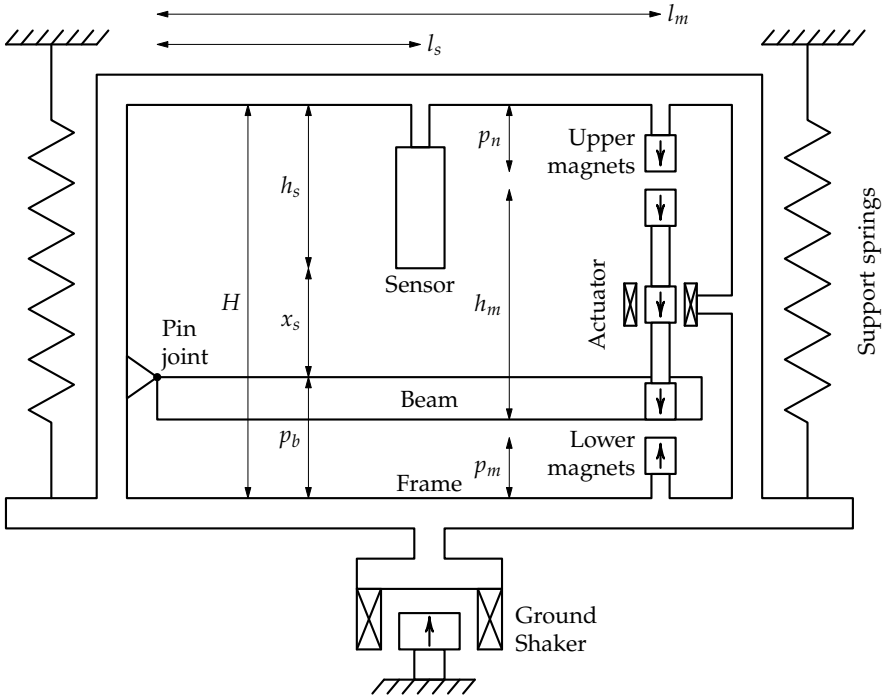

FIGURE 7.1: Schematic of the experimental apparatus (not to scale). Position shown is the marginally stable configuration with equal gap between the lower and upper pairs of magnets.

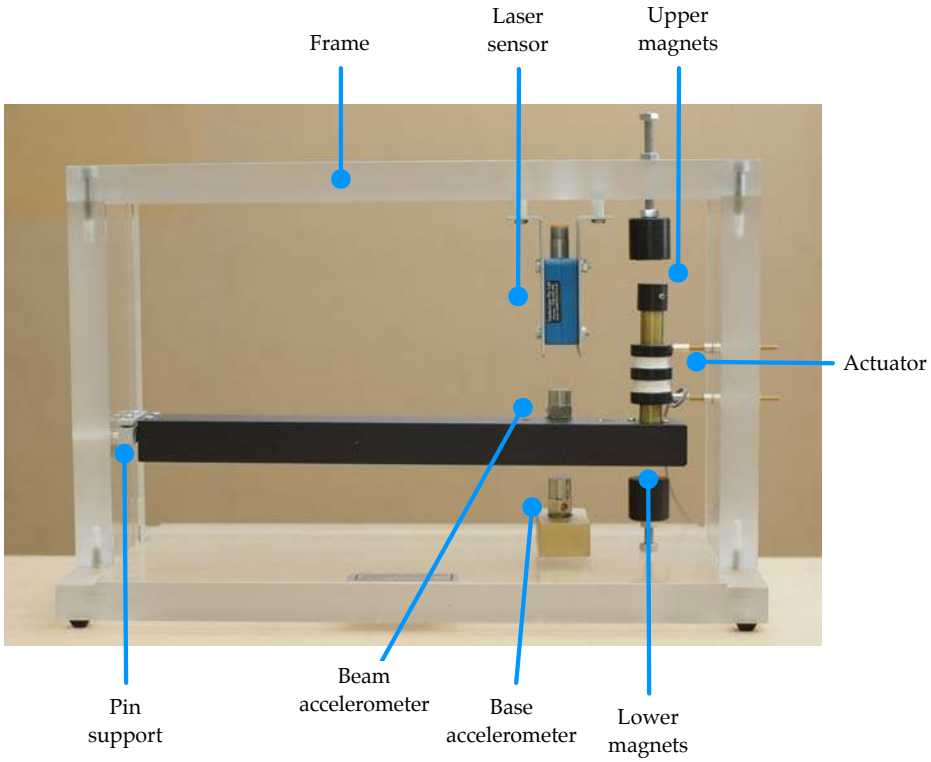

FIGURE 7.2: Photo of the experimental apparatus. Base shaker is not shown.

Table 7.1: Physical properties of the experimental apparatus.

Apparatus height	H	209 mm
Beam mass		266 g [a]
Beam length	L_b	320 mm
Beam height	h_b	25 mm
Beam width	w_b	40 mm
Beam thickness	t_b	2 mm
Beam vertical offset	p_b	82 mm
Magnet support height	h_m	105 mm
Magnet support lever arm	l_m	300 mm
Magnet support mass		87 g
Magnets height	L_m	9.5 mm
Magnets diameter	$2R_m$	12.7 mm
Magnets remanence	B_r	1.3 T
Lower fixed magnet origin	p_m	44 mm
Upper fixed magnet origin	p_n	30 mm plus offset [b]
Sensor height	h_s	85 mm
Sensor horizontal offset	l_s	252 mm
Sensor displacement measurement	x_s	43 mm–53 mm

a. Mass of the accelerometer is accounted for in this value.
b. Offset varied to adjust the amount of added negative stiffness.

this beam can be assumed to correspond to largely vertical displacements of the end magnets. This is ensured in the design, which is addressed in Section 7.2.2.

The beam itself was chosen as a hollow rectangular section in order to minimise weight and maximise stiffness; it is assumed to be a rigid body for the purposes of these experiments (especially at the low vibrational frequencies under investigation).

The pin support was constructed by clamping the beam to a thin piece of flexible plastic which was in turn clamped to the frame. The use of a flexural element was chosen to avoid static friction that would be present in a bearing or hinge joint. The stiffness of this plastic can be assumed to be negligible as it played no part in the load bearing of the beam. Having a physical constraint on the motion of the floating magnets compromises the non-contact idea of using magnets for vibration isolation. For a completely non-contact system, a control system with electromagnets may be used to apply the horizontal constraint.

TABLE 7.2: Material properties for the magnets in the experimental apparatus. Magnet properties taken as minimum grade values from K&J Magnetics [157].

Diameter	12.7 mm
Height	9.5 mm
Grade	N42
Remanence	1.3 T
Intrinsic coercivity	960 kA/m
Maximum energy product	325 kJ/m^3

§7.2.1 *Magnets*

The magnets used for the experimental apparatus were chosen based on ease of availability and construction. Cylindrical magnets were used of dimensions $\varnothing 12.7\,\text{mm} \times 9.5\,\text{mm}$ and material properties as shown in Table 7.2. The magnets were held in place within a hollow brass cylinder of outer diameter 13.5 mm.

Cylindrical magnets were chosen for their ease of integration into the construction of the apparatus; for example, it is much easier to fix a cylindrical magnet into an object by boring a round hole as opposed to milling a square one.

§7.2.2 *Translational effects of the rotating beam*

Three moving magnets were required in the system: one at the main end of the motional beam to be repelled for positive stiffness by the fixed lower magnet; a second to be used with electromagnetic coil for control forces; and the third to be attracted for negative stiffness by the fixed upper magnet.

The beam added a horizontal constraint to the system for stability. As the beam rotates, the magnets move predominantly in the vertical direction; there is still some horizontal motion, however, and the area restricted by the electromagnetic coil requires attention to ensure that there is no contact between the moving magnet and the fixed coil. However, the smaller the air gap between the coil and the magnet, and thus the smaller the inner radius of the coil, the greater the forces imparted by the coil on the magnet (see Figure 5.7(b) on page 165), so the smaller the tolerance the better.

A simplified geometry of the moving magnet arrangement is used to calculate the minimum tolerance required to avoid contact with the coil as a function of the vertical motion of the magnets. This geometry is shown in Figure 7.3, where the L-shaped magnet support is shown in the 'rest' position $\overline{OAB}$ and in a rotated position $\overline{OA'B'}$.

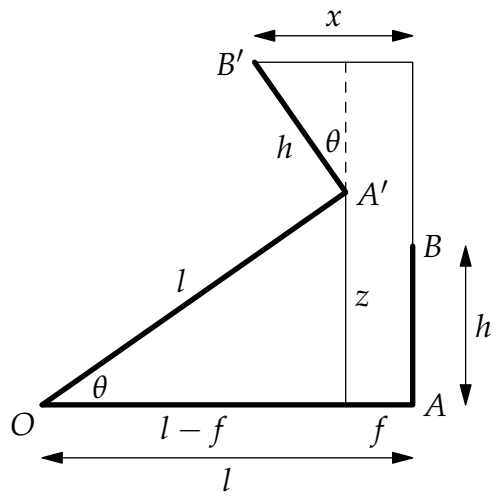

FIGURE 7.3: Geometry for calculating the minimum horizontal tolerance x of the inner dimensions of the coil due to vertical displacement z of the magnet arrangement pinned at point O.

The horizontal displacement of the highest point after rotation, x, can be calculated as a function of rotation angle θ

$$x = h\sin(\theta) + f\,, \tag{7.1a}$$
$$f = l - l\cos(\theta)\,, \tag{7.1b}$$

where l is the horizontal length of the magnet arrangement, and h is the vertical height. This can be expressed in terms of the vertical displacement of the main beam, z, with $\sin(\theta) = z/l$ and using the trigonometric relationship $\cos(\arcsin(a)\,) = \sqrt{1-a^2}$:

$$x = hz/l + l - \sqrt{l^2 - z^2}\,. \tag{7.2}$$

From the dimensions chosen for the apparatus, $l = 300\,\text{mm}$ and $h \approx 50\,\text{mm}$, the minimum horizontal tolerance for a vertical displacement $z = 1\,\text{mm}$ is $x = 0.168\,\text{mm}$ and for $z = 2\,\text{mm}$ is $x = 0.34\,\text{mm}$. (The relationship between x and z being fairly linear for most values of l and h with small ranges of z.) The actual clearance between the outer radius of the brass cylinder holding the magnets and the inner radius of the coil former was $0.35\,\text{mm}$. This tolerance was judged to be small enough to allow a surrounding coil without having a significantly diminished force characteristic from the air gap required to avoid contact. It should be noted that this tolerance caused a degree of inconvenience since the attachment and positioning of the coil required careful alignment in order to allow free movement of the cylinder holding the magnets.

§7.2.3 *Actuators*

To highlight the dynamics of the magnetic support as much as possible, any additional actuators for applying control forces should affect the dynamics of the system as little as possible. Fitting with the theme of non-contact support, a non-contact actuator should be chosen if possible. An electromagnetic force was the obvious choice to satisfy these requirements.

Electromagnetic actuators are often designed in push-pull configurations, with fixed soft-iron-core coils applying force on a moving ferrous but non-magnetised material. Since only attractive forces can be generated in this configuration, such electromagnets must be used in pairs to achieve forces in two directions.

An alternative is to use biased electromagnets, such that either the coil itself contains a permanent magnet, or the coil acts against a permanent magnet, or both. For a biased coil, instability results due to the presence of the negative stiffness attractive forces between the permanent magnet and the ferrous moving material. In these cases, pairs of electromagnets are no longer strictly necessary since the current in the coil may be reversed and a repulsive force generated.

For example, Nandi et al. [210] demonstrate a single-sided actuator design in which a bias current is used to keep the structure in a permanently 'sprung' position; relaxing the current is the equivalent of a repulsive force, while increasing the current is the usual 'pull' or attractive force of a regular electromagnetic actuator. This design is inefficient since it requires a continuous energy expenditure to remain in equilibrium.

Alternatively, using a non-ferrous coil to apply forces to a moving permanent magnet is passively stable and requires no steady current for operation. However, the forces applied by a coil to an external magnet are relatively small; larger forces are achieved when the magnet can be inserted within the coil itself. This suits a secondary requirement for the electromagnetic actuator to keep it aligned with the load-bearing magnets, and is suitable for a future application of such an arrangement for an apparatus built to support multiple degrees of freedom.

The dual-coil electromagnetic arrangement described in Section 5.4 was custom-built for the actuator for the experimental apparatus. A schematic of the dual-coil system is shown in Figure 7.4 with parameters in Table 7.3. The coil was designed to have an impedance of $R = 8\,\Omega$, from which the outer radius of the coil was calculated given a certain wire diameter and resistance.

The dimensions of the coil were chosen based on the trends shown in the analytical calculations from Section 5.4 to ensure sufficient force over the

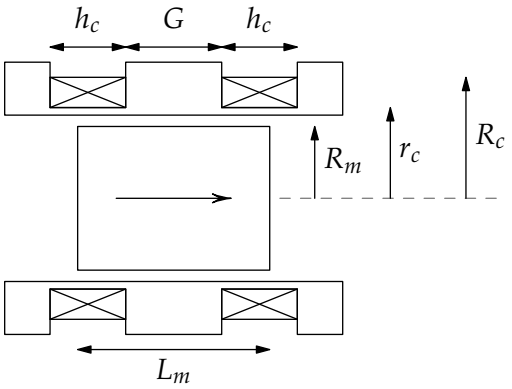

FIGURE 7.4: Schematic of the dual-coil electromagnet built for the apparatus. (Not to scale.)

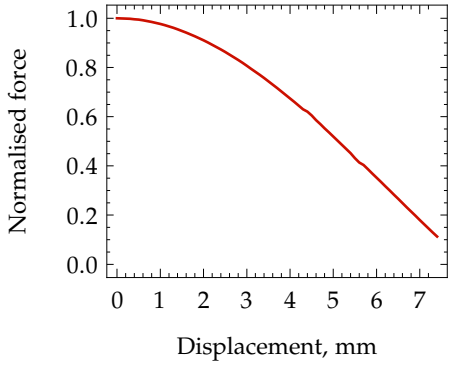

FIGURE 7.5: Normalised force versus displacement curve for the electromagnet. Force is normalised to the maximum value at zero displacement.

TABLE 7.3: Dual-coil electromagnet parameters.

Magnet radius	R_m	6.4 mm
Magnet height	L_m	9.5 mm
Coil height	h_c	7 mm
Coil inner radius	r_c	10 mm
Coil outer radius	R_c	10.7 mm
Coil gap	G	7 mm
Turns (approx.)		105
Resistance (total)	R	8 Ω
Former inner radius		14.2 mm

displacement range expected from the system. A normalised force versus displacement curve of this particuar coil is shown in Figure 7.5; from this graph, it can be seen that around the centred position (displacement of zero in the curve), the force imparted by the coil remains within 10 % of maximum over a displacement range of around ±2 mm, which is acceptable for the purposes of the design.

§7.2.4 *Sensors*

The requirements for the sensing equipment is similar to that of the actuators; noncontact spatial measurement is desired to remove any possibility of adding further dynamics to the system. A displacement sensor is required to measure the position of the fixed and moving magnets in the system. Velocity

sensors can be used for feedback control to add damping to the system (see Section 1.2.3 on page 10) in order to aid the vibration isolation characteristic of the system. Accelerometers are used to measure the vibration response on the beam and on the base and thus determine the transmissibility of the system.

Displacement sensors

There are five main choices for non-contact distance sensing: ultrasonic, inductive, capacitive, linear variable differential transformers, and laser sensors [42]. The sensor purchased for the experimental apparatus was a Wenglor 05 MGV 80 opto-electronic sensor, which uses a laser to measure distance over a range of 10 mm. It was selected for its convenient availability, flexibility of application due to its large working range, and good performance characteristics. Relevant operating properties are listed in Table 7.4.

TABLE 7.4: Relevant properties of the Wenglor 05 MGV 80 laser distance sensor.

Measurement offset	43 mm
Measurement range	10 mm
Working range	43 mm–53 mm
Output range	10 V–0 V
Resolution	$< 10\,\mu m$
Response time	0.5 ms

Velocity sensors

As velocity is defined in terms of a change in displacement from some reference point, it is only meaningful to refer to the velocity of an object with respect to an inertial reference frame. With a sensor attached to another body, separate from the object, relative velocity can be measured between the disturbance and the resulting excitation ($\left[\dot{x}_2 - \dot{x}_1\right]$ in terms of Figure 1.1(b)). Laser vibrometer sensors and capacitive sensors [211] may be used to measure relative velocity directly.

Low frequency relative velocity signals can also be estimated by differentiating a displacement measurement. If the displacement sensor is fixed to a fixed inertial reference frame, then this estimate may be combined with an integrated accelerometer measurement to obtain a more accurate estimate of the velocity [38]. However, if relative displacement is measured between two coupled systems (as often the case for vibration isolation) then this tech-

Table 7.5: Relevant properties of the accelerometers used in the experimentation.

	Model	Charge sensitivity	Weight
Base	4367	20.1 pC/g	13 g
Beam	4332	75.4 pC/g	30 g

nique does not capture the absolute velocity. (For example, with reference to Figure 1.1(b), the signal $\left[\dot{x}_2 - \dot{x}_1\right]$ is being estimated, not $\dot{x}_2$.)

Absolute velocity sensors must use more complex physical processes to obtain a measure of an object with respect to the 'fixed' earth. Absolute angular velocity can be infered by measuring the coriolis force induced on a vibrating element due to the rotational energy of the earth [158] and is the basis of solid state gyroscope sensors. A geophone uses a moving magnet or moving coil arrangement to generate back–electromotive force from the motion of an inertial mass [212] from which absolute velocity can be estimated. This process is limited in the low frequency by the resonance frequency of the inertial mass and in the high frequency by the roll-off of the frequency response.

Acceleration sensors

For the beam, a Brüel & Kjær 4367 accelerometer was used to measure the 'output' signal; for the base, a 4332 accelerometer measured the 'input' signal of the system (Table 7.5). The accelerometers were used with Brüel & Kjær 2635 charge amplifiers set to appropriate gain values for the input signals. The signals were low-pass filtered at 50 Hz to avoid aliasing effects using a Krohn-Hite Model 3362 digital filter (using a 4-pole Butterworth filter).

For open loop measurements, these accelerometers were used to measure acceleration directly; for closed loop control, the charge amplifier was used to integrate the measured signals to estimate the absolute velocities. The high-pass filter in the charge amplifiers used a 0.1 Hz cut-on frequency when measuring acceleration and 1 Hz for velocity. The higher frequency is necessary for velocity to avoid drift due to accumulation of errors in the integrator circuit. A potential alternative is the use of 'drift-free' integrators [109], in which the drift is compensated for using alternative signal processing methods, but this approach is only advantageous for measuring low-frequency periodic signals; for transient or wide-band signals, the typical approach is better suited.

Recently, Williams [290] showed a filter system designed to estimate absolute velocity from accelerometer measurements that can mitigate the

low-frequency resonance issues seen due the high-pass filters present in the charge amplifiers used (seen in the experimental results in §7.3.7). This research was published after experimental measurements for this thesis had been completed and their ideas were not able to be tested in the apparatus discussed in this section. As will be shown (§7.3.6), the control methodology used for the results later in this chapter was indeed successful; it is expected that the method of Williams [290] may further improve the performance at low frequencies.

§7.3 Experimental results

A number of measurements were performed using the experimental apparatus. In the sections following, measured data is presented for: magnet gap versus beam displacement; open loop frequency responses for a range of magnet gaps; and, velocity feedback in a single configuration.

§7.3.1 *Static displacement measurements*

The position of the upper magnet was varied until the limit of stability was reached. The lower fixed magnet was kept fixed, which means that the position of quasi–zero stiffness was changing; with counter-threaded mounts for the upper and lower magnets, they could be adjusted in parallel to achieve a fixed quasi–zero stiffness location.

As the upper magnet placement was lowered, the rest position of the beam moved closer to the quasi–zero stiffness position (as more force was supported by the upper magnet). This relationship is shown in Figure 7.6. The normalised magnet gap g is used in the following sections to represent the varied configuration of the spring in the experiments, defined as $g = p_g/L_m$, where p_g is the magnet gap at quasi–zero stiffness and L_m is the height of the magnets. From the geometry of the apparatus, the position of the upper magnet was used to calculate the gap between the magnets at quasi–zero stiffness:

$$p_g(p_n) = \tfrac{1}{2}\left[H - p_m - p_n - h_m\right] + L_m - h_\epsilon\,, \tag{7.3}$$

where geometrical properties are described in Table 7.1 and $h_\epsilon = 2.5\,\text{mm}$ is an extra clearance to account for space taken up by the thicknesses of the magnet mounting. The height of the quasi–zero stiffness location itself, p_q, is given by

$$p_q(p_n) = \tfrac{1}{2}\left[H - p_m + p_n\right]. \tag{7.4}$$

The measured output of the sensor x_s was used to infer a magnet displacement, x, (referenced from the quasi–zero stiffness position) with the

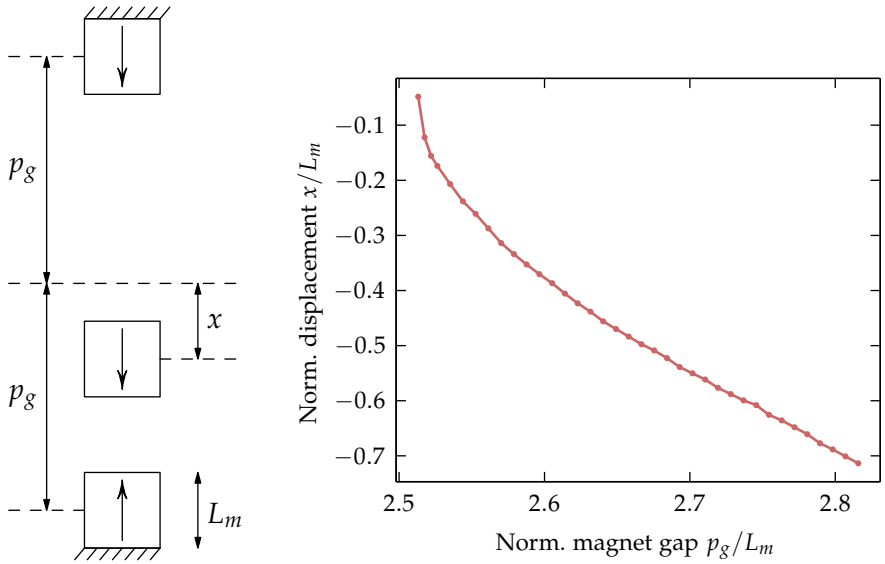

FIGURE 7.6: Rest position of the system as the magnet position varies. For simplicity, only a single floating magnet is shown here.

following relationships. Firstly, the rotational origin of the beam was used as a vertical reference point, and the displacement of the beam x_b at the laser sensor location calculated as

$$x_b(x_s) = H - p_b - h_s - x_s\,, \tag{7.5}$$

which can be extrapolated using the respective lever arms to calculate the resultant vertical displacement of the moving magnets with respect to the beam origin with

$$x_p(x_b) = x_b \frac{l_m}{l_s}\,. \tag{7.6}$$

This moving magnet displacement can be written with respect to the origin of the frame of the apparatus with

$$x_m\left(x_p\right) = p_b + x_p - h_b + t_b + \tfrac{1}{2}h_m\,. \tag{7.7}$$

Accordingly, the displacement of the system x from the quasi–zero stiffness location is given by

$$x\left(x_s, p_n\right) = x_m - p_q\,, \tag{7.8}$$

where x is written as a function of measured sensor output x_s and known upper magnet position p_n.

The displacements between the centres of each magnet in the interacting pairs can be similarly calculated based on the displacement of the moving

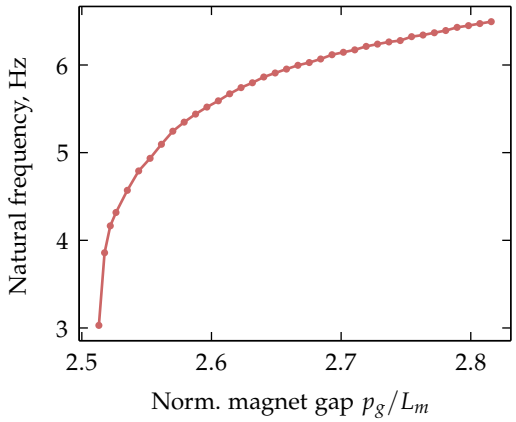

FIGURE 7.7: Expected natural frequency as the magnet position varies.

magnet assembly x_m. With respect to the frame origin, the magnet centres for the base magnet x_{m1}, upper magnet x_{m2}, lower moving magnet x_{m3}, and upper moving magnet x_{m4} are

$$x_{m1} = p_m - h_e - \tfrac{1}{2}L_m\,, \tag{7.9}$$
$$x_{m2} = H - \left[p_n - h_e - \tfrac{1}{2}L_m\right]\,, \tag{7.10}$$
$$x_{m3} = x_m - \tfrac{1}{2}h_m + \tfrac{1}{2}L_m\,, \tag{7.11}$$
$$x_{m4} = x_m + \tfrac{1}{2}h_m - \tfrac{1}{2}L_m\,. \tag{7.12}$$

§7.3.2 *Predicted resonance frequencies*

From the displacement results shown in Section 7.3.1, predicted resonance frequencies can be calculated for this system as a function of magnet gap. The expected magnetic forces F due to the measured displacements were calculated using the theory for coaxial cylindrical magnets (Section 2.7 on page 75) based on magnet centre displacements $x_{m3} - x_{m1}$ and $x_{m2} - x_{m4}$. Numerical differentiation was used to calculate the stiffnesses k at these displacements, and the natural frequency at each location calculated with $\omega_n = \sqrt{k/m_{\text{eq}}}$ where $m_{\text{eq}} = F/g$ is the equivalent mass borne by the static force F due to gravity g. With parameters as specified, the expected natural frequency versus magnet gap results are shown in Figure 7.7.

§7.3.3 *Open loop dynamic measurements*

As the position of the upper magnet is varied, the amount of negative stiffness added to the system changes. This predominantly affects the rest position and the resonance frequency, along with small changes in damping. Frequency

Table 7.6: Parameters used in the signal and spectrum analysis for the experimental measurements.

Sample rate	1000 Hz
FFT points	2^{16}
Sample time	≈17.5 min
Average overlap	0.75
Number of non-overlapping averages	16

response measurements were taken at a number of discrete locations of the upper fixed magnet to observe the changes in dynamics as the rest position of the system approached the quasi–zero stiffness position.

The parameters used to perform the spectral analysis for each measurement are shown in Table 7.6. Due to the low damping and low resonance frequency of the system, very long sample times were required to achieve results with enough frequency resolution and sufficient coherence to characterise the response. A high sample rate (1000 Hz) was chosen to reduce the possibility of controller time delays influencing the feedback control, as discussed in Section 1.2.5.

Open loop measurements were taken both with and without the electromagnetic actuator connected (wired as both a short circuit and an open circuit). In the closed circuit configuration, the coil adds damping via induced eddy currents from the moving magnet due to their mutual inductance. As an open circuit, the coil has no effect on the dynamics of the system.

Open loop transmissibility measurements without the coil connected are shown in Figure 7.8(a) and measurements taken with the coil (that is, with added damping) are shown in Figure 7.8(b). An alternate 'nonlinear transmissibility' analysis of the measurements is performed in Section 7.3.5.

§7.3.4 *Analysis of the open loop data*

From the measurements shown in the previous section, data fitting of the frequency response functions was used to extract a linear model of the system in each configuration. While more sophisticated techniques are possible [69], fitting the data to a known exact frequency response function yielded acceptable results in this case since the linear model is relatively simple.

The model used to fit the data was a single degree of freedom vibration isolation system given by Eq. 1.2 in terms of the natural frequency, ω_n =

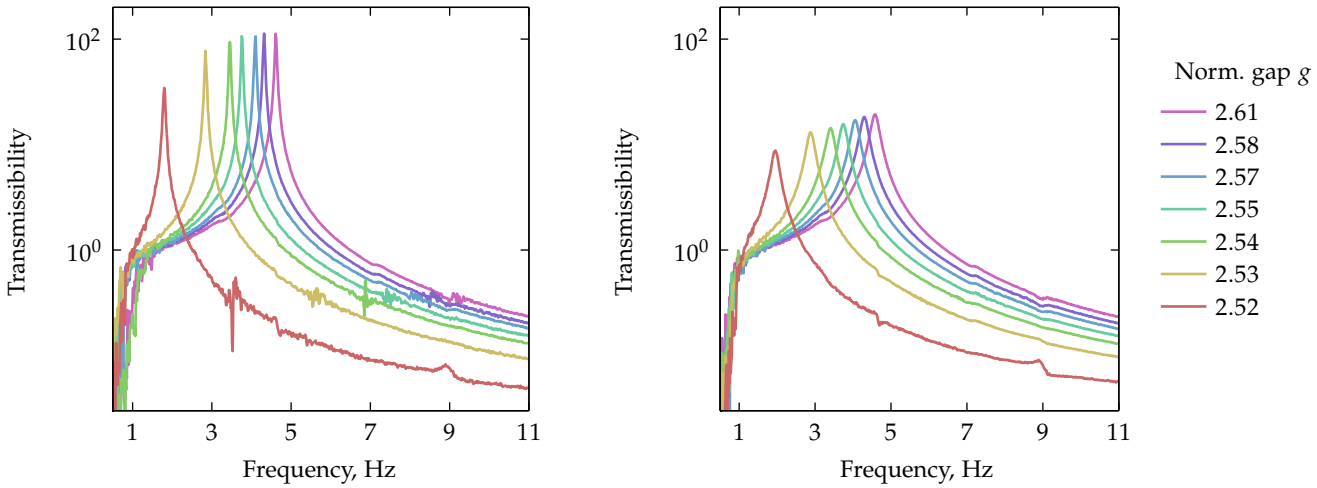

(a) Open circuit coil; no additional damping is added to the system.

(b) Closed circuit coil. The coil adds damping to the system, which can be seen by the reduction in height of the resonance peaks in comparison to Figure 7.8(a).

FIGURE 7.8: Open loop measurements of transmissibility with the electromagnetic coil connected in an open and closed circuit as a function of normalised gap g.

$\sqrt{k/m}$, and damping ratio $\zeta = c/(2\sqrt{km})$:

$$T(\omega) = \left| \frac{2i\zeta\omega\omega_n + \omega_n^2}{-\omega^2 + 2i\zeta\omega\omega_n + \omega_n^2} \right|, \tag{7.13}$$

where ω is the frequency at which to calculate the transmissibility $T(\omega)$. The data was fit[1] to Eq. 7.13 between $\frac{1}{2}\omega_n \leq \omega \leq 2\omega_n$, with well-fit transmissibility around the resonance peak at each measurement taken. Plots of the curve fit models shown against the measured data are shown in Figures 7.9 and 7.10. Due to the influence of unmodelled dynamics in the system, the model starts to deviate from the measured data at higher frequencies. The natural frequencies and damping ratios calculated from this curve fitting are shown in Figure 7.11. Comparing the results with the coil circuit open and closed, the resonance frequencies remained constant (Fig. 7.11(a)) but the damping ratios changed (Fig. 7.11(b)). With the actuator connected, movement of the actuator magnet causes eddy currents to be induced in the coil, adding damping to the system.

The curve of the measured resonance frequencies (Fig. 7.11(a)) follows the same trend as the predicted natural frequencies (redrawn from Figure 7.7). However, their magnitudes are not well matched. As the system approaches

1. Using Matlab's `fminsearch`.

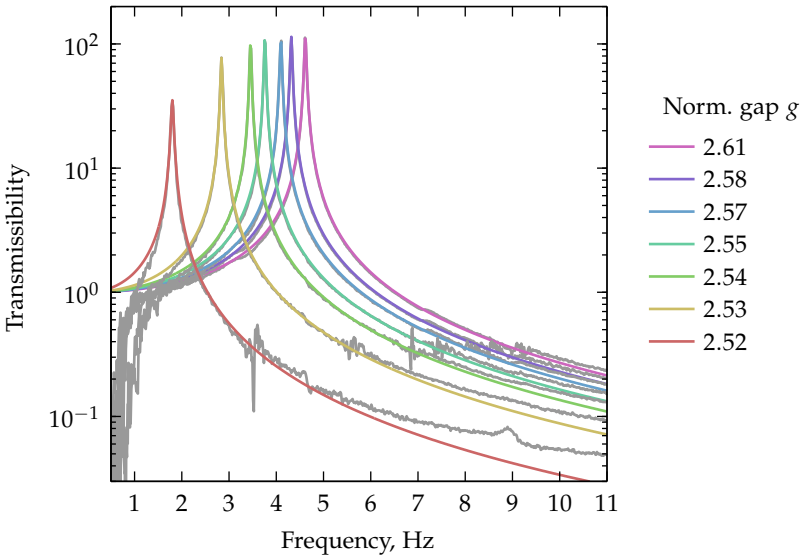

FIGURE 7.9: Curve fit model of measurements with actuator disconnected, Figure 7.8(a). Gray lines show the original data.

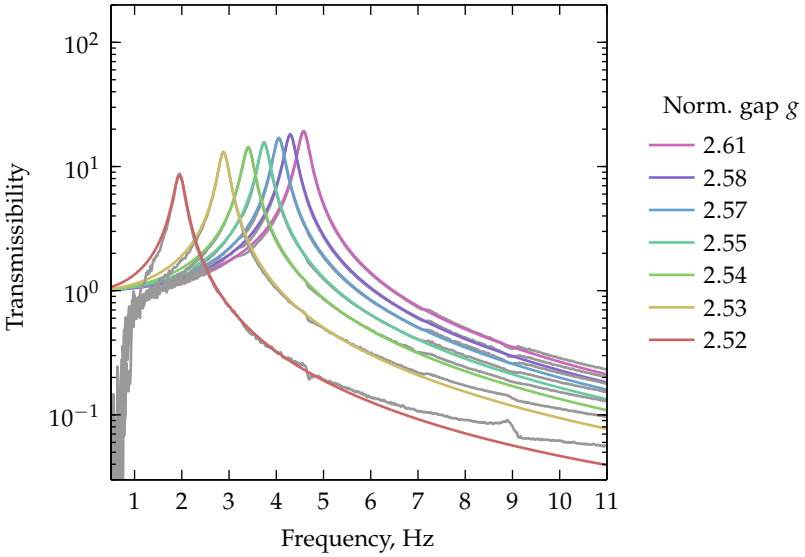

FIGURE 7.10: Curve fit model of measurements with actuator connected, Figure 7.8(b). Gray lines show the original data.

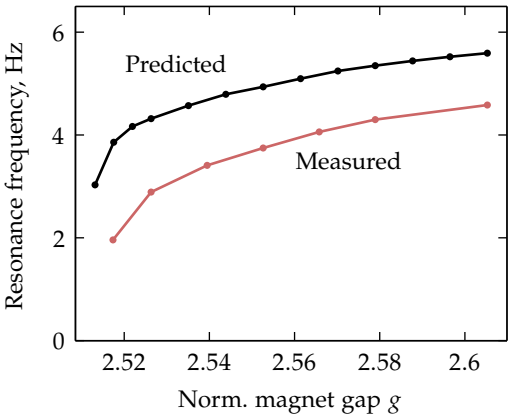

(a) Model-derived resonance frequencies shown with predicted values.

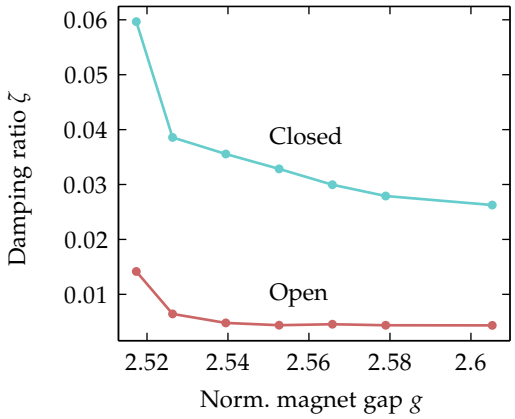

(b) Model-derived damping ratios.

FIGURE 7.11: Analysed results from fitting the open loop measurements to the isolator model of Eq. 7.13.

the quasi–zero stiffness position, even small changes in alignment and physical tolerances have significant effects on the calculated instability region; as seen in the low end of the quasi-static measurements (Fig. 7.7), a fraction of a millimetre change in the position of the top magnet can change the natural frequency by 25%. Associatively, with larger magnet gaps the discrepancy becomes lower. Therefore, the discrepancy seen between theoretical and measured results should be expected due to experimental limitations.

§7.3.5 *Observed nonlinear behaviour*

The dynamics shown in the undamped case are more nonlinear than the damped case; this is due to the greater displacements experienced by the beam moving the magnets through greater ranges of stiffness variation. When the transmissibility is used to examine the broadband behaviour, the system is assumed to be linear and nonlinearities are rejected by the ratio of the cross-spectrum and power-spectrum terms in Eq. 1.13 on page 39. An alternative to transmissibility that does not reject nonlinearities can be calculated using the ratio of the individual power spectra of the magnet and base:

$$T(\omega) = \sqrt{\frac{P_{mm}(\omega)}{P_{bb}(\omega)}}, \tag{7.14}$$

where $P_{mm}(\omega)$ and $P_{bb}(\omega)$ are the power spectral densities of the output magnet vibration and input base disturbance, respectively. In this case, any nonlinearities in the signals are retained in the final result, and this calculation

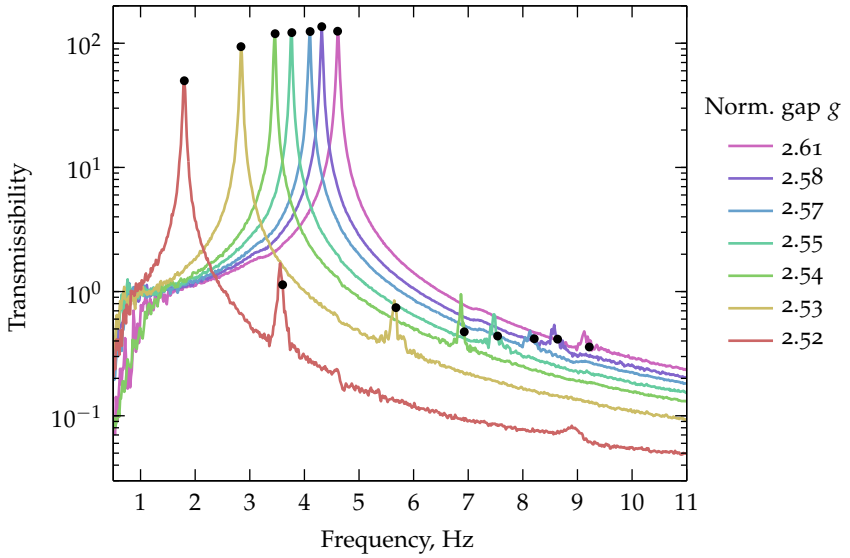

FIGURE 7.12: Open loop measurements without the coil connected; the transmissibility is calculated with Eq. 7.14. Black markers show resonance frequencies and the points at twice each resonance frequency, indicating the nonlinear behaviour.

is referred to as the 'nonlinear transmissibility' in this section. (Recall a similar idea in Section 1.4.4 comparing transmissibility with the variance gain.)

The nonlinear transmissibility for the coil in an open circuit (that is, low damping) is shown in Figure 7.12. In this case, there are significant nonlinearities present in the data, seen by a clear peak in each spectrum at close to twice the 'linear' resonance frequency. This superharmonic behaviour is similar to that seen in previous simulations in this thesis of such a quasi–zero stiffness system (Figure 6.24 on page 211). When the coil is connected and the damping present in the system increased, these nonlinearities are no longer apparent (the results are indistinguishable to those shown in Figure 7.8(b)). The reduced nonlinearity with increased damping is consistent with the work of other researchers [144].

§7.3.6 *Closed loop velocity feedback dynamic measurements*

In this section, results are shown using closed loop feedback control to improve the vibration isolation characteristics of the system. For this experiment, the rest position of the spring was chosen to achieve an arbitrary low resonance frequency (approximately 3.5 Hz). In this position, the electromagnetic coil was used in a simple absolute velocity feedback controller in an attempt to reduce the magnitude of the resonance peak. The gain of the feedback

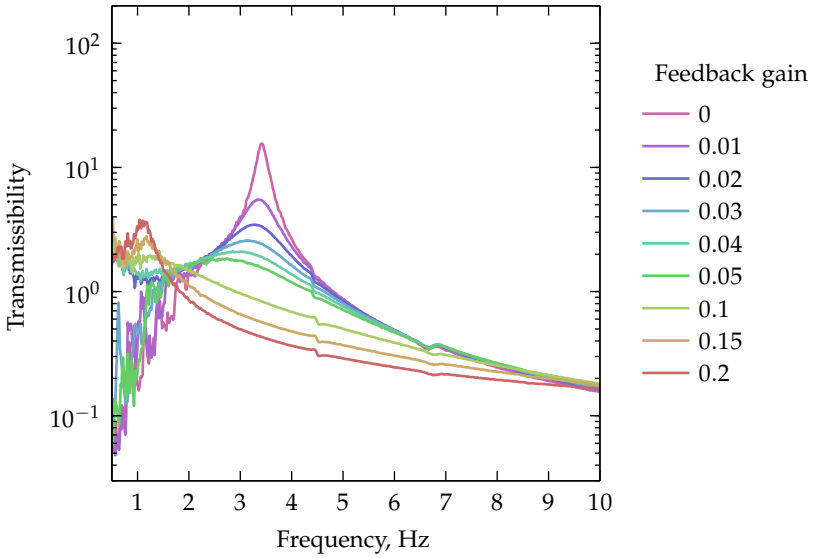

FIGURE 7.13: Closed loop frequency response measurements for a range of velocity feedback gains. The maximum feedback gain is close to instability for the system.

control was increased until the system became close to instability. Frequency response measurements over this range of feedback gains are shown in Figure 7.13. Sampling parameters were as shown previously in Table 7.6.

To estimate the velocity of the moving beam, the accelerometer measurement was integrated by the charge amplifier with a cut-on frequency of 1 Hz. Because the accelerometers were being used to measure velocity (via integrators in the charge amplifiers), the transmissibility curves shown in Figure 7.13 were calculated from the ratio of the velocity measurements instead of acceleration measurements.

Due to the presence of higher-order dynamics in the structure, a low pass filter was used to reject signals above 50 Hz. This also ensured that aliasing was avoided when taking the frequency response measurements and when using the velocity signal for feedback control.

A metric of improvement to the vibration isolation characteristics of the system can be shown by calculating the root-sum-square transmissibility over a certain frequency range (recall Eq. 1.9 on page 10):

$$T_{\text{RSS}} = \sqrt{\sum_{\omega=\omega_1}^{\omega_2} |T(\omega)|^2}\,. \tag{7.15}$$

For the experimental results reported here, the lower frequency limit is defined as $\omega_1 = 1$ Hz, as the results become very noisy below this frequency. The

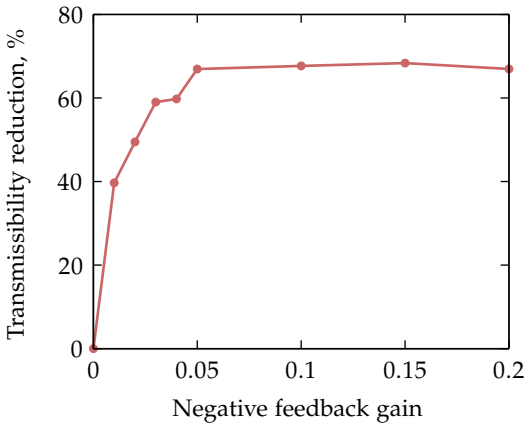

FIGURE 7.14: Effect on overall transmissiblity reduction between 1 Hz and 11 Hz as velocity feedback gain was increased.

upper frequency limit $\omega_2 = 11$ Hz was chosen as the higher-order dynamics (not shown in Figure 7.13) have little impact below this frequency.

Figure 7.14 shows the reduction in root-sum-square transmissibility T_{RSS} as the negative feedback gain increases. The overall transmissibility reduction is calculated as $1 - T_{\text{RSS}}/T_0$, where T_0 is the root-sum-square transmissibility of the open loop system. The resonance at 1 Hz observed in Figure 7.13 as the feedback gain increases causes the overall transmissibility reduction to have a local maximum.

§7.3.7 *Analysis of the gain-induced resonance*

The appearance of a low frequency peak in Figure 7.13 as the feedback gain is increased can be explained by the presence of the 1 Hz high-pass filter incorporated in the accelerometer charge amplifier. This behaviour has been shown previously for single degree of freedom structures with velocity feedback [49]. Here, the same type of analysis will be used to investigate the response of a linear vibration isolation system (shown in Figure 7.15) with integrated accelerometer measurements used for velocity feedback control.

In the time domain, the response of this linear system is given by

$$m\ddot{x}_2(t) = f(t) - c\left[\dot{x}_2(t) - \dot{x}_1(t)\right] - k\left[x_2(t) - x_1(t)\right], \tag{7.16}$$

which can be re-written in the Laplace domain as

$$s^2 X_2 \underbrace{\left[m + c/s + k/s^2\right]}_{1/G_2(s)} = F(s) + s^2 X_1 \underbrace{\left[c/s + k/s^2\right]}_{G_1(s)}. \tag{7.17}$$

This is shown as a block diagram in Figure 7.16. If the control force is written as a function of the acceleration of the mass, $F(s) = s^2 X_2 K_c(s)$, the transmissibility of the system is

$$\frac{X_2(s)}{X_1(s)} = \frac{G_1(s)G_2(s)}{1 + K_c(s)G_2(s)}\,. \tag{7.18}$$

When the controller is some gain g_v in series with an ideal integration of the accelerometer signal, $K_c(s) = g_v/s$, Eq. 7.18 simplifies to the idealised absolute velocity feedback expression:

$$\frac{X_2(s)}{X_1(s)} = \frac{k + cs}{k + \left[c + g_v\right] s + ms^2}\,. \tag{7.19}$$

This result is plotted in Figure 7.17(a) for equivalent values of stiffness and damping as the experimental setup.

A more complex model for the controller block is required to account for the signal processing involved with amplifying and filtering the accelerometer signal to measure the velocity in reality. Assuming that the entire process between acceleration measurement and velocity output from the charge amplifier can be approximated as an ideal integrator in series with two high pass filters[2] [49], the controller block is defined as

$$K_c(s) = \frac{g_v}{s}\left[\frac{s}{s + \omega_c}\right]^2, \tag{7.20}$$

where g_v is the absolute velocity feedback gain and ω_c is the corner frequency of the two high pass filters in the charge amplifier.

Using Eq. 7.20 in Eq. 7.18 gives the final transfer function between the mass and base states,

$$\frac{X_2(s)}{X_1(s)} = \frac{\left[cs + k\right]\left[s + \omega_c\right]^2}{g_v s^3 + \left[ms^2 + cs + k\right]\left[s + \omega_c\right]^2}\,. \tag{7.21}$$

This is plotted versus frequency in Figure 7.17(b), where the resonance induced by the high pass filter becomes apparent as the feedback gain is increased to 99% of the gain margin, which is the gain when the system becomes unstable. The simulation uses linear parameters $\omega = 3.5\,\text{Hz}$ and $\zeta = 0.023$ in order to show results at similar behaviour to Figure 7.13.

In order to calculate the gain margin of Eq. 7.21, $K_c(s)G_2(s)$ was evaluated equal to -1, where the system response of Eq. 7.18 becomes unbounded. To do this, first the critical frequency was found as the frequency

2. One filter for the integration of the acceleration signal, another for the conditioning electronics in the amplifier; assume for simplicity that they have the same cut-on frequency.

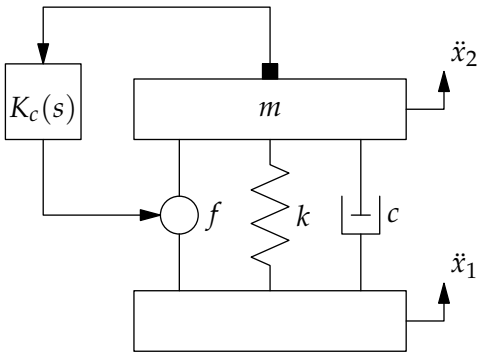

FIGURE 7.15: Vibration isolation schematic with active feedback.

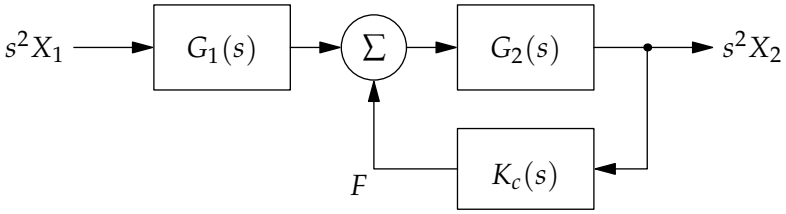

FIGURE 7.16: Block diagram of Eq. 7.17 representing the system shown in Figure 7.15.

at which $\mathrm{Im}(K_c(s)G_2(s)) = 0$; this frequency was then substituted into $\mathrm{Re}(K_c(s)G_2(s)) = -1$, which was solved for g_v to find the gain margin.

Comparing the simulated results of Figure 7.17(b) with the experimental results of Figure 7.13 shows a clear similarity between the two. The corner frequency of the high pass filter at 1 Hz in the charge amplifier to measure velocity is an impediment to the vibration isolation properties of the feedback-controlled system. This is a fundamental limitation in the use of accelerometers for estimating velocity for vibration control. To avoid this issue, the use of geophone sensors which measure velocity directly (such as used by Hong and Park [129]) are a promising alternative to integrated accelerometer measurements. However, geophones are not a panacea since their response rolls off at low frequencies, limiting their performance at the frequency range of interest in this case.

§7.4 Conclusion on the experimental results

In this chapter, the experimental results from a magnetic device have been presented. The magnetic device was designed to demonstrate the ability of variable stiffness through position changes of the load-bearing magnets. The magnetic system exhibited expected static and dynamic behaviour.

As the system was brought closer to quasi–zero stiffness, the resonance frequency reduced until the operating point became too close to the position of marginal stability where even slight disturbances would yield instability. The minimum resonance frequency that could be achieved passively with this system was around 2 Hz. A lower resonance frequency than this could potentially be achieved with larger magnets with larger equilibrium magnet gaps, which would result in a larger physical region of stable operation near

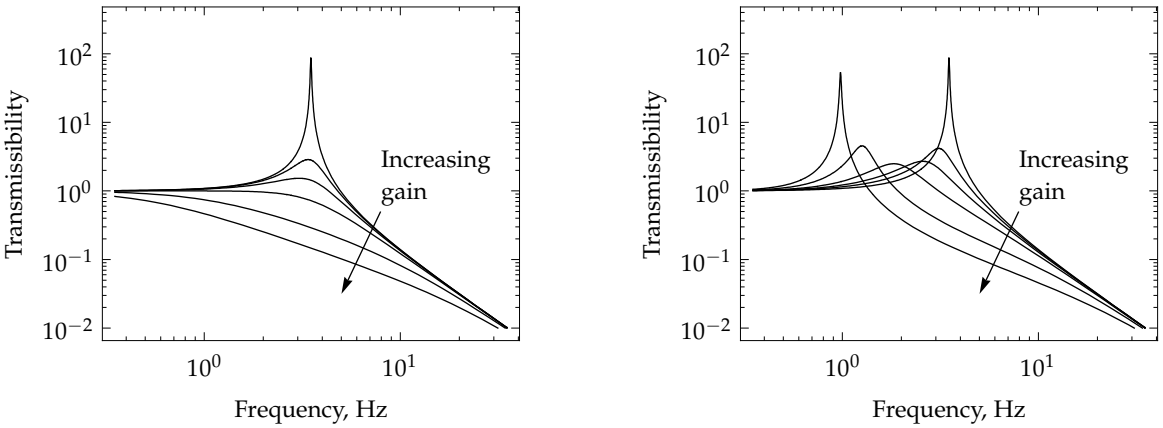

(a) Ideal velocity signal.

(b) Integrated accelerometer feedback with a second order high pass filter.

FIGURE 7.17: Closed loop simulation with gains $\{0, 5, 10, 20, 50, 99\}$ percent of the gain margin in Figure 7.17(b).

the quasi–zero stiffness position.

Without feedback control and without the actuator coil connected, the system showed very small damping ratios of around 0.005; these were dependent on the distance between the magnets at equilibrium. Connecting the non-contact electromagnetic actuator increased this damping ratio to around 0.03–0.04 due to eddy currents induced in the coils from the permanent magnet.

Dynamically, the system showed transmissibilities which could be modelled well by standard linear vibration isolator models. With the very low damping of the open loop system, superharmonics were clearly visible in the 'nonlinear transmissibility' but the resonance peaks remained linear-like. Once the actuator was connected, the additional eddy current damping suppressed these nonlinearities.

Absolute velocity feedback control was successful in reducing the transmissibility peaks, but as the gain was increased the additional poles added by the integration filters caused an additional lower frequency peak to appear as the closed loop system approached the gain margin. At best, the resonance peak was reduced by over an order of magnitude and the root-sum-square transmissibility was reduced by around 65%.

CHAPTER 8

Conclusion

This chapter consists of a summary of the thesis (§8.1) and a list of suggestions for future work (§8.2). The summary presented here complements the detailed concluding remarks for the individual chapters.

§8.1 Thesis summary

Vibration disturbance from environmental sources is a continual problem. The work of this thesis has been an investigation into developing magnetic and electromagnetic systems for providing vibration isolation for sensitive equipment. As this work was cross-disciplinary, a broad literature review was presented on vibration isolations systems, magnetic and electromagnetic devices, and nonlinear quasi–zero stiffness structures. The perceived advantages of quasi–zero stiffness for vibration isolation formed an inspiration for the type of magnetic system investigated in this work.

The modelling of magnetic forces for complex magnet geometries is still an active field of research. The main contribution in this area from this thesis is the significant simplification of the force equation between coaxial cylindrical magnets (Section 2.7 on page 75). The forces between pairs of both cuboid and cylindrical shaped magnets can be calculated from equations from the literature, and since these equations can often be time-consuming to transcribe, a compilation of this theory is provided in a Matlab and Mathematica program which has been made available for use by the general public.

There are numerous geometric possibilities for permanent magnet systems for load bearing ('magnetic springs', Chapter 3 on page 79); an overview of such magnetic springs using cuboid magnets was presented. For single-axis load bearing, magnetic force is maximised for a magnet depth of around 40 % the face size; magnetic cylinders will generate slightly greater forces than square-faced cuboids. Magnetic systems tend to exhibit significant trade-offs in their force and stiffness characteristics, especially involving degrees of instability. A rotationally-stable magnetic spring was proposed but initial results from simulation suggest the system is highly sensitive to perturbations and imbalances. In addition, achieving rotational stability decreases the load-bearing ability of the system. As more discrete magnets are used

in a magnetic spring design, the cross-coupling force–displacement characteristics become increasingly difficult to analyse. It is suggested that the fewer magnets used to achieve a desired behaviour the more robust and well-characterised the system will be.

It has been shown that magnetic springs are highly versatile in the design objectives they can achieve. Three major analyses of different magnetic springs were presented. The first of these was an inclined magnet spring design proposed to achieve a load-independent resonance frequency (Section 3.4 on page 107). Primarily designed for single-axis operation, cross-coupling between axes resulted in planar instability even for positive stiffnesses in each direction. The study of this instability demonstrated the theoretical complexity of designing such systems.

The second magnetic study focussed on multipole magnet arrays in various configurations. For this study, the geometric parameters to define a multipole array were introduced, and the effect of varying these parameters to achieve larger peak forces for a given array volume were presented (Chapter 4 on page 129). Multipole arrays have increased cost involved with fabrication and system design, but provide unique advantages over using discrete magnets. In particular, the single-sided nature of the magnetic field is an advantage in systems where shielding of the magnetic field is required. An investigation on linear magnet arrays showed that significant numbers of magnetisation wavelengths are needed to show an appreciable improvement over homogeneous magnets, and the more wavelengthsthat are included the greater the benefit of using an increased number of magnets per wavelenth of magnetisation. A comparison of linear and planar multipole arrays was performed, and it was shown that the cross-coupling behaviour between horizontal displacement and vertical force differs significantly between the two.

The third magnetic study was a theoretical investigation leading into an experimental component. A preliminary analysis was performed on a quasi–zero stiffness system using inclined linear mechanical springs (Section 6.2 on page 180) where it was shown that although planar quasi–zero stiffness was possible to achieve it required careful tuning. This was followed by a detailed analysis of the parameters involved in a quasi–zero stiffness design with one repulsive and one attractive set of magnet forces (Section 6.3 on page 191).

Continuing from the theoretical analysis of the quasi–zero stiffness magnetic spring, a one degree of freedom prototype was built and low frequency vibration isolation demonstrated (Chapter 7 on page 213). Experimental measurements demonstrated that the damping induced by eddy currents in the permanent magnets for this system was very low ($\zeta < 1\,\%$), but increased the closer the magnets became. This damping ratio was negligible compared

to the eddy currents induced in the electromagnetic actuator of the system. Due to this low damping ratio, the resonance peaks for the system were significant, and active control was investigated as a method to improve the transmissibility at resonance. One major obstacle with improving vibration isolation at these low frequencies is the difficulty with measuring inertial properties, specifically velocity, for performing active feedback control.

In the construction of the apparatus for the quasi–zero stiffness experiments, an electromagnetic actuator was constructed using a dual-coil design. An optimisation was deemed necessary to reduce the size and cost of constructing such devices. This required a model of the magnetic forces between a cylindrical magnet and a coil, and a particularly efficient new method for calculating the axial force between a cylindrical magnet and an electromagnetic coil with many radial windings was presented (Section 5.2.1 on page 155).

The developed method was then used in an optimisation for designing electromagnetic actuators (Section 5.3 on page 165). In this case, the optimised variable was peak force, and it was shown that optimal geometric parameters can be derived given magnet volume and coil resistance alone. A wire diameter of around 1.5 mm was shown to produce the most efficient actuators, with a cylindrical magnet length to diameter aspect ratio of approximately 0.75 and a coil length to diameter aspect ratio of approximately 2.5.

§8.2 Future work

This work leaves open many areas of investigation for the future. Some of these are highlighted here.

§8.2.1 *Magnetic forces*

1. While a number of force and torque magnet interaction equations have been published for various geometries, there are still a number of unmodelled scenarios. Future research in this area should consider consolidating theory for the forces and torques between magnets for additional magnet shapes and under arbitrary poses. Some examples of unexplored areas of research are:
    a) Forces between cylindrical magnets with rotation around one axis.
    b) Forces between cuboid magnets and between cylindrical magnets with arbitrary rotation.
    c) Torque between cuboid and cylindrical magnets with rotation.
    d) Forces and torques between spherical magnets.

e) Forces and torques between triangular-shaped magnets of various orientations.

f) Force between pairs of differently-shaped magnets (such as the force between one cuboid and one cylindrical magnet).

Development of theory for these scenarios would mean that finite element analysis would not be required to conduct a dynamic simulation with realistic forces and torques of a six degree of freedom electromagnetic system.

2. Investigate the non-ideal effects seen with respect to magnet forces; for example, given some experimental evidence that larger magnets produce magnetic fields with smaller magnitudes than expected, what is the influence between magnet size and ability to create magnetisation homogeneously?

3. Similarly, the design of multipole magnet arrays has seen comparatively little experimental validation.

   a) What are the practical limitations to designing such multipole arrays?

   b) It requires significant computational effort to calculate forces between multipole arrays with large numbers of magnets. Can models for such arrays be reduced to consider only the significant magnet interactions, hence reducing calculation time?

   c) It is expected that their cross-coupling effects will be non-negligible for many applications; can six degree of freedom behaviour of such devices be realistically simulated?

§8.2.2 *Electromagnetic forces*

1. For designing coil actuators, the inductance of the system determines the bandwidth of operation. This should be included in any optimisation routine; it is suspected this will have significant effects on the suitability of certain geometries in some cases, such as the high-frequency operation of coils designed for maximum force.

2. An extension on calculating coil forces to include the interaction between curved and straight sections could allow very fast analytic solutions compared to finite element analysis for more complex coil geometries such as 'race-track' shapes.

3. A thermal model could be incorporated into the analysis to ensure specific temperature bounds are not exceeded during dynamic operation.

The development of a multi-physics simulation involving magnetic forces, eddy current forces, induction effects, and thermal effects would provide a powerful tool for electromagnet design.

4. The 'sleeve-coil' electromagnet design analysed in this thesis allows for little off-axis motion. Further work is necessary to optimise alternate actuator designs, such as 'pancake' coils for use in longer-stroke multi-directional actuators.

§8.2.3 *Vibration control*

1. 'Skyhook damping' requires an estimate of the absolute velocity for feedback control. Integrating accelerometer measurements has limitations at low frequencies due to filters in the charge amplification and the integration technique itself. Magnetic geophones offer an alternative sensing option and other estimation filters have been presented; to what degree can low-frequency vibration be measured for active control?
2. Nonlinear viscous damping elements have been shown to produce results approaching that of the ideal case of skyhook damping. Can this technique be emulated in practise using a nonlinear active control system? If so, how do the results compare against a passive nonlinear system? Finally, what side-effects do the nonlinearities add to the vibration response?
3. Is it possible to construct a highly sensitive acceleration sensor based on the motion of a levitating magnet near its quasi–zero stiffness position?

§8.2.4 *Quasi–zero stiffness*

1. The experimental results shown for the quasi–zero stiffness magnetic system are for a single degree of freedom only, and the constraints imposed on such systems can limit their high-frequency performance (seen for example in friction in linear bearings); a project to extend the quasi–zero stiffness system to six degrees of freedom is of practical interest and is already under way.
2. Load balancing for maintaining quasi–zero stiffness and avoiding instability is required for practical application. This is also being investigated separately in a parallel project.
3. Is it possible to design a nonlinear controller to maintain quasi–zero stiffness for a magnetic device? Intuitively, there cannot be a stable system that achieves perfect quasi–zero stiffness; therefore, what are the limits to which such a system can be bound?

References

[1] O. Agamennoni, I. Skrjanc, M. Lepetic, H. Chiacchiarini, and D. Matko. 'Nonlinear uncertainty model of a magnetic suspension system'. *Mathematical and Computer Modelling* 40.9-10 (11/2004), pp. 1075–1087. DOI: 10.1016/j.mcm.2003.09.043 (cit. on p. 31).

[2] J. S. Agashe and D. P. Arnold. 'A study of scaling and geometry effects on the forces between cuboidal and cylindrical magnets using analytical force solutions'. *Journal of Physics D: Applied Physics* 41.10 (2008), p. 105001. DOI: 10.1088/0022-3727/41/10/105001 (cit. on p. 75).

[3] M. Ahmadian, B. Reichert, and X. Song. 'System non-linearities induced by skyhook dampers'. *Shock and Vibration* 8.2 (2001), pp. 95–105. URL: http://iospress.metapress.com/content/nbjj7j71e10p71qf (cit. on p. 13).

[4] M. Ahmadian, X. Song, and S. C. Southward. 'No-jerk skyhook control methods for semiactive suspensions'. *Journal of Vibration and Acoustics* 126.4 (2004), pp. 580–584. DOI: 10.1115/1.1805001 (cit. on p. 13).

[5] G. Akoun and J.-P. Yonnet. '3D analytical calculation of the forces exerted between two cuboidal magnets'. *IEEE Transactions on Magnetics* MAG-20.5 (09/1984), pp. 1962–1964. DOI: 10.1109/TMAG.1984.1063554 (cit. on pp. 58–60, 65, 78, 80, 108, 193).

[6] C. Akyel, S. Babic, and S. Salon. 'New expressions for calculating the magnetic force of the system: Filament coil–disk coil'. *IEEE International Magnetics Conference (INTERMAG)*. 2003. DOI: 10.1109/INTMAG.2003.1230719 (cit. on p. 162).

[7] C. Akyel, S. I. Babic, and M.-M. Mahmoudi. 'Mutual inductance calculation for non-coaxial circular air coils with parallel axes'. *Progress In Electromagnetics Research* 91 (2009), pp. 287–301. DOI: 10.2528/PIER09021907 (cit. on p. 156).

[8] P. Alabuzhev, A. Gritchin, L. Kim, G. Migirenko, V. Chon, and P. Stepanov. *Vibration protecting and measuring systems with quasi-zero stiffness*. Ed. by E. Rivin. Applications of Vibration. Hemisphere Publishing Corporation, 1989 (cit. on pp. 37, 180).

[9] H. Allag, J.-P. Yonnet, and M. Latreche. '3D analytical calculation of forces between linear Halbach-type permanent-magnet arrays'.
8th International Symposium on Advanced Electromechanical Motion Systems & Electric Drives Joint Symposium (ELECTROMOTION). 07/2009.
DOI: 10.1109/ELECTROMOTION.2009.5259084 (cit. on pp. 66, 132, 136).

[10] H. Allag, J. Yonnet, M. Fassenet, and M. Latreche.
'3D analytical calculation of interactions between perpendicularly magnetized magnets—Application to any magnetization direction'.
Sensor Letters 7.3 (2009), pp. 486–491. DOI: 10.1166/sl.2009.1094
(cit. on pp. 63, 78).

[11] H. Allag and J.-P. Yonnet. '3-D analytical calculation of the torque and force exerted between two cuboidal magnets'.
IEEE Transactions on Magnetics 45.10 (10/2009), pp. 3969–3972.
DOI: 10.1109/TMAG.2009.2025047 (cit. on p. 72).

[12] K. A. Ananthaganeshan, M. J. Brennan, and S. J. Elliott.
Low and high frequency instabilities in feedback control of a vibrating single degree of freedom system. ISVR Technical Memorandum 870.
University of Southampton, 03/2001.
URL: http://www.isvr.soton.ac.uk/STAFF/Pubs/Pubpdfs/Pub1274.pdf
(cit. on p. 14).

[13] C. Anderson and S. Salter.
'Optimum geometry analyses for rectangular "hard" magnet pairs'.
Magnetics, IEEE Transactions on 23.5 (1987), pp. 3836–3844.
DOI: 10.1109/TMAG.1987.1065495 (cit. on pp. 26, 81).

[14] Y. Araki, T. Asai, K. Kimura, K. Maezawa, and T. Masui.
'Nonlinear vibration isolator with adjustable restoring force'.
Journal of Sound and Vibration (2013). DOI: 10.1016/j.jsv.2013.06.030
(cit. on p. 38).

[15] D. P. Arnold. 'Review of microscale magnetic power generation'.
IEEE Transactions on Magnetics 43.11 (11/2007), pp. 3940–3951.
DOI: 10.1109/TMAG.2007.906150 (cit. on p. 21).

[16] K. Asami, A. Chiba, M. Rahman, T. Hoshino, and A. Nakajima.
'Stiffness analysis of a magnetically suspended bearingless motor with permanent magnet passive positioning'.
IEEE Transactions on Magnetics 41.10 (2005), pp. 3820–3822.
DOI: 10.1109/TMAG.2005.854933 (cit. on p. 25).

[17] B. Azzerboni, E. Cardelli, M. Raugi, A. Tellini, and G. Tina.
'Magnetic field evaluation for thick annular conductors'.
IEEE Transactions on Magnetics 29.3 (05/1993), pp. 2090 –2094.
DOI: 10.1109/20.211324 (cit. on p. 59).

[18] S. Babic, Z. Andjelic, B. Krstajic, and S. Salon.
'Analytical calculation of the 3D magnetostatic field of a toroidal conductor with rectangular cross section'.
IEEE Transactions on Magnetics 24.6 (11/1988), pp. 3162–3164.
DOI: 10.1109/20.92368 (cit. on p. 59).

[19] S. Babic, F. Sirois, C. Akyel, G. Lemarquand, V. Lemarquand, and R. Ravaud.
'New formulas for mutual inductance and axial magnetic force between a thin wall solenoid and a thick circular coil of rectangular cross-section'.
IEEE Transactions on Magnetics 47.8 (2011), pp. 2034–2044.
DOI: 10.1109/TMAG.2011.2125796 (cit. on pp. 159, 161).

[20] S. Babic, F. Sirois, C. Akyel, G. Lemarquand, V. Lemarquand, and R. Ravaud.
'Correction to "New formulas for mutual inductance and axial magnetic force between a thin wall solenoid and a thick circular coil of rectangular cross-section"'. *IEEE Transactions on Magnetics* 48.6 (2012), pp. 2096–2096.
DOI: 10.1109/TMAG.2011.2180733 (cit. on p. 159).

[21] S. Babic and C. Akyel.
'Magnetic force calculation between thin coaxial circular coils in air'.
IEEE Transactions on Magnetics 44.4 (04/2008), pp. 445–452.
DOI: 10.1109/TMAG.2007.915292 (cit. on pp. 75, 153, 156).

[22] S. Babic and C. Akyel. 'Magnetic force between inclined circular filaments placed in any desired position'.
IEEE Transactions on Magnetics 48.1 (2011), pp. 69–80 (cit. on pp. 76, 78, 164).

[23] S. Babic, C. Akyel, and N. Boudjada.
'The simplest formulas for self inductance, mutual inductance and magnetic force of coaxial cylindrical magnets and thin coils'.
Recent Researches in Circuits and Systems.
Kos Island, Greece: WSEAS Press, 2012. URL: http://www.wseas.us/e-library/conferences/2012/Kos/CIRSYS/CIRSYS-03.pdf (cit. on p. 177).

[24] F. T. Backers. 'A magnetic journal bearing'.
Philips Technical Review 22.7 (1961), pp. 232–238 (cit. on pp. 26, 129).

[25] V. S. Baklanov. 'Low-frequency vibroisolation mounting of power plants for new-generation airplanes with engines of extra-high bypass ratio'.
Journal of Sound and Vibration 308.3–5 (12/2007), pp. 709–720.
DOI: 10.1016/j.jsv.2007.04.042 (cit. on p. 38).

[26] Balandin, Bolotnik, and Pilkey.
'Review: Optimal shock and vibration isolation'.
Shock and Vibration 5.2 (1998), pp. 73–87.
URL: http://iospress.metapress.com/content/th5ykc0afb1q0tgd/ (cit. on p. 6).

[27] F. Bancel. 'Magnetic nodes'.
Journal of Physics D: Applied Physics 32 (09/1999), pp. 2155–2161.
DOI: 10.1088/0022-3727/32/17/304 (cit. on pp. 60, 61).

[28] S. Banerjee, T. K. S. Kumar, J. Pal, and D. Prasad.
'Controller design for large-gap control of electromagnetically levitated system by using an optimization technique'.
IEEE Transactions on Control Systems Technology 16.3 (05/2008), pp. 408–415.
DOI: 10.1109/TCST.2007.906272 (cit. on p. 32).

[29] R. Bassani. 'Earnshaw (1805–1888) and passive magnetic levitation'.
Meccanica 41.4 (08/2006), pp. 375–389. DOI: 10.1007/s11012-005-4503-x (cit. on pp. 28, 29).

[30] R. Bassani. 'Levitation of passive magnetic bearings and systems'.
Tribology International 39.9 (2006), pp. 963–970.
DOI: 10.1016/j.triboint.2005.10.003 (cit. on pp. 26, 75).

[31] R. Bassani. 'A stability space of a magnetomechanical bearing'.
Journal of Dynamic Systems, Measurement, and Control 129.2 (2007), pp. 178–181.
DOI: 10.1115/1.2431812 (cit. on p. 30).

[32] M. Beccaria, M. Bernardini, E. Bougleux, S. Braccini, C. Bradaschia, C. Casciano, G. Cella, E. Cuoco, E. D'Ambrosio, G. De Carolis, et al.
'Extending the VIRGO gravitational wave detection band down to a few Hz: Metal blade springs and magnetic antisprings'.
Nuclear Instruments and Methods in Physics Research Section A: Accelerators, Spectrometers, Detectors and Associated Equipment 394.3 (1997), pp. 397–408.
DOI: 10.1016/S0168-9002(97)00661-X (cit. on pp. 38, 108).

[33] G. Becherini, S. Di Fraia, R. Ciolini, M. Schneider, and B. Tellini.
'Shielding of high magnetic fields'.
IEEE Transactions on Magnetics 45.1 (01/2009), pp. 604–609.
DOI: 10.1109/TMAG.2008.2008537 (cit. on p. 130).

[34] S. P. Beeby and T. O'Donnell. *Electromagnetic energy harvesting*.
Ed. by S. Priya and D. J. Inman. Energy Harvesting Technologies. 2009.
DOI: 10.1007/978-0-387-76464-1_5 (cit. on p. 21).

[35] L. Benassi, P. Gardonio, and S. J. Elliott. *Equipment isolation of a SDOF system with an inertial actuator using feedback control strategie – Part 2: Experiment*.
ISVR Technical Memorandum 896. University of Southampton, 10/2002.
URL: http://www.isvr.soton.ac.uk/STAFF/Pubs/Pubpdfs/Pub1661.pdf (cit. on p. 16).

[36] L. Benassi, P. Gardonio, and S. J. Elliott. *Equipment isolation of a SDOF system with an inertial acutator using double feedback control strategies*.
ISVR Technical Memorandum 8893. University of Southampton, 10/2002.
URL: http://www.isvr.soton.ac.uk/STAFF/Pubs/Pubpdfs/Pub1659.pdf (cit. on p. 16).

[37] J. S. Bendat and A. G. Piersol.
Engineering applications of correlation and spectral analysis. Vol. Second Edition.
Wiley InterScience, 1993 (cit. on p. 40).

[38] G. J. Bennett, J. Antunes, J. A. Fitzpatrick, and V. Debut.
'A method for optimal reconstruction of velocity response using experimental displacement and acceleration signals'.
Proceedings of the 14th International Congress on Sound and Vibration.
Cairns, Australia, 07/2007 (cit. on p. 220).

[39] M. V. Berry. 'The Levitron™: An adiabatic trap for spins'. *Proceedings of the Royal Society of London, Series A* 452.1948 (05/1996), pp. 1207–1220.
URL: http://www.jstor.org/view/13645021/ap000005/00a00130
(cit. on p. 30).

[40] M. V. Berry and A. K. Geim. 'Of flying frogs and levitrons'.
The European Physical Society 18 (1997), pp. 307–313.
DOI: 10.1088/0143-0807/18/4/012 (cit. on p. 30).

[41] H. Bleuler. 'A survey of magnetic levitation and magnetic bearing types'.
JSME International Journal, Series III 35.3 (1992), pp. 335–342.
URL: http://ci.nii.ac.jp/naid/110002503299/en (cit. on pp. 17, 30).

[42] J Boehm, R Gerber, and N. R. C. Kiley. 'Sensors for magnetic bearings'.
IEEE Transactions on Magnetics 29.6 (11/1993), pp. 2962–2964.
DOI: 10.1109/20.280903 (cit. on p. 220).

[43] A. H. Boerdijk. 'Levitation by static magnetic fields'.
Philips Technical Review 18 (1956), pp. 125–127 (cit. on pp. 29, 30).

[44] A. H. Boerdijk. 'Technical aspects of levitation'.
Philips Research Reports 11 (1956), pp. 45–56 (cit. on pp. 28–30).

[45] N. Bolotnik, D. Balandin, and W. Pilkey. *Optimum shock isolation*. Tech. rep.
Virginia Univ. Charlottesville, Dept. of Mechanical And Aerospace Engineering, 03/2001. DOI: http://handle.dtic.mil/100.2/ADA389239
(cit. on p. 7).

[46] E. Bonisoli and A. Vigliani.
'Identification techniques applied to a passive elasto-magnetic suspension'.
Mechanical Systems and Signal Processing 21.3 (04/2007), pp. 1479–1488.
DOI: 10.1016/j.ymssp.2006.05.009 (cit. on pp. 37, 108, 195).

[47] E. Bonisoli and A. Vigliani. 'Passive elasto-magnetic suspensions: Nonlinear models and experimental outcomes'.
Mechanics Research Communications 34.4 (06/2007), pp. 385–394.
DOI: 10.1016/j.mechrescom.2007.02.005 (cit. on pp. 37, 108, 195, 210).

[48] E. Bonisoli and A. Vigliani. 'Passive effects of rare-earth permanent magnets on flexible conductive structures'.
Mechanics Research Communications 33.3 (2006), pp. 302–319.
DOI: 10.1016/j.mechrescom.2005.08.011 (cit. on pp. 32, 60, 208).

[49] M. J. Brennan, K. A. Ananthaganeshan, and S. J. Elliott.
'Instabilities due to instrumentation phase-lead and phase-lag in the feedback control of a simple vibrating system'.
Journal of Sound and Vibration 304.3–5 (07/2007), pp. 466–478.
DOI: 10.1016/j.jsv.2007.01.046 (cit. on pp. 14, 15, 231, 232).

[50] M. J. Brennan. 'Some recent developments in adaptive tuned vibration absorbers/neutralisers'. *Shock and Vibration* 13.4/5 (2006), pp. 531–543.
URL: http://iospress.metapress.com/link.asp?id=55dxl8kwh0wmvfr0 (cit. on p. 20).

[51] S. Bruno, A. Liu, Y. Lu, and H. S. Vu.
Design and build of a prosthetic attachment. Honours Thesis.
School of Mechanical Engineering, The University of Adelaide, 2011 (cit. on p. 56).

[52] C. Byfield and D. Fordred. *Analysis and force modelling of permanent magnets*. Honours Thesis.
School of Mechanical Engineering, The University of Adelaide, 2012 (cit. on p. 70).

[53] A. M. Campbell. 'Forces between arrays of magnets and superconductors'.
Superconductor Science and Technology 15 (2002), pp. 759–762.
DOI: 10.1088/0953-2048/15/5/323 (cit. on p. 148).

[54] P. Campbell. *Permanent magnet materials and their application*.
Cambridge University Press, 1994 (cit. on pp. 48, 51).

[55] A. Carrella, M. J. Brennan, and T. P. Waters. 'Static analysis of a passive vibration isolator with quasi-zero-stiffness characteristic'.
Journal of Sound and Vibration 301.3–5 (04/2007), pp. 678–689.
DOI: 10.1016/j.jsv.2006.10.011 (cit. on pp. 37, 180, 182).

[56] A. Carrella, M. J. Brennan, T. P Waters, and K. Shin.
'On the design of a high-static-low-dynamic stiffness isolator using linear mechanical springs and magnets'.
Journal of Sound and Vibration 315.3 (2008), pp. 712–720.
DOI: 10.1016/j.jsv.2008.01.046 (cit. on pp. 38, 108, 114).

[57] A. Carrella, M. J. Brennan, I. Kovacic, and T. P. Waters.
'On the force transmissibility of a vibration isolator with quasi-zero-stiffness'.
Journal of Sound and Vibration 322.4–5 (05/2009), pp. 707–717.
DOI: 10.1016/j.jsv.2008.11.034 (cit. on pp. 37, 41, 180, 182).

[58] F. Casciati and F. Ubertini.
'Nonlinear vibration of shallow cables with semiactive tuned mass damper'.
Nonlinear Dynamics 53.1–2 (09/2007), pp. 89–106.
DOI: 10.1007/s11071-007-9298-y (cit. on p. 20).

[59] G. Cella, V. Sannibale, R. DeSalvo, S. Marka, and A. Takamori.
'Monolithic geometric anti-spring blades'.
Nuclear Instruments and Methods in Physics Research Section A: Accelerators, Spectrometers, Detectors and Associated Equipment 540.2-3 (2005), pp. 502–519.
DOI: 10.1016/j.nima.2004.10.042 (cit. on p. 38).

[60] V. R. Challa, M. G. Prasad, Y. Shi, and F. T. Fisher. 'A vibration energy harvesting device with bidirectional resonance frequency tunability'.
Smart Materials and Structures 17.1 (2008), 015035 (10pp).
DOI: 10.1088/0964-1726/17/01/015035 (cit. on pp. 21, 89).

[61] S.-C. Chang.
'Dynamics of a magnetically levitated table with hybrid magnets'.
The Japan Society of Applied Physics 40.10 (10/2001), pp. 6163–6170.
DOI: 10.1143/JJAP.40.6163 (cit. on p. 32).

[62] J. F. Charpentier and G Lemarquand. 'Study of permanent-magnet couplings with progressive magnetization using an analytical formulation'.
IEEE Transactions on Magnetics 35.5 (09/1999), pp. 4206–4217.
DOI: 10.1109/20.799069 (cit. on pp. 27, 67).

[63] J. F. Charpentier and G. Lemarquand. 'Calculation of ironless permanent magnet couplings using semi-numerical magnetic pole theory method'.
The International Journal for Computation and Mathematics in Electrical and Electronic Engineering 20.1 (03/2001), pp. 72–89.
DOI: 10.1108/03321640110359769 (cit. on pp. 27, 58, 69).

[64] J.-F. Charpentier and G. Lemarquand. 'Optimal design of cylindrical air-gap synchronous permanent magnet couplings'.
IEEE Transactions on Magnetics 35.2 (03/1999), pp. 1037–1046.
DOI: 10.1109/20.748851 (cit. on pp. 27, 67).

[65] C. H. Chen, J. Talnagi, J. Liu, P. Vora, A. Higgins, and S. Liu.
'The effect of neutron irradiation on Nd-Fe-B and Sm_2-Co_{17}-based high-temperature magnets'.
IEEE Transactions on Magnetics 41.10 (2005), pp. 3832–3834.
DOI: 10.1109/TMAG.2005.854985 (cit. on p. 32).

[66] C. Chen, B. Paden, J. Antaki, J. Ludlow, D. Paden, R. Crowson, and G. Bearnson. 'A magnetic suspension theory and its application to the HeartQuest ventricular assist device'.
Artificial Organs 26.11 (2002), pp. 947–951.
DOI: 10.1046/j.1525-1594.2002.07125.x (cit. on p. 129).

[67] C. Chen, B. Paden, J. Antaki, J. Ludlow, and G. Bearnson.
'Optimal design of permanent magnet bearings with application to the HeartQuest™ ventricular assist device'.
JSME International Journal, Series C: Mechanical Systems, Machine Elements and Manufacturing 46.2 (2003), pp. 403–408. DOI: 10.1299/jsmec.46.403
(cit. on p. 27).

[68] P.-C. Chen and M.-C. Shih.
'Modeling and robust active control of a pneumatic vibration isolator'.
Journal of Vibration and Control 13.11 (2007), pp. 1553–1571.
DOI: 10.1177/1077546307078246 (cit. on p. 2).

[69] S.-L. Chen, J.-J. Liu, and H.-C. Lai. 'Wavelet analysis for identification of damping ratios and natural frequencies'.
Journal of Sound and Vibration 323.1-2 (2009), pp. 130–147.
DOI: 10.1016/j.jsv.2009.01.029 (cit. on p. 225).

[70] Y.-D. Chen, C.-C. Fuh, and P.-C. Tung.
'Application of voice coil motors in active dynamic vibration absorbers'.
IEEE Transactions on Magnetics 41.3 (2005), pp. 1149–1154.
DOI: 10.1109/TMAG.2004.843329 (cit. on p. 20).

[71] H.-S. Cho, C.-H. Im, and H.-K. Jung.
'Magnetic field analysis of 2-D permanent magnet array for planar motor'.
IEEE Transactions on Magnetics 37.3 (09/2001), pp. 3762–3766.
DOI: 10.1109/20.952708 (cit. on pp. 131, 143, 144).

[72] J.-S. Choi and J. Yoo.
'Design of a Halbach magnet array based on optimization techniques'.
IEEE Transactions on Magnetics 44.10 (10/2008), pp. 2361–2366.
DOI: 10.1109/TMAG.2008.2001482 (cit. on pp. 131, 144).

[73] J. S. Choi, J. Yoo, S. Nishiwaki, and K. Izui.
'Optimization of magnetization directions in a 3-D magnetic structure'.
IEEE Transactions on Magnetics 46.6 (2010), pp. 1603–1606.
DOI: 10.1109/TMAG.2010.2040251 (cit. on p. 144).

[74] J. Choi, S. Hong, W. Lee, S. Kang, and M. Kim.
'A robot joint with variable stiffness using leaf springs'.
IEEE Transactions on Robotics 27.2 (04/2011), pp. 229–238.
DOI: 10.1109/TRO.2010.2100450 (cit. on p. 191).

[75] K.-B. Choi, Y. G. Cho, T. Shinshi, and A. Shimokohbe.
'Stabilization of one degree-of-freedom control type levitation table with permanent magnet repulsive forces'.
Mechatronics 13.6 (07/2003), pp. 587–603.
DOI: 10.1016/S0957-4158(02)00032-6 (cit. on pp. 99, 107).

[76] Y.-T. Choi and N. M. Wereley. 'Self-powered magnetorheological dampers'.
Journal of Vibration and Acoustics 131.4 (2009), p. 044501.
DOI: 10.1115/1.3142882 (cit. on p. 21).

[77] J. M. D. Coey. 'Permanent magnet applications'.
Journal of Magnetism and Magnetic Materials 248.3 (2002), pp. 441–456.
DOI: 10.1016/S0304-8853(02)00335-9 (cit. on pp. 22, 23).

[78] J. Coey. 'Hard magnetic materials: A perspective'.
IEEE Transactions on Magnetics 47.12 (2011), pp. 4671–4681.
DOI: 10.1109/TMAG.2011.2166975 (cit. on p. 54).

[79] J. C. Compter, J. L. G. Janssen, and E. A. Lomonova.
'Ampere's circuital 3-D model for noncuboidal magnets'.
IEEE Transactions on Magnetics 46.12 (12/2010), pp. 4009–4015.
DOI: 10.1109/TMAG.2010.2070804 (cit. on p. 59).

[80] J. Conway.
'Forces between thin coils with parallel axes using Bessel functions'.
IEEE Transactions on Magnetics 49.9 (2013).
DOI: 10.1109/TMAG.2013.2251652 (cit. on pp. 75, 78).

[81] R. K. Cooper, V. K. Neil, and W. R. Woodruff.
'Optimum permanent-magnet dimensions for repulsion applications'.
IEEE Transactions on Magnetics MAG-9.2 (1973), pp. 125–127.
DOI: 10.1109/TMAG.1973.1067575 (cit. on pp. 75, 81).

[82] G. Csernák and G. Stépán. 'Sometimes digital control leads to chaos'.
Proceedings of the 14th International Congress on Sound and Vibration.
Cairns, Australia, 07/2007 (cit. on p. 14).

[83] A. D'Angola, G. Carbone, L. Mangialardi, and C. Serio.
'Non-linear oscillations in a passive magnetic suspension'.
International Journal of Non-Linear Mechanics 41.9 (11/2006), pp. 1039–1049.
DOI: 10.1016/j.ijnonlinmec.2006.10.013 (cit. on pp. 37, 210).

[84] V. Danilov and M. Ianovici. 'Magnetic field of thick finite DC solenoids'.
Nuclear Instruments and Methods 94.3 (1971), pp. 541–550.
DOI: 10.1016/0029-554X(71)90019-X (cit. on p. 59).

[85] L. Darabant, M. Plesa, D. D. Micu, D. Stet, R. Ciupa, and A. Darabant.
'Energy efficient coils for magnetic stimulation of peripheral nerves'.
IEEE Transactions on Magnetics 45.3 (03/2009), pp. 1690–1693.
DOI: 10.1109/TMAG.2009.2012783 (cit. on p. 23).

[86] J. Delamare, J. P. Yonnet, and E. Rullière.
'A compact magnetic suspension with only one axis control'.
IEEE Transactions on Magnetics 30.6 (11/1994), pp. 4746–4748.
DOI: 10.1109/20.334209 (cit. on pp. 25, 100, 102, 107).

[87] K. Demachi, S. Rybalko, and M. Fujita.
'Inverse analysis of the current dipoles distribution in a human brain applied with the shifting-aperture method'.
IEEE Transactions on Magnetics 44.6 (06/2008), pp. 1426–1429.
DOI: 10.1109/TMAG.2007.916366 (cit. on p. 23).

[88] G. G. Denisov, V. V. Novikov, and A. E. Fedorov.
'To the problem of a passive levitation of bodies in physical fields'.
Journal of Applied Mechanics 77.3, 031017 (2010), p. 031017.
DOI: 10.1115/1.4000384 (cit. on p. 30).

[89] C. Diaz and P. Gardonio. *Proportional, integral, derivative, PID-, PI- and PD-velocity feedback control with inertial actuators*.
ISVR Technical Memorandum 956. University of Southampton, 03/2005.
URL: http://www.isvr.soton.ac.uk/STAFF/Pubs/Pubpdfs/Pub8285.pdf (cit. on p. 17).

[90] *Digital library of mathematical functions*.
National Institute of Standards and Technology, 2010.
URL: http://dlmf.nist.gov/ (cit. on p. 77).

[91] S. Earnshaw. 'On the nature of the molecular forces which regulate the constitution of the luminiferous ether'. *Transactions of the Cambridge Philosophical Society* 3.1 (1842). Digital version via Google Books., pp. 97–112.
URL: http://tinyurl.com/earnshaw (cit. on pp. 3, 28, 52, 63, 87).

[92] B. Ebrahimi, M. B. Khamesee, and M. F. Golnaraghi. 'Design and modeling of a magnetic shock absorber based on eddy current damping effect'.
Journal of Sound and Vibration 315.4-5 (2008), pp. 875–889.
DOI: 10.1016/j.jsv.2008.02.022 (cit. on p. 32).

[93] C Elbuken, M. B. Khamesee, and M Yavuz. 'Eddy current damping for magnetic levitation: Downscaling from macro- to micro-levitation'.
Journal of Physics D: Applied Physics 39.18 (2006), pp. 3932–3938.
DOI: 10.1088/0022-3727/39/18/002 (cit. on p. 32).

[94] P Eliès and G Lemarquand. 'Analytical optimization of the torque of a permanent-magnet coaxial synchronous coupling'.
IEEE Transactions on Magnetics 34.4 (07/1998), pp. 2267–2273.
DOI: 10.1109/20.703865 (cit. on p. 67).

[95] P Eliès and G Lemarquand. 'Analytical study of radial stability of permanent-magnet synchronous couplings'.
IEEE Transactions on Magnetics 35.4 (07/1999), pp. 2133–2136.
DOI: 10.1109/20.774183 (cit. on p. 67).

[96] S. J. Elliott, M. Serrand, and P. Gardonio. 'Feedback stability limits for active isolation systems with reactive and inertial actuators'.
Journal of Vibration and Acoustics 123.2 (2001), pp. 250–261.
DOI: 10.1115/1.1350822 (cit. on p. 10).

[97] S. J. Elliott, L. Benassi, M. J. Brennan, P. Gardonio, and X. Huang. 'Mobility analysis of active isolation systems'.
Journal of Sound and Vibration 271.1-2 (03/2004), pp. 297–321.
DOI: 10.1016/S0022-460X(03)00770-3 (cit. on p. 10).

[98] W. P. Engels and S. J. Elliott.
'Optimal centralized and decentralized velocity feedback control on a beam'.
Smart Materials and Structures 17.2 (2008).
DOI: 10.1088/0964-1726/17/2/025009 (cit. on p. 15).

[99] M. Ferrari, V. Ferrari, M. Guizzetti, and D. Marioli.
'An autonomous battery-less sensor module powered by piezoelectric energy harvesting with rf transmission of multiple measurement signals'.
Smart Materials and Structures 18.8 (2009).
DOI: 10.1088/0964-1726/18/8/085023 (cit. on p. 21).

[100] T. Finocchiaro, T. Butschen, P. Kwant, U. Steinseifer, T. Schmitz-Rode, K. Hameyer, and M. Lessmann.
'New linear motor concepts for artificial hearts'.
IEEE Transactions on Magnetics 44.6 (2008), pp. 678–681.
DOI: 10.1109/TMAG.2007.916110 (cit. on p. 129).

[101] Y. Frizenschaf, S. Giles, J. Miller, T. Pitman, C. Stapleton, B. Cazzolato, and W. Robertson. 'Development of a magnetic levitation vibration isolator using inclined permanent magnet springs'. *Proceedings of Acoustics 2011*.
Gold Coast, Australia, 11/2011. URL: http://hdl.handle.net/2440/69529 (cit. on pp. 45, 123).

[102] Y. Frizenschaf, S. Giles, J. Miller, T. Pitman, and C. Stapleton.
Magnetic levitation vibration isolation device. Honours Thesis.
School of Mechanical Engineering, The University of Adelaide, 2011 (cit. on pp. 123, 125).

[103] C. Fulford, M. Maggiore, and J. Apkarian.
'Control of a 5DOF magnetically levitated positioning stage'.
IEEE Transactions on Control Systems Technology 17.4 (07/2009), pp. 844–852.
DOI: 10.1109/TCST.2008.2002755 (cit. on p. 25).

[104] R.-F. Fung, Y.-T. Liu, and C.-C. Wang. 'Dynamic model of an electromagnetic actuator for vibration control of a cantilever beam with a tip mass'.
Journal of Sound and Vibration 288.4-5 (2005), pp. 957–980.
DOI: 10.1016/j.jsv.2005.01.046 (cit. on p. 208).

[105] E. P. Furlani. 'A formula for the levitation force between magnetic disks'.
IEEE Transactions on Magnetics 29.6 (11/1993), pp. 4165–4169.
DOI: 10.1109/20.280867 (cit. on pp. 58, 75).

[106] E. P. Furlani. *Permanent magnet and electromechanical devices*.
Ed. by I. Mayergoyz. Academic Press, 2001 (cit. on pp. 58, 157).

[107] E. Furlani. 'Formulas for the force and torque of axial couplings'.
IEEE Transactions on Magnetics 29.5 (09/1993), pp. 2295–2301.
DOI: 10.1109/20.231636 (cit. on p. 75).

[108] E. Furlani, S. Reznik, and A. Kroll.
'A three-dimensional field solution for radially polarized cylinders'.
IEEE Transactions on Magnetics 31.1 (01/1995), pp. 844–851.
DOI: 10.1109/20.364587 (cit. on p. 59).

[109] H. P. Gavin, R. Morales, and K. Reilly. 'Drift-free integrators'.
Review of Scientific Instruments 69 (1998), p. 2171. DOI: 10.1063/1.1148918 (cit. on p. 221).

[110] H. P. Gavin and A. Zaicenco.
'Performance and reliability of semi-active equipment isolation'.
Journal of Sound and Vibration 306.1-2 (09/2007), pp. 74–90.
DOI: 10.1016/j.jsv.2007.05.039 (cit. on p. 15).

[111] A. K. Geim, M. D. Simon, M. I. Boamfa, and L. O. Heflinger.
'Magnetic levitation at your fingertips'. *Nature* 400 (07/1999), pp. 323–324.
DOI: 10.1038/22444 (cit. on p. 30).

[112] A. Geim. 'Everyone's magnetism'. *Physics Today* (09/1998), pp. 36–39.
DOI: 10.1063/1.882437 (cit. on p. 30).

[113] L. Gentili and L. Marconi.
'Robust nonlinear disturbance suppression of a magnetic levitation system'.
Automatica 39.4 (04/2003), pp. 735–742.
DOI: 10.1016/S0005-1098(02)00307-2 (cit. on p. 32).

[114] K. Gjini, T. Maeno, K. Iramina, and S. Ueno. 'Short-term episodic memory encoding in the human brain: A MEG and EEG study'.
IEEE Transactions on Magnetics 41.10 (2005), pp. 4149–4151.
DOI: 10.1109/TMAG.2005.854856 (cit. on p. 23).

[115] J. Glaros and M. Hergott.
Design of an active vibration isolation unit for optical applications.
Honours Thesis.
School of Mechanical Engineering, The University of Adelaide, 2001
(cit. on p. 4).

[116] E. Gouda, S. Mezani, L. Baghli, and A. Rezzoug.
'Comparative study between mechanical and magnetic planetary gears'.
IEEE Transactions on Magnetics 47.2 (02/2011), pp. 439–450.
DOI: 10.1109/TMAG.2010.2090890 (cit. on p. 27).

[117] K. E. Graves, D. Toncich, and P. G. Iovenitti. 'Theoretical comparison of motional and transformer emf device damping efficiency'.
Journal of Sound and Vibration 233.3 (06/2000), pp. 441–453.
DOI: 10.1006/jsvi.1999.2820 (cit. on p. 12).

[118] K. E. Graves. 'Electromagnetic energy regenerative vibration damping'.
PhD thesis. Swinburne University of Technology, 2000.
DOI: http://adt.lib.swin.edu.au/public/adt-VSWT20060307.120939/
(cit. on pp. 21, 32).

[119] B. L. J. Gysen, J. J. H. Paulides, J. L. G. Janssen, and E. Lomonova.
'Active electromagnetic suspension system for improved vehicle dynamics'.
Vehicle Power and Propulsion Conference, 2008. 2008, pp. 1–6.
DOI: 10.1109/VPPC.2008.4677555 (cit. on p. 13).

[120] K. Halbach. 'Physical and optical properties of rare earth cobalt magnets'.
Nuclear Instruments and Methods 187 (1981), pp. 109–117.
DOI: 10.1016/0029-554X(81)90477-8 (cit. on p. 130).

[121] X. Han, H. Seki, Y. Kamiya, and M. Hikizu.
'Wearable handwriting input device using magnetic field-geomagnetism cancellation in position calculation'.
Precision Engineering 33.1 (2008), pp. 37–43.
DOI: 10.1016/j.precisioneng.2008.03.008 (cit. on p. 23).

[122] S. Hashi, Y. Tokunaga, S. Yabukami, M. Toyoda, K. Ishiyama, Y. Okazaki, and K. I. Arai. 'Development of real-time and highly accurate wireless motion capture system utilizing soft magnetic core'.
IEEE Transactions on Magnetics 41.10 (2005), pp. 4191–4193.
DOI: 10.1109/TMAG.2005.854839 (cit. on p. 23).

[123] U. Hasirci, A. Balikci, Z. Zabar, and L. Birenbaum. 'A novel magnetic-levitation system: Design, implementation, and nonlinear control'.
IEEE Transactions on Plasma Science 39.1 (2011), p. 1.
DOI: 10.1109/TPS.2010.2053389 (cit. on p. 24).

[124] H. Higuchi, H. Sawada, and H. Kato.
'Sting-free measurements on a magnetically supported right circular cylinder aligned with the free stream sting-free measurements on a magnetically supported right circular cylinder aligned with the free stream'.
Journal of Fluid Mechanics 596 (2008), pp. 49–72.
DOI: 10.1017/S0022112007008956 (cit. on p. 24).

[125] E. W. Hobson. *''Squaring the circle": A history of the problem*.
Cambridge University Press, 1913 (cit. on p. 84).

[126] J. F. Hoburg. 'Modeling maglev passenger compartment static magnetic fields from linear Halbach permanent magnet arrays'.
IEEE Transactions on Magnetics 37.5 (09/2004), pp. 59–64.
DOI: 10.1109/TMAG.2003.821559 (cit. on p. 130).

[127] S. A. J. Hol, E. Lomonova, and A. J. A. Vandenput.
'Design of a magnetic gravity compensation system'.
Precision Engineering 30.3 (07/2006), pp. 265–273.
DOI: 10.1016/j.precisioneng.2005.09.005 (cit. on p. 39).

[128] M. H. Holdhusen and K. A. Cunefare.
'A state-switched absorber used for vibration control of continuous systems'.
Journal of Vibration and Acoustics 129.5 (2007), pp. 577–589.
DOI: 10.1115/1.2748465 (cit. on p. 20).

[129] J. Hong and K. Park.
'Design and control of six degree-of-freedom active vibration isolation table'.
Review of Scientific Instruments 81.3 (2010). DOI: 10.1063/1.3298605 (cit. on pp. 2, 233).

[130] M. E. Hoque, M. Takasaki, Y. I. Ishino, and T. Mizuno. 'Development of a three-axis active vibration isolator using zero-power control'.
IEEE/ASME Transactions on Mechatronics 11.4 (2006), pp. 462–470.
DOI: 10.1109/TMECH.2006.878536 (cit. on pp. 15, 39).

[131] J. R. Hull and A. Cansiz. 'Vertical and lateral forces between a permanent magnet and a high-temperature superconductor'.
Journal of Applied Physics 86.11 (12/1999), pp. 6396–6404.
DOI: 10.1063/1.371703 (cit. on pp. 75, 164).

[132] R. A. Ibrahim. 'Recent advances in nonlinear passive vibration isolators'.
Journal of Sound and Vibration 314.3–5 (07/2008), pp. 371–452.
DOI: 10.1016/j.jsv.2008.01.014 (cit. on pp. 36, 38).

[133] D. Ivers, R. Wilson, and D. Margolis.
'Whirling-beam self-tuning vibration absorber'.
Journal of Dynamic Systems, Measurement, and Control 130.3 (2008).
DOI: 10.1115/1.2907399 (cit. on p. 20).

[134] S. M. Jang, J. Y. Choi, H. W. Cho, and S. H. Lee.
'Dynamic characteristic analysis and experiments of moving-magnet linear actuator with cylindrical Halbach array'.
IEEE Transactions on Magnetics 41.10 (2005), pp. 3814–3816.
DOI: 10.1109/TMAG.2005.854931 (cit. on p. 131).

[135] S. M. Jang, J. C. Seo, J. Y. Choi, H. W. Cho, and J. K. Kown. 'Experiment and characteristic analysis of disk type PMLSM with Halbach array'.
IEEE Transactions on Magnetics 41.10 (2005), pp. 3817–3819.
DOI: 10.1109/TMAG.2005.854932 (cit. on p. 131).

[136] J. W. Jansen, C. M. M. van Lierop, E. A. Lomonova, and A. J. A. Vandenput.
'Magnetically levitated planar actuator with moving magnets'.
IEEE Transactions on Industry Applications 44.4 (2008), pp. 1108–1115.
DOI: 10.1109/TIA.2008.926065 (cit. on p. 25).

[137] J. L. G. Janssen, J. J. H. Paulides, E. Lomonova, F. Bölöni, A. Tounzi, and F. Piriou. 'Analytical calculation of interaction force between orthogonally magnetized permanent magnets'. *Sensor Letters* 7.3 (2009).
DOI: 10.1166/sl.2009.1049 (cit. on pp. 63, 78).

[138] J. L. G. Janssen, J. J. H. Paulides, and E. A. Lomonova.
'Study of magnetic gravity compensator topologies using an abstraction in the analytical interaction equations'.
Progress In Electromagnetics Research 128 (2012), pp. 75–90.
DOI: 10.2528/PIER11101408 (cit. on p. 148).

[139] J. L. G. Janssen, J. J. H. Paulides, and E. A. Lomonova.
'Passive limitations for a magnetic gravity compensator'.
Journal of System Design and Dynamics 3.4 (2009), pp. 671–680.
DOI: 10.1299/jsdd.3.671 (cit. on pp. 39, 132, 143, 147, 148).

[140] J. Janssen, J. Paulides, and E. Lomonova. 'Three-dimensional analytical field calculation of pyramidal-frustum shaped permanent magnets'.
IEEE Transactions on Magnetics 45.10 (10/2009), pp. 4628–4631.
DOI: 10.1109/TMAG.2009.2021861 (cit. on pp. 59, 130, 132, 144).

[141] J. Janssen, J. Paulides, and E. Lomonova.
'3D analytical field calculation using triangular magnet segments applied to a skewed linear permanent magnet actuator'.
COMPEL: The International Journal for Computation and Mathematics in Electrical and Electronic Engineering 29.4 (2010).
DOI: 10.1108/03321641011044406 (cit. on pp. 58, 59).

[142] J. Janssen, J. Paulides, J. Compter, and E. Lomonova.
'Three-dimensional analytical calculation of the torque between permanent magnets in magnetic bearings'. *IEEE Transactions on Magnetics* 46.6 (06/2010).
DOI: 10.1109/TMAG.2010.2043224 (cit. on pp. 74, 78, 102, 116, 118).

[143] J. Janssen, J. Paulides, and E. Lomonova.
'3-D analytical calculation of the torque between perpendicular magnetized magnets in magnetic suspensions'.
IEEE Transactions on Magnetics 47.10 (10/2011), pp. 4286–4289.
DOI: 10.1109/TMAG.2011.2154315 (cit. on pp. 74, 78).

[144] G. N. Jazar, R. Houim, A. Narimani, and M. F. Golnaraghi. 'Frequency response and jump avoidance in a nonlinear passive engine mount'.
Journal of Vibration and Control 12 (2006), pp. 1205–1237.
DOI: 10.1177/1077546306068059 (cit. on pp. 36, 229).

[145] H. Jo and H. Yabuno.
'Amplitude reduction of primary resonance of nonlinear oscillator by a dynamic vibration absorber using nonlinear coupling'.
Nonlinear Dynamics 55.1–2 (2008), pp. 67–78.
DOI: 10.1007/s11071-008-9345-3 (cit. on p. 36).

[146] D. Karnopp, M. J. Crosby, and R. A. Harwood.
'Vibration control using semi-active force generators'.
Journal of Engineering for Industry 96.2 (1974), pp. 619–626.
DOI: 10.1115/1.3438373 (cit. on p. 13).

[147] K. Kawashima, T. Kato, K. Sawamoto, and T. Kagawa.
'Realization of virtual sub chamber on active controlled pneumatic isolation table with pressure differentiator'.
Precision Engineering 31.2 (04/2007), pp. 139–145.
DOI: 10.1016/j.precisioneng.2006.05.002 (cit. on p. 2).

[148] F. Kerber, S. Hurlebaus, B. M. Beadle, and U. Stobener.
'Control concepts for an active vibration isolation system'.
Mechanical Systems and Signal Processing 21.8 (11/2007), pp. 3042–3059.
DOI: 10.1016/j.ymssp.2007.04.003 (cit. on p. 15).

[149] M. R. F. Kidner and M. J. Brennan.
Improving the performance of a vibration neutraliser by actively removing damping.
ISVR Technical Memorandum 829. University of Southampton, 07/1998
(cit. on pp. 10, 17, 19).

[150] M. R. F. Kidner and M. J. Brennan.
'Varying the stiffness of a beam-like neutralizer under fuzzy logic control'.
Journal of Vibration and Acoustics 124.1 (2002), pp. 90–99.
DOI: 10.1115/1.1423634 (cit. on pp. 13, 20).

[151] K.-B. Kim, E. Levi, Z. Zabar, and L. Birenbaum.
'Restoring force between two noncoaxial circular coils'.
IEEE Transactions on Magnetics 32.2 (03/1996), pp. 478–484.
DOI: 10.1109/20.486535 (cit. on pp. 75, 164).

[152] S. M. Kim, S. J. Elliott, and M. J. Brennan. *Active vibration isolation of a 3-dimensional structure using velocity feedback control*.
ISVR Technical Memorandum 845. University of Southampton, 10/1999.
URL: http://www.isvr.soton.ac.uk/STAFF/Pubs/Pubpdfs/Pub645.pdf
(cit. on p. 14).

[153] S.-M. Kim, S. Pietrzko, and M. J. Brennan. 'Active vibration isolation using an electrical damper or an electrical dynamic absorber'.
IEEE Transactions on Control Systems Technology 16.2 (03/2008), pp. 245–254.
DOI: 10.1109/TCST.2007.903376 (cit. on pp. 10, 20).

[154] W.-j. Kim. 'High-precision planar magnetic levitation'.
PhD thesis. Massachusetts Institute of Technology, 06/1997
(cit. on pp. 25, 143, 144).

[155] W.-j. Kim and S. Verma. 'Multiaxis maglev positioner with nanometer resolution over extended travel range'.
Journal of Dynamic Systems, Measurement, and Control 129.6 (2007), pp. 777–785.
DOI: 10.1115/1.2789468 (cit. on p. 25).

[156] N. M. Kimoulakis, A. G. Kladas, and J. A. Tegopoulos.
'Power generation optimization from sea waves by using a permanent magnet linear generator drive'.
IEEE Transactions on Magnetics 44.6 (06/2008), pp. 1530–1533.
DOI: 10.1109/TMAG.2007.914854 (cit. on p. 131).

[157] *K & J Magnetics*. URL: http://www.kjmagnetics.com/
(cit. on pp. 54, 55, 216).

[158] M. Konno, S. Sugawara, and S. Kudo.
'Piezoelectric vibratory gyroscope as an angular velocity sensor'. *Electronics and Communications in Japan (Part II: Electronics)* 79.7 (1996), pp. 40–52.
DOI: 10.1002/ecjb.4420790705 (cit. on p. 221).

[159] J. Kovacevic. 'How to encourage and publish reproducible research'. *IEEE International Conference on Acoustics, Speech and Signal Processing (ICASSP)*.
Vol. 4. 2007. DOI: 10.1109/ICASSP.2007.367309 (cit. on pp. 44, 273).

[160] I. Kovacic, M. J. Brennan, and T. P. Waters. 'A study of a nonlinear vibration isolator with a quasi-zero stiffness characteristic'.
Journal of Sound and Vibration 315.3 (2008), pp. 700–711.
DOI: 10.1016/j.jsv.2007.12.019 (cit. on pp. 37, 38, 181).

[161] I. Kovacic, M. J. Brennan, and B. Lineton. 'Effect of a static force on the dynamic behaviour of a harmonically excited quasi-zero stiffness system'. *Journal of Sound and Vibration* 325.4-5 (2009), pp. 870–883. DOI: 10.1016/j.jsv.2009.03.036 (cit. on p. 38).

[162] M. Kremers, J. Paulides, E. Ilhan, J. Janssen, and E. Lomonova. 'Relative permeability in a 3d analytical surface charge model of permanent magnets'. *IEEE Transactions on Magnetics* 49.5 (2013), pp. 2299–2302. DOI: 10.1109/TMAG.2013.2239976 (cit. on pp. 50, 56).

[163] G. Kustler, I. Nemoianu, and E. Cazacu. 'Theoretical and experimental investigation of multiple horizontal diamagnetically stabilized levitation with permanent magnets'. *IEEE Transactions on Magnetics* 48.12 (2012), pp. 4793–4801. DOI: 10.1109/TMAG.2012.2204273 (cit. on p. 30).

[164] V. Labinac, N. Erceg, and D. Kotnik-Karuza. 'Magnetic field of a cylindrical coil'. *American Journal of Physics* 74.7 (2006). DOI: 10.1119/1.2198885 (cit. on p. 59).

[165] E. R. Laithwaite. 'Electromagnetic levitation'. *Proceedings of the Institution of Electrical Engineers* 112.12 (12/1965), pp. 2361–2375 (cit. on pp. 29, 33).

[166] Z. Q. Lang, S. A. Billings, R. Yue, and J. Li. 'Output frequency response function of nonlinear Volterra systems'. *Automatica* 43.5 (05/2007), pp. 805–816. DOI: 10.1016/j.automatica.2006.11.013 (cit. on p. 40).

[167] Z. Q. Lang, X. J. Jing, S. A. Billings, G. R. Tomlinson, and Z. K. Peng. 'Theoretical study of the effects of nonlinear viscous damping on vibration isolation of sdof systems'. *Journal of Sound and Vibration* 323.1-2 (2009), pp. 352–365. DOI: 10.1016/j.jsv.2009.01.001 (cit. on p. 12).

[168] J. Leavitt, F. Jabbari, and J. E. Bobrow. 'Optimal performance of variable stiffness devices for structural control'. *Journal of Dynamic Systems, Measurement, and Control* 129.2 (2007), pp. 171–177. DOI: 10.1115/1.2432360 (cit. on p. 13).

[169] C.-M. Lee, V. N. Goverdovskiy, and S. B. Samoilenko. 'Prediction of non-chaotic motion of the elastic system with small stiffness'. *Journal of Sound and Vibration* 272.3–5 (05/2004), pp. 643–655. DOI: 10.1016/S0022-460X(03)00390-0 (cit. on p. 38).

[170] C.-M. Lee, V. N. Goverdovskiy, and A. I. Temnikov. 'Design of springs with "negative" stiffness to improve vehicle driver vibration isolation'. *Journal of Sound and Vibration* 302.4–5 (05/2007), pp. 865–874. DOI: 10.1016/j.jsv.2006.12.024 (cit. on pp. 12, 38).

[171] H.-W. Lee, K.-C. Kim, and J. Lee. 'Review of maglev train technologies'. *IEEE Transactions on Magnetics* 42.7 (2006), pp. 1917–1925. DOI: 10.1109/TMAG.2006.875842 (cit. on p. 24).

[172] M. G. Lee, S. Q. Lee, and D.-G. Gweon.
'Analysis of Halbach magnet array and its application to linear motor'.
Mechatronics 14 (2004), pp. 115–128. DOI: 10.1016/S0957-4158(03)00015-1 (cit. on p. 131).

[173] M. G. Lee, Y.-M. Choi, S. Q. Lee, D.-c. Lim, and D.-G. Gweon.
'Design of high precision linear stage with double-sided multi-segmented trapezoidal magnet array and its compensations for force ripples'.
Mechatronics 16.6 (07/2006), pp. 331–340.
DOI: 10.1016/j.mechatronics.2006.01.006 (cit. on pp. 131, 144).

[174] Q.-M. Li, L. Wan, J.-A. Duan, and H. Ouyang.
'Coupled electromechanical dynamic model of magnetically suspended table system and its stability analysis'. Chinese. *Guangxue Jingmi Gongcheng/Optics and Precision Engineering* 15.4 (2007), pp. 535–542 (cit. on p. 32).

[175] H. K. Lim, N. Chung, Y.-G. Ko, Y.-H. Lee, and Y. K. Park.
'Magnetocardiogram difference between healthy subjects and ischemic heart disease patients'.
IEEE Transactions on Magnetics 45.6 (06/2009), pp. 2890–2893.
DOI: 10.1109/TMAG.2009.2018878 (cit. on p. 23).

[176] C. Liu, K. T. Chau, J. Z. Jiang, and L. Jian. 'Design of a new outer-rotor permanent magnet hybrid machine for wind power generation'.
IEEE Transactions on Magnetics 44.6 (06/2008), pp. 1494–1497.
DOI: 10.1109/TMAG.2007.916503 (cit. on p. 129).

[177] J. Liu and K. Liu. 'A tunable electromagnetic vibration absorber: Characterization and application'.
Journal of Sound and Vibration 295.3–5 (08/2006), pp. 708–724.
DOI: 10.1016/j.jsv.2006.01.033 (cit. on p. 13).

[178] Y. Liu, T. P. Waters, and M. J. Brennan. 'A comparison of semi-active damping control strategies for vibration isolation of harmonic disturbances'.
Journal of Sound and Vibration 280.1-2 (02/2005), pp. 21–39.
DOI: 10.1016/j.jsv.2003.11.048 (cit. on p. 13).

[179] Y. Liu, H. Matsuhisa, and H. Utsuno. 'Semi-active vibration isolation system with variable stiffness and damping control'.
Journal of Sound and Vibration 313.1-2 (2008), pp. 16–28.
DOI: 10.1016/j.jsv.2007.11.045 (cit. on p. 13).

[180] Y. Liu, D.-M. Zhu, D. M. Strayer, and U. E. Israelsson.
'Magnetic levitation of large water droplets and mice'.
Advances in Space Research 45.1 (2009), pp. 208–213.
DOI: 10.1016/j.asr.2009.08.033, (cit. on p. 30).

[181] M. Lu, S. Ueno, T. Thorlin, and M. Persson. 'Calculating the activating function in the human brain by transcranial magnetic stimulation'.
IEEE Transactions on Magnetics 44.6 (06/2008), pp. 1438–1441.
DOI: 10.1109/TMAG.2007.916022 (cit. on p. 23).

[182] Y. Luo and B. Chen. 'Improvement of self-inductance calculations for circular coils of rectangular cross section'.
IEEE Transactions on Magnetics 49.3 (2013), pp. 1249–1255.
DOI: 10.1109/TMAG.2012.2228499 (cit. on p. 177).

[183] K. B. Ma, Y. V. Postrekhin, and W. K. Chu.
'Superconductor and magnet levitation devices'.
Review of Scientific Instruments 74.12 (12/2003), pp. 4989–5017.
DOI: 10.1063/1.1622973 (cit. on p. 31).

[184] N. I. Mahmoud.
'A backstepping design of a control system for a magnetic levitation system'.
PhD thesis. Linköping University, 2003.
URL: http://www.ep.liu.se/exjobb/isy/2003/3383/ (cit. on p. 31).

[185] B. P. Mann and N. D. Sims.
'Energy harvesting from the nonlinear oscillations of magnetic levitation'.
Journal of Sound and Vibration 319.1–2 (2008).
DOI: 10.1016/j.jsv.2008.06.011 (cit. on p. 36).

[186] A. E. Marble. 'Strong, stray static magnetic fields'.
IEEE Transactions on Magnetics 44.5 (05/2008), pp. 576–580.
DOI: 10.1109/TMAG.2008.918278 (cit. on p. 131).

[187] M Marinescu and N Marinescu. 'New concept of permanent magnet excitation for electrical machines. analytical and numerical computation'.
IEEE Transactions on Magnetics 28.2 (03/1992), pp. 1390–1393.
DOI: 10.1109/20.123952 (cit. on p. 131).

[188] E. Matta and A. De Stefano. 'Robust design of mass-uncertain rolling-pendulum TMDs for the seismic protection of buildings'.
Mechanical Systems and Signal Processing 23.1 (2008), pp. 127–147.
DOI: 10.1016/j.ymssp.2007.08.012 (cit. on p. 20).

[189] E. Matta and A. De Stefano.
'Seismic performance of pendulum and translational roof-garden TMDs'.
Mechanical Systems and Signal Processing 23.3 (2009), pp. 908–921.
DOI: 10.1016/j.ymssp.2008.07.007 (cit. on p. 20).

[190] K. Meessen, B. Gysen, J. Paulides, and E. Lomonova.
'Halbach permanent magnet shape selection for slotless tubular actuators'.
IEEE Transactions on Magnetics 44.11 (11/2008), pp. 4305–4308.
DOI: 10.1109/TMAG.2008.2001536 (cit. on pp. 130, 131).

[191] B. Merit, G. Lemarquand, and V. Lemarquand.
'In pursuit of increasingly linear loudspeaker motors'.
IEEE Transactions on Magnetics 45.6 (06/2009), pp. 2867–2870.
DOI: 10.1109/TMAG.2009.2018780 (cit. on p. 154).

[192] W. Min, M. Zhang, Y. Zhu, B. Chen, G. Duan, J. Hu, and W. Yin. 'Analysis and optimization of a new 2-D magnet array for planar motor'. *IEEE Transactions on Magnetics* 46.5 (05/2010), pp. 1167 –1171. DOI: 10.1109/TMAG.2010.2040922 (cit. on pp. 131, 144).

[193] T. Mizuno and M. Aizawa. 'Repulsive magnetic bearing stabilized by the motion control of magnets with a piezoelectric actuator'. *International Journal of Applied Electromagnetics and Mechanics* 13 (2001/2002), pp. 155–162. URL: http://iospress.metapress.com/content/jg880fxgkmgxet3q (cit. on p. 39).

[194] T. Mizuno and Y. Takemori. 'A transfer-function approach to the analysis and design of zero-power controllers for magnetic suspension systems'. *Electrical Engineering in Japan* 141.2 (2002), pp. 67–75. DOI: 10.1002/eej.10049 (cit. on p. 39).

[195] T. Mizuno, H. Suzuki, M. Takasaki, and Y. Ishino. 'Development of a three-axis active vibration isolation system using zero-power magnetic suspension'. *Proceedings of the 42nd IEEE Conference on Decision and Control*. Maui, Hawaii USA, 12/2003, pp. 4493–4498 (cit. on p. 39).

[196] T. Mizuno, H. Suzuki, and M. Takasaki. 'Development of an active vibration isolation system using zero-power magnetic suspension'. *Tenth International Congress on Sound and Vibration*. Stockholm, Sweden, 07/2003, pp. 887–894 (cit. on p. 39).

[197] T. Mizuno, T. Toumiya, and M. Takasaki. 'Vibration isolation system using negative stiffness'. *JSME International Journal, Series C: Mechanical Systems, Machine Elements and Manufacturing* 46.3 (2003), pp. 807–812. DOI: 10.1299/jsmec.46.807 (cit. on p. 39).

[198] T. Mizuno, M. Takasaki, D. Kishita, and K. Hirakawa. 'Vibration isolation system combining zero-power magnetic suspension with springs'. *Control Engineering Practice* 15.2 (02/2007), pp. 187–196. DOI: 10.1016/j.conengprac.2006.06.001 (cit. on p. 39).

[199] T. Mizuno, T. Furushima, Y. Ishino, and M. Takasaki. 'Realization of a zero-compliance system by using displacement cancellation control'. *Journal of Vibration and Control* 16.4 (2010), pp. 585–599. DOI: 10.1177/1077546309106151 (cit. on p. 39).

[200] L. Molenaar. 'A novel planar magnetic bearing and motor configuration applied in a positioning stage'. PhD thesis. Department of Mechanical Engineering and Marine Technology, Delft University of Technology, the Netherlands, 2000 (cit. on p. 25).

[201] W. G. Molyneux. *Supports for vibration isolation*. ARC/CP-322. Aeronautical Research Council, Great Britain, 1957. URL: http://nsdl.org/resource/2200/20061003060308472T (cit. on pp. 37, 180).

[202] R. Moser, J. Sandtner, and H. Bleuler. 'Optimization of repulsive passive magnetic bearings'. *IEEE Transactions on Magnetics* 42.8 (2006), pp. 2038–2042. DOI: 10.1109/TMAG.2005.861160 (cit. on p. 129).

[203] R. Moser, F. Barrot, J. Sandtner, and H. Bleuler. 'Optimization of two-dimensional permanent magnet arrays for diamagnetic levitation'. *17th International Conference on Magnetically Levitated Systems and Linear Drives (Maglev)*. 2002 (cit. on pp. 143, 148).

[204] L. R. Moskowitz. *Permanent magnet design and application handbook*. Second Edition. Kreiger Drive, Malabar, Florida 32950: Kreiger Publishing Company, 1995 (cit. on pp. 2, 53, 61).

[205] S. C. Mukhopadhyay, C. P. Gooneratne, G. S. Gupta, and S. Yamada. 'Characterization and comparative evaluation of novel planar electromagnetic sensors'. *IEEE Transactions on Magnetics* 41.10 (10/2005), pp. 3658–3660. DOI: 10.1109/TMAG.2005.854792 (cit. on p. 23).

[206] A. Musolino, R. Rizzo, M. Tucci, and V. M. Matrosov. 'A new passive maglev system based on eddy current stabilization'. *IEEE Transactions on Magnetics* 45.3 (03/2009), pp. 984–987. DOI: 10.1109/TMAG.2009.2012533 (cit. on p. 24).

[207] H. S. Nagaraj. 'Investigation of magnetic fields and forces arising in open-circuit-type magnetic bearings'. *Tribology Transactions* 31.2 (1988), pp. 192–201. DOI: 10.1080/10402008808981815 (cit. on pp. 60, 75, 84).

[208] K. Nagaya and M. Ishikawa. 'A noncontact permanent magnet levitation table with electromagnetic control and its vibration isolation method using direct disturbance cancellation combining optimal regulators'. *IEEE Transactions on Magnetics* 31.1 (01/1995), pp. 885–895. DOI: 10.1109/20.364582 (cit. on p. 35).

[209] K. Nagaya, M. Atsumi, and M. Endoh. 'Simplified vibration isolation control using disturbance cancellation and velocity feedback controls for a magnetic levitation table'. *International Journal of Applied Electromagnetics in Materials* 4 4.4 (09/1993), pp. 115–122 (cit. on p. 35).

[210] A. Nandi, S. Neogy, and H. Irretier.
'Vibration control of a structure and a rotor using one-sided magnetic actuator and a digital proportional-derivative control'.
Journal of Vibration and Control 15.2 (2009), pp. 163–181.
DOI: 10.1177/1077546307085212 (cit. on p. 218).

[211] G.-J. P. Nijsse. 'Linear motion systems: A modular approach for improved straightness performance'. PhD thesis. Delft University of Technology, 2001.
URL: http://repository.tudelft.nl/file/80827/161960
(cit. on pp. 39, 87, 89, 192, 194, 208, 220).

[212] A. J. J. A. Oome, J. L. G. Janssen, L. Encica, E. Lomonova, and J. A. A. T. Dams.
'Modeling of an electromagnetic geophone with passive magnetic spring'.
Sensors and Actuators A: Physical 153.2 (2009), pp. 142–154.
DOI: 10.1016/j.sna.2009.04.019 (cit. on p. 221).

[213] S. S. Oueini, C.-M. Chin, and A. H. Nayfeh.
'Dynamics of a cubic nonlinear vibration absorber'.
Nonlinear Dynamics 20.3 (11/1999), pp. 283–295.
DOI: 10.1023/A:1008358825502 (cit. on p. 35).

[214] C. Paulitsch, P. Gardonio, and S. J. Elliott.
Investigation of an electrodynamic actuator for self-sensing active vibration control.
ISVR Technical Memorandum 917. University of Southampton, 08/2003.
URL: http://eprints.soton.ac.uk/10982/ (cit. on p. 17).

[215] A. Pechenkov. 'Calculation of the three-dimensional magnetic field produced by a circular dc-carrying coil of rectangular cross section'.
Russian Journal of Nondestructive Testing 42.9 (2006), pp. 610–615.
DOI: 10.1134/S1061830906090051 (cit. on p. 59).

[216] Z. K. Peng and Z. Q. Lang. 'The effects of nonlinearity on the output frequency response of a passive engine mount'.
Journal of Sound and Vibration 318.1 (2008), pp. 313–328.
DOI: 10.1016/j.jsv.2008.04.016 (cit. on p. 40).

[217] Z. K. Peng, Z. Q. Lang, S. A. Billings, and G. R. Tomlinson.
'Comparisons between harmonic balance and nonlinear output frequency response function in nonlinear system analysis'.
Journal of Sound and Vibration 311.1-2 (2008), pp. 56–73.
DOI: 10.1016/j.jsv.2007.08.035 (cit. on p. 40).

[218] F. Petit, M. Loccufier, and D. Aeyels.
'On the attachment location of dynamic vibration absorbers'.
Journal of Vibration and Acoustics 131.3 (2009), p. 034501.
DOI: 10.1115/1.3085888 (cit. on p. 21).

[219] B. A. D. Piombo, A. Vigliani, and E. Bonisolo.
'Dynamics of suspensions with rare-earth permanent magnets'.
Proceedings of the SPIE 5052 (2003), pp. 106–115. DOI: 10.1117/12.483817
(cit. on p. 195).

[220] D. L. Platus. 'Negative-stiffness-mechanism vibration isolation systems'.
Proceedings of SPIE — The International Society for Optical Engineering 3786
(1999), pp. 98 –105. DOI: 10.1117/12.363841 (cit. on p. 38).

[221] A. Preumont, A. Francois, F. Bossens, and A. Abu-Hanieh.
'Force feedback versus acceleration feedback in active vibration isolation'.
Journal of Sound and Vibration 257.4 (2002), pp. 605–613.
DOI: 10.1006/jsvi.2002.5047 (cit. on p. 7).

[222] *Proceedings of the 14th international congress on sound and vibration*.
Cairns, Australia, 07/2007.

[223] E. Puppin and V. Fratello. 'Vibration isolation with magnet springs'.
Review of Scientific Instruments 73.11 (11/2002), pp. 4034–4036.
DOI: 10.1063/1.1512325 (cit. on pp. 35, 79).

[224] M. S. de Queiroz and S. Pradhananga. 'Control of magnetic levitation
systems with reduced steady-state power losses'.
IEEE Transactions on Control Systems Technology 15.6 (11/2007), pp. 1096–1102.
DOI: 10.1109/TCST.2006.890298 (cit. on p. 31).

[225] R. Ramlan, M. Brennan, B. Mace, and I. Kovacic.
'Potential benefits of a non-linear stiffness in an energy harvesting device'.
Nonlinear Dynamics 59.4 (03/2009), pp. 545–558.
DOI: 10.1007/s11071-009-9561-5 (cit. on pp. 43, 185).

[226] R. Ravaud and G. Lemarquand. 'Comparison of the Coulombian and
Amperian current models for calculating the magnetic field produced by
radially magnetized arc-shaped permanent magnets'.
Progress In Electromagnetics Research 95 (2009), pp. 309–327.
DOI: 10.2528/PIER09042105 (cit. on p. 58).

[227] R. Ravaud and G. Lemarquand. 'Magnetic field produced by a
parallelepipedic magnet of various and uniform polarization'.
Progress In Electromagnetics Research 98 (2009), pp. 207–219.
DOI: 10.2528/PIER09091704 (cit. on pp. 59, 65).

[228] R. Ravaud, G. Lemarquand, V. Lemarquand, and C. Depollier.
'Permanent magnet couplings: Field and torque three-dimensional
expressions based on the Coulombian model'.
IEEE Transactions on Magnetics 45.4 (04/2009), pp. 1950–1958.
DOI: 10.1109/TMAG.2008.2010623 (cit. on p. 27).

[229] R. Ravaud, V. Lemarquand, and G. Lemarquand.
'Analytical design of permanent magnet radial couplings'.
IEEE Transactions on Magnetics 46.11 (11/2010), pp. 3860–3865.
DOI: 10.1109/TMAG.2010.2056379 (cit. on p. 27).

[230] R. Ravaud, G. Lemarquand, V. Lemarquand, S. Babic, and C. Akyel. 'Calculation of the magnetic field created by a thick coil'. *Journal of Electromagnetic Waves and Applications* 24.14 (07/2010), pp. 1405–1418. DOI: 10.1163/156939310791958653 (cit. on pp. 59, 158).

[231] R. Ravaud, G. Lemarquand, S. Babic, V. Lemarquand, and C. Akyel. 'Cylindrical magnets and coils: Fields, forces, and inductances'. *IEEE Transactions on Magnetics* 46.9 (09/2010), pp. 3585–3590. DOI: 10.1109/TMAG.2010.2049026 (cit. on pp. 59, 76, 77, 153).

[232] R. Ravaud, G. Lemarquand, V. Lemarquand, S. I. Babic, and C. Akyel. 'Mutual inductance and force exerted between thick coils'. *Progress In Electromagnetics Research* 102 (2010), pp. 367–380. DOI: 10.2528/PIER10012806 (cit. on p. 75).

[233] J. Rens, K. Atallah, S. Calverley, and D. Howe. 'A novel magnetic harmonic gear'. *IEEE Transactions on Industry Applications* 46.1 (01/2010), pp. 206–212. DOI: 10.1109/TIA.2009.2036507 (cit. on p. 27).

[234] M. F. Reusch. 'A problem related to Earnshaw's theorem'. *IEEE Transactions on Magnetics* 30.3 (05/1994), pp. 1324–1326. DOI: 10.1109/20.297771 (cit. on pp. 28, 30).

[235] S.-K. Ro, S. Kim, Y. Kwak, and C. H. Park. 'A linear air bearing stage with active magnetic preloads for ultraprecise straight motion'. *Precision Engineering* (2009). DOI: 10.1016/j.precisioneng.2009.06.010 (cit. on p. 25).

[236] W. Robertson, B. Cazzolato, and A. Zander. 'A multipole array magnetic spring'. *IEEE Transactions on Magnetics* 41.10 (2005), pp. 3826–3828. DOI: 10.1109/TMAG.2005.854981 (cit. on pp. 45, 129).

[237] W. Robertson, R. Wood, B. Cazzolato, and A. Zander. 'Zero-stiffness magnetic springs for active vibration isolation'. *Proceedings of the Sixth International Symposium on Active Noise and Vibration Control*. 2006. URL: http://hdl.handle.net/2440/35429 (cit. on pp. 38, 45, 192, 194).

[238] W. Robertson, B. Cazzolato, and A. Zander. 'Nonlinear control of a one axis magnetic spring'. *Proceedings of the 14th International Congress on Sound and Vibration*. Cairns, Australia, 07/2007. URL: http://hdl.handle.net/2440/44996 (cit. on pp. 38, 45, 192).

[239] W. Robertson, B. Cazzolato, and A. Zander. 'Maximising the force between two cuboid magnets'. *IEEE Magnetics Letters* 1 (2010). DOI: 10.1109/LMAG.2010.2081351 (cit. on p. 45).

[240] W. Robertson, B. Cazzolato, and A. Zander. 'Parameters for optimizing the forces between linear multipole magnet arrays'. *Magnetics Letters, IEEE* 1 (12/2010). DOI: 10.1109/LMAG.2010.2047716 (cit. on pp. 45, 129).

[241] W. Robertson, B. Cazzolato, and A. Zander. 'A simplified force equation for coaxial cylindrical magnets and thin coils'. *IEEE Transactions on Magnetics* 47.8 (2011), pp. 2045–2049. DOI: 10.1109/TMAG.2011.2129524 (cit. on pp. 45, 47, 75, 76, 78, 153).

[242] W. Robertson, B. Cazzolato, and A. Zander. 'Axial force between a thick coil and a cylindrical permanent magnet: Optimising the geometry of an electromagnetic actuator'. *IEEE Transactions on Magnets* 48.9 (2012). DOI: 10.1109/TMAG.2012.2194789 (cit. on pp. 45, 153).

[243] W. Robertson, B. Cazzolato, and A. Zander. 'Theoretical analysis of a non-contact spring with inclined permanent magnets for load-independent resonance frequency'. *Journal of Sound and Vibration* 331.6 (2012), pp. 1331–1341. DOI: 10.1016/j.jsv.2011.11.011 (cit. on pp. 45, 79).

[244] W. S. Robertson, M. R. F. Kidner, B. S. Cazzolato, and A. C. Zander. 'Theoretical design parameters for a quasi-zero stiffness magnetic spring for vibration isolation'. *Journal of Sound and Vibration* 326.1–2 (2009), pp. 88–103. DOI: 10.1016/j.jsv.2009.04.015 (cit. on pp. 45, 179).

[245] W. S. P. Robertson, B. Cazzolato, and A. Zander. 'Experimental results of a 1D passive magnetic spring approaching quasi-zero stiffness and using active skyhook damping'. *Proceedings of Acoustics 2013*. Victor Harbor, Australia, 11/2013 (cit. on pp. 45, 179).

[246] W. S. P. Robertson, B. Cazzolato, and A. Zander. 'Planar analysis of a quasi-zero stiffness mechanism using inclined linear springs'. *Proceedings of Acoustics 2013*. Victor Harbor, Australia, 11/2013 (cit. on pp. 45, 213).

[247] J. Rovers, J. Jansen, E. Lomonova, and M. Ronde. 'Calculation of the static forces among the permanent magnets in a Halbach array'. *IEEE Transactions on Magnetics* 45.10 (2009), pp. 4372–4375. DOI: 10.1109/TMAG.2009.2021860 (cit. on pp. 132, 143, 148).

[248] J. Rovers, J. Jansen, and E. Lomonova. 'Analytical calculation of the force between a rectangular coil and a cuboidal permanent magnet'. *IEEE Transactions on Magnetics* 46.6 (06/2010), pp. 1656–1659. DOI: 10.1109/TMAG.2010.2040589 (cit. on p. 58).

[249] C. Rubeck, J. Yonnet, H. Allag, B. Delinchant, and O. Chadebec. 'Analytical calculation of magnet systems: Magnetic field created by charged triangles and polyhedra'. *IEEE Transactions on Magnetics* 49.1 (2013), pp. 144–147. DOI: 10.1109/TMAG.2012.2219511 (cit. on p. 59).

[250] C. Samiappan, N. Mirnateghi, B. E. Paden, and J. F. Antaki. 'Maglev apparatus for power minimization and control of artificial hearts'. *IEEE Transactions on Control Systems Technology* 16.1 (01/2008), pp. 13–18. DOI: 10.1109/TCST.2007.903063 (cit. on p. 129).

[251] H. W. Sams. *Handbook of electronics tables and formulas*. Sams, 1986 (cit. on pp. 170, 172).

[252] T. Sato and D. L. Trumper. 'A novel single degree-of-freedom active vibration isolation system'. *Sixteenth Annual Meeting of the ASPE*. Crystal City, VA, 11/2001 (cit. on p. 38).

[253] S. M. Savaresi and C. Spelta. 'Mixed sky-hook and ADD: Approaching the filtering limits of a semi-active suspension'. *Journal of Dynamic Systems, Measurement, and Control* 129.4 (2007), pp. 382–392. DOI: 10.1115/1.2745846 (cit. on pp. 15, 40).

[254] J. Schoukens, R. Pintelon, Y. Rolain, and T. Dobrowiecki. 'Frequency response function measurements in the presence of nonlinear distortions'. *Automatica* 37.6 (06/2001), pp. 939–946. DOI: 10.1016/S0005-1098(01)00037-1 (cit. on p. 40).

[255] M. Sekino, Y. Inoue, and S. Ueno. 'Magnetic resonance imaging of electrical conductivity in the human brain'. *IEEE Transactions on Magnetics* 41.10 (2005), pp. 4203–4205. DOI: 10.1109/TMAG.2005.854804 (cit. on p. 23).

[256] D. J. Sellmyer. 'Strong magnets by self-assembly'. *Nature* 420 (2002), p. 374. DOI: 10.1038/420374a (cit. on p. 55).

[257] M. Serrand and S. J. Elliott. 'Multichannel feedback control for the isolation of base-excited vibration'. *Journal of Sound and Vibration* 234.4 (07/2000), pp. 681–704. DOI: 10.1006/jsvi.2000.2891 (cit. on p. 14).

[258] S. M. Shahruz. 'Increasing the efficiency of energy scavengers by magnets'. *Journal of Computational and Nonlinear Dynamics* 3.4 (2008). DOI: 10.1115/1.2960486 (cit. on p. 36).

[259] H. Shimizu and O. Taniguchi. 'A magnetic journal bearing'. *Bulletin of JSME* 11.47 (1968), pp. 805–812. URL: http://ci.nii.ac.jp/naid/110002361268/en/ (cit. on p. 25).

[260] A. Shiri and A. Shoulaie. 'A new methodology for magnetic force calculations between planar spiral coils'.
Progress In Electromagnetics Research 95 (2009), pp. 39–57.
DOI: 10.2528/PIER09031608 (cit. on pp. 156, 162).

[261] H. A. Shute, J. C. Mallinson, D. T. Wilton, and D. J. Mapps.
'One-sided fluxes in planar, cylindrical, and spherical magnetized structures'.
IEEE Transactions on Magnetics 36.2 (03/2000), pp. 440–451.
DOI: 10.1109/20.825805 (cit. on p. 130).

[262] M. D. Simon and A. K. Geim.
'Diamagnetic levitation: Flying frogs and floating magnets'.
Journal of Applied Physics 87.9 (05/2000), pp. 6200–6204.
DOI: 10.1063/1.372654 (cit. on p. 30).

[263] M. D. Simon, L. O. Heflinger, and A. K. Geim.
'Diamagnetically stabilized magnetic levitation'.
American Journal of Physics 69.6 (06/2001), pp. 702–713.
DOI: 10.1119/1.1375157 (cit. on pp. 30, 31).

[264] M. D. Simon, L. O. Heflinger, and S. L. Ridgway.
'Spin stabilized magnetic levitation'.
American Journal of Physics 65.4 (04/1997), pp. 286–292.
DOI: 10.1119/1.18488 (cit. on p. 30).

[265] H. A. Sodano. 'Development of novel eddy current dampers for the suppression of structural vibrations'.
PhD thesis. Virginia Polytechnic Institute and State University, 05/2005. URL: http://scholar.lib.vt.edu/theses/available/etd-05122005-114434/ (cit. on p. 32).

[266] H. A. Sodano and D. J. Inman. 'Non-contact vibration control system employing an active eddy current damper'.
Journal of Sound and Vibration 305.4-5 (09/2007), pp. 596–613.
DOI: 10.1016/j.jsv.2007.04.050 (cit. on p. 32).

[267] H. A. Sodano and D. J. Inman.
'Modeling of a new active eddy current vibration control system'.
Journal of Dynamic Systems, Measurement, and Control 130.2 (2008).
DOI: 10.1115/1.2837436 (cit. on pp. 32, 36).

[268] H. A. Sodano, J.-S. Bae, D. J. Inman, and W. Keith Belvin. 'Concept and model of eddy current damper for vibration suppression of a beam'.
Journal of Sound and Vibration 288.4–5 (2005), pp. 1177–1196.
DOI: 10.1016/j.jsv.2005.01.016 (cit. on p. 32).

[269] H. A. Sodano, J.-S. Bae, D. J. Inman, and W. K. Belvin.
'Improved concept and model of eddy current damper'.
Journal of Vibration and Acoustics 128.3 (2006), pp. 294–302.
DOI: 10.1115/1.2172256 (cit. on p. 32).

[270] I. J. Sokolov, V. I. Babitsky, and N. A. Halliwell.
'Hand-held percussion machines with low emission of hazardous vibration'.
Journal of Sound and Vibration 306.1–2 (09/2007), pp. 59–73.
DOI: 10.1016/j.jsv.2007.05.044 (cit. on p. 38).

[271] X. Song, M. Ahmadian, and S. Southward. 'Analysis and strategy for superharmonics with semiactive suspension control systems'.
Journal of Dynamic Systems, Measurement, and Control 129.6 (2007), pp. 795–803.
DOI: 10.1115/1.2789470 (cit. on p. 13).

[272] Y. Starosvetsky and O. V. Gendelman.
'Dynamics of a strongly nonlinear vibration absorber coupled to a harmonically excited two-degree-of-freedom system'.
Journal of Sound and Vibration 312.1-2 (2008), pp. 234–256.
DOI: 10.1016/j.jsv.2007.10.035 (cit. on p. 36).

[273] N. G. Stephen. 'On energy harvesting from ambient vibration'.
Journal of Sound and Vibration 293.1-2 (2006), pp. 409–425.
DOI: 10.1016/j.jsv.2005.10.003 (cit. on pp. 12, 21).

[274] T. Tarnai. 'Zero stiffness elastic structures'.
International Journal of Mechanical Sciences 45.3 (03/2003), pp. 425–431.
DOI: 10.1016/S0020-7403(03)00063-8 (cit. on p. 38).

[275] L. B. Tentor.
'Characterization of an electromagnetic tuned vibration absorber'.
PhD thesis. Blacksburg, Virginia: Virginia Polytechnic Institute and State University, 08/2001. URL:
http://scholar.lib.vt.edu/theses/available/etd-05272002-194631/
(cit. on pp. 21, 41).

[276] C. Ting-Kong. 'Design of an adaptive dynamic vibration absorber'.
MA thesis. School of Mechanical Engineering, University of Adelaide, 1999.
URL: http://hdl.handle.net/2440/37922 (cit. on p. 20).

[277] T. Todaka, M. Enokizono, E. Fujita, and T. Ogura.
'Moving simulation of vibration systems using permanent magnets'.
IEEE Transactions on Magnetics 37.5 (09/2001), pp. 3456–3459.
DOI: 10.1109/20.952636 (cit. on pp. 37, 107).

[278] M. Tomie, A. Takiguchi, T. Honda, and J. Yamasaki. 'Turning performance of fish-type microrobot driven by external magnetic field'.
IEEE Transactions on Magnetics 41.10 (2005), pp. 4015–4017.
DOI: 10.1109/TMAG.2005.855154 (cit. on p. 23).

[279] L. Tonks. 'Note on Earnshaw's theorem'.
Electrical Engineering 59.3 (03/1940), pp. 118–119 (cit. on pp. 28, 87).

[280] M. S. Trimboli, R. Wimmel, and E. J. Breitbach.
'Quasi-active approach to vibration isolation using magnetic springs'.
Proc. SPIE 2193, Smart Structures and Materials 1994: Passive Damping.
Ed. by C. D. Johnson. Vol. 2193. 1. 1994, pp. 73–83. DOI: 10.1117/12.174116
(cit. on p. 108).

[281] D. L. Trumper and M. A. Queen. 'Control and actuator design for a precision magnetic suspension linear bearing'. *Controls for Optical Systems*. Vol. 1696. Proceedings of SPIE — The International Society for Optical Engineering. Orlando, FL, USA, 04/1992, pp. 2–15 (cit. on p. 25).

[282] D. Trumper, M. Williams, and T. Nguyen.
'Magnet arrays for synchronous machines'.
Conference Record of the IEEE Industry Applications Society Annual Meeting.
10/1993, pp. 9–18. DOI: 10.1109/IAS.1993.298897 (cit. on p. 131).

[283] L. Urankar.
'Vector potential and magnetic field of current-carrying finite arc segment in analytical form, Part III: Exact computation for rectangular cross section'.
IEEE Transactions on Magnetics 18.6 (11/1982), pp. 1860–1867.
DOI: 10.1109/TMAG.1982.1062166 (cit. on p. 59).

[284] S. Verma, W.-j. Kim, and J. Gu. 'Six-axis nanopositioning device with precision magnetic levitation technology'.
IEEE/ASME Transactions on Mechatronics 9.2 (06/2004), pp. 384–391.
DOI: 10.1109/TMECH.2004.828648 (cit. on p. 25).

[285] L. N. Virgin, S. T. Santillan, and R. H. Plaut.
'Vibration isolation using extreme geometric nonlinearity'.
Journal of Sound and Vibration (2008). DOI: 10.1016/j.jsv.2007.12.025
(cit. on p. 38).

[286] D Vischer and H Bleuler. 'Self-sensing active magnetic levitation'.
IEEE Transactions on Magnetics 29.3 (03/1993), pp. 1276–1281.
DOI: 10.1109/20.250632 (cit. on pp. 17, 30).

[287] D. Vokoun, M. Beleggia, L. Heller, and P. Sittner. 'Magnetostatic interactions and forces between cylindrical permanent magnets'.
Journal of Magnetism and Magnetic Materials 321.22 (2009), pp. 3758–3763.
DOI: 10.1016/j.jmmm.2009.07.030 (cit. on p. 75).

[288] K. Watanabe, S. Hara, Y. Kanemitsu, T. Haga, K. Yano, T. Mizuno, and R. Katamura. 'Combination of H^∞ and PI control for an electromagnetically levitated vibration isolation system'.
Proceedings of the 35th IEEE Conference on Decision and Control. Vol. 2. 1996, pp. 1223–1228. DOI: 10.1109/CDC.1996.572661 (cit. on p. 35).

[289] E. van West, A. Yamamoto, and T. Higuchi.
'The concept of "haptic tweezer", a non-contact object handling system using levitation techniques and haptics'. *Mechatronics* 17.7 (09/2007), pp. 345–356.
DOI: 10.1016/j.mechatronics.2007.04.008 (cit. on p. 23).

[290] D. E. Williams. 'Complementary filter to estimate inertial velocity'. *Journal of Dynamic Systems, Measurement, and Control* 131.5 (2009). DOI: 10.1115/1.3155012 (cit. on pp. 14, 221, 222).

[291] S.-T. Wu and Y.-J. Shao. 'Adaptive vibration control using a virtual-vibration-absorber controller'. *Journal of Sound and Vibration* 305.4–5 (09/2007), pp. 891–903. DOI: 10.1016/j.jsv.2007.04.046 (cit. on p. 20).

[292] C. Xia, H. Li, and T. Shi. '3-D magnetic field and torque analysis of a novel Halbach array permanent-magnet spherical motor'. *IEEE Transactions on Magnetics* 44.8 (08/2008), pp. 2016–2020. DOI: 10.1109/TMAG.2008.922782 (cit. on p. 131).

[293] J. T. Xing, Y. P. Xiong, and W. G. Price. 'Passive-active vibration isolation systems to produce zero or infinite dynamic modulus: Theoretical and conceptual design strategies'. *Journal of Sound and Vibration* 286.3 (2005), pp. 615–636. DOI: 10.1016/j.jsv.2004.10.018 (cit. on pp. 12, 39).

[294] D. Xu, Q. Yu, J. Zhou, and S. Bishop. 'Theoretical and experimental analyses of a nonlinear magnetic vibration isolator with quasi-zero-stiffness characteristic'. *Journal of Sound and Vibration* 332.14 (07/2013), pp. 3377–3389. DOI: 10.1016/j.jsv.2013.01.034 (cit. on p. 38).

[295] Z. Xu and H. Tamura. 'Analyses of the chaotic vibration of a magnetically levitated body'. *Memoirs of the Faculty of Engineering, Kyushu University* 53.4 (12/1993), pp. 209–233. DOI: http://ci.nii.ac.jp/naid/110000020124/en/ (cit. on p. 195).

[296] S. Yamaguchi, M. Ogiue-Ikeda, M. Sekino, and S. Ueno. 'Effects of magnetic stimulation on tumors and immune functions'. *IEEE Transactions on Magnetics* 41.10 (2005), pp. 4182–4184. DOI: 10.1109/TMAG.2005.854841 (cit. on p. 23).

[297] B. Yan, M. J. Brennan, S. J. Elliott, and N. S. Ferguson. *Velocity feedback control of vibration isolation systems*. ISVR Technical Memorandum 962. University of Southampton, 03/2006. URL: http://www.isvr.soton.ac.uk/STAFF/Pubs/Pubpdfs/Pub8483.pdf (cit. on p. 10).

[298] L. Yan, I.-M. Chen, G. Yang, and K.-M. Lee. 'Analytical and experimental investigation on the magnetic field and torque of a permanent magnet spherical actuator'. *IEEE/ASME Transactions on Mechatronics* 11.4 (08/2006), pp. 409–419. DOI: 10.1109/TMECH.2006.878545 (cit. on p. 131).

[299] L. Yan, I.-M. Chen, C. K. Lim, G. Yang, W. Lin, and K.-M. Lee.
'Design and analysis of a permanent magnet spherical actuator'.
IEEE/ASME Transactions on Mechatronics 13.2 (04/2008), pp. 239–248.
DOI: 10.1109/TMECH.2008.918573 (cit. on p. 166).

[300] W. Yang, C. Hu, M. Q.-H. Meng, S. Song, and H. Dai.
'A six-dimensional magnetic localization algorithm for a rectangular magnet objective based on a particle swarm optimizer'.
IEEE Transactions on Magnetics 45.8 (08/2009), pp. 3092–3099.
DOI: 10.1109/TMAG.2009.2019116 (cit. on p. 23).

[301] J.-P. Yonnet. 'Passive magnetic bearings with permanent magnets'.
IEEE Transactions on Magnetics MAG-14.5 (1978), pp. 803–805.
DOI: 10.1109/TMAG.1978.1060019 (cit. on pp. 26, 82).

[302] J.-P. Yonnet. 'Permanent magnet bearings and couplings'.
IEEE Transactions on Magnetics MAG-17.1 (01/1981), pp. 1169–1173.
DOI: 10.1109/TMAG.1981.1061166 (cit. on p. 26).

[303] J.-P. Yonnet and H. Allag. 'Three-dimensional analytical calculation of permanent magnet interactions by "magnetic node" representation'.
IEEE Transactions on Magnetics 47.8 (2011).
DOI: 10.1109/TMAG.2011.2122339 (cit. on pp. 72, 74).

[304] J.-P. Yonnet, G. Lemarquand, S. Hemmerlin, and E. Olivier-Rulliere.
'Stacked structures of passive magnetic bearings'.
Journal of Applied Physics 70.10 (11/1991), pp. 6633–6635.
DOI: 10.1063/1.349857 (cit. on p. 129).

[305] H. Yoshioka, Y. Takahashi, K. Katayama, T. Imazawa, and N. Murai. 'An active microvibration isolation system for hi-tech manufacturing facilities'.
Journal of Vibration and Acoustics 123.2 (2001), pp. 269–275.
DOI: 10.1115/1.1350566 (cit. on p. 2).

[306] B. Zhang, S. A. Billings, Z.-Q. Lang, and G. R. Tomlinson.
'A novel nonlinear approach to suppress resonant vibrations'.
Journal of Sound and Vibration 317.3 (2008), pp. 918–936.
DOI: 10.1016/j.jsv.2008.03.041 (cit. on p. 36).

[307] D. Zhang and C. S. Koh. 'An efficient semianalytic computation method of magnetic field for a circular coil with rectangular cross section'.
IEEE Transactions on Magnetics 48.1 (01/2012), pp. 62–68.
DOI: 10.1109/TMAG.2011.2167981 (cit. on p. 59).

[308] Y.-Y. Zhao and J. Xu.
'Effects of delayed feedback control on nonlinear vibration absorber system'.
Journal of Sound and Vibration 308.1–2 (11/2007), pp. 212–230.
DOI: 10.1016/j.jsv.2007.07.041 (cit. on p. 15).

[309] N. Zhou and K. Liu.
'A tunable high-static-low-dynamic stiffness vibration isolator'.
Journal of Sound and Vibration 329.9 (2010), pp. 1254–1273.
DOI: 10.1016/j.jsv.2009.11.001 (cit. on pp. 38, 108).

[310] T. Zhu, B. Cazzolato, W. Robertson, and A. Zander.
'The development of a 6 degree of freedom quasi-zero stiffness maglev vibration isolator with adaptive-passive load support'.
15th International Conference on Mechatronics Technology. 2011.
URL: http://hdl.handle.net/2440/72548 (cit. on pp. 45, 212).

[311] W.-H. Zhu, B. Tryggvason, and J.-C. Piedboeuf.
'On active acceleration control of vibration isolation systems'.
Control Engineering Practice 14.8 (08/2006), pp. 863–873.
DOI: 10.1016/j.conengprac.2005.04.016 (cit. on pp. 9, 14).

[312] Z. Zhu and D. Howe.
'Halbach permanent magnet machines and applications: A review'.
IEE Proceedings - Electric Power Applications 148.4 (07/2001), pp. 299–308.
DOI: 10.1049/ip-epa:20010479 (cit. on p. 131).

APPENDIX

A

Reproducible research

One of my strong beliefs that has arisen from my short time in the academic world is that as work is distributed electronically and the sheer amount of human knowledge grows ever larger, the utility of academic work in a vacuum grows smaller. My views here follow closely in the wake of the 'reproducible research' movement, which is pithily espoused by Kovacevic [159]:

> [*A*] *scientific article is merely advertisement of scholarship; the real scholarship includes software and data which went into producing the article.*

Reproducible research, therefore, is not just a clear explanation of the work in a thesis or article, but includes a publicly accessible repository of software and data by which means other researchers can follow directly without the inefficiences of re-inventing the wheel. It would be a great and noble achievement to apply this principle to every postgraduate thesis; unfortunately, only aspects of my work live up to this promise.

The principle contribution of my work in the area of reproducible research is the publication of a compilation of code for calculating the forces between magnets and magnetic systems at the following address:

⟨`http://www.github.com/wspr/magcode`⟩

Without delving into the details too fully, the main motivation for publishing this code is that there are a myriad of typographical errors in the literature for calculating the forces and torques between magnets. (Examples omitted as no blame is wished to be placed; suffice it to say that my own publications have errors of their own.) Equations in a journal manuscript have no meaning aside their typographical representation which can often be unclear or contain errors from the publication process. On the other hand, equations in a piece of computer code have intrinsic meaning in that they are a concrete instantiation of a particular mathematical theory.

The specific advantage of publishing code and not just equations in a typeset form are that errors are almost impossible to transmit in this form — unless the theory itself has not been validated correctly, which should rarely happen. Being able to take another researcher's code and re-purpose it for a new piece of scholarship decreases the chances of error, improves efficiency,

and in the long run builds a more stable basis for the hypothetical 'pyramid of knowledge' that we are slowly constructing in the academic world.

Clarifying example

In this thesis, I have not included any programming code as part of the main text. To help clarify my point for this section, consider the equation for the force exerted between two coaxial circular current carrying coils:

$$F_f(r_1, r_2, z) = \mu_0 I_1 I_2 z \sqrt{\frac{m}{4 r_1 r_2}} \left[K(m) - \frac{m/2 - 1}{m - 1} E(m) \right], \tag{A.1}$$

where

$$m = \frac{4 r_1 r_2}{\left[r_1 + r_2\right]^2 + z^2}.$$

The exact terms are not important at this point (for reference, they are explained in context in Section 5.2.1).

My point is that Eq. A.1 is of academic merit only; it cannot be used directly in any computational system to calculate this force. By contrast, if I provide some Mathematica code for the same, it now becomes straightforward[1] to use it for some calculation:

```
CoilCoilForce[I1_,I2_,r_,R_,z_] = With[ {m=4 r R/((r+R)^2+z^2)},
  I1 I2 4 \[Pi] 10^-7 Sqrt[m] z
  ( 2 EllipticK[m] - (2-m)/(1-m) EllipticE[m] ) / (4 Sqrt[r R])
];
```

As this code is used directly to produce calculations of results, it is much more likely to be correct than a transcribed equation.

This equation has not been chosen randomly; it emphasises one of the advantages of sharing code rather than just equations. When one comes across the elliptic integrals $K(\cdot)$ and $E(\cdot)$ it can be unclear what notation is being used (which is not always clarified); in some cases, the argument might be for the elliptic parameter m, other times the elliptic modulus k; they are equivalent and related by $K(m) = K\left(k^2\right)$ but without context it can be hard to know which is intended. If code is provided, there is no chance of misunderstanding.

1. If you indeed have Mathematica; I'll not go into that philosophical can of worms here.

Sections of this thesis which are reproducible

As mentioned previously, the source for the reproducible material in this thesis is located in the 'magcode' Github repository, which contains both Matlab and Mathematica libraries for various magnetic calculations. (And even a bridge from Matlab to ANSYS for certain types of magnetic force calculation, although this work is preliminary.) The libraries have evolved independently for each mathematical language and currently contain differences in their coverage of this work and the literature; the principle goal is to have them extended (beyond the lifetime of this thesis) to complete coverage across a wide range of magnetic systems for a multitude of programming languages.

The following list ties sections of this thesis with code from the repository. Not all figures in each section will be reproducible from this list, but most should be.

Section 3.2	'examples/mag_ratio.m'
Section 3.4	'examples/oblique/'
Chapter 4	'examples/multipole_example.m'
Section 4.3	'examples/magspring/'
Section 4.4	'examples/planar_compare/'
	'examples/multipole_example.m'
Sections 5.2 and 5.3	'examples/Thick-Coil-Magnet-Forces.nb'

The LaTeX source for this thesis itself, including the programmatically drawn figures, is available in

⟨http://www.github.com/wspr/thesis⟩.

While use of this material is restricted under the copyright of The University of Adelaide, the methods used for writing may be instructive for others following a similar path to my own.